**POLYTECHNIQUE MONTRÉAL**

affiliée à l'Université de Montréal

# Artificial neural network model-based optimization on the mapping between equivalent circuit model and physical field model

**CHANDAN ROY**

Département de génie électrique

Thèse présentée en vue de l'obtention du diplôme de *Philosophiæ Doctor*

Génie électrique

Septembre 2023

**POLYTECHNIQUE MONTRÉAL**

affiliée à l'Université de Montréal

Cette thèse intitulée :

# Artificial neural network model-based optimization on the mapping between equivalent circuit model and physical field model

présentée par **Chandan ROY**

en vue de l'obtention du diplôme de *Philosophiæ Doctor*

a été dûment acceptée par le jury d'examen constitué de :

**Raman KASHYAP**, président

**Ke WU**, membre et directeur de recherche

**Tarek DJERAFI**, membre

**Costas SARRIS**, membre externe

# DEDICATION

*To my mother Luxmi Roy and my father Ajoy Kumar Roy*

*To my wife Shreyasee Barai*

# ACKNOWLEDGEMENTS

Foremost, I would like to express my deepest appreciation and sincere gratitude to my supervisor, Professor Ke Wu, for granting me the invaluable opportunity to conduct research under his expert guidance. I am deeply grateful to Professor for his vast knowledge and broad perspectives, which have continuously motivated me to maintain my focus throughout my research journey. His unwavering support has significantly contributed to my growth as a researcher, and I cannot imagine completing all the research work on schedule without his invaluable feedback and encouragement. I want to express my heartfelt thanks to Professor for inspiring and guiding me right from the outset of my PhD research.

I would also like to express my gratitude to the president Prof. Raman Kashyap and other committee members Prof. Tarek Djerafi, and Prof. Costas Sarris for reviewing my thesis and providing me with their valuable support and insightful comments.

I would also like to extend my gratitude to the technician and administrative team at Poly-GRAMES Research Center, especially Mr. Jean-Sébastien Décarie, Mr. Jules Gauthier, Mr.Traian Antonescu, Mr. Steve Dube, Mrs. Rachel Lortie , and Mrs. Brigitte.

I am deeply grateful to my colleagues in our research group for their friendship and assistance. I would like to express my gratitude to Dr. Ping Zhao, especially for guiding me during the initial stage of my PhD journey. Furthermore, I would like to thank Dr. David Dousset, Dr. Louis Philippe, Dr. Pascal Burasa, Dr. Wentao Lin, Dr. Srinaga Nikhil Nallandhigal and Dr. Xiaoqiang Gu for our constructive discussion towards my research. I would like to extend a special thank you to my friends, Dr. Muhibur Rahman and Mr. Amirhossein Askarian, for their emotional support since my first day at Polytechnique Montreal. I also acknowledge everyone who have helped in numerous ways during my Ph.D study in Canada.

Finally, yet most importantly, I express my immense gratitude to my parents, Luxmi Roy and Ajoy Kumar Roy, whose lifelong dedication and unwavering support have played a crucial role in my professional success. I am profoundly thankful to my wife, Shreyasee Barai, who has consistently supported me in every important decision I have made since we first met two years ago. Her unwavering love and support during my Ph.D. study in Canada have been indispensable, and I could not have reached where I am today without her constant encouragement and understanding.

# RÉSUMÉ

Le système de communication sans fil actuel et futur se compose de composants passifs tels qu'un filtre, un filtre accordable, un diviseur, un coupleur directionnel, etc. en tant que blocs de construction fondamentaux. Ces composants passifs ont été développés pour de nombreuses applications en ondes millimétriques (mmW) et térahertz (THz) afin de répondre aux exigences des technologies en constante évolution. De telles applications haute fréquence rendent ces circuits passifs ultra-sensibles aux paramètres géométriques. Les équations de conception empiriques existantes fournissent un point de référence pour la conception du circuit en fonction des performances souhaitées. Cependant, des simulations électromagnétiques (EM) pleine onde sont nécessaires pour la vérification de la conception du circuit. Le plus souvent, nous devons mettre en œuvre des méthodes d'optimisation afin de trouver le modèle EM optimal de la structure cible. Le processus de va-et-vient intimidant de la procédure de modélisation et d'optimisation EM est une pratique courante de nos jours.

En conséquence, il est grand temps de développer des modèles et des techniques numériques avancés pour réduire le temps de développement et les dépenses de calcul des modèles EM réussis, qui font l'objet de nombreuses recherches ces dernières années. Le réseau de neurones artificiels (ANN) est largement utilisé dans la littérature pour minimiser le temps de conception global du circuit en remplaçant le modèle EM. De plus, différents types de modèles d'optimisation sont utilisés pour optimiser le modèle EM cible. De plus, la technique de cartographie spatiale utilise le modèle de circuit équivalent comme modèle grossier pour optimiser efficacement le modèle EM. Motivés par tous ces travaux, nous avons proposé et développé la cartographie entre le modèle de circuit équivalent et le modèle de champ physique en introduisant le modèle ANN. Une technique d'optimisation hybride est utilisée pour les optimisations nécessaires. L'objectif de cette recherche est de développer un modèle de circuit équivalent du modèle de champ d'une structure cible et de créer une technique de cartographie précise entre ces deux.

Une architecture neuronale basée sur une équation d'impédance de ligne de transmission fondamentale est développée pour une meilleure mise en œuvre du modèle ANN dans le cas de problèmes spécifiques à l'ingénierie des micro-ondes. Le réseau d'alimentation directe et l'algorithme de rétropropagation sont dérivés et expliqués mathématiquement. Le modèle ANN proposé est validé par la conception d'un coupleur cruciforme en bande D. En outre, une technique

de développement de modèle ANN est décrite pour trouver les paramètres de circuit équivalents appropriés par rapport aux performances de coupleur souhaitées. Toutes ces contributions sont discutées dans le chapitre 3.

Une technique d'optimisation hybride a été introduite pour la génération de données du modèle ANN de filtres accordables. Les modèles basés sur les métaheuristiques et les modèles basés sur les mathématiques sont hybrides pour le problème d'optimisation compliqué tel que les filtres accordables. De plus, une méthode de mise en œuvre du modèle ANN est expliquée pour la conception de filtres accordables. Aux fins de validation, un filtre accordable bimode et un filtre accordable à bande passante absolue constante sont caractérisés. Ces contributions sont bien articulées au chapitre 4.

Dans le chapitre 5, une méthode est développée pour la cartographie basée sur le modèle ANN entre le modèle de circuit équivalent et le modèle de champ physique. Encore une fois, le filtre passe-bande accordable est considéré comme un exemple de conception pour démontrer la méthodologie initiale vers le mappage réussi entre ces deux modèles. Un exemple pratique de filtre à cavité circulaire accordable en fréquence est présenté ici comme preuve de concept.

Une technique d'étalonnage numérique est présentée au chapitre 6, appelée short-open-thru (SOT), qui surmonte les lacunes de la technique de short-open-load-thru (SOL) récemment publiée. En outre, une technique de développement de modèle de circuit équivalent précis est expliquée étape par étape pour les discontinuités de la ligne de transmission. Trois discontinuités élémentaires telles que la discontinuité de l'espacement de la ligne microruban (MSL), la discontinuité de l'étape MSL et la discontinuité du trou d'interconnexion dans un substrat à deux couches sont illustrées. Un filtre tripolaire couplé aux extrémités est démontré comme validation expérimentale. Le chapitre 6 détaille toutes ces contributions.

Le chapitre 7 présente la méthode de développement d'un modèle de circuit équivalent complet à partir d'un modèle de champ cible d'une structure prenant en compte des couplages mutuels d'ordre différent. Le chapitre 8 décrit une méthodologie de développement du modèle ANN pour trouver le mappage approprié entre les paramètres de circuit équivalents et les paramètres géométriques du modèle EM correspondant. Enfin, l'algorithme d'optimisation est appliqué sur un modèle de circuit équivalent et les paramètres géométriques du modèle EM généré par le modèle ANN sont déterminés. Un filtre à ouverture résonnante (RA) à double bande et un filtre passe-bande de guide

d'ondes diélectrique non radiatif (NRD) sont présentés à titre d'exemples illustratifs. Enfin, le chapitre 9 est consacré aux discussions générales et le chapitre 10 propose des travaux futurs et des recommandations.

# ABSTRACT

Current and future wireless systems consist of numerous passive components such as filter, tunable filter, divider, directional coupler etc. as fundamental building blocks. These passive components have been developed for many millimeter-wave (mmW) and terahertz (THz) applications to meet the requirements of continuously evolving technologies. Such high-frequency applications make these passive circuits ultra-sensitive to their geometric and material parameters. The existing empirical design equations provide a reference point for the circuit design according to the desired performance. However, full-wave electromagnetic (EM) simulations are generally required for the verification of such a circuit design. More often, we need to implement optimization methods to find the optimum EM model of the target structure. The intimidating back and forth process of EM modeling and optimization procedure is a matter of common practice these days.

As a result, it is a high time to develop advanced numerical models and techniques to reduce the developing time and computational expense of successful EM models, which are being widely studied in the recent years. Artificial neural network (ANN) is widely used in the literature to minimize the overall circuit design time by replacing the EM model. In addition, different types of optimization models are used to optimize the target EM model. Furthermore, the space-mapping technique utilizes an equivalent circuit model as a coarse model to optimize the EM model efficiently. Motivated by all these works, we have proposed and developed the mapping between equivalent circuit model and physical field model by introducing an ANN model. A hybrid optimization technique is used for required optimizations. The objective of this research is to develop an equivalent circuit model of a target structure's field model and to create an accurate mapping technique between these two models.

A fundamental transmission line impedance equation-based neural architecture is developed for a better implementation of ANN models in the case of specific microwave engineering problems. The feedforward network and back propagation algorithms are mathematically derived and explained. The proposed ANN model is validated by designing a D-band cruciform coupler. In addition, an ANN model development technique is outlined for finding appropriate equivalent circuit parameters against desired coupler performance. All these contributions are discussed in Chapter 3.

Further, a hybrid optimization technique has been introduced for the ANN model data generation of tunable filters. Metaheuristic-based models and mathematics-based models are hybridized for complex optimization problems such as tunable filters. Moreover, an ANN model implementation method is explained for the design of tunable filters. For validation purpose, a dual-mode tunable filter and a constant absolute bandwidth tunable filter are characterized. These contributions are well articulated in Chapter 4.

In Chapter 5, a method is developed for the ANN model-based mapping between equivalent circuit model and physical field model. Again, tunable bandpass filter is considered as a design example for demonstrating the initial methodology towards a successful mapping between those two models. A practical example of frequency tunable circular cavity filter is demonstrated here as a proof of concept.

A numerical calibration technique is introduced in Chapter 6 named as short-open-thru (SOT) calibration that overcomes the shortcomings of recently published short-open-load (SOL) de-embedding technique. Furthermore, an accurate equivalent circuit model development technique is explained step-by-step for transmission line discontinuities. Three elementary discontinuities such as microstrip line (MSL) gap discontinuity, MSL step discontinuity, and via-hole discontinuity in two-layered substrate are exampled and characterized. An end-coupled three pole filter is demonstrated as an experimental validation. Chapter 6 discusses all these contributions in details.

Chapter 7 presents a method for developing a complete equivalent circuit model from a target field model of a structure considering mutual couplings of different order. Chapter 8 outlines a methodology of developing the ANN model to find an appropriate mapping between the equivalent circuit parameters and corresponding EM model's geometric parameters. Finally, the optimization algorithm is applied to equivalent circuit model and calculate the optimized geometric parameters from the proposed mapping technique. A dual-band resonant aperture (RA) filter and a nonradiative dielectric (NRD) waveguide bandpass filter are demonstrated as illustrative examples. Finally, Chapter 9 is dedicated to general discussions and Chapter 10 comes up with future works and recommendation.

# TABLE OF CONTENTS

DEDICATION ..... III

ACKNOWLEDGEMENTS ..... IV

RÉSUMÉ ..... V

ABSTRACT ..... VIII

LIST OF TABLES ..... XVI

LIST OF FIGURES ..... XVIII

LISTE OF SYMBOLS AND ABBREVIATIONS ..... XXV

LIST OF APPENDICES ..... XXVII

CHAPTER 1 INTRODUCTION ..... 1

1.1 Motivation and objectives ..... 1

1.2 Outline and contributions of this thesis ..... 2

CHAPTER 2 ARTICLE 1: A REVIEW ON ELECTROMAGNETIC-BASED MICROWAVE CIRCUIT DESIGN OPTIMIZATION ..... 8

2.1 Introduction ..... 8

2.2 Direct optimization methods ..... 13

2.2.1 Gradient-based optimization methods ..... 13

2.2.2 Meta-heuristic-based optimization algorithm ..... 15

2.3 ANN based surrogate model optimization ..... 23

2.3.1 ANN structure and training strategy ..... 23

2.3.2 ANN-based surrogate model for EM optimization ..... 27

2.4 SM-based surrogate model optimization ..... 28

2.4.1 Space mapping technology ..... 29

2.4.2 Aggressive space mapping (ASM) approach ..... 32

2.4.3 Trust region ASM approach ..... 33
2.5 ANN and SM crossover ..... 35
2.6 Illustrative examples ..... 38
2.6.1 Microstrip lines with discontinuities ..... 38
2.6.2 Microwave filters ..... 40
2.6.3 Microwave tunable filters ..... 44
2.6.4 Coupler and divider ..... 44
2.6.5 Antennas ..... 46
2.7 Discussions and future directions ..... 48
2.8 Conclusion ..... 52
CHAPTER 3 ARTICLE 2: HOMOTOPY OPTIMIZATION AND ANN MODELING OF MILLIMETER-WAVE SIW CRUCIFORM COUPLER ..... 54
3.1 Introduction ..... 55
3.2 ANN model ..... 58
3.2.1 ANN model feedforward network ..... 58
3.2.2 Data preprocessing ..... 59
3.2.3 Parameters initialization ..... 60
3.2.4 Levenberg Marquardt's algorithm ..... 60
3.3 Homotopy optimization technique ..... 62
3.4 Optimization of cruciform coupler ..... 63
3.4.1 EM-ANN model ..... 64
3.4.2 Homotopy optimization ..... 67
3.4.3 SIW cruciform coupler measurement ..... 71
3.4.4 SIW cruciform coupler bandwidth and equivalent circuit ..... 73
3.4.5 Related results ..... 74

3.5 ANN modeling of cruciform coupler equivalent circuit ..... 75
3.5.1 ANN model development algorithm ..... 76
3.5.2 Example model and results ..... 78
3.6 General discussion ..... 81
3.7 Conclusion ..... 82
CHAPTER 4 ARTICLE 3: SWARM INTELLIGENCE-HOMOTOPY HYBRID OPTIMIZATION-BASED ANN MODEL FOR TUNABLE BANDPASS FILTER ..... 84
4.1 Introduction ..... 84
4.2 ANN model and homotopy optimization ..... 88
4.2.1 ANN model ..... 88
4.2.2 Homotopy optimization ..... 89
4.3 Swarm-based meta-heuristic algorithms ..... 89
4.3.1 Whale optimization algorithm (WOA) ..... 89
4.3.2 Improved whale optimization algorithm (NGS-WOA) ..... 91
4.3.3 Grey wolf optimization (GWO) ..... 92
4.4 Hybrid optimizer assisted ANN model development algorithm ..... 94
4.4.1 Cost function definition ..... 95
4.4.2 ANN model development algorithm ..... 97
4.5 Illustrative examples ..... 101
4.5.1 Lumped element tunable filter circuit ..... 101
4.5.2 Electromagnetic model of tunable filter-1 ..... 104
4.5.3 Electromagnetic model of tunable filter-2 ..... 108
4.6 Related works and discussions ..... 111
4.7 Conclusion ..... 114

CHAPTER 5 ARTICLE 4: ANN-ENABLED MAPPING BETWEEN EQUIVALENT CIRCUIT MODEL AND PHYSICAL FIELD MODEL FOR TUNABLE BANDPASS FILTER ..... 115

5.1 Introduction ..... 115

5.2 Equivalent circuit model and ANN model ..... 116

5.3 ANN model development algorithm ..... 117

5.4 Design example ..... 120

5.5 Conclusion ..... 122

CHAPTER 6 ARTICLE 5: A GENERALIZED CIRCUIT MODEL DEVELOPMENT APPROACH WITH SHORT OPEN THRU (SOT) DE-EMBEDDING TECHNIQUE AND ITS APPLICATIONS ..... 123

6.1 Introduction ..... 123

6.2 Numerical SOT de-embedding technique ..... 127

6.2.1 TRL calibration ..... 127

6.2.2 SOC technique ..... 128

6.2.3 Implementation of the proposed SOT method ..... 129

6.3 Holistic circuit model development ..... 132

6.4 Illustrative examples of elementary discontinuities ..... 140

6.4.1 Microstrip gap discontinuity ..... 140

6.4.2 Microstrip step discontinuity ..... 143

6.4.3 Via-hole discontinuity in a two-layered substrate ..... 146

6.5 Circuit design and experimental validation ..... 149

6.6 Discussions ..... 151

6.7 Conclusion ..... 152

CHAPTER 7 ARTICLE 6: HIGH-ORDER EQUIVALENT CIRCUIT MODEL DEVELOPMENT ACCOUNTING FOR MUTUAL- COUPLING EFFECTS ..... 154

7.1 Introduction ..... 154

7.2 Equivalent circuit model development technique ..... 157

7.3 Equivalent network of transmission line discontinuities ..... 158

7.4 Equivalent network of mutual couplings ..... 161

7.4.1 Equivalent network of first order mutual coupling ..... 161

7.4.2 Equivalent network of higher order mutual coupling ..... 163

7.5 Illustrative examples ..... 165

7.5.1 Application example of fifth-order microstrip filter ..... 166

7.5.2 Application example of parallel-coupled microstrip filter ..... 171

7.6 Discussions ..... 173

7.7 Conclusion ..... 174

CHAPTER 8 ARTICLE 7: ANN MODEL-BASED ELECTROMAGNETIC OPTIMIZATION BY FIELD-CIRCUIT MODEL MAPPING ..... 175

8.1 Introduction ..... 175

8.2 Equivalent circuit model development technique ..... 178

8.2.1 Equivalent circuit model of elementary discontinuity ..... 179

8.2.2 Equivalent circuit model of mutual couplings ..... 183

8.3 ANN model and hybrid optimization algorithm ..... 184

8.3.1 ANN model ..... 184

8.3.2 Hybrid optimization algorithm ..... 185

8.4 ANN model development and mapping technique ..... 186

8.5 Illustrative Examples ..... 189

8.5.1 Dual-band resonant aperture (RA) filter ..... 189

8.5.2 Three-pole bandpass NRD filter ..... 194
8.6 Discussions ..... 196
8.7 Conclusion ..... 198
CHAPTER 9 GENERAL DISCUSSIONS ..... 199
CHAPTER 10 CONCLUSION AND RECOMMENDATIONS ..... 201
10.1 Conclusion ..... 201
10.2 Recommendations ..... 202
REFERENCES ..... 203
APPENDICES ..... 221

# LIST OF TABLES

Table 2.1 Comparison of optimization algorithms ..... 48

Table 2.2 Comparison of optimization algorithms (cont'd) ..... 49

Table 2.3 Comparison of optimization algorithms (cont'd) ..... 50

Table 2.4 Comparison of optimization algorithms (cont'd) ..... 51

Table 3.1 Comparison of Conventional and Proposed ANN Formulation with AMG [113] and Manual Step-by-step ANN Models ..... 66

Table 3.2 Design parameters of the cruciform coupler obtained in each homotopy optimization step ..... 70

Table 3.3 Design parameters of the cruciform coupler obtained from different optimization algorithms ..... 74

Table 3.4 Performance comparison of different optimization algorithms ..... 75

Table 3.5 ANN model inputs and outputs of the exampled coupler circuits ..... 80

Table 4.1 State variables at different tuning state (ANN model inputs) ..... 102

Table 4.2 Tunable circuit parameters of lumped element circuit model (ANN model outputs). 103

Table 4.3 Target tunable-ANN model inputs and outputs ..... 107

Table 4.4 Different tuning state of tunable BPF-2 EM model (ANN inputs) ..... 109

Table 4.5 Height of tuning posts of tunable BPF-2 (ANN outputs) ..... 110

Table 4.6 Reduced cost function from different optimizers ..... 112

Table 5.1 EM model tunable parameters against equivalent circuit model parameters at different tuning states ..... 122

Table 6.1 Bandwidth invariant circuit parameters ..... 152

Table 7.1 Inductances at different model development stages (Fifth order microstrip filter example) ..... 170

Table 7.2 Inductances at different model development stages (Fifth order microstrip filter example) ..... 171

Table 8.1 Circuit parameters at different model development stages (RA filter example) ..... 197

Table 8.2 Circuit parameters at different model development stages (NRD filter example)..... 197

# LIST OF FIGURES

Figure 2.1 Holistic classification of EM-based optimization techniques..... 12

Figure 2.2 A mapping between coarse model and fine model [53] ..... 30

Figure 2.3 Basic notation of space mapping technique [53] ..... 30

Figure 2.4 Variation of SM based neuromodeling concept [53]; (a) SMN; (b) FDSMN; (c) FSMN; (d) FMN concept. ..... 36

Figure 2.5 Linear-input neural-output space mapping technique [132] ..... 37

Figure 2.6 Microstrip discontinuity (a) Bend (b) Step [125] ..... 39

Figure 2.7 Microstrip-shaped T-junction (a) Fine model (b) Coarse model [125] ..... 39

Figure 2.8 Three-section microstrip impedance transformer (a) Fine model (b) Coarse model [135] ..... 40

Figure 2.9 Six-section H-plane waveguide filter [127] (a) fine-model (b) coarse model ..... 41

Figure 2.10 EM model of a four-pole H-plane waveguide filter with tuning elements [119] ..... 41

Figure 2.11 The DFS filter [127] (a) fine-model (b) coarse model..... 42

Figure 2.12 The HTS filter [51] (a) fine-model (b) coarse model ..... 43

Figure 2.13 Microstrip notch filter with mitered bends [42] (a) fine model (b) coarse model ..... 43

Figure 2.14 Tunable waveguide filters [41] (a) dual-mode filter (b) constant bandwidth filter ... 44

Figure 2.15 SIW cruciform coupler [32]..... 45

Figure 2.16 Dual-band branch-line coupler [18]..... 45

Figure 2.17 Dual-band equal split power divider [18] ..... 45

Figure 2.18 SIW cavity-backed slot antenna [38]..... 46

Figure 2.19 Geometry of the four-element LAA [38]..... 46

Figure 2.20 Multiband monopole antenna structure [39]..... 47

Figure 3.1 Sketch of a SIW cruciform coupler ..... 56

Figure 3.2 SIW cruciform coupler (top view) sketched with geometric dimensions ..... 64

Figure 3.3 ANN model for the cruciform coupler ..... 67

Figure 3.4 SIW cruciform coupler responses calculated by four surrogate models using the initial design values. (a) AMG [113] (Conventional Architecture). (b) AMG [113] (Proposed Architecture). (c) Manual Modeling (Conventional Architecture). (d) Manual Modeling (Proposed Architecture). ..... 67

Figure 3.5 Cruciform coupler's optimized performance in the homotopy optimization steps. (a) $\rho = 0$. (b) $\rho = 0.2$. (c) $\rho = 0.4$. (d) $\rho = 0.6$. (e) $\rho = 0.8$. (f) $\rho = 1.0$. ..... 69

Figure 3.6 Comparison between S-parameters computed by full-wave EM simulation and its related ANN surrogate model. ..... 70

Figure 3.7 Fabricated prototype. (a) Planar circuit. (b) Metallic mount ..... 72

Figure 3.8 Measurement setup of SIW cruciform coupler ..... 72

Figure 3.9 S-Parameters comparison between simulation and measurement ..... 72

Figure 3.10 Bandwidth analysis of the SIW cruciform coupler ..... 73

Figure 3.11 Equivalent circuit model of the SIW cruciform coupler ..... 74

Figure 3.12 S-Parameters from different optimization algorithms (a) Quasi-newton (b) Genetic algorithm (c) Sequential non-linear programming ..... 75

Figure 3.13 ANN model-assisted circuit parameter extraction. (a) Automatic data generation process (b) ANN model ..... 79

Figure 3.14 Coupler circuit performance comparison between ANN model extracted parameters based lumped element circuit and full wave EM simulation from (a) [148] , (b) [149] and (c) this work ..... 80

Figure 4.1 Typical S-Parameters of a sixth order BPF ..... 95

Figure 4.2 Flowchart of training data generation ..... 96

Figure 4.3 Pseudo code of the proposed hybrid algorithm ..... 99

Figure 4.4 Fifth order tunable BPF prototype ..... 102

Figure 4.5 Tunable ANN model ..... 102

Figure 4.6 S-Parameters from tunable ANN model generated BPF circuit parameters ..... 102

Figure 4.7 Tunable BPF (a) Electromagnetic model [180]. (b) EM-ANN model ..... 105

Figure 4.8 S-Parameters comparison between full wave EM model and ANN Surrogate model ..... 106

Figure 4.9 Target-tunable ANN model ..... 107

Figure 4.10 Simulated and measured performance from ANN model generated via heights. (a) Reflection responses (b) Transmission responses ..... 107

Figure 4.11 Photograph of the fabricated prototype [180] ..... 107

Figure 4.12 Electromagnetic model of a constant absolute bandwidth tunable BPF [181] ..... 109

Figure 4.13 Target-tunable ANN model ..... 109

Figure 4.14 Simulated performance from ANN model generated post heights of tunable BPF-2. (a) Reflection responses (b) Transmission responses ..... 110

Figure 4.15 Convergence comparison between different optimizers at tuning (a) state-1 (b) state-2 (c) state-3 ..... 112

Figure 5.1 Flowchart of the complete model development procedure ..... 119

Figure 5.2 Target tBPF (a) EM model [189] (b) Equivalent circuit model ..... 121

Figure 5.3 Target ANN model for equivalent circuit parameters mapping to EM model tunable parameters ..... 121

Figure 5.4 HFSS generated S Parameters of the target tunable filter at different tuning states .. 122

Figure 6.1 Schematic of SOT methods with cascaded equivalent error boxes and 3D geometries: (a) The whole equivalent circuit representation; (b) Equivalent short-end circuit standard for ideal SOC and SOT techniques; (c) Equivalent open-end circuit standard for ideal SOC and SOT techniques. (d) Equivalent thru connection standard of SOT technique ..... 128

Figure 6.2 Sampling strategy of arbitrary circuit parameters over a frequency band of interest 133

Figure 6.3 Flowchart of the proposed circuit model generation ..... 136

Figure 6.4 Step-by-step first stage network decomposition (T-T Combination) ..... 138

Figure 6.5 Evolution of T-equivalent circuit through different stages (a) Primary topology (b) $1st$ stage decomposed topology $[T-T]$ (c) $2nd$ stage decomposed topology $[T-T-T]$ (d) $Nth$ stage decomposed topology $[T-T-\cdots-T]$ ..... 138

Figure 6.6 Network topology after $Nth$ stage decomposition (a) $[T-T-T-\cdots-T-T]$ (b) $[T-\pi-T-\cdots-\pi-T]$ (c) $[\pi-\pi-\pi-\cdots-\pi-\pi]$ (d) $[\pi-T-\pi-\cdots-T-\pi]$ . 139

Figure 6.7 Microstrip line gap discontinuity: (a) Layout; (b) Primary circuit topology; (c) Circuit topology from 1st stage decomposition ..... 141

Figure 6.8 Extracted circuit parameters by the SOL and the proposed SOT: (a) primary circuit; (b) 1st stage decomposed circuit. In all the cases, S=0.4mm ..... 142

Figure 6.9 SOT-Extracted (1st stage decomposed) circuit parameters at different gap length $S$. (a) $C_1$; (b) $C_2$; (c) C; (d) L ..... 143

Figure 6.10 MSL step discontinuity: (a) Layout; (b) Primary circuit topology; (c) Circuit topology from 1st stage decomposition ..... 144

Figure 6.11 Extracted primary circuit parameters by the SOL and proposed SOT ..... 144

Figure 6.12 Extracted 1st stage decomposed circuit parameters by the SOL and proposed SOT: (a) Inductances; (b) Capacitances ..... 144

Figure 6.13 SOT extracted (1st stage decomposed) circuit parameters at different $W_1$ width: (a) $L_p$; (b) $L_q$; (c) $L_r$; (d) $L_s$; (e) $C_a$; (f) $C_b$ ..... 146

Figure 6.14 Via-hole discontinuity in two-layered substrate: (a) 3D Layout; (b) Primary circuit topology; (c) Circuit topology from 1st stage decomposition; (d) Circuit topology from 2nd stage decomposition ..... 147

Figure 6.15 Extracted primary circuit parameters by the SOL and proposed SOT ..... 148

Figure 6.16 Extracted 2nd stage decomposed circuit parameters by the SOL and proposed SOT: (a) Inductances (b); Capacitances ..... 149

Figure 6.17 SOT-extracted (2nd stage decomposed) circuit parameters at different inner diameter $d_1$: (a) $L_x$; (b) $L_y$; (c) $L_z$; (d) $C_x$; (e) $C_y$; (f) $C_z$ ..... 149

Figure 6.18 Three-pole microstrip end-coupled half-wavelength resonator filter. (a) Layout; (b) Equivalent circuit ..... 150

Figure 6.19 Comparison of S-parameters among equivalent circuits, EM simulation, and measurement results ..... 151

Figure 7.1 Maximum 3rd order mutual coupling involved target structure with K-number of discontinuities ..... 158

Figure 7.2 Network topology after $Nth$ stage decomposition [9] (a) $[T-T-T-\cdots-T-T]$; (b) $[T-\pi-T-\cdots-\pi-T]$; (c) $[\pi-\pi-\pi-\cdots-\pi-\pi]$; (d) $[\pi-T-\pi-\cdots-T-\pi]$ 161

Figure 7.3 Mutual couplings of different order in circuits (a) three transmission line discontinuities (b) four transmission line discontinuities (c) five transmission line discontinuities ..... 161

Figure 7.4 Complete equivalent circuit consisting of two mutually coupled transmission line discontinuities ..... 163

Figure 7.5 Complete equivalent circuit consisting of three mutually coupled transmission line discontinuities ..... 164

Figure 7.6 Target structure of a fifth-order microstrip filter ..... 166

Figure 7.7 Two gap coupled U-shaped resonators. (a) Full-wave structure (b) block diagram (c) equivalent circuit ..... 167

Figure 7.8 Three cascaded gap coupled U-shaped resonators represented by (a) block diagram (b) equivalent circuit ..... 168

Figure 7.9 Four cascaded gap coupled hairpin resonators setup (a) block diagram (b) equivalent circuit. ..... 169

Figure 7.10 Complete equivalent model of the target structure (a) block diagram (b) equivalent circuit model ..... 169

Figure 7.11 Target five-order microstrip filter response comparison between EM simulation and equivalent circuit simulation ..... 170

Figure 7.12 Equivalent circuit performance comparison of Example-1 at different mutual coupling situation (a) $S_{11}$(dB) (b) $S_{21}$(dB) ..... 171

Figure 7.13 Third-order parallel-coupled microstrip filter. (a) Layout (b) Equivalent circuit.... 172

Figure 7.14 Target three-order parallel-coupled microstrip filter response comparison between measurement, EM simulation and equivalent circuit simulation results..... 173

Figure 8.1 Frequency sampling of an arbitrary circuit parameter, $K1$ over the band of interest 180

Figure 8.2 Network topology after $Nth$ stage decomposition [218] (a) $[T-T-T-\cdots-T-T]$; (b) $[T-\pi-T-\cdots-\pi-T]$; (c) $[\pi-\pi-\pi-\cdots-\pi-\pi]$; (d) $[\pi-T-\pi-\cdots-T-\pi]$ ..... 182

Figure 8.3 Component decomposition (a) ideal component; (b) Series RL combination; (c) Parallel RL combination; (d) Series RC combination; (e) Parallel RC combination; (f) Series RLC combination; (c) Parallel RLC combination ..... 182

Figure 8.4 Mutual coupling between discontinuities (a) 1st order mutual coupling in two discontinuity scenario (b) 1st and 2nd order mutual coupling in three discontinuity scenario ..... 184

Figure 8.5 Flowchart of proposed mapping technique..... 187

Figure 8.6 Resonant aperture in a rectangular waveguide ..... 190

Figure 8.7 EM model of a dual-band RA filter structure ..... 190

Figure 8.8 Equivalent circuit model (a) Conventional model [223]; (b) Proposed circuit model191

Figure 8.9 S parameters generated from; (a) Conventional equivalent circuit model; (b) Proposed equivalent circuit model ..... 192

Figure 8.10 ANN model for geometric variables calculation against circuit model parameters 192

Figure 8.11 Simulated and measured performance of the designed dual-band RA filter ..... 193

Figure 8.12 Third order NRD BPF (a) EM model [224]; (b) Conventional equivalent circuit model; (c) Proposed equivalent circuit model..... 194

Figure 8.13 Performance comparison between conventional circuit model, proposed circuit model and EM model. (a) $S_{21}$; (b) $S_{11}$ ..... 195

Figure 8.14 ANN model for geometric variables calculation against circuit model parameters 196

Figure 8.15 Transmission loss characteristics in primary circuit model, proposed circuit model with in-line coupling only, and proposed circuit model with in-line and cross coupling. (a) RA filter example; (b) NRD filter example ..... 197

# LISTE OF SYMBOLS AND ABBREVIATIONS

| | |
|---|---|
| AI | Artificial intelligence |
| AMG | Automatic model generation |
| ANN | Artificial neural network |
| AROC | Average rate of change |
| ASM | Aggressive space mapping |
| BPF | Bandpass filter |
| CPU | Central processing unit |
| CPW | Coplanar waveguide |
| CAD | Computer-aided design |
| DE | Differential evolution |
| DNN | Deep neural network |
| FFNN | Feed forward neural network |
| EA | Evolutionary algorithm |
| EM | Electromagnetic |
| GA | Genetic algorithm |
| GWO | Grey wolf optimizer |
| HAM | Homotopy analysis method |
| HFSS | High frequency structure simulator |
| KBNN | Knowledge based neural network |
| LMA | Levenberg Marquardt’s algorithm |
| MHMIC | Miniature hybrid microwave integrated circuits |
| ML | Machine learning |
| MLP | Multilayer perceptron |

| | |
|---|---|
| mmW | Millimeter-wave |
| MSL | Microstrip line |
| NRD | Nonradiative dielectric |
| NSM | Neural space mapping |
| PSO | Particle swarm optimization |
| RA | Resonant Aperture |
| RBF | Radial basis function |
| RF | Radio frequency |
| RWG | Rectangular waveguide |
| SIW | Substrate integrated waveguide |
| SM | Space mapping |
| SOC | Short open calibration |
| TZ | Transmission zero |
| tBPF | Tunable bandpass filter |
| WOA | Whale optimization algorithm |

# LIST OF APPENDICES

APPENDIX A LIST OF PUBLICATIONS ..... 220

# CHAPTER 1 INTRODUCTION

## 1.1 Motivation and objectives

The constant growth of wireless technologies has resulted in the criticality of electromagnetic (EM) optimization as a necessary design phase for the development of passive circuits. In recent years, the continuous expansion of wireless communication and sensing technologies has led to the development of increasingly complex passive circuits. The design of these circuits requires a thorough understanding of EM optimization principles to ensure optimal performance in terms of signal quality, power efficiency, and noise reduction among many other aspects. The importance of EM optimization in passive circuit design cannot be overstated, as it plays a critical role in achieving the desired performance metrics or design specifications. During the past few decades, the field of EM optimization for passive circuits has been centered on the advancement of optimization techniques aimed at enhancing the design process and attaining superior performance metrics.

During the initial stages of microwave design, direct optimization techniques were initially employed on the distributed and lumped element circuit models. This involved the adoption of gradient-based optimization algorithms, such as quasi-Newton [1]. Subsequently, for the first time, during the design of a bandpass microstrip filter structure, EM simulations were directly integrated into a gradient-based optimizer [2]. A variety of direct optimizers have been employed for the optimal solution of EM based optimization problems. However, implementing optimization algorithms directly on EM simulations is an intimidating task due to its massive computational expense and prohibitive simulation time.

Artificial neural networks (ANNs) have been used extensively in the literature to replace the computationally expensive EM simulations. A wide range of ANN modeling strategies are developed to solve different types of structures under the EM simulations [3], [4], [5]. These ANN modeling strategies are focused on different challenges of model development process. Automated model generation techniques have also been explored in the literature [6]. To better learn the problem related to microwave applications, the ANN model should be generalized in terms of well-established microwave theory.

Prior knowledge from physical model has also been detailed in the existing ANN model studies. Such knowledge is often based on existing empirical formula, coarse model or physical relationships between model inputs and outputs [7], [8]. In order to integrate the physical interpretation of a target EM model structure into the ANN model, it is absolutely necessary to develop an accurate equivalent circuit model from the target EM model structure first.

Equivalent circuit parameter extraction from numerically calibrated scattering parameters of transmission line discontinuities is well studied in the literature [9]. Such studies are mainly focused on the characteristics of the elementary discontinuities over a narrow band of frequency. In order to generalize the equivalent circuit of a particular structure's EM model, it is important to introduce an equivalent circuit model development technique where the extracted circuit parameters remain stable over a broad frequency range.

If the equivalent circuit model is successfully developed from a target structure's field model, an ANN model can be trained for the mapping between equivalent circuit model parameters and EM model geometric parameters. A suitable optimization algorithm can then be applied on the equivalent circuit model to get the optimized parameters according to the desired circuit performance. Finally, the ANN model maps the optimized equivalent circuit parameters to the geometric parameters of the target EM model structure. The main contribution of this thesis can be summarized as:

(a) **ANN model development.** Transmission line impedance equation-based ANN model is developed for the specific microwave engineering design problems.
(b) **Hybrid optimization model development.** Metaheuristic and mathematics-based optimizers are hybridized to solve complicated microwave structure-based optimization problems.
(c) **Equivalent circuit model development.** Equivalent circuit model development strategy is outlined from the target EM model structure.
(d) **Field-Circuit Model Mapping.** ANN modelling technique for the field-circuit model mapping.

## 1.2 Outline and contributions of this thesis

This thesis is organized in the article-based format, containing six original journal papers and a conference paper:

**Chapter 1:** Introduction

This chapter presents a brief introduction and motivation of ANN modeling and optimization of EM-based structures. The development of ANN-based field-circuit model mapping is the primary goal of this Ph.D. thesis.

**Chapter 2:** Article 1: A Review on Electromagnetics-Based Microwave Circuit Design Optimization

This article revisits optimization techniques for microwave circuit design based on full-wave electromagnetic (EM) field models. Generally, EM optimization is computationally expensive and time-consuming. Over the past few decades, a variety of optimization models and techniques have been developed and implemented for fast and accurate EM field model development of active/passive circuits. In this review, disseminated works related to microwave circuit design are categorized into three major optimization groups. First, different direct optimization techniques are discussed, including fundamental concepts, formulations, and applications. Second, as a subset of surrogate model optimization methods, ANN modeling and space mapping techniques are described, including different types, modeling methodologies, and implementations. A detailed comparison is presented, highlighting recent trends and challenges in EM-based optimization of microwave and extremely high-frequency structures, such as sub-THz and THz circuits. Third, the emerging and existing applications of EM-based optimization through these techniques are identified, including the optimization of transmission lines with discontinuities, microwave filters, tunable filters, couplers, and antennas. These circuital components are widely manufactured in a variety of realizations such as microstrip line, substrate integrated waveguide (SIW), and conventional waveguide.

**Chapter 3:** Article 2: Homotopy Optimization and ANN Modeling of Millimeter-Wave SIW Cruciform Coupler

The development of millimeter-wave and terahertz (THz) passive components such as couplers and filters is an intimidating task because of underlying ultra-sensitivity of electrical performances to geometric dimensions and processing tolerances. It is a common practice for us to use an integrated optimizer of commercial electromagnetic (EM) software packages for the design and optimization of such geometric parameters. However, those optimizers may fail to achieve a desired performance if initial variables are not in a range close enough to the optimal solution. In

this paper, we introduce an homotopy approach to optimizing the geometric parameters of a D-band cruciform coupler based on substrate integrated waveguide (SIW) technique in conjunction with an artificial neural network (ANN) model. Starting from a set of initial variables, a homotopy optimization is set to search for an optimum solution. The ANN technique is adopted as the surrogate in place of a usual time-consuming electromagnetic model to accelerate the homotopy optimization process of the cruciform coupler. We propose a feed-forward computational formulation inspired by the fundamental transmission line impedance equation. Such a transmission line knowledge-based feedforward network results in a faster convergence with better accuracy than its conventional counterpart. To demonstrate the homotopy optimization method based on the ANN model, an example of multi-parameterized cruciform coupler design is detailed. This cruciform coupler with optimized geometric dimensions is simulated, fabricated, and measured. Measured and simulated results validate the combined ANN model and homotopy method. An equivalent lumped-element circuit model of the cruciform coupler is also proposed in this work. An ANN model development technique is described how to extract the equivalent circuit parameters for given coupler specifications. Extracted circuit parameters in connection with the desired coupler performance are then compared with published results which verify the ANN model development algorithm.

**Chapter 4:** Article 3: Swarm Intelligence-Homotopy Hybrid Optimization-Based ANN Model for Tunable Bandpass Filter

High-performance tunable RF/microwave and millimeter-wave filter design is a challenging task due to the lack of a basic theory. The filtering characteristics are highly sensitive to the variation of tuning elements which are commonly modeled and achieved by optimization algorithms. However, those optimizations only provide satisfactory results with a good set of initial parameters. Such range-limited optimization algorithms generally have issues of falling into local optima, slow convergence, and cumbersome implementation. To mitigate this problem, for the first time, a topology-based local optimizer is integrated with metaheuristic global optimization algorithms in this work. We have hybridized the homotopy method with an improved whale optimization algorithm (WOA) and a grey wolf optimization (GWO) algorithm. In this work, an artificial neural network (ANN) is formulated and studied, which has two-fold applications. First, ANN is used as a surrogate model to represent the time-consuming electromagnetic (EM) model in expediting the hybrid optimization process of tunable filters. Second, an ANN model is developed on data

generated by the proposed optimization algorithm for predicting tunable circuit parameters at different tuning stages. The proposed ANN model-based algorithm is then applied to a fifth-order lumped-element tunable circuit and two fourth-order full-wave EM simulation models of two tunable bandpass filters (tBPFs). The calculated results out of the ANN model demonstrate a good agreement with simulation and measurement counterparts.

**Chapter 5:** Article 4: ANN-enabled Mapping Between Equivalent Circuit Model and Physical Field Model for Tunable Bandpass Filter

In this paper, an ANN model development approach is outlined and studied for the development of tunable bandpass filter (tBPF). Circuit models are fast and efficient for design and optimization while physical models based on electromagnetic full-wave fields are accurate but computationally expensive and slow. In this work, an equivalent circuit model is developed from a full-wave tBPF structure. Then, equivalent circuit parameters are generated and mapped to tunable geometric parameters of the physical field model of the tBPF. The optimization is thus carried out on the equivalent circuit model. Finally, the geometric parameters are obtained by the ANN model from the optimized equivalent circuit parameters. A practical example of tBPF is used to demonstrate the proof of concept.

**Chapter 6:** Article 5: A Generalized Circuit Model Development Approach with Short Open Thru (SOT) De-Embedding Technique and its Applications

A short-open-thru (SOT) numerical de-embedding technique is proposed and studied in this work. In particular, a generalized methodology for circuit model development is derived for the extraction of accurate circuit parameters over a wide range of frequency. The entire de-embedding process is described, and the circuit model development strategy is explained step-by-step. A variety of electrically small planar circuit elements, such as microstrip line (MSL) gap discontinuities, step discontinuities, and via-holes in two-layered substrate discontinuities, are numerically de-embedded and extracted conventional circuit model parameters are compared with results generated by a recently published short-open-load (SOL) technique. In addition, the circuit parameters extracted by the proposed generalized decomposition technique are comparatively studied through both SOT and SOL methods. The outcomes confirm that the circuit parameters extracted by the proposed circuit model has better model behavior over a wide range of frequency as opposed to those coming out of its conventional counterpart. Furthermore, the SOT technique-

based circuit parametrization provides better stability as compared to the SOL scheme. Numerical convergence over a wide range of frequency is demonstrated for each example. Finally, a third-order Chebyshev end-coupled filter is designed by the proposed technique. Its equivalent circuit model, full-wave electromagnetic S-parameters simulation, and measured results have validated the approach.

**Chapter 7**: Article 6: High-Order Equivalent Circuit Model Development Accounting for Mutual-Coupling Effects

Mutual-coupling effects are of utmost importance in high-frequency circuits and systems as they may significantly impact the overall performances. However, it is a common practice that unintentionally overlooks or deliberately ignores these couplings when developing equivalent circuit models. Neglecting these couplings may lead to inaccurate circuit models and characteristics. Therefore, it becomes imperative to account for mutual couplings in the development of accurate equivalent circuit models. By incorporating these models into the circuit analysis, we can effectively capture the intricate interconnections and behaviors among different components and elements, leading to a more precise representation of a complete circuit. This work presents a systematic process for synthesizing the equivalent circuit model of a target field model structure that incorporates mutual and cross couplings of varying orders. The proposed high-order framework begins by developing the equivalent circuit models for each individual transmission line discontinuity within the target circuit. Subsequently, the mutual couplings of different orders are meticulously modeled in a step-by-step manner when a series of mutually-coupled blocks are considered from low-to-high orders. Throughout this process, full-wave electromagnetic (EM) simulations are deployed, along with a circuit parameter extraction method that utilizes de-embedded circuit responses. By combining these techniques, a comprehensive and accurate equivalent circuit model is generated, enabling a detailed analysis of the target field model structure, and facilitating a deeper understanding of its electrical behavior and performance. This paper utilizes two microstrip filter examples for theoretical and experimental demonstration of the proposed technique.

**Chapter 8:** Article 7: ANN Model-Based Electromagnetic Optimization by a Field-Circuit Model Mapping

In this paper, an ANN model development technique is described for efficient and fast high frequency structure design and optimization. Unlike the well-documented space mapping and aggressive space mapping technology, we map equivalent circuit model parameters to field model geometric parameters through a neural modeling. First, a complete EM structure is segmented into a series of different discontinuities. Then, the equivalent circuit model corresponding to each discontinuity is derived from a set of calibrated circuit parameters. Next, couplings of different orders between the discontinuities are represented as a part of equivalent circuits. Finally, the complete equivalent circuit model of a full-wave EM structure is developed. All the circuit parameters are extracted against different combinations of critical geometric parameters of the target EM structure. This dataset is used to develop the ANN model for mapping the equivalent circuit model parameters to EM model geometric parameters. At this stage, the circuit model can be used for optimization purposes. The optimized circuit parameters are then mapped back to the geometric parameters in connection with the pre-designated performance. In this work, a dual-band resonant-aperture (RA) rectangular waveguide filter and a third order nonradiative dielectric (NRD) waveguide filter are exampled to demonstrate the proposed methodology. Both the examples show a good agreement between simulation and measurement results.

**Chapter 9:** General Discussion

This chapter will provide a general discussion of the proposed research outcomes in this thesis work.

**Chapter 10:** Conclusion and recommendations

This chapter summarizes the entire thesis research and highlights key research contributions in a compact manner. Additionally, some potential future extensions of this research work are described as part of this research endeavour.

# CHAPTER 2 ARTICLE 1: A REVIEW ON ELECTROMAGNETIC-BASED MICROWAVE CIRCUIT DESIGN OPTIMIZATION

Chandan Roy and Ke Wu

Submitted to the *IEEE Microwave Magazine* on 27 June 2023

This article revisits optimization techniques for microwave circuit design based on full-wave electromagnetic (EM) field models. Generally, EM optimization is computationally expensive and time-consuming. Over the past few decades, a variety of optimization models and techniques have been developed and implemented for fast and accurate EM field model development of active/passive circuits. In this review, disseminated works related to microwave circuit design are categorized into three major optimization groups. First, different direct optimization techniques are discussed, including fundamental concepts, formulations, and applications. Second, as a subset of surrogate model optimization methods, ANN modeling and space mapping techniques are described, including different types, modeling methodologies, and implementations. A detailed comparison is presented, highlighting recent trends and challenges in EM-based optimization of microwave and extremely high-frequency structures, such as sub-THz and THz circuits. Third, the emerging and existing applications of EM-based optimization through these techniques are identified, including the optimization of transmission lines with discontinuities, microwave filters, tunable filters, couplers, and antennas. These circuital components are widely manufactured in a variety of realizations such as microstrip line, substrate integrated waveguide (SIW), and conventional waveguide.

## 2.1 Introduction

Electromagnetics (EM)-based based optimization techniques have always been a major interest in the microwave research community due to their vital role in the design and development of microwave circuits and systems. Achieving desired specifications in terms of S-parameters over different frequency bands regarding the design of microwave circuits and systems is one of the critical steps to follow in the design and development process [10], [11]. An optimal design can be accomplished by utilizing an optimization algorithm. Such optimizer is set to iteratively find out the optimized design with respect to the pre-defined specifications starting from an initial design stage by invoking an electromagnetic (EM) simulator each time for evaluating design evolution

and optimization feasibility. This iterative approach takes exceptionally long time as many EM simulations are generally required for different sets of combinatory geometrical parameters during the optimization process [12], [13].

In the early days of microwave design, direct optimization techniques were first implemented on distributed- and lumped-element circuit models where the gradient-based optimization algorithms such as quasi-Newton were adopted [1]. EM simulations, for example, were directly put into a gradient-based optimizer for the design of a bandpass microstrip filter structure for the first time [2]. Afterwards, a wide range of direct optimizers have successfully been applied to the EM-based optimization for the design of many other microwave circuits. Generally, existing direct optimizers in the literature can be divided into three groups, namely gradient-based optimizers, meta-heuristic-based optimizers, and hybrid optimizers. Gradient-based optimization algorithms are a class of optimization techniques that use the gradient (or derivative) of an objective function to navigate the search for an optimal solution. Examples of some of the recently used gradient-based optimizers for the EM-based circuit design are the following, Fletcher–Powell (FP) algorithm [14], simulation-inserted optimization (SIO) algorithm using combined Quasi-Newton method with Lagrangian method [15], Minimax design optimization [16], adjoint network method (ANM) [17], selective broyden updates [18], quasi-Newton method [19], etc.

Even though the gradient-based methods were commonly applied to EM based optimizations, they suffer from the local minima problem. To overcome the problem of gradient-based methods, many gradient-free optimizers are explored in the literature. Reported gradient-free optimizers may mainly be classified into evolutionary algorithms, math/physics algorithms, and swarm-based algorithms. Methods based on the evolutionary algorithm (EA) are essentially inspired by the laws of natural evolution. The search process of such algorithms starts with a randomly generated population that evolves over subsequent generations. In such methods, the best individuals are combined to form the next generation of individuals. Such strategy of population generation is set to optimize the population over the course of iterations. Genetic algorithm (GA) is the most used EA for the EM-based optimization [20], [21], [22], [23]. The math or physics-based algorithm, on the other hand, mimics the physics- or mathematics-related rules for the optimization purpose. Simulated annealing (SA) algorithm is the most popular physics-based algorithm [24], [25]. However, mathematics-based optimizers have been applied successfully in the case of various EM-based optimizations. Some of the examples are equal ripple optimization [26], rational model [27],

Model order reduction (MOR) [28], linear optimization [29], Yield-driven optimization [30] and homotopy optimization [31], [32], [33]. Swarm-based techniques are the third group of nature-inspired methods that follow the social behavior of groups of animals. Particle Swarm Optimization is the commonly used swarm-based technique which was originally developed in [34]. PSO is basically inspired by the social behavior of bird flocking. PSO technique utilizes a number of particles named candidate solutions which fly around in the search space to find the best solution. Meanwhile, they all trace the best solution in their paths. Particles consider their own best solutions as well as the best solution the swarm has obtained so far. PSO technique is used in bandpass filter and antenna structure optimizations [35], [36], [37], [38], [39], [40]. Hybridization of EA is an innovative idea to solve complicated EM based optimization problems. In [41], two swarm based optimizers named whale optimization algorithm (WOA) and grey wolf optimizers (GWO) hybridized with mathematics based homotopy optimization to solve multidimensional tunable bandpass filter optimization problem.

Surrogate modeling of EM structures is an effective way prior to the application of any optimization algorithm. Surrogate models are often constructed by artificial intelligence (AI) or machine learning (ML) based models to map the EM model design parameters to the target EM structure responses or features extracted from those responses. These techniques are computationally much cheaper than conventional EM simulations [42]. Some of the examples of surrogate model-based EM structure optimization are transfer function-based feature surrogate [43], hybrid surrogate model-assisted evolutionary algorithm [44], surrogate model-assisted global optimization by evolutionary algorithm [45] and yield optimization method-based surrogate model-assisted evolutionary algorithm [46]. Artificial neural networks (ANNs) based surrogate models are commonly used for fast optimization computations [47]. A wide range of ANN architectures, data processing techniques, training methodologies and optimization techniques are well-described in the literature [47], [48]. Commonly used ANN model development methods will be reviewed in the later part of this paper.

J. W. Bandler introduced space mapping (SM) optimization and aggressive space mapping (ASM) technique, which led to a breakthrough in EM based RF and microwave structure designing [49], [50], [51], [52]. To avoid applying direct optimization algorithms into computationally expensive fine models (full-wave EM models), the space mapping technology maps a coarse model (computationally fast model) into a corresponding fine model. The fundamental idea behind such

space mapping optimization is to utilize the coarse model to guide the search for an optimal solution in the more detailed model. This approach significantly reduces the CPU time in consideration of accurate EM model. The coarse model in space mapping is a physics-based quasi-global model. Space mapping allows us to run the optimization algorithms on a fast coarse model and map coarse model parameters into accurate EM model geometric parameters. This scheme minimizes the EM optimization time significantly as the optimizer is operated on a fast coarse model rather than a computationally expensive and slow full-wave EM model of the target structure. Several space mapping variants with different strategies are also made available in the literature to overcome different design challenges [53], [54], [55]. The space mapping and its variants will be discussed in detail with different EM model structure applications in this article.

ANNs can be utilized in the space mapping optimization as a surrogate model to represent the coarse model so that a limited set of data is enough to train the ANNs from the coarse model, accurately. This trained neural network can then replace the coarse model in the space mapping optimization process. Such a surrogate model handles the non-linear behavior of the coarse model efficiently. A large set of data can train the ANN model for more accurate approximations of the coarse model. Therefore, the use of ANNs as surrogate models in the space mapping optimization improves the efficiency and accuracy of an optimization process. Microwave circuit modeling using ANNs based on the space-mapping (SM) technology is a recent trend in the EM model optimization. Such SM-based neuro models minimize the training cost, enhance the generalization ability, and keep the ANN topology simple as compared to the classical ANN-based circuit modeling technique [56]. A novel method is proposed in [42] for efficient and precise EM-based statistical analysis and yield prediction by the help of a linear-input neural-output space-mapped model. A neural space-mapping (NSM) optimization for electromagnetics-based design is proposed in [57]. This method exploits space-mapping-based neuromodeling techniques in order to approximate the accurate mapping without the requirement of parameter extraction process. A recent technique is proposed in [58] namely statistical neuro-space mapping for large-signal statistical modeling of nonlinear microwave devices which advances the current linear statistical mapping technique. Nonlinear mapping is used in this technique to maximize the accuracy in the modeling of large statistical variations among different devices.

Different optimizers applied to EM-based optimization through direct modeling or surrogate modeling are picturized briefly in the above discussion. These optimizers are described through a

classification chart as shown in Figure 2.1. EM-based optimization techniques are primarily categorized into direct optimization and surrogate model optimization. Direct optimization techniques are then divided into two major groups: gradient-based optimizers and gradient-free meta-heuristic-based optimizations. On the other hand, surrogate model-based optimizations are mainly grouped into neural network models, space-mapping-based models and neuro-SM-based models. The major techniques and methodologies of the recently used optimizers are discussed in this review work. Illustrative examples as the applications of different optimization methods are overviewed.

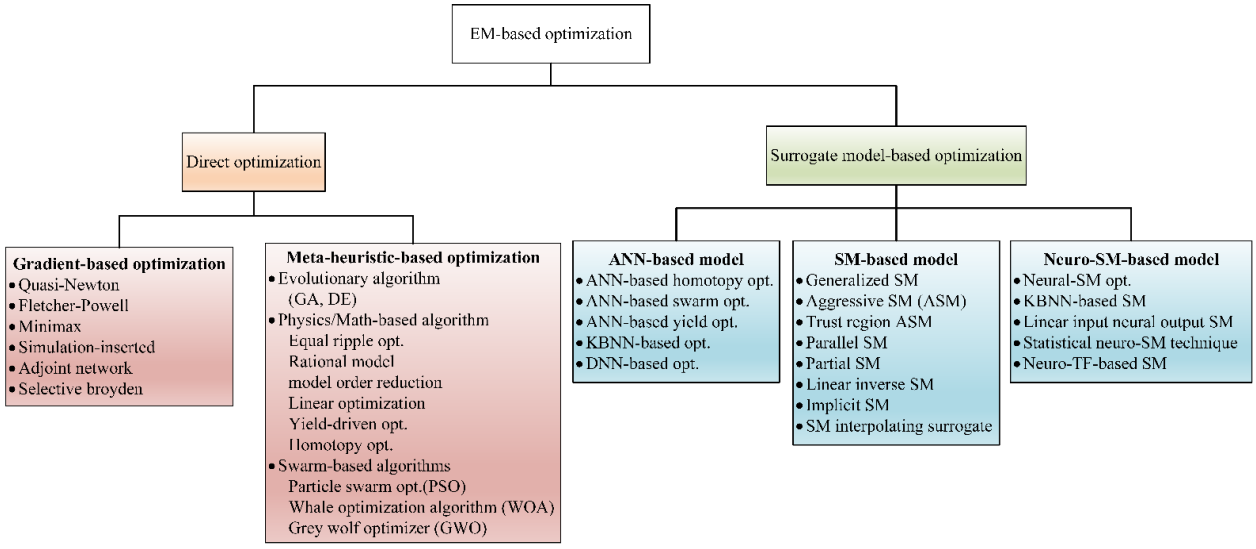


Figure 2.1 Holistic classification of EM-based optimization techniques

This review article is organized as follows. Section II first presents different gradient-based optimization algorithms for EM-based design optimizations. Meta-heuristic-based optimization algorithms are then discussed in Section III. Three major types of meta-heuristic-based optimization algorithms are described in detail. In section IV, different ANN model development techniques are revisited briefly along with data generation techniques and model architectures. A few recent ANN-based surrogate model optimization techniques are then discussed. Section V is dedicated to various space mapping techniques that are extensively explored for EM-based design optimizations. Neuro-space mapping techniques from the literature are showcased in section VI, followed by different EM design structures as illustrative examples for different optimization techniques in section VII. Comparisons and future trends from recent EM-based optimization works are examined in Section VIII, followed by the conclusion.

## 2.2 Direct optimization methods

As mentioned in the previous section, direct optimizers applied on EM-based optimizations are mainly categorized into gradient based optimizers and gradient free meta-heuristic-based optimizers. These optimization algorithms are described briefly in the following discussion.

### 2.2.1 Gradient-based optimization methods

The studies from past few decades on the algorithmic and theoretical perspectives of optimization techniques have demonstrated a significant impact on microwave engineering. Current state-of-the-art methods have notably replaced the old-fashioned trial-and-error approaches. Gradient-based optimization techniques are widely used for their efficiency and effectiveness. Gauss-Newton, quasi-Newton and conjugate gradient are the roots of most of the gradient-based methods. These algorithms start from a given point $a_0$ and generate a series of points $[a_k]$. The algorithms are successful if the series of point $[a_k]$ are set to converge to a fixed point, $a^*$. The algorithms are usually formulated on the process of obtaining $a_{k+1}$ from $a_k$. C(a) is denoted as the cost function and $\nabla C$ implies the gradient vector of C. An $L_p$ function defines C(a) and F denotes individual error function sets to satisfy $C = H(F)$. $F_j'$ and J stand for the first-degree derivatives of $F$ and Jacobian matrix, respectively.

#### 2.2.1.1 Gauss-Newton Method

A generalized problem demands for substituting F by a linearized term $\bar{F}$ to solve $P(a, F)$. $P(a, F)$ denotes mathematical programs which can either be a linear or a quadratic function. For a linear function $F$, $P(a, F)$ remains a linear or quadratic function which can be solved by well known techniques. Necessary linear constraints can be incorporated into $P(a, F)$ to become $P(a, F, Q)$ where Q represents a set of linear constraints.

In the case of a Gauss-Newton method, at any given point $a_k$, F can be linearized as

$$\bar{F}(h) = F(a_k) + J(a_k)h \tag{2.1}$$

$J$ is Jacobian matrix here and $\bar{F}$ is treated as appropriate approximation to $F$.

Alternatively, a semi-linearization can be applied to $C(a) = H(F)$ which gives us

$$\bar{C}(h) = H\big(\bar{F}(h)\big) \tag{2.2}$$

Here, (2.2) is different from a normal linearization as $C(h) \approx C(a_k) + [\nabla C(a_k)]^T h$ which represents the steepest descent technique. Let us assume that $h_k$ is the solution of $P(h, \bar{F}, Q)$. If $(a_k + h_k)$ minimize the cost function, it is considered as the next iteration. Otherwise, $a_{k+1} = a_k$ where the trust region is large, and it should be reduced. The local bound is adjusted in each iteration for the betterment of the linearized model. This algorithm description is developed by Madsen [59].

### 2.2.1.2 Quasi-Newton Method

Quasi-Newton methods were established and updated through the works of Broyden [60], [61] as well as Fletcher and Powell [62]. A quasi-Newton step for a differentiable cost function can be expressed as

$$h_k = -\gamma_k D_k^{-1} \nabla C(a_k) \tag{2.3}$$

Here, $D_k$ represents the approximation function to the Hessian of $C(a)$ and $\gamma_k$ is the step size controlling parameter which is usually determined by the line search method. In some of the cases such as minimax case, the gradient may not exist. By using the Kuhn-Tucker conditions for nonlinear programming [63] to the similar problem, we will be able to deduce a set of optimality equations.

$$S(a) = 0 \tag{2.4}$$

To minimize the C(a), (4) will be solvable as a local optimum $a^{\#}$ satisfies the equations. A quasi-Newton step for the solution of non-linear equations (4) is formulated as

$$h_k = -\gamma_k J_k^{-1} \mathrm{S}(a_k) \tag{2.5}$$

Here, approximate Jacobian of $S(a)$ is $J_k$. For the differentiable cost function, $S(a) = \nabla C(a) = 0$ and (2.5) becomes (2.3).

The upgrade of a given approximate Hessians is required for any of the Quasi-Newton methods, whether it is as expressed in (2.3) or (2.5). Lots of formulas are available in the literature. Some of these well-known formulas are Broyden-Fletcher-Goldfarb-Shanno (BFGS) [64], [65], [66], [67], Davidon-Fletcher-Powell (DFP) [68], [62], and the Powell symmetric Broyden (PSB) [69]. These formulas and their variations are often compared in terms of their convergence to characteristics and numerical performance.

#### 2.2.1.3 Hybrid methods

The Quasi-Newton method entertains a great convergence rate near a solution. However, in practice, it requires a good starting point for acceptable optimization. Therefore, it is not reliable once it is fed with a bad starting point of reference. To overcome such problem, two-stage algorithms were used often in the literature [70], [71], [59]. First, A Gauss-Newton type method is applied in its first stage to find a global convergence to a nearby solution. In the case of a singular solution, this method has a slow rate of convergence problem. Then, switch to a quasi-Newton method (second stage). Such switching between the two methods may be required till the global convergence of the combined algorithm is achieved. Illustrative examples of circuit applications with such a hybrid method demonstrated satisfactory results [72], [73]. In addition, the popular Levenberg-Marquardt algorithm was extended, and a trust-region strategy was developed to interpolate between a Newton step and a steepest descent step [69]. A full Newton step provides fast final convergence when it is close to the solution.

Implementing full-wave EM simulators into any of the optimization loops was unthinkable due to the massive computational cost for the repetitive calculations in the early history of EM research. However, due to the highly capable modern computational resource, direct optimization processes are easily applied to the commercial EM simulation software nowadays. Gradient-based optimizers were first implemented on such scenario.

### 2.2.2 Meta-heuristic-based optimization algorithm

Gradient-free optimizers are mostly meta-heuristic-based algorithms. Meta-heuristic optimization algorithms are getting more attention from the engineering research community and becoming more popular in engineering applications [74].. Commonly used variations of these three optimization methods are described below.

#### 2.2.2.1 Genetic algorithm (GA)

A commonly applied evolution-inspired optimization technique is Genetic Algorithms (GA) that simulates the Darwinian evolution [75].

In the first step of GA, the ‘X’ matrix and ‘y’ vector of the set of linear equations ($Xa = y$) are formulated. These linear equations are derived from Poisson’s equation [76]. Random population (chromosomes) is then generated that represents the vector solution a. The cost function (fitness)

is then computed for all the randomly generated chromosomes. Two parents are generated either by tournament selection or by roulette-wheel methods according to the fitness function. Then, mutation and crossover are performed on the parents to produce two children. Replacement is done as the fitness of children is compared with the parents. After the comparison, the worst two chromosomes are eliminated from the population. The best fitness is provided by the best chromosomes. At the end, a check is carried out against a given stopping criteria to stop or continue a further iteration. The details of implementing the proposed algorithm are as follows [22].

1) In the initialization stage, N chromosomes are generated randomly which is known as the GA population. Genes are contained by each chromosome, which corresponds to the variables in the vector solution. The randomly generated populations have a range associated with the target problem.
2) In the fitness evaluation stage, each chromosome is calculated based on a pre-defined cost function or objective function which accurately determines how close the randomly generated solutions are to the optimal solution.
3) In the regeneration stage, two types of methods are used in order to generate parents. The first method is known as Roulette-Wheel selection. In this method, parents are chosen randomly according to the fitness function. This method mimics the roulette-wheel game, where the thrown dice will end being in the slot with the largest area. It can be concluded that the chromosome that fits better is most likely to be chosen as it has the largest slot size. The second method is called tournament selection where two groups from the population are randomly selected (sub-populations). The better chromosome from each of the sub-populations should represent a parent.
4) In the crossover stage, two parents are chosen for their genes to be crossed over and mutated. Crossover is performed by randomly selecting a crossover point within the chromosome first. Then two children are conceived by mixing up the parental genes at the crossover point. Two different parameters such as number of crossover points and number of genes involved in each crossover point can be analyzed.
5) In the mutation stage, one or more genes of the generated offspring are randomly changed. Then, two mutation parameters should be studied. These parameters are the number of mutated genes (variables) and the value of mutation.

6) In the replacement stage, the fitness of the parents is compared with their offspring and the best two chromosomes are added in the population for the next iteration.
7) The stopping criteria of the algorithm is decided by the predefined error value. The algorithm only stops when this value is satisfied.

Genetic algorithm is used in the optimization of various filters and antennas optimization.

#### 2.2.2.2 Differential evolution (DE)

Differential evolution (DE) is one of the major algorithms that has the strength of handling multidimensional optimization problems and are widely applied as a global optimizer [77]. Similar to the genetic algorithm, DE consists of different steps of initialization, selection, genetic operators, and termination. Through out these processes, the fitness of individuals in the population is enhanced and the fittest variables can be obtained.

In the recent research paradigm of microwave design optimization, DE is one of the most efficient evolutionary algorithms [45], [78]. Over the course of iteration, it mutates, apply the crossover for the generation of new population, and select operators. The mutation operator generates difference vector(s) from selected individual vectors and adds it/them to other selected individual vectors, so as to explore the search space. Crossover is done due to the enhancement of the population diversity. The survived vector for the next generation is determined by the selection operator based on a greedy selection criterion.

#### 2.2.2.3 Homotopy optimization

Homotopy analysis method (HAM) is a mathematics-based optimization tool which is also known as the continuation method. The main concept of this method is adopted from differential geometry and topology that can be deployed in many numerical techniques to solve differential equations and nonlinear equations. This method is not dependent of physical parameters. Homotopy variable can be introduced in the range [0,1] in order to build a zeroth order deformation equation and find a homotopy series solution. Such an equation is valid for the representation of a non-linear problem that involves arbitrary number of physical variables [31]. In this way, a non-linear equation is converted into an infinite number of linear equations. The homotopy optimization problem is formulated as follows:

$$s(y, \delta) = (1 - \delta)P(y) + \delta Q(y) \tag{2.6}$$

Here, $P(y)$ is an optimization problem, whose solution is known. $Q(y)$ is the target optimization problem, and a good set of initial variables is unavailable. Homotopy variable is indicated by $\delta$. For $\delta = 0$, $s(y, 0) = P(y)$ and for $\delta = 1$, $s(y, 1) = Q(y)$. Thus, as the value of $\delta$ changes from 0 to 1, the function deforms from $P(y)$ to $Q(y)$. The homotopy series can be expressed as $0 < \delta_1 < \delta_2 < \cdots < \delta_t < 1$. Here, the assigned value of $\delta$ increases linearly from 0 to 1 with N number of homotopy steps. For instance, in case of five homotopy steps, the homotopy problem is expressed as $0 < \delta_1 < \delta_2 < \delta_3 < 1$ where $\delta_1 = 0.25$, $\delta_2 = 0.5$ and $\delta_3 = 0.75$. In each small increment in $\rho$, the new problem remains similar to its previous state. Consequently, the optimized solution of the newly introduced problem should be close to the previous solution. How much intermediate homotopy steps is required is usually decided based on the difficulty level of the problem. A highly nonlinear problem requires more intermediate steps to find the optimum solution.

Finding an optimum solution of the target problem becomes convenient if the previous problem's solution is used to find the solution of the current problem. For example, if the homotopy variable has a linear increment in the range [0, 1], two prior solutions can be combined linearly as a starting point for the next optimization step

$$T_{i+1} = 2T_i' - T_{i-1}' \tag{7}$$

Here, $T_i'$ and $T_{i-1}'$ represents the optimized solutions at the i$^{th}$ and (i-1)$^{th}$ homotopy step when the primary solution is $T_{i+1}$ for the (i+1)$^{th}$ homotopy optimization.

#### 2.2.2.4 Particle swarm optimization (PSO)

Swarm-based algorithms are advantageous over evolution-based algorithms as they preserve the search space information over subsequent iterations while evolution-based algorithms discard any information as soon as a new population is formed. Such behavior of swarm-based algorithms involves fewer parameters that can be implemented easily. The logical behavior of bird flocking, and fish schooling inspired swarm intelligence-based particle optimization technique was proposed in order to solve continuous nonlinear functions [34]. The optimization process of PSO involves a population of n number of particles which is initialized in order to form the population with randomly generated solutions. These randomly generated populations/swarms are distributed in the design space. The velocity and the position of the particle are updated over the course of iteration. These updates are carried out based on following equations:

$$V_i^{s+1} = V_i^s + a_1 b_1 (q_h^s - y_i^s) + a_2 b_2 (q_i^s - y_i^s) \quad (2.8)$$

$$y_i^{s+1} = y_i^s + V_i^{s+1} \quad (2.9)$$

where the velocity vector and position vector of particle $i$ at iteration $s$ are represented by $V_i^s = [V_{i1}^s, \ldots, V_{iD}^s]$ and $y_i^s = [y_{i1}^s, \ldots, y_{iD}^s]$, respectively. $r_1$ and $r_2$ are the random variables in the range of [0 1]. Acceleration coefficients are indicated as $a_1$ and $a_2$. The global best position is denoted by $q_h^s$ and $q_i^s$ denotes the previous best position of 'i' particle till the s[th] iteration. Over the course of iteration, $q_h^s$ and $q_i^s$ are updated according to exact function evaluations for all the particles. The PSO terminates the exportation of the global best position $q_h$ after the stopping criteria is met.

### 2.2.2.5 Whale optimization algorithm (WOA)

Whale optimization algorithm (WOA) is one of the recent advanced swarm-intelligence based algorithms [74]. The WOA is inspired by the bubble-net hunting behavior of humpback whales. Such behavior is executed by following steps: encircle prey, bubble-net attack (exploitation phase), and search for prey (exploration phase). The WOA involves a few operators which can be implemented easily. This technique introduces a stochastic method for population initialization as it does not have any prior knowledge about the global optimal solution. An uneven distribution of the population introduces uncertainty to the extraction of useful information from the solution space.

In the prey encircling stage of WOA, the whales identify the location of prey and encircle them. Initially, the current best candidate solution is assigned to the target prey as the optimal solution is unknown. If a better candidate solution is identified, this search candidate will be updated accordingly. Such characteristics can be mathematically formulated as

$$\vec{Q} = \left| \vec{P}. \overrightarrow{Y^*}(s) - \vec{Y}(s) \right| \quad (2.10)$$

$$\vec{Y}(s+1) = \overrightarrow{Y^*}(s) - \vec{B}.\vec{Q} \quad (2.11)$$

In which the coefficient vectors are denoted by $\vec{B}$ and $\vec{P}$, achieved best solution of the position vector ($\vec{Y}$) is denoted by $\overrightarrow{Y^*}$, $||$ refers to the absolute value sign and . refers to the element-by-element multiplication sign. In each iteration $s$, the numeric value of $\overrightarrow{Y^*}$ get updated for the better solution. Here, $\vec{B}$ and $\vec{Q}$ are formulated in relation with a random vector $\vec{z}$ in the range of [0,1] and

a linearly reduced vector $\vec{b}$ in the range of [2,0] over the course of iterations (in both exploration and exploitation phases). Various positions nearby to the best agent can be found with respect to the current position by tuning the value of $\vec{B}$ and $\vec{P}$ vectors.

$$\vec{B} = \left|2\vec{b}.\vec{z} - \vec{b}\right| \tag{2.12}$$

$$\vec{P} = 2.\vec{z} \tag{2.13}$$

where $\vec{Q}$ represents the distance between the i[th] whale and the prey, *l* denotes a random number in the range of [-1,1] and *c* represents the logarithmic spiral's shape that is fixed at 1 to keep the spiral update stable. In consideration of the balancing between shrinking encircling mechanism and spiral update mechanism, the probability of applying these models is equally balanced. To develop the mathematical model, the algorithm produces a random number $r$ in the range of [0,1]. The shrinking encircling mechanism and the spiral update mechanism are chosen for $r < 0.5$ and $r \geq 0.5$, respectively. These mechanisms are expressed as

$$\vec{Y}(s+1) = \begin{cases} \overrightarrow{Y^*}(s) - \vec{B}.\vec{Q}, & r < 0.5 \\ \overrightarrow{Q'}.e^{cl}.cos(2\pi l) - \overrightarrow{Y^*}(s), & r \geq 0.5 \end{cases} \tag{2.14}$$

where r is a random number in the range of [0,1].

In the final stage of prey searching, an equivalent strategy is applied based on the variation of $\vec{B}$. For the global search step, the random $\vec{B}$ value ($> 1$) is selected. This can be mathematically formulated as

$$\vec{Q} = \left|\vec{P}.\ \vec{Y}_{rand} - \vec{Y}\right| \tag{2.15}$$

$$\vec{Y}(s+1) = \vec{Y}_{rand}(s) - \vec{B}.\vec{Q} \tag{2.16}$$

where $\vec{Y}_{rand}$ denotes a random value that represents a random whale selected based on the current population.

### 2.2.2.6 Grey wolf optimization (GWO)

Grey wolf optimization algorithm (GWO) is another swarm-intelligence based algorithm that drew attention of engineering optimization researchers recently [79]. GWO uses the hunting behavior of grey wolves who follow the leadership hierarchy. The leadership hierarchy can be simulated by four types of grey wolves named alpha, beta, delta, and omega. The overall optimization is executed

by three steps: hunting, prey searching, prey encircling, and attacking prey.

In the mathematical formulations of GWO, the best three solutions in the search space are represented by alpha (α), beta (β) and delta (δ) wolves. These three candidates supervise the complete optimization process. The rest of the candidates are considered as omegas (ω). Each candidate solution is considered as a vector as shown in (2.17)

$$\vec{Y} = y_1, y_2, \dots\dots, y_n \tag{2.17}$$

Here, current position of the wolf is represented by $y_i$ and $n$ is indicated as dimension of the search space.

The first step of prey encircling is formulated as

$$\vec{Q} = \left|\vec{P}.\ \overrightarrow{Y_p}(t) - \vec{Y}(s)\right| \tag{2.18}$$

$$\vec{Y}(s+1) = \overrightarrow{Y_p}(s) - \vec{B}.\vec{Q} \tag{2.19}$$

where current iteration is denoted by $s$, coefficient vectors are represented by $\vec{B}$ and $\vec{P}$, position vector of the prey is indicated by $\overrightarrow{Y_p}$, a grey wolf's position vector is denoted by $\vec{Y}$, $|\ |$ is the sign of absolute value and . represents element-by-element multiplication. $\vec{B}$ and $\vec{P}$ are expressed in terms of two randomly generated vectors $\overrightarrow{r_1}$ and $\overrightarrow{r_2}$ in the range of [0,1] and a linearly diminishing vector $\vec{a}$ in the range of [2,0] over the course of iterations.

$$\vec{B} = 2\vec{b}.\overrightarrow{r_1} - \vec{b} \tag{2.20}$$

$$\vec{P} = 2.\overrightarrow{r_2} \tag{2.21}$$

In the second step of prey hunting, the grey wolves indicate the possible prey's position for hunting that is guided by the previous best solutions, namely alpha (α), beta (β), and delta (δ). These best solutions will be updated over the course of iteration in order to support other omegas (ω) for locating their positions. This hunting strategy is formulated as

$$\vec{Q}_\alpha = \left|\vec{P}_1.\vec{Y}_\alpha - \vec{Y}\right| \tag{2.22}$$

$$\vec{Q}_\beta = \left|\vec{P}_2.\vec{Y}_\beta - \vec{Y}\right| \tag{2.23}$$

$$\vec{Q}_\delta = \left|\vec{P}_3.\vec{Y}_\delta - \vec{Y}\right| \tag{2.24}$$

where $\vec{Q}_\alpha$, $\vec{Q}_\beta$ and $\vec{Q}_\delta$ are the updated distance vectors between the position of omegas and leader wolves. Coefficient vectors $\vec{P}$ are computed from (2.21), and omegas position is indicated by $\vec{Y}$. Each $\vec{Y}_i$ provides a possible position from the distance vector between omegas and other leader wolves of $\vec{Q}_\alpha$, $\vec{Q}_\beta$ and $\vec{Q}_\delta$, respectively. The mathematical formulations are

$$\vec{Y}_1 = \vec{Y}_\alpha - \overrightarrow{B_1}.(\vec{Q}_\alpha) \tag{2.25}$$

$$\vec{Y}_2 = \vec{Y}_\beta - \overrightarrow{B_2}.(\vec{Q}_\beta) \tag{2.26}$$

$$\vec{Y}_3 = \vec{Y}_\delta - \overrightarrow{B_3}.(\vec{Q}_\delta) \tag{2.27}$$

The final updated position vectors are formulated as $\vec{Y}_i$ where $\vec{Y}_1$ is the newly updated location from alpha position $\vec{Y}_\alpha$ and the distance vector $\vec{Q}_\alpha$. The coefficient vectors $\overrightarrow{B_i}$ are computed from (2.20). $\vec{Y}_2$ and $\vec{Y}_3$ are calculated similarly as $\vec{Y}_1$. The new position vector can be found from algebraic average as

$$\vec{Y}(s+1) = \frac{\vec{Y}_1 + \vec{Y}_2 + \vec{Y}_3}{3} \tag{2.28}$$

In the final step of attacking prey, the $\vec{b}$ value is reduced from 2 to 0 over the course of iterations which reduce $\vec{B}$ in the interval of [*-b,b*].

### 2.2.2.7 Hybrid optimization algorithms

So far, we have examined some of the major/commonly used meta-heuristic-based algorithms for the EM based design optimizations. Different optimization algorithms are equipped with different benefits. However, according to the No Free Lunch (NFL) theorem, a single optimization algorithm cannot provide the best solution to all types of optimization problems [80]. Therefore, optimization algorithms are carefully selected according to the nature of the target problem. In recent days, hybridization of mixed types of optimizers are applied in order to get the efficient electromagnetic optimization for complicated structures. For example, two swarm based optimization methods (WOA and GWO) are hybridized with mathematics based homotopy optimization technique in [41]. Such hybrid optimization technique brings the strength of swarm-based global optimizer and mathematics-based local optimizer in single point in order to solve high-dimensional EM design optimization problem. In [39], a modified comprehensive learning particle swarm optimization

(CLPSO) with a more efficient learning strategy is demonstrated on antenna designing problem. Such method is called the adaptive comprehensive learning particle swarm optimization (A-CLPSO) which solves multimodal problems more efficiently. In [44], an automated or unsupervised filter design optimization introduces a new method called hybrid surrogate model-assisted evolutionary algorithm for filter optimization (H-SMEAFO) which is designed to automatically obtain a highly optimal filter 3D design.

These are only three state-of-the-art hybrid optimization model examples from the literature. These examples suggest that complex and emerging EM design optimization problems often require characteristics of more than one algorithm to meet the design goals with a reasonable computational resource.

## 2.3 ANN based surrogate model optimization

To minimize the computational load, surrogate model optimization is mostly used nowadays for EM-based optimization problems. Artificial neural networks (ANNs) are widely used to develop the surrogate model of a target EM structure. Neural modeling techniques are popular for microwave computer-aided design (CAD) in both forward and inverse design problems. ANN models can be trained with simulated or measured results out of microwave circuits and learn the input-output relationships. The trained ANN model can replace a computationally expensive full-wave electromagnetic model. Such a surrogate model can predict the outputs in terms of given inputs with circuit-level fast computational time and EM/physics-level high accuracies [81], [82].

ANNs address two major challenges in microwave CAD, namely the computational expense in the case of a forward modeling, and the absence of analytical equations for an inverse design. A variety of ANNs have been reported in the literature to address different challenges in microwave structure design, such as multilayer perceptrons (MLPs), radial basis function (RBF) networks, deep neural networks (DNN), and knowledge-based neural networks (KBNNs) [83]. In this section, we begin with a brief review of basic ANN types, data management techniques, optimization techniques, and training/testing criteria. Then, different surrogate ANN models for EM-based optimization are discussed from available publications.

### 2.3.1 ANN structure and training strategy

A neural network is made of a group of neurons along with a connecting set of weights between

the neurons from adjacent layers and biasing value to each individual neuron. Different types of neurons and/or different ways of connecting different neurons result in a variety of neural network structures [81].

#### 2.3.1.1 Feedforward neural networks

Feedforward neural networks (FFNNs) are a most common type of ANN that consists of several layers of interconnected neurons. In FFNN, information flows in one direction, from the input layer through one or more hidden layers, to the output layer. There are no feedback connections in a FFNN, meaning that the output of one neuron in a layer does not affect the input of any other neuron in the same layer. In other words, connections between the neurons do not form a cycle. The input layer of a FFNN accepts the input data in the form of a vector of numerical values. Each neuron in the input layer represents one element of the input vector. The input data is then fed through different hidden layers. The neurons usually implement a series of weighted transformations to the input data. The weights of these neural connections are updated through training, in which the network is presented to a large set of input-output data and adjusts the weights in order to minimize the difference between the calculated output and the desired output [81], [82]. FFNNs are commonly applied to solve non-dynamic modeling problems. Multilayer perceptrons (MLPs) are widely used FFNN structures for microwave modeling [84], [85], [86], [87], [88], [89], [90], [91], [92], [93].

RBF network is another popular type of FFNN in microwave design [94], [95], [96]. The hidden layer of an RBF network consists of a set of radial basis functions. These mathematical functions are set to measure the distance between the input data and a set of predefined centers. Such centers are usually chosen based on some heuristic or clustering algorithm applied to the training data. Each radial basis function computes a similarity measure between the input data and one of the centers, producing an output that decreases with distance from the center. The RBF network is advantageous over other types of ANNs. For example, training is easy due to a small number of parameters, which reduces overfitting problem.

#### 2.3.1.2 Knowledge based neural networks and neuro-TF model

A knowledge-based neural network (KBNN) is a type of neural network that is usually developed to incorporate physical knowledge or domain-specific information during the learning stage. Such

networks are often used in applications where a prior knowledge improves the model accuracy and/or reduce the required amount of training data. The common strategy for building a KBNN is to introduce additional layers that encode a problem of interest in connection with its specific prior knowledge. Alternatively, the prior knowledge can be incorporated into the training process itself, by using techniques such as regularization or weight initialization, which guide the network to learn patterns that are consistent with the provided knowledge. In the literature, KBNN are built with available equivalent circuit knowledge for the target EM-based models [56], [58], [97], [98], [99], [100], [101].

The integration of a system transfer function with neural networks is a recent knowledge-based modeling strategy, which is also known as neuro-transfer function or neuro-TF model. Such models can be used to build efficient and effective parametric models for EM-based structures [102], [103], [104]. This type of knowledge-based network is also effective where an accurate equivalent circuits model or empirical model is unavailable.

#### 2.3.1.3 Deep neural networks

A Deep neural network (DNN) is a type of ANN with multiple layers of neurons between the input and output layers. The "depth" of a neural network refers to the total number of hidden layers it has. Deep neural networks usually consist of many more layers than traditional shallow neural networks, which typically have only one or two hidden layers. More hidden layers help the network to learn increasingly complex features and patterns, which leads to better accuracy and performance on complex tasks. DNNs are usually trained with a large set of data [105], [106], [107].

Deep MLP is one type of deep neural network that is commonly used in the literature for microwave applications [108]. The choice of activation function in the deep MLP has a significant impact on the final model accuracy. rectified linear unit (ReLU) is the most used activation function in the deep MLP. The ReLU solves one of the major problems of vanishing gradient issue during the training period of the deep neural networks.

#### 2.3.1.4 ANN training and data generation

The most significant part of ANN model development is the quality training with corresponding data sets. A microwave circuit can be represented by an ANN model accurately only after the training period of the model. Training data are generated out of a target system to guide the update

routine of neural network weight and bias matrix. Test data sets are used to evaluate the trained neural network model quality which were unseen during the training period of the model. The ANN model development process consists of the following steps:

1) Find out the inputs and outputs of a target EM based microwave circuit structure.
2) Generate the training and testing data sets in terms of selected inputs and outputs.
3) Introduce physical knowledge/formulations from the target problem into the ANN model to escalate the training process by minimizing the training datasets.
4) Execute the training sessions and model validation steps.
5) Measure the efficiency/accuracy of the developed model with the help of testing datasets.
6) If the model accuracy does not meet the desired performance, adjust model architecture and/or generate training data thoughtfully.
7) Once the desired model accuracy is achieved, replace EM-based model with the surrogate ANN model for fast optimization and other post-processing of the circuit.

Data generation plays a vital role on the development of ANN model. ANN model accuracy can be enhanced significantly by careful choice of data sampling. On the contrary, large datasets require huge computational resources and simulation time. Different types of data sampling strategies have been introduced in the literature for ANN model development for a wide range of applications. For example, uniform/nonuniform grid distribution [81], star distribution [56], random distribution [109], adaptive sampling [110], and design of experiment (DoE) with orthogonal distribution [111], [112]. Grid distribution is the most used data sampling strategy where each input parameter is sampled over uniform or nonuniform intervals. In the case of a star distribution, a central point is perturbed twice along each input dimension to generate the sample points. One perturbation should be done toward the positive direction and the other perturbation should be done toward the negative direction. The data samples raise exponentially with the input dimension increment in case of a grid distribution. On the other hand, the number of data samples in case of a star distribution increases linearly. Even though the grid distribution provides us with sufficient training data, it is not practically implementable where the input dimension is high. The star distribution fails to provide sufficient data for the training of a pure neural network. However, it is useful for training knowledge-based neural networks. Random distribution considers each input sample as a vector of random variables inside the input parameter range. To sample the data adaptively, an interaction between the available data and the intermediate surrogate model is established. It distinguishes the

area where data are required in the input modeling space. Adaptive sampling achieves the desired model accuracy from the fewest data samples which makes the data generation process efficient, flexible, and fast. To generate a number of samples in high-dimensional parameter spaces, DoE with orthogonal distribution can be applied. In such a sampling strategy, divisions in the subspace are done orthogonally while sampled with the same density. Such a distribution only requires fewer sampling points as compared to the grid distribution. As the model dimension and complexity are increasing day by day, data generation for ANN modeling becomes more challenging.

Automated model generation (AMG) algorithms for neural network training reduce human intervention significantly [113], [114] while the conventional step-by-step neural modeling technique requires constant human surveillance and experience. Such algorithms intelligently indicate smooth and nonlinear regions of model behavior and applies fewer samples in relatively smooth subregions and more samples in highly nonlinear subregions. These algorithms generate a neural network model that satisfies the expected accuracy.

### 2.3.2 ANN-based surrogate model for EM optimization

An ANN surrogate model is used to approximate the behavior of a computationally heavy full-wave EM model. The surrogate model uses a neural network to learn the input-output relationship of the target EM model of a structure and can then be used to predict its electrical behavior against geometric parameters. The advantage of using an ANN surrogate model is that it provides fast and efficient predictions of the electrical characteristics of the target EM model structure without requiring the use of the computationally expensive EM model. This becomes especially useful for the optimization purpose where the EM model of the target structure is required to set up in a repetitive optimization loop. EM model-based optimization is often done by an ANN surrogate model in order to minimize the simulation time and computational cost. Some of the recent examples are given below.

Most common EM-based artificial neural network (ANN) surrogate model considers the model inputs as frequency points as well as geometric parameters of the target structure and the outputs are performance parameters such as S-parameters. Homotopy optimization method is used on the ANN surrogate model for finding the optimized geometric parameters of tunable filters, fixed filters, and couplers [31], [32], [33]. In [46], RBFNN is hybridized with support vector machine

(SVM) to perform yield-global optimization for the bandpass filters. A novel ANN surrogate-based method is proposed in [115] to escalate the yield optimization of multiport microwave structures by applying combined quadratic mappings and matrix-valued transfer functions. In [116], a novel ANN-based surrogate-assisted multistate tuning-driven EM optimization technique is proposed in order to overcome the microwave tunable filter designing challenges with multiple tuning states. In [117], an inverse ANN model assisted with self-adaptive local surrogates (SALS) technique is proposed to automate the coupler designs. In [41], ANN based surrogate model was used to implement swarm-homotopy hybrid optimization technique for the design of tunable filters. In [118], a novel procedure for microwave passive components modeling is proposed that involves a customized deep neural network (DNN) along with reference-design-free domain confinement. In [119], a multifeature-assisted neuro-transfer function (neuro-TF) surrogate-based electromagnetic (EM) optimization method exploiting trust-region algorithms for microwave filter design is presented.

Above discussion summarizes some of the ANN-based surrogate models that are used for the optimization of EM model-based structures. These examples suggest that the EM-based ANN surrogate models are well recognized by recent microwave researchers due to their attractive features towards fast and efficient optimization. The ANN basics are roughly explained in section III.A. As the main objective of this review paper is to provide an overall picture of EM-based optimizations, we could not cover all the detailed ANN modeling strategies. However, interested readers may refer to the microwave application-based ANN model development related works conducted by the research group of Q. -J. Zhang.

## 2.4 SM-based surrogate model optimization

In a space mapping surrogate model, a high-fidelity, computationally expensive model (the so called "fine model") is used to simulate the system being optimized. However, instead of directly optimizing the system using the fine model, a simpler, computationally less expensive model (usually known as the "coarse model") is used as a surrogate to the fine model. The space mapping technique then maps the design variables from the coarse model domain to the fine model domain. Such a mapping allows more accurate optimization of the target system with incredibly reduced computational cost. The mapping is typically achieved through an iterative process of refining the surrogate model based on feedback from the fine model [12], [52], [53]. In this section, we will

introduce the space-mapping technique first, followed by its predecessors such as aggressive space mapping and other techniques. Some recent advances on SM optimization will then be described in detail.

### 2.4.1 Space mapping technology

Choice of physical design parameters is a crucial step of microwave component designing in order to satisfy desired design specifications. Conventional optimization techniques directly use the EM model simulated responses of the target structure and utilize derivatives to align the responses close to the design specifications. Equivalent-circuit-based computation and empirical equation-based models are fast. Full-wave electromagnetic (EM) simulators are used to verify the design which is required to be exploited in the optimization process. However, applying direct optimization on high fidelity EM simulation is computationally expensive. As an alternative, iteratively refined surrogate models of accurate EM models, and the space mapping (SM) technologies implementation minimize the optimization time and maximize the accuracy simultaneously. An appropriate surrogate model can be developed by constructing an SM which is faster than the full-wave EM model (fine model) and more accurate than the empirical model (coarse model). The SM approach updates the surrogate in order to get a better approximation corresponds to the fine model. Figure 2.2 illustrates the basic idea of SM concept. SM-based optimization is usually executed in four steps. 1) EM/fine model should be simulated; 2) the parameters of the surrogate model (coarse) should be extracted; 3) the surrogate model should be updated; and 4) the surrogate should be reoptimized if necessary.

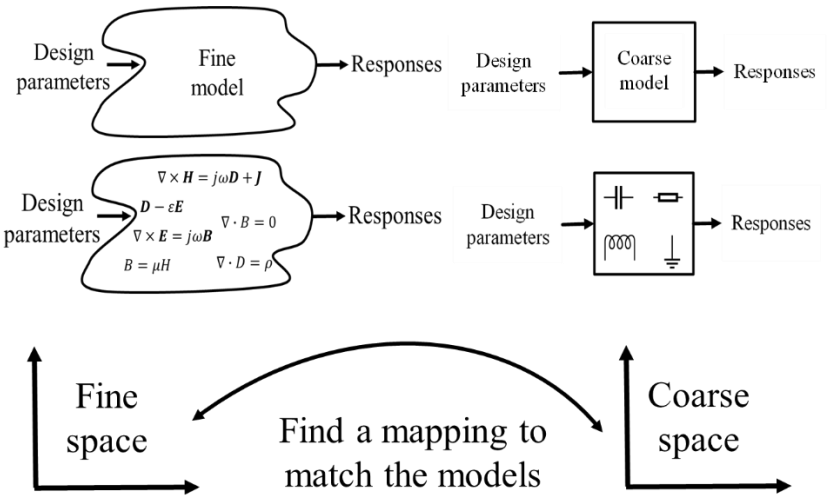


Figure 2.2 A mapping between coarse model and fine model [53]

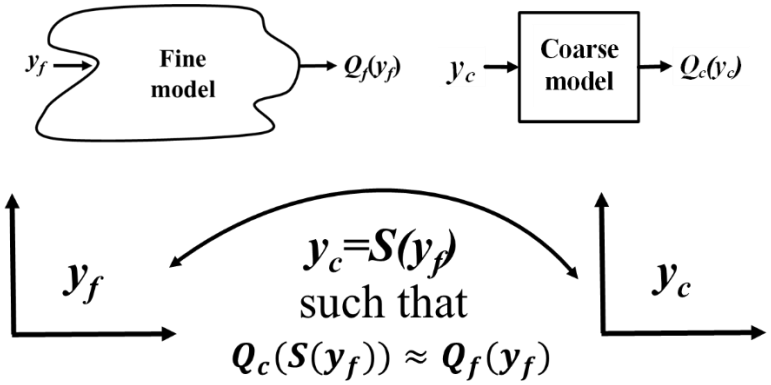


Figure 2.3 Basic notation of space mapping technique [53]

Before diving into the space mapping concept, let us define a design optimization problem first.

$$y^* \triangleq \arg\min O\big(Q(y)\big) \tag{2.29}$$

Here, (2.29) is the mathematical formulation of a target optimization problem where $O$ represents a vector of $n$ responses (such as $n$ frequency points of $S_{11}$ parameter) of the model, a vector of $p$ design parameters is indicated by $y$, cost function/objective function is denoted by $O$, and $y^*$ is the optimized solution to calculate.

Figure 2.3 illustrates the basic notation of SM technique where fine model and coarse model parameters are denoted by $y_f$ and $y_c$, respectively. Responses out of the fine model and coarse model are represented by $Q_f$ and $Q_c$, respectively. The goal is to find a mapping $S$ that relates

coarse model and fine model parameters as

$$y_c = S(y_f) \tag{2.30}$$

Such that

$$Q_c\left(S(y_f)\right) \approx Q_f(y_f) \tag{2.31}$$

In a region of interest.

The direct optimization can be bypassed by formulating $\bar{y}_f$ as follows:

$$\bar{y}_f \triangleq S^{-1}(y_c^*) \tag{2.32}$$

Where $y_c^*$ comes out of the optimized coarse model.

In the SM technique, the mapped solution is usually found by the minimization of the objective function which is formulated as

$$h = h(y_f) \triangleq Q_f(y_f) - Q_c(y_c^*) \tag{2.33}$$

Where, $Q_c(y_c^*)$ presents a surrogate coarse model. Therefore, the optimization problem can be expressed as

$$\bar{y}_f = \arg\min O\left(Q_c\left(S(y_f)\right)\right) \tag{2.34}$$

Here, $\bar{y}_f$ and $y_f^*$ are close while $Q_c$ is close to $Q_f$. For unique value of $y_c^*$, solution of (2.34) tends to drive the following residual vector $F$ to zero.

$$F = F(y_f) \triangleq S(y_f) - y_c^* \tag{2.35}$$

In the original SM approach, a primary approximation of the mapping $S^0$ is achieved from the fine model computation at a preselected set of $M_0$ basepoints while $M_0 \geq p + 1$. One base point is considered as the optimized coarse model solution. Rest $M_0 - 1$ base points are selected by perturbation. Parameter extraction (PE) process is applied to construct corresponding set of coarse model points as

$$y_c^j \triangleq \arg min\left\|Q_f(y_f^j) - Q_c(y_c)\right\| \tag{2.36}$$

For which PE error is expressed as

$$\epsilon \triangleq \left\| Q_f\left(y_f^j\right) - Q_c\left(y_c^j\right) \right\| = min \left\| Q_f\left(y_f^j\right) - Q_c(y_c) \right\| \tag{2.37}$$

Additional $M_0 - 1$ basepoints except $y_f^1$ should be established. A linear mapping between fine and coarse model space is assumed as

$$y_c = S^j\left(y_f\right) = b^j y_f + c^j \tag{2.38}$$

SM utilizes the current approximation at the jth iteration as,

$$\bar{y}_f \approx y_f^{M_j+1} = \left(S^j\right)^{-1}(y_c^*) \tag{2.39}$$

Till the $S_f(y_f^{M_j+1})$ is close to $Q_c(y_c^*)$, the iterative process continues. After the stopping condition is met, the space-mapped is set as formulated in (2.39).

### 2.4.2 Aggressive space mapping (ASM) approach

The ASM algorithm was first introduced in [51] by incorporating a quasi-Newton iteration utilizing the classical Broyden formula [60]. A significantly improved design is anticipated following each fine model simulation, while computational operations such as optimization and parameter extraction are carried out in the coarse model space.

The ASM technique iteratively solves the nonlinear system as

$$F\left(y_f\right) = 0 \tag{2.40}$$

At the jth iteration, $F^j$ as an error vector needs the evaluation of $S^j(y_f^j)$ which is indirectly calculated through the parameter extraction. The quasi-Newton step is formulated for the fine space as

$$b^j g^j = -F^j \tag{2.41}$$

Here, $b^j$ is the approximation of the Jacobian of $S$ [51] that is updated utilizing Broyden's rank one update. The solution of (2.41) for $g^j$ drives the next iteration as

$$y_f^{j+1} = y_f^j + g^j \tag{2.42}$$

The algorithm stops when the terminating condition is met which is a negligible value of $\left\| F^j \right\|$ in this case. The algorithm's output approximates (2.39) and $b$ denotes the mapping matrix which is popularly obtained by Broyden formula [60].

$b^0 = I$, is considered as the initial approximation where $I$ is the identity matrix. Then, $b^j$ is updated by utilizing Broyden's rank one formula [60]

$$b^{(j+1)} = b^j + \frac{F^{j+1} - F^j - b^j g^j}{[g^j]^T g^j} [g^j]^T \tag{2.43}$$

Here, quasi-Newton step is indicated as $g^j$. By utilizing (2.41), (2.43) can be expressed as

$$b^{(j+1)} = b^j + \frac{F^{j+1}}{[g^j]^T g^j} [g^j]^T \tag{2.44}$$

### 2.4.3 Trust region ASM approach

The main aim of present nonlinear programming is global behavior of the algorithms. Such robust global behavior provides the mathematical assurance that the optimization algorithm iteration starts from an arbitrary initial condition and converge to a stationary point or local minimizer for the problem [120]. Trust-region strategies achieve this property accurately. Trust-region methods adjust the length of the steps at each iteration based on the prediction accuracy of the linear/quadratic model structured objective function. This model is trusted to present the target objective/cost function only within a region of specific area surrounding by the current iteration. The minimum of the local model inside the trust region can be achieved by solving a trust-region subproblem. For sufficient actual minimization in the objective function, the trust-region size is enlarged. On the other hand, for the insufficient reduction, the trust region is reduced. Otherwise, the trust region remains the same [121].

Let us assume $F(y)$ as a scalar objective function. In the jth iteration, $K^j(y)$ is used as a local approximate model to approximate the objective function, $F(y)$. It is important for $K^j(y)$ to interpolate $F$ at $y^j$. Mathematically it has the property $K^j(y^j + g^j) - F(y^j) \to 0$ as $g^j \to 0$. The step $g^j$ to the next iteration can be achieved by solving the trust-region subproblem $K^j(y^j + g^j)$ which is subject to $\|g\| \leq \gamma^j$. Here, trust-region size is denoted by $\gamma^j$. A ratio $\mu^j$ is considered as a quality measure which is expressed as

$$\mu^j = \frac{F(y^j) - F(y^j + g^j)}{K^j(y^j) - K^j(y^j + g^j)} \tag{2.45}$$

Here, the actual reduction is represented by the numerator and the denominator denotes the reduction predicted by the local approximation. The trust-region size can be adjusted after each iteration based on (2.45). The next iteration is allowed if the objective function further reduction is possible. An excellent survey of techniques for trust-region size updating is found in [122].

The trust-region methodology integrated with the ASM technique is called as trust-region ASM algorithm [123]. In ASM, a quasi-Newton step is removed by solving a trust-region sub-problem within a certain trust region in order to minimize the objective function.

$$K^j\left(y^j, g^j\right) \triangleq F^j + b^j g^j \tag{2.46}$$

The linearized function is considered as (2.46). The following trust-region sub-problem should be solved in order to obtain the next step.

$$g^j = \arg\min\left\|K^j\left(y^j, g\right)\right\|_2^2 \tag{2.47}$$

Which is subject to $\|g\|_2 \leq \gamma^j$. Therefore, the step taken is constrained by a suitable trust region $\gamma^j$. Applying the constraints on (2.47) we get the following expression to solve.

$$\left(\left(b^j\right)^T b^j + \sigma I\right) g^j = -\left(b^j\right)^T F^j \tag{2.48}$$

Here, $b^j$ is the approximation to the Jacobian of the mapping $S$ at the j[th] iteration. $\sigma$ should selected so that the step remains identical to (2.47). $b^j$ should be updated by Broyden's formula.

In this section, we have explained the methodologies and mathematical foundations of fundamental SM techniques such as original SM, ASM and trust region ASM in detail. There are lots of variations of SM technique proposed in the literature for encountering different EM-based designing challenges. Such as space mapping (MSM) [124], generalized space mapping (GSM) [125], implicit space mapping (ISM) optimization [126], hybrid ASM algorithm [127], tuning space mapping [128], parallel space mapping [129], partial space mapping [130], space-mapping interpolating surrogate (SMIS) model [131] etc. These algorithms are advanced forms of original space mapping technique which are adopted for much complicated EM based structures and wide range of applications. The detailed methodologies and optimization techniques of these advanced algorithms are not added in this work as we focus on broader aspects of the EM-based optimization techniques. Interested readers may check out the references added here, and other related works conducted by the research group of J. W. Bandler.

## 2.5 ANN and SM crossover

ANN and SM are two novel concepts that are extensively used in EM-based surrogate model optimizations. A combination of these two powerful concepts was first introduced in [56] and generally named as space-mapped neouromodeling (SMN). ANNs are capable of modeling high-dimensional and highly nonlinear problems which is exploited in the SM concept's implementation. Readily available large set of empirical models can be used to develop SM-based neuromodels where a reduced number of electromagnetic (EM) simulations are required for training. Such a model improves the generalization ability as well as minimizes the ANN model complexity as compared to the classical neuromodeling approach. Different space-mapped neouromodeling techniques are discussed below.

Different innovative combinational technology of SM technique and ANN modeling have been presented in [56] and [57]. The main idea behind such a combined model is to construct a highly nonlinear input-output multidimensional mapping function from fine model to coarse model utilizing an ANN. Such mapping can be executed in various ways considering an optimum use of the coarse-model information for developing the target neuromodel. Such coarse model-based implicit knowledge decreases the number of required learning points as well as reduces the ANN model complexity to improve the generalization performance. The fine to the coarse parameter space mapping is implemented by an ANN in the space-mapped neuromodel (SMN) strategy which is illustrated in Figure 2.4(a). Here, $y_f$ and $y_c$ represent the input variables of the fine model and coarse model, respectively. In addition, *freq* is the frequency variable, w is the weight matrix of the ANN model, $R_c$ and $R_f$ indicates the coarse and fine model responses, respectively. The main challenge in this approach is to find the optimal weight and bias matrix of the ANN, so that the coarse model response becomes close to the fine model response in case of all the learning points.

The majority of the available empirical models for microwave circuits utilize the methods for quasistatic analysis which provides us good accuracy at low frequencies with narrow bandwidth. A frequency-sensitive mapping from the fine to the coarse input spaces can overcome this limitation. Such a mapping can be realized by considering frequency as another input variable to the target ANN model. Figure 2.4(b) illustrates the FDSMN approach where both coarse and fine models are simulated at the same frequency while the fine to coarse parameter space mapping is frequency dependent. Figure 2.4(c) illustrates the FSMN technique which establishes a mapping

for the design parameters along with frequency variable so that the coarse model is simulated at a mapped frequency in order to match the fine model response. This is done by introducing an extra output to the ANN that implements the mapping.

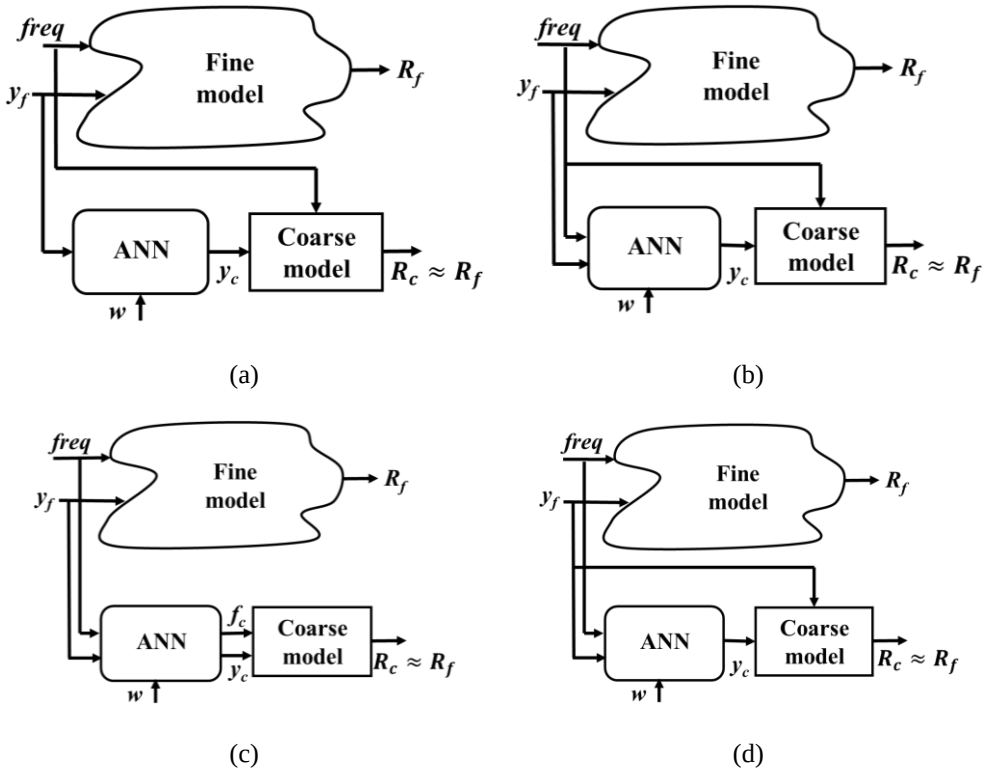


Figure 2.4 Variation of SM based neuromodeling concept [53]; (a) SMN; (b) FDSMN; (c) FSMN; (d) FMN concept.

In lots of microwave problems, the coarse model behaves similarly to the fine model does while the frequency response is shifted a little bit. For such cases, a good agreement between coarse and fine model responses can be achieved by simulating the coarse model at a different frequency. Figure 2.4(d) illustrates the FMN technique where the coarse model is simulated with the same physical parameters as the fine model, but at a mapped frequency to match both responses with respect to the frequency.

The complete set of physical parameters' mapping in SMN, FDSMN, and FSMN techniques lead to singularity problem in the coarse model response during the training session. Such a problem can be overcome by developing a partial mapping for the physical parameters which makes the more efficient use of the implicit knowledge in the coarse model. In many microwave problems,

only a few physical parameters' mapping can be enough to obtain acceptable accuracy in the neuromodel which significantly reduces the ANN model complexity and training time as compared to the SMN, FDSMN, and FSMN techniques.

The linear input neural space mapping strategy was first proposed in [132] as illustrated in Figure 2.5. Here, $\delta$ represents the independent variable (usually frequency). P is the linear mapping function which is achieved by an algorithm-based design procedure that reveals $y_f$ and brings fine model response, $R_f$ close to a target response that is generated by the coarse model response, $R_c$. An ANN model, $Q$ is used in the output whose weight matrix, $w$ is trained around $y_f$ to remove the residual between $R_f$ and $R_c$. This LINO-SM strategy has three steps as follows: find a desired coarse model response by optimization, find space mapped fine model parameters and $P$ through a linear input space mapping optimization and finally develop an ANN model. Once the ANN model is available, it is used to perform statistical analysis and yield calculation around space mapped fine model parameters.

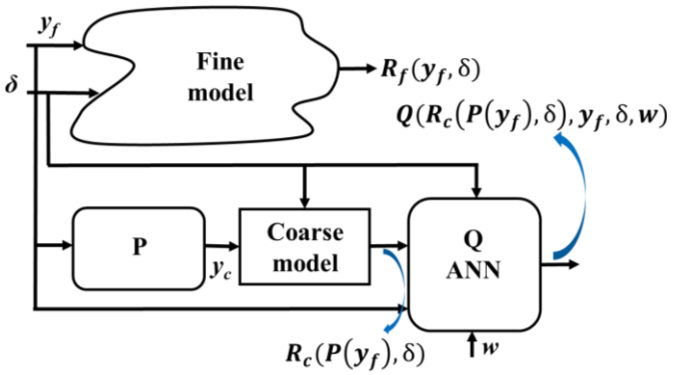


Figure 2.5 Linear-input neural-output space mapping technique [132]

ANN model and space mapping are combinedly used for other applications. In [100], a robust knowledge-based automatic model generation (KAMG) technique is proposed that uses fine and coarse model data generators and take advantage of knowledge based neural networks to generate accurate microwave neural models utilizing fewest accurate training data. This KAMG technique achieves efficient neural model generation by using coarse model data along with minimized use of fine data. Different KBNN architectures are used to enable both coarse and fine data to contribute toward reinforced neural-network learning of detailed or fine microwave behaviors. An efficient method for accurate EM-based statistical analysis and yield estimation of RF and

microwave circuits is proposed in [42]. The proposed method consists of applying a constrained Broyden-based linear input space mapping approach to design along with an output neural space mapping modeling process.

## 2.6 Illustrative examples

So far, we have discussed a wide variety of optimization methods that are used in EM-based designs. In this section, we list some design examples to demonstrate the applications of major types of optimization techniques. We cover examples of following optimization types: gradient-based optimization, gradient-free optimization, ANN-based optimization, space mapping-based optimization and neuro-SM-based optimization. Firstly, we divide commonly demonstrated examples into the following classes: transmission lines with discontinuity, microwave passive circuits (fixed filters, tunable filters, divider, coupler), and antennas. Then we discuss respective algorithms.

### 2.6.1 Microstrip lines with discontinuities

Microstrip lines are commonly used as transmission line due to its low cost and ease of fabrication on the microwave circuits. Discontinuities in the microstrip lines are widely applied in order to match the impedance between different sections of the transmission lines for different applications. Microstrip discontinuities such as gap, step, bend, T-junction etc. are the common elements in a wide variety of microwave circuits. Figure 2.6 illustrates microstrip right angle bend and microstrip step junction. These discontinuities are usually modelled as a T or π section of network with inductance and/or capacitance combination. Different coarse models for these microstrip discontinuities are presented in [133] and [134]. A generalized space-mapping (GSM) strategy is applied in [125] to model different microstrip discontinuities. Three fundamental illustrations are presented in [125]: a basic space-mapping super model (SMSM), frequency-space-mapping super model (FSMSM) and multiple space mapping (MSM). Two variations of MSM are presented: MSM for device responses and MSM for frequency intervals. Microstrip bend, step and T-junction are modelled to verify the SMSM, FSMSM, and MSM concepts.

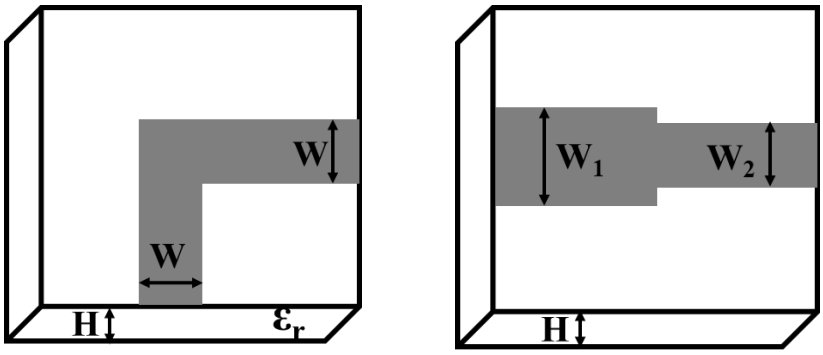


(a) (b)

Figure 2.6 Microstrip discontinuity (a) Bend (b) Step [125]

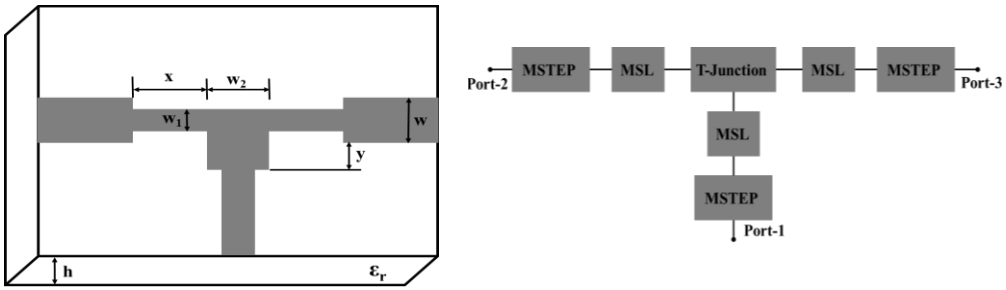


(a) (b)

Figure 2.7 Microstrip-shaped T-junction (a) Fine model (b) Coarse model [125]

Optimization of the design of a three section 3:1 microstrip impedance transformer is exampled in different works. Figure 2.8(a) and Figure 2.8(b) illustrate the fine model and coarse model of a three section 3:1 microstrip impedance transformer. Classical space mapping technique [49] was first applied to model such a microstrip impedance transformer. Other optimization strategies such as yield-driven EM optimization via multidimensional models [30], space-mapping-based interpolation [135] are used to the design optimization of microstrip impedance transformer. In [136], a space mapping design framework is also outlined by exploiting tuning elements for the same example.

Similar to the microstrip impedance transformers, seven section waveguide transformers are exampled for the demonstration of hybrid aggressive space-mapping algorithm in [127]. A systematic method of considering the discontinuity effect directly into the optimization process is demonstrated in the case of two section, three section, five section and seven section waveguide transformer design optimization [137].

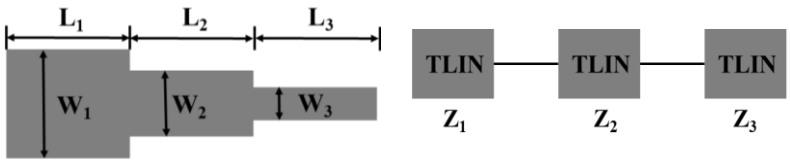


(a) (b)

Figure 2.8 Three-section microstrip impedance transformer (a) Fine model (b) Coarse model [135]

### 2.6.2 Microwave filters

Microwave filters are the commonly used examples for the demonstration of optimization techniques. Microwave filters are usually consisting of high dimensional design variables and their performances are highly sensitive to these variables. Therefore, such variables are required to be optimized accurately in order to meet the desired filter performances. That is the reason why optimization algorithms play a significant role on the successful design of microwave filters. Commonly exampled filters in the optimization related literature are categorized as H-plane rectangular waveguide filter, DFS filter, HTS filter, microstrip notch filter and tunable filters.

#### 2.6.2.1 H-plane waveguide filters

H-plane waveguide filter of different section is a classic example of microwave optimization problem. A bandpass filter response is usually expected to provide a minimum in-band return loss and a maximum stop-band insertion loss according to the design specifications. Figure 2.9 illustrates fine and coarse model of a six-section H-plane waveguide filter. In case of such waveguide filters, iris width and resonator lengths are the optimization variables. Six sections of such a waveguide filter are separated by seven H-plane septa with a finite thickness. Various optimization strategies have been employed for the optimization of such waveguide filter structures. This example has been employed in order to demonstrate hybrid aggressive space-mapping technique [127], space mapping interpolating surrogate algorithm [131], tuning by space mapping technique [138], combination of Fletcher–Powell (FP) algorithm and Step–Wise (SW) algorithm [14], and response-residual space-mapping (RRSM) [136].

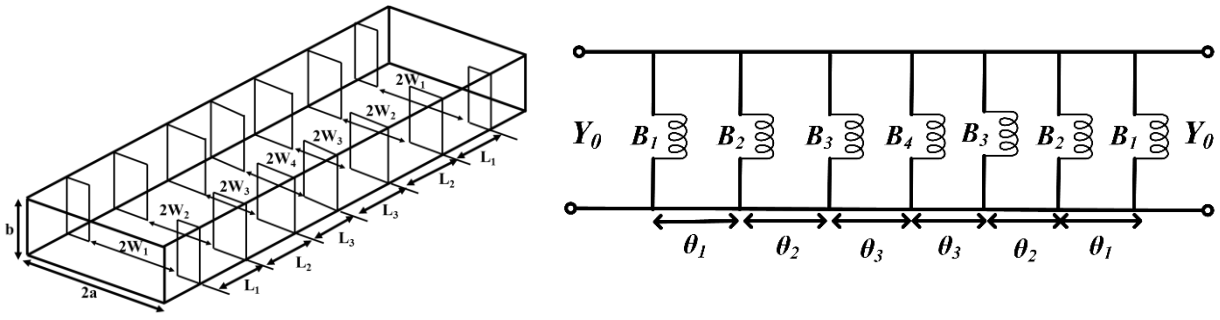


(a) (b)

Figure 2.9 Six-section H-plane waveguide filter [127] (a) fine-model (b) coarse model

Similar to the six-section H-plane waveguide filter, a three-pole H-plane filter is exampled to demonstrate an advanced cognition-driven EM optimization technique that incorporates the transfer function-based feature surrogate model [43] and an advanced simulation-inserted optimization using combined Quasi-Newton method with Lagrangian method [15]. Four-cavity H-plane rectangular waveguide filter is optimized by the aggressive space mapping with a new segmentation strategy and a hybrid optimization algorithm [138]. Five-pole H-plane filters are applied for the demonstration of an advanced parallel space-mapping-based multiphysics optimization [93] and ANN model-based homotopy optimization [31].

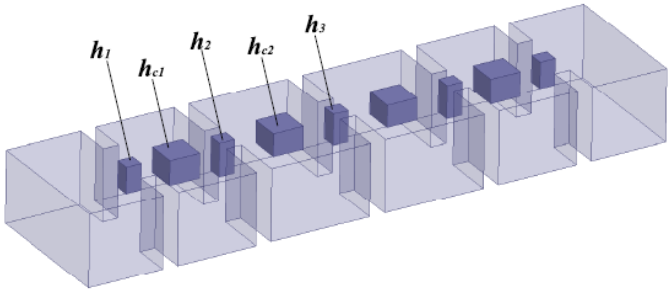


Figure 2.10 EM model of a four-pole H-plane waveguide filter with tuning elements [119]

A four pole waveguide filter shown in the Figure 2.10 is commonly used as different optimization algorithms such as multi-feature assisted neuro-transfer function surrogate-based EM optimization exploiting trust-region algorithms [119], advanced parallel space-mapping-based multiphysics optimization [93], cognition-driven space mapping optimization [139] and advanced cognition-driven EM optimization technique incorporating the transfer function-based feature surrogate model [43].

### 2.6.2.2 Double-folded stub filter

The design of the double-folded stub (DFS) microstrip structure is another common example of filter optimization problem. Figure 2.11 illustrates the fine model and coarse model of the double-folded stub filter. Folded stubs reduces the filter area as compared to the conventional double stub structure. The filter is characterized five design variables as shown in Figure 2.11(a). Apart from $W_1$ and $W_2$, other geometric parameters are considered as the optimization variables. Following optimization techniques are demonstrated for the designing of DFS filter: classical space mapping technique [49], hybrid aggressive space-mapping technique [127], fuzzy system exploited space mapping technique [140] and a trust region aggressive space mapping technique [123].

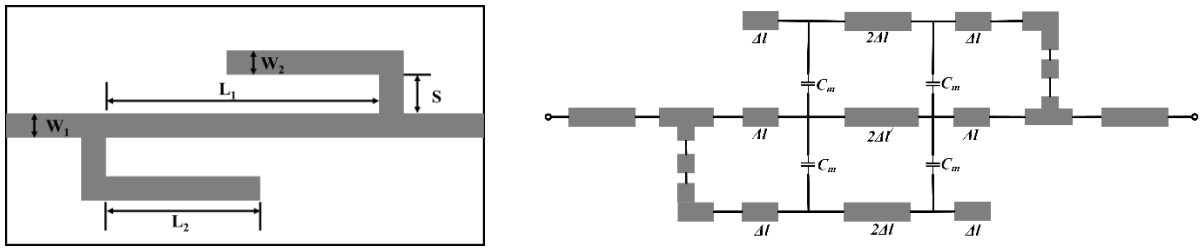


(a) (b)

Figure 2.11 The DFS filter [127] (a) fine-model (b) coarse model

### 2.6.2.3 HTS filter

HTS filter is exampled in the literature for the optimization algorithm demonstration. Figure 2.12 shows the fine model and coarse model of a HTS filter. The length of the coupled microstrip line and the distance between two coupled lines are considered as optimization variables of a HTS filter. The optimization of such a HTS filter structure is performed by several optimization techniques such as the classical aggressive space mapping technique [51], a trust region aggressive space mapping technique [123], tuning space mapping [128], implicit space mapping optimization exploiting preassigned parameters [126], neural space mapping [57] and parallel space mapping [129].

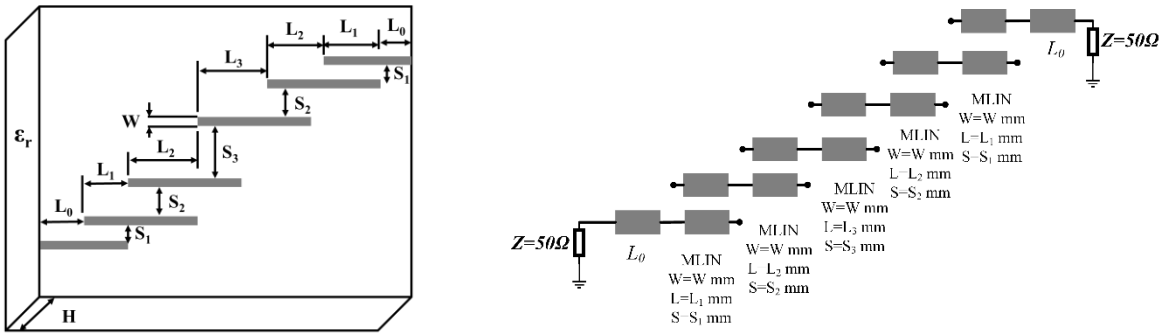


(a) (b)

Figure 2.12 The HTS filter [51] (a) fine-model (b) coarse model

### 2.6.2.4 Microstrip notch filter

Another well known optimization example is considered in this review paper is the microstrip notch filter with mitered bends as illustrated in Figure 2.13 [42] where $L_0$ is the open stubs length and $L_c$ is the length of the coupled lines, and $S_g$ is the separation gap. All the microstrip linewidth are same, $W$ . The substrate thickness is $H$ and relative dielectric constant is $\varepsilon_r$. The optimization variables are $L_c$, $L_0$ and $S_g$. In [42], EM-Based Monte Carlo analysis and yield prediction of microwave circuits using linear-input neural-output space mapping is used for the optimization of a microstrip notch filter with mitered bends. An interpolated coarse model is used for the design optimization of a microstrip notch filter along with space mapping technique [141].

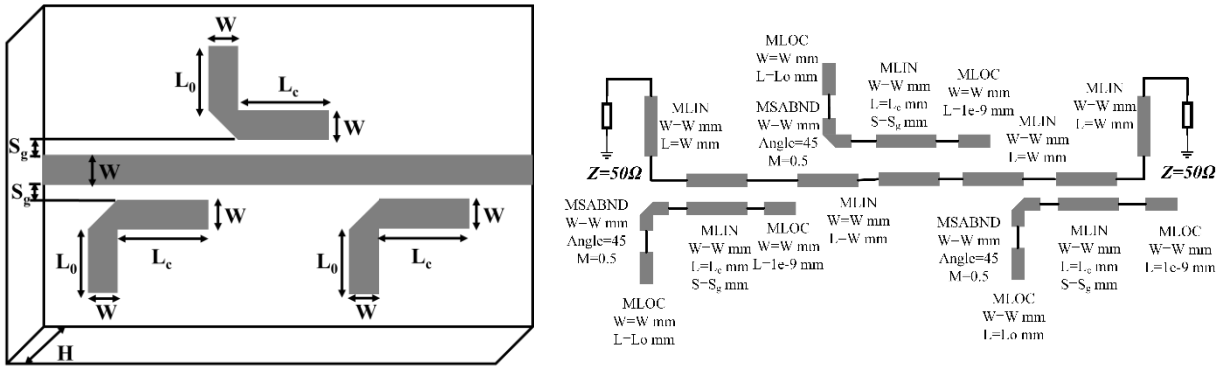


(a) (b)

Figure 2.13 Microstrip notch filter with mitered bends [42] (a) fine model (b) coarse model

### 2.6.3 Microwave tunable filters

Tunable and reconfigurable microwave circuits and techniques are studied extensively in the literature due to the limitless demand of multiband and multifunction microwave communication systems. Recently, optimization techniques based on ANN surrogate model have been utilized on predicting tunable filter parameters according to the desired tuning criteria [33], [41]. In [41], swarm intelligence-based optimization techniques have been hybridized with mathematics-based homotopy optimization technique. A fourth order dual mode tunable bandpass filter and a constant absolute bandwidth tunable filter is demonstrated in [41] as shown in Figure 2.14(a) and Figure 2.14(b), respectively. In both the cases, the optimization variables are the height of the tuning screws. An ANN modeling approach is outlined in [41] for calculating these design variables in terms of desired response from a tunable filter.

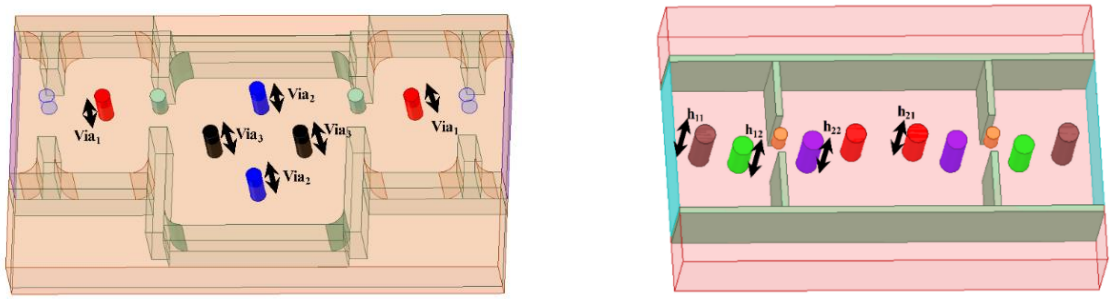


(a) (b)

Figure 2.14 Tunable waveguide filters [41] (a) dual-mode filter (b) constant bandwidth filter

### 2.6.4 Coupler and divider

Low-profile passive components are fundamental building blocks of ever-increasing wireless communication system. Directional coupler and power divider are some of the major components those are required to be designed over certain frequency range with specific size and performance requirement. Millimeter-wave and THz applicable couplers are highly sensitive to the design variables. In [32], a SIW cruciform coupler is designed for D-band application with the help of an ANN surrogate model and homotopy optimization. Figure 2.15 illustrates the schematic of SIW cruciform coupler where the optimization variables are the location and diameter of the tuning posts and matching posts. In [18], a direct local optimization technique is demonstrated by designing a dual-band branch-line coupler (Figure 2.16) and a dual-band equal split power divider

(Figure 2.17). This algorithm increases its computational efficiency by exploiting two mechanisms: multi-fidelity EM simulations and selective Broyden updates.

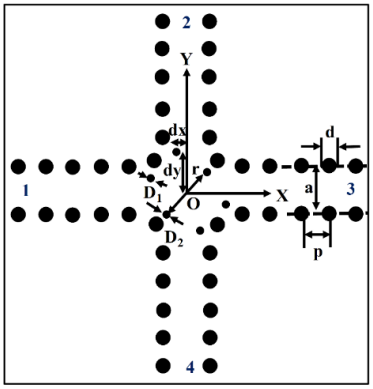


Figure 2.15 SIW cruciform coupler [32]

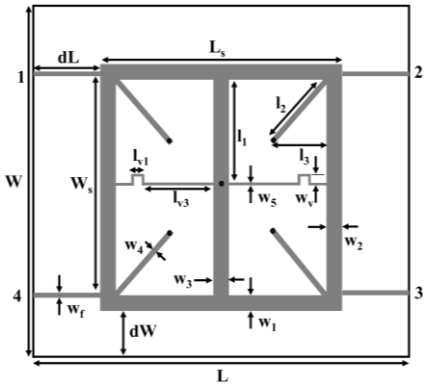


Figure 2.16 Dual-band branch-line coupler [18]

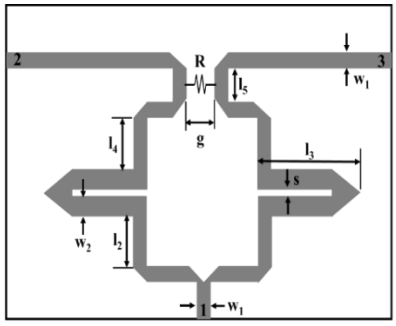


Figure 2.17 Dual-band equal split power divider [18]

### 2.6.5 Antennas

Successful antenna designing is an iterative approach of parameter sweeping which is computationally expensive and time-consuming process. Evolutionary algorithms (EAs) such as particle swarm optimization (PSO) and genetic algorithm (GA) are widely used for antenna optimization tasks.

In [38], an efficient machine learning method-based surrogate-assisted particle swarm optimization (SAPSO) is proposed that combines the particle swarm optimization with two machine learning-based models. A mixed prescreening (mixP) strategy is then integrated to choose promising individuals for full-wave EM simulations. A SIW cavity-backed slot antenna (Fig. 18) is optimized by the proposed SAPSO algorithm where a pair of cross-shaped slots are etched on the ground plane along with a 50Ω microstrip feedline at the top layer. The optimization variables are indicated in the respective antenna geometry shown in Fig. 18. The other example used in [38] is a four-element linear array antenna (LAA) which has 19 design variables to optimize in order to operate at the WLAN band. Fig. 19 illustrates the geometrical structure of LAA.

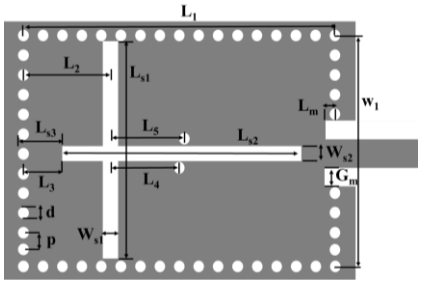


Figure 2.18 SIW cavity-backed slot antenna [38]

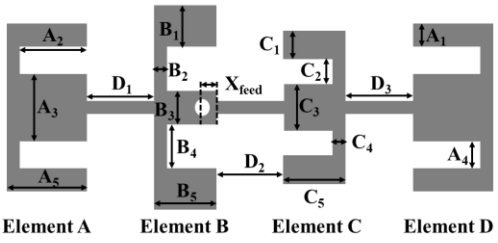


Figure 2.19 Geometry of the four-element LAA [38]

In [39], an improved version of comprehensive learning particle swarm optimization (CLPSO) is proposed which is named as adaptive comprehensive learning particle swarm optimization (A-

CLPSO). In this designing technique, the rough design and only little experience in the prototype modification replaces the designer's experience in foreseeing the antenna prototype. The precise design guarantees that the antenna's structure meets the desired characteristic. This advanced PSO technique is employed to design a multiband monopole antenna. The final structure of the a multiband monopole antenna that meets the desired antenna reflection coefficient is illustrated in Figure 2.20. The optimization variables are indicated in the respective figure.

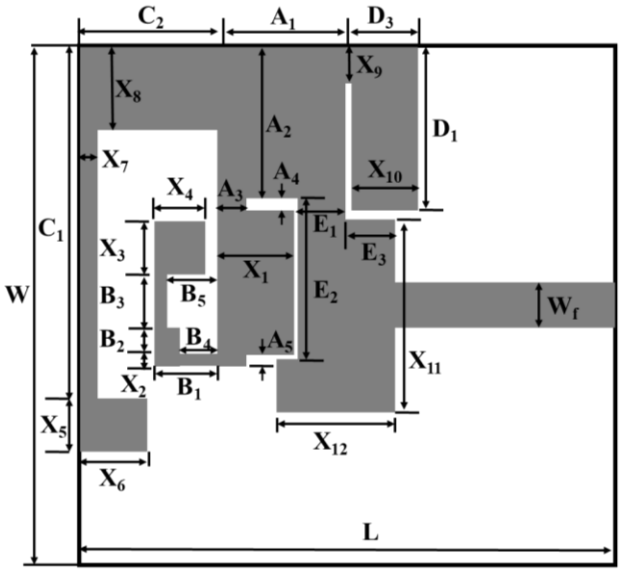


Figure 2.20 Multiband monopole antenna structure [39]

This section presents several microwave circuit structures designed with state-of-the-art optimization techniques. Various examples from transmission lines, microwave filters, tunable filters, couplers, dividers, and antennas are covered to demonstrate the wide range of microwave, millimeter-wave, and sub-THz circuits that require optimization algorithms for successful design. The variety of examples clearly illustrates the significance of optimization techniques in microwave circuit design. Due to page limitations, it was not feasible to summarize all examples from the literature. However, interested readers may refer to the respective papers listed in the reference section of this paper.

## 2.7 Discussions and future directions

This review paper has examined various optimization techniques used in microwave circuit designs and implementations. In this section, we present a comparative analysis of these optimization algorithms in terms of complexity, primary methodology, demonstrated examples, and variables. Moreover, future research directions for optimization techniques are speculated based on current research trends.

Table 2.1 Comparison of optimization algorithms

| Ref. | Optimization Method | Optimizer Type | Demonstrated Example | Optimization Variables | Total opt. Variables | Total Iterations | CPU Time | Optimization Complexity |
|---|---|---|---|---|---|---|---|---|
| [14] | Fletcher-Powell and Stepwise algorithm | Gradient-based optimizer | 6 and 9 pole waveguide filter | Waveguide dimensions | 7,19 | 59, N/A | N/A | Multiple steps but Simple |
| [15] | Simulation inserted optimization using Quasi-Newton | | 3 pole and 5 pole waveguide filter | Waveguide dimensions | 4, 6 | 97, 78 | 5.3h, 6h | Complicated |
| [16] | Minimax optimizer | | Lowpass microstrip filter, DFS band-stop filter, mmW BPF | Microstrip dimensions | N/A, 3, 13 | N/A | N/A | Simple |
| [17] | Quasi-Newton | | 4×4 Butler Matrices in waveguide | Elbows in waveguide | 62 | N/A | 1h | ANM is used for fast opt. |
| [18] | Selective Broyden update | | Power divider, Branch-line coupler | Microstrip dimensions | 7, 9 | N/A | N/A | Complicated framework |

Table 2.2 Comparison of optimization algorithms (cont'd)

| Ref. | Optimization Method | Optimizer Type | Demonstrated Example | Optimization Variables | Total opt. Variables | Total Iterations | CPU Time | Optimization Complexity |
|---|---|---|---|---|---|---|---|---|
| [26] | Equal-ripple optimization | Meta-heuristic-based (Mathematics) optimizer | Ridged waveguide BPF | Gaps in ridged waveguide | 5 | N/A | N/A | Theoretically simple |
| [27] | Rational model | | E-plane waveguide filter, diplexer | Length and distance of metal inserts | 11, 26 | 10, 37 | N/A | Complicated workflow |
| [28] | Model order reduction | | E-plane waveguide filter, diplexer | Resonator lengths and coupling inset lengths | 5, 23 | N/A | 30 m, N/A | Little complicated |
| [29] | Linear optimization | | 2 dual-band BPFs, 1 triple-band BPF | Rib heights, copper heights | 13, 13,14 | N/A | N/A | Simple |
| [31] | Homotopy optimization | | H-plane waveguide BPF without and with TZ | Iris window length and resonator length | 6, 12 | 11, 12 | 8.3 m, 12 m | Simple |
| [35] | Particle swarm optimization | Meta-heuristic-based (Swarm) optimizer | Microstrip BPF, Dual band BPF | Microstrip and slot dimensions | 6, 13 | N/A | N/A | Simple |
| [38] | Surrogate-assisted PSO | | SIW slot antenna, linear antenna array | Microstrip and SIW dimensions | 11, 19 | 100, 300 | N/A | Complicated (due to ML) |
| [39] | Comprehensive learning PSO | | Multiband monopole antenna | Microstrip dimensions | 12 | N/A | N/A | Simple |

Table 2.3 Comparison of optimization algorithms (cont'd)

| Ref. | Optimization Method | Optimizer Type | Demonstrated Example | Optimization Variables | Total opt. Variables | Total Iterations | CPU Time | Optimization Complexity |
|---|---|---|---|---|---|---|---|---|
| [41] | Swarm-homotopy hybrid | Hybrid optimizer | Tunable waveguide filters | Post heights | 3, 4 | N/A | N/A | Complicated (due to ANN) |
| [43] | Cognition-Driven, TF incorporated EM optimization | ANN-based surrogate optimization | 3 pole and 4 pole waveguide filter | Resonator and window length, tuning posts' | 4, 5 | 6, 8 | 22.5 m, 45.1 m | Complicated (due to TF integration) |
| [44] | Hybrid Surrogate Model-Assisted Optimization | | 8th-order dual-band BPF, C-band 6th-order BPF | waveguide dimensions | 10, 14 | EM simulations: 678, 776 | N/A | Complicated (surrogate modeling) |
| [46] | Surrogate model-assisted EA-based yield optimization | | X-band and C-band waveguide filter | waveguide dimensions | 11, 14 | N/A | 120 h | Complicated (surrogate modeling) |
| [49] | Classical SM | Space mapping | Impedance transformer, DFS filter | Microstrip line widths; lengths and spacing | 3, 3 | N/A | 3 days | Simple |
| [51] | Aggressive SM | | HTS filter | Coupled line parameters | 6 | N/A | N/A | Simple |
| [123] | Trust region ASM | | DFS and HTS filter | Microstrip lines | 3, 6 | N/A | N/A | Simple |

Table 2.4 Comparison of optimization algorithms (cont'd)

| Ref. | Optimization Method | Optimizer Type | Demonstrated Example | Optimization Variables | Total opt. Variables | Total Iterations | CPU Time | Optimization Complexity |
|---|---|---|---|---|---|---|---|---|
| [42] | Linear-input neural-output SM | Neuro-SM | microstrip notch filter | Open stub lengths, coupled lines lengths, and separation gap | 3 | N/A | N/A | Complicated |
| [56] | SM-based neuromodeling | | HTS filter | Coupled line parameters | 6 | N/A | N/A | Simple |
| [57] | FSM-based neuromodeling | | HTS filter, band stop filter with open stubs | Microstrip lines | 6, 5 | N/A | N/A | Simple |

Table 2.1, Table 2.2, Table 2.3 and Table 2.4 is presented here to provide a comprehensive overview of current research trends on EM-based optimization for microwave structures. The table summarizes various optimization techniques utilized in different EM-based design environments and provides references for each method. The examples listed in the table are categorized into six major types of optimization algorithms, including gradient, meta-heuristic (gradient-free), ANN, space mapping, neuro-space mapping, and hybrid optimization techniques. Furthermore, the Tables include demonstrated examples from the respective references, along with the total CPU time, number of optimization variables, total number of iterations, and complexity level of the optimization process. The table indicates that most of the optimization algorithms are demonstrated by filter examples. Microwave filters often require optimization to meet design specifications, as their responses are highly sensitive to geometric parameters. It is also evident that surrogate models require a significant amount of CPU power to build through EM simulations. However, CPU time is not indicated in most references, which is a crucial criterion for comparing optimization models. Although Table I only provides a few examples, it offers a brief observation of current trends in EM optimization research.

Table 2.1, Table 2.2, Table 2.3 and Table 2.4 provide insights into the potential future research directions of EM-based optimization. As direct optimization, ANN modeling, and space-mapping optimizations are already widely utilized in the literature, researchers are likely to combine these algorithms to leverage their respective advantages. Furthermore, current optimization methods are unable to provide a unique solution to a specific target problem. In other words, different optimization cycles can yield distinct results even when initial conditions and optimizer remain the same. Additionally, current optimization algorithms lack generalizability and are typically tailored to specific target problems. Although the NFL theorem proves that no optimization can offer the best solution to all problems, researchers may strive to generalize optimization algorithms for microwave-specific applications.

## 2.8 Conclusion

This article presents a comprehensive survey of EM-based optimization algorithms. The article begins by introducing the common types of optimization techniques. Next, the current state-of-the-art EM-based optimization methods are classified into two main categories: direct and surrogate optimizations. The direct optimization category is further divided into gradient-based and swarm-

based optimizers. On the other hand, surrogate optimizations are mainly classified into space-mapping optimization and ANN-based optimizations. The article explains the methodology of major types of algorithms under each category. Additionally, other optimizers are briefly discussed with relevant references. The design examples are grouped into transmission lines, filters, and antennas. The work illustrates these examples with corresponding algorithms available in the literature. Finally, the article presents a comparison chart of commonly used optimizers with corresponding examples and other design details. Based on the current research trends on optimization algorithms and artificial intelligence, the article concludes with a brief discussion on future research directions.

# CHAPTER 3 ARTICLE 2: HOMOTOPY OPTIMIZATION AND ANN MODELING OF MILLIMETER-WAVE SIW CRUCIFORM COUPLER

Chandan Roy and Ke Wu

Published in the *IEEE Transactions on Microwave Theory and Techniques*, vol. 70, no. 11, pp. 4751-4764, 29 August 2022

The development of millimeter-wave and terahertz (THz) passive components such as couplers and filters is an intimidating task because of underlying ultra-sensitivity of electrical performances to geometric dimensions and processing tolerances. It is a common practice for us to use an integrated optimizer of commercial electromagnetic (EM) software packages for the design and optimization of such geometric parameters. However, those optimizers may fail to achieve a desired performance if initial variables are not in a range close enough to the optimal solution. In this paper, we introduce an homotopy approach to optimizing the geometric parameters of a D-band cruciform coupler based on substrate integrated waveguide (SIW) technique in conjunction with an artificial neural network (ANN) model. Starting from a set of initial variables, a homotopy optimization is set to search for an optimum solution. The ANN technique is adopted as the surrogate in place of a usual time-consuming electromagnetic model to accelerate the homotopy optimization process of the cruciform coupler. We propose a feed-forward computational formulation inspired by the fundamental transmission line impedance equation. Such a transmission line knowledge-based feedforward network results in a faster convergence with better accuracy than its conventional counterpart. To demonstrate the homotopy optimization method based on the ANN model, an example of multi-parameterized cruciform coupler design is detailed. This cruciform coupler with optimized geometric dimensions is simulated, fabricated, and measured. Measured and simulated results validate the combined ANN model and homotopy method. An equivalent lumped-element circuit model of the cruciform coupler is also proposed in this work. An ANN model development technique is described how to extract the equivalent circuit parameters for given coupler specifications. Extracted circuit parameters in connection with the desired coupler performance are then compared with published results which verify the ANN model development algorithm.

## 3.1 Introduction

Millimeter-wave (mmW) and terahertz (THz) technologies are foundational and crucial in various applications of current and future wireless communication, astrophysics, atmosphere monitoring, and security systems in which lightweight and low-profile integrated passive components are fundamental building blocks such as directional couplers for power splitting over a certain frequency range with specific size and performance requirement [142], [143], [144], [145]. Different types of directional coupler have been developed for a multitude of mmW and THz applications such as beamforming network, precision measurement, antenna feeder, frontend mixer, six-port transceiver etc. Among them, rectangular waveguide and substrate integrated waveguide (SIW) technologies have been investigated thoroughly for the development of such directional couplers [146], [147], [148], [149], [150], [151]. Rectangular waveguide couplers can deliver superior performances, but the manufacturing is expensive with bulky volumes. On the other hand, SIW directional couplers have been extensively studied due to the low-cost fabrication, low-loss performances, and easy integration with planar circuits. Among all the SIW coupler structures and techniques proposed to date, the cruciform coupler, as described in Figure 3.1, is one of the most attractive and outstanding schemes thanks to its low-loss and extremely compact geometry formed simply by two perpendicular rectangular guides with few metallic posts embedded in the cross-region [148], [150]. So far, the cruciform coupler has been investigated theoretically through full-wave analyses, which were well validated experimentally. This coupler involves an irregularly shaped junction and its accurate analysis, design procedure, and performance optimization are further complicated by multiple posts of multiple sensitive dimensions. On the other hand, a lumped element equivalent circuit of such a coupler has not been reported yet which should be set to guide the design and development of such couplers according to specifications. In this work, we come up with the development of an equivalent circuit for the cruciform coupler.

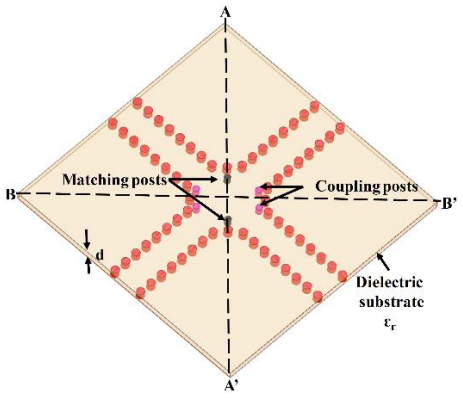


Figure 3.1 Sketch of a SIW cruciform coupler

The cruciform coupler exhibits great flexibility of coupling control over a reasonable bandwidth [148], [149], [150], [151], whose properties are usually featured by specifications in terms of center frequency, bandwidth, coupling, return loss, and isolation. Depending on applications, a desired coupling may vary from 1 to 20 dB. In addition, 15 to 25 dB of return loss and more for isolation are highly appreciated. In the design of a cruciform coupler, the desired coupling can be achieved by symmetrically placing two metallic posts for controlling the signal flow along with two extra-via posts diagonally positioned as reflecting obstacles, as shown in Figure 3.1. Coupler performance is greatly affected by the location and diameter of these metallic posts. Developing such a coupler with optimization at mmW and THz frequencies is challenging because of the high sensitivity of performance to its physical dimensions. Even though a few design parameters are involved in the cruciform coupler design, it is cumbersome to preselect these parameters simply by observing simulated S-parameters. This is because its extreme compact size galvanizes a strong correlation effect of those parameters on the performances. Conventionally, the coupler optimization starting from a set of initial values of the design parameters is a common practice. Such optimization may be achieved by the evolutionary algorithm (EAs) and sequential nonlinear programming among many others, which have been integrated into commercial electromagnetic (EM) software packages such as HFSS [148]. In such an optimization process, the geometric parameters are varied within a boundary and the search region is restricted in proximity of the initial values. This type of EM-based optimization has two challenges. First, it may fail if the initial values are far from an optimal solution. Second, it presents a time- and resource-consuming process as it makes use of a 3D EM model accounting for different combinatory sets of geometric parameters. Other optimization algorithms such as Powell's optimization method also suffer from

the same problems [146], [151]. A genetic algorithm (GA) has been used to optimize these design parameters, but present disadvantages of overfitting and long optimization time caused by its slow convergence behavior [147].

To overcome the hurdle of optimization, we introduce a homotopy approach in this work to optimizing the cruciform coupler structure. The homotopy method implements the concept of topology for generating a series of solutions for nonlinear systems with a convergence control parameter [152]. This method sets up nonlinear optimization problems instead of solving the target coupler problem directly. These intermediate problems are solved by using preceding solutions as the initial variable of the current optimization in an iterative manner. In this way, the coupler performance gets improved slowly but surely meets the specification through this process of homotopy optimization. The homotopy method is set to find out the desired parameters accurately even if the initial parameters are far away from the optimal solution. The homotopy optimization technique was successfully introduced in the design of bandpass filters [31]. A coupler performance is characterized by its in-band return loss, isolation, and coupling while a microwave filter performance is characterized by passband return loss and stopband insertion loss. In this work, we investigate and extend the capability of the homotopy method in dealing with such more complicated cost functions.

On the other hand, we develop an efficient artificial neural network (ANN) to mimic the EM model of the coupler, which has been popularly known as the EM-ANN model. The ANN model is trained by EM simulation results where the inputs are geometric variables, and the outputs are S-parameters. Such input variables are distributed over a certain boundary with a specific interval. The trained ANN model can replace the computationally expensive full-wave EM model as it predicts the outputs accurately due to its generalization capability [82]. Such an ANN model demonstrates the corresponding EM level accuracy and the circuit-level simulation speed simultaneously. Indeed, ANN model-assisted microwave component design strategy has recently become a smart practice [3]. Common microwave component design problem is usually defined by geometric parameters as the inputs and electrical parameters as the outputs by a forward ANN model [153]. On the other hand, synthesis problems can also be handled by various inverse ANN models [4], [88]. Deep neural networks and model decomposition techniques were introduced to solve high-dimensional synthesis problems [154], [5]. Currently, the automation of modeling becomes an emerging topic [6]. In this work, we use the ANN model for two purposes. First, the

ANN model is used as a surrogate model of the cruciform coupler for expediting the homotopy optimization process. Second, the ANN model is set to extract the equivalent circuit parameters of the cruciform coupler in connection with such specifications as bandwidth, return loss, isolation, and coupling.

The rest of the paper is organized as follows. Section II introduces the newly proposed feedforward neural network, data preparation, and training algorithm with error backpropagation for the ANN model used in this work. Section III introduces the homotopy optimization technique. Section IV explains the deployment of the homotopy method for coupler optimization along with the cruciform coupler's equivalent circuit model, and the measurement setup. Section V proposes an ANN model development procedure for extracting the equivalent circuit parameters from the coupler specification, followed by general discussion in Section VI and a conclusion in Section VII.

## 3.2 ANN model

### 3.2.1 ANN model feedforward network

A multilayer perceptron is used as the ANN model architecture in this work where neurons are organized in layers and neurons connected from adjacent layers. A weight is assigned to each connection and a biasing value is applied to each neuron. The inputs are fed into the input layer as a form of vector. This input is computed along the layers sequentially by a feedforward computation. In this work, we adopt the transmission line impedance equation for the feedforward computation for the first time. This idea is inspired by the fact that the transmission line equation naturally describes fundamental lumped-element effects as well as voltage-current relationships between any two terminals for a wave propagation system. The normalized transmission line impedance equation is formulated as [155]

$$\frac{Z_{in}}{Z_0} = \frac{\frac{Z_L}{Z_0} + (i \times tan\beta L)}{1 + (i \times \frac{Z_L}{Z_0} \times tan\beta L)} \tag{3.1}$$

where $Z_{in}$, $Z_L$ and $Z_0$ denote input, load, and characteristic impedances, respectively. $tan$ refers to the trigonometric tangent operator and $i$ denotes the imaginary unit. $L$ denotes the length of transmission line and $\beta$ stands for the phase constant. Equation (3.1) can simply be written for

output, $Y$ as a function of input, $X$ and weight, $W$ as

$$Y = \frac{X+(i\times tanW)}{1+(i\times X\times tanW)} \tag{3.2}$$

We consider the real part only to adopt (3.2) as a feedforward computational equation.

In this work, we use $w_{jk}^{l}$ to denote the weight as the connection between $k^{th}$ neuron of $(l-1)^{th}$ layer and $j^{th}$ neuron of $l^{th}$ layer. We use $b_j^l$ as the bias of the $j^{th}$ neuron in the $l^{th}$ layer and $a_j^l$ as the activation of the $j^{th}$ neuron in the $l^{th}$ layer. The intermediate quantity is $z_j^l$. In this case, $z_j^l$ and $a_j^l$ are expressed as

$$z_j^l = \sum_k Re\left[\frac{a_k^{l-1}+(i\times tanw_{jk}^l)}{1+(i\times a_k^{l-1}\times tanw_{jk}^l)}\right] + b_j^l \tag{3.3}$$

$$a_j^l = \sigma\left(\sum_k Re\left[\frac{a_k^{l-1} + (i \times tanw_{jk}^l)}{1 + (i \times a_k^{l-1} \times tanw_{jk}^l)}\right] + b_j^l\right) \tag{3.4}$$

The logistic sigmoid activation function, $\sigma$ is used in the hidden neurons of the ANN models developed in this work that is expressed as

$$\sigma(z) = \frac{1}{1+e^{-z}} \tag{3.5}$$

In this equation, $z$ is an input vector. A linear activation function is used in the output layer where the neurons simply calculate the weighted sum.

### 3.2.2 Data preprocessing

In this work, we have developed two ANN models. The first model is the EM-ANN model of the cruciform coupler that calculates S-parameters from geometric dimensions and frequency variables. The second model extracts the coupler circuit parameters from the circuit model specification. Such geometric values, frequency variables and different specifications may vary by many orders of magnitude. Since the sigmoid activation function is used in the hidden neurons, these sigmoid neurons become saturated for large inputs where the derivatives become close to 0. Such derivatives reduce the ANN model training speed. To overcome this problem, the input values are preprocessed. Let's assume the input variable $a$ in the range [$a_{min}$, $a_{max}$]. The value of $a$ can be scaled linearly in the range of [-1,+1] by

$$\bar{a} = 2\frac{a-a_{min}}{a_{max}-a_{min}} - 1 \tag{3.6}$$

A linear mapping between the original value $a$ and the ANN model input value $\bar{a}$ is defined in (3.6). Such value can be inversely mapped from the ANN output value to the physical value by

$$a = \frac{a_{max}-a_{min}}{2}(\bar{a}+1) + a_{min} \tag{3.7}$$

For the first ANN model, the outputs are S-parameters whose magnitude always remains in the range of 0 to 1 for a passive network. Thus, no preprocessing is required at the outputs of this ANN model.

For the second ANN model, the outputs are the equivalent circuit parameters of the coupler. These variables may vary by many orders of magnitude. Thus, a preprocessing is required for the outputs of this ANN model.

### 3.2.3 Parameters initialization

The biases and weights of the ANN model get updated through the training process to minimize the error. Thus, these parameters can be initialized randomly. However, these parameters are required to be initialized by small numbers so that the sigmoid neurons do not get saturated, and the training does not get slowed down. In this work, the biases are sampled from a Gaussian distribution with 0 mean and 0.1 standard deviation. The weights are also sampled from a Gaussian distribution with 0 mean and $0.1/sqrt(N_{k-1})$ standard deviation where $N_{k-1}$is the total number of neurons in the $(k-1)^{th}$layer.

### 3.2.4 Levenberg Marquardt's algorithm

The main objective of the ANN model training is to learn the input-output mapping for a specific problem by minimizing the cost function. Let us assume that $m$ sets of training data have been produced as $(x_1, d_1), (x_2, d_2), \dots, (x_m, d_m)$. The quadratic cost function, $E$ in this work is defined as

$$E = \frac{1}{2m}\sum_{i=1}^{m}(d_i - a_i^L)^T(d_i - a_i^L) = \frac{1}{2m}\sum_{i=1}^{m}p_i^T p_i \tag{3.8}$$

Here, T denotes the transpose vector, $p_i$ refers to the error vector for $i^{th}$ training data and the vector activation output is $a_i^L$ from input.

The ANN model is trained through the adjustment of its weight and bias matrix via an error backpropagation algorithm [82]. This calculates the partial derivative of the cost function with respect to the weights and biases which are denoted by $\delta E/\delta w_{jk}^{l}$ and $\delta E/\delta b_{j}^{l}$, respectively. An intermediate quantity, $\Delta_j^l$ , can be introduced as an error in the $j^{th}$ neuron in the $l^{th}$ layer. The backpropagation provides us with a process to calculate $\Delta_j^l$ and then it will contribute to the formulation of $\delta E/\delta w_{jk}^{l}$ and $\delta E/\delta b_{j}^{l}$. This error $\Delta_j^l$ can be defined as

$$\Delta_j^l = \frac{\delta E}{\delta z_j^l} \tag{3.9}$$

where $E$ and $z_j^l$ are formulated in (3.8) and (3.3). After applying the chain rule and using a few mathematical manipulations, (3.9) can be rewritten as

$$\Delta_j^l = \sum_k \frac{\delta z_k^{l+1}}{\delta z_j^l} \Delta_k^{l+1} \tag{3.10}$$

$z_k^{l+1}$ can be derived from (3.3) as

$$z_k^{l+1} = \sum_k Re\left[\frac{\sigma\left(z_j^l\right)+(i\times tanw_{jk}^{l+1})}{1+\{i\times\sigma\left(z_j^l\right)\times tanw_{jk}^{l+1}\}}\right] + b_k^{l+1} \tag{3.11}$$

The partial derivative of $z_k^{l+1}$with respect to $z_j^l$ can be expressed as

$$\frac{\delta z_k^{l+1}}{\delta z_j^l} = Re\left[\frac{\sigma'(z^l)\times\left(1+tan^2 w_{jk}^{l+1}\right)}{\left[1+\{i\times\sigma\left(z_j^l\right)\times tanw_{jk}^{l+1}\}\right]^2}\right] \tag{3.12}$$

Here, $\sigma'(z^l)$ denotes the first derivative of the sigmoid function with respect to the input vector, which is expressed as

$$\sigma'(z^l) = \sigma(z^l) \times \left\{1 - \left(\sigma'(z^l)\right)\right\} \tag{3.13}$$

Substituting (3.12) into (3.10) gives us the error term as

$$\Delta_j^l = \sum_k Re\left[\frac{\sigma'(z^l)\times\left(1+tan^2 w_{jk}^{l+1}\right)}{\left[1+\{i\times\sigma\left(z_j^l\right)\times tanw_{jk}^{l+1}\}\right]^2}\right]\Delta_k^{l+1} \tag{3.14}$$

$\delta E/\delta b_{j}^{l}$ can be calculated as

$$\frac{\delta E}{\delta b_j^l} = \Delta_j^l \tag{3.15}$$

The chain rule can be employed on $\delta E/\delta w_{jk}^{l}$ which yields

$$\frac{\delta E}{\delta w_{jk}^{l}} = \Delta_j^l \times \frac{\delta z_j^l}{\delta w_{jk}^{l}} \tag{3.16}$$

We can calculate the partial derivative of $z_j^l$ with respect to $w_{jk}^{l}$ by using (3.3) as follows

$$\frac{\delta E}{\delta w_{jk}^{l}} = Re\left[\frac{i \times sec^2 w_{jk}^{l} \times (1-\sigma^2(z^l))}{\left(1+i\times\sigma\left(z_j^l\right)\times tan w_{jk}^{l}\right)^2}\right] \times \Delta_j^l \tag{3.17}$$

From (15) and (17), the weight and bias matrix can be updated from the gradient descent update rule as

$$b_j^{l'} = b_j^l - \eta \frac{\delta E}{\delta b_j^l} \tag{3.18}$$

$$w_{jk}^{l'} = w_{jk}^{l} - \eta \frac{\delta E}{\delta w_{jk}^{l}} \tag{3.19}$$

Here, $\eta$ denotes the learning rate. The Levenberg-Marquardt's algorithm (LMA) [156] is used for training the ANN models in this work. This algorithm is fast and efficient for a small-sized network where a few hundred parameters are involved.

## 3.3 Homotopy optimization technique

The homotopy optimization method is independent of any physical parameters. One can introduce the homotopy variable in the range [0,1] to build a zeroth-order deformation equation and yield a homotopy series solution. Such formulation is valid for a nonlinear problem containing any number of physical parameters [31]. This transforms a nonlinear equation into an infinite number of linear sub-problems with a small or large number of parameters. The homotopy optimization problem can be defined as

$$q(x,\rho) = (1-\rho)F(x) + \rho G(x) \tag{3.20}$$

Here, $F(x)$ is an optimization problem, whose optimal solution is already known or trivial to solve. $G(x)$ is the target optimization problem where a good set of initial value is unavailable. $\rho$ is the homotopy variable. For $\rho = 0$, $q(x,0) = F(x)$, and $q(x,1) = G(x)$ while $\rho = 1$. The function $F(x)$ deforms to $G(x)$ with the change of $\rho$ from 0 to 1. The series of homotopy problem $q(x,\rho)$ can be defined as $0 < \rho_1 < \rho_2 < \cdots < \rho_s < 1$ where the value of $\rho$ linearly increases from 0 to 1 with $n$ number of homotopy steps. For example, if the total number of homotopy steps, $n = 5$, the

homotopy problem is defined as $0 < \rho_1 < \rho_2 < \rho_3 < 1$ where $\rho_1 = 0.25, \rho_2 = 0.50, and\ \rho_3 = 0.75$. By a small amount of increment in $\rho$ each time, the new problem remains close to its previous state. As a result, the optimized solution of a new problem should be nearby to the previous solution. The number of intermediate homotopy steps is usually decided by the difficulty level of the problem. A precise solution of a highly nonlinear problem requires a higher number of intermediate steps.

Optimum solution of the problem becomes easier if the solution of the previous problem is deployed to find the solution of the current problem. For instance, if the homotopy variables increase linearly in the range [0,1], two previous solutions can be linearly combined as a reference point for the next optimization step.

$$U_{i+1} = 2U_i' - U_{i-1}' \tag{3.21}$$

where $U_i'$ and $U_{i-1}'$ are the optimum solutions of the $ith$ and $(i-1)th$ homotopy optimization step while the initial solution is $U_{i+1}$ for the $(i+1)th$ homotopy optimization.

The homotopy method is a concept in differential geometry and topology that is deployed in many numerical techniques to solve differential equations and nonlinear equations. In this work, we demonstrate how an SIW cruciform coupler structure can be optimized by the homotopy method.

## 3.4 Optimization of cruciform coupler

Figure 3.2 illustrates the top view of an SIW cruciform coupler. In this demonstration, port 1 and port 2 are considered as the input and through port while port 3 and port 4 are considered as the coupled and isolated port. The SIW cruciform coupler contains the following geometric variables: distance of coupling posts' center (dx, dy) from the center of coupler O, diagonal spacing between matching posts r while the diagonal crosses the center of coupler O and makes an angle of $45^0$ with the X-axis of the coupler, diameter of coupling posts and matching posts $D_1$ and $D_2$, respectively. The ANN model for the SIW cruciform coupler has these variables along with frequency as its input and the real and imaginary parts of $S_{11}$, $S_{21}$, $S_{31}$ and $S_{41}$ as its output.

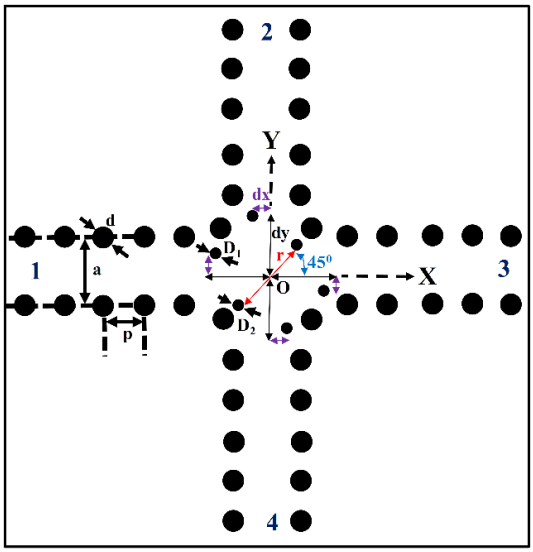


Figure 3.2 SIW cruciform coupler (top view) sketched with geometric dimensions

### 3.4.1 EM-ANN model

In this work, a D-band SIW cruciform coupler is considered. The diameter of those metalized via holes is d=0.3mm, with p=0.5mm spacing between the centers of two adjacent via holes. The two via hole arrays are spaced by a=1mm. The substrate is Rogers RT Duroid 5880, with length and width of 10 mm, thickness of 0.254mm and relative permittivity of 2.2. The user-desired input space is bounded by $dx = 0.2\ to\ 0.6\ mm, dy = 0.6\ to\ 1.0mm, r = 0.4\ to\ 1.2mm, D_1 = 0.06\ to\ 0.14mm\ and\ D_2 = 0.06\ to\ 0.14mm$. The frequency range is from 110GHz to 160GHz.

The feedforward computational formulation of our proposed model replaces the conventional simple multiplication of neuron input and the weight with fundamental transmission line impedance equation inspired formula as described in Section II. For comparison purpose, we perform MLP automatic model generation (AMG) [113] and MLP step-by-step manual training, respectively with both of conventional and proposed ANN modeling equations. The model accuracy can be calculated by (3.22) where the output vector of the ANN model is $y_m$ and the desired output vector is $t_m$. T denotes the training, validation, or test set of data and $N_s$ is the total amount of data in that set.

$$Error = \frac{1}{N_s}\sum_{m\in T}\|y_m - t_m\|^2 \tag{3.22}$$

In case of AMG proposed in [113], the required number of training and validation samples and the distribution in $(dx, dy, r, D_1, D_2, f)$ space along with the neural network size is unknown for user desired modeling accuracy. The algorithm from [113] is implemented to develop an ANN model for finding S parameters of the SIW cruciform coupler shown in Figure 3.2. The algorithm starts with an initial ANN model of four-layer MLP that consists of 15 hidden neurons in each hidden layer. In the first stage of the algorithm, 80 training samples and 5 validation samples are dynamically generated for training and testing of the model, respectively. In the consecutive stages of the automatic algorithm, it decides the required additional number and distribution of training and validation samples and drives the Ansoft-HFSS simulator dynamically. Additional hidden neurons are also added whenever it is required. To achieve 0.2% of validation error, 35 model development stages were required by the automatic algorithm. In total, 1699 set of training samples and 695 set of validation samples are used and the final model has 88 hidden neurons in each hidden layer. After finishing the model development according to [113], we implement our proposed feedforward and backpropagation formula on this algorithm to test the advantage. Bias term is ignored in the basic formulation as it is done in [113]. Rest of the methodology is followed in same manner. After 22 stages, the final ANN model consists of 61 hidden neurons in each hidden layer, 1137 training samples and 463 validation samples, achieved 0.18% validation error.

In addition, the manual step-by-step ANN modeling approach is also used for demonstrating the advantage of proposed formulation over the conventional formulation. For these manual ANN models, uniform-grid sampling technique is used for data generation. The same number of training and validation samples are used in these manual ANN models. In manual ANN modeling methods, the manual model training is done for several times with different number of hidden neurons, and the model achieving the expected accuracy with fewest hidden neurons is selected. A set of test data (1045) which was unseen during the training phase, is used to test all these four ANN models.

Table 3.1 shows total number of training samples, achieved error and CPU time for each model. The comparison table clearly shows that the AMG and step-by-step model with proposed ANN formulations result in significantly less CPU time to achieve similar user desired accuracy as compared to the models with conventional ANN formulations. Models with proposed ANN formulations require less training data and a smaller number of hidden neurons. Even though the proposed formulation takes much time for relatively complex computation at each derivative and

error calculation, the overall CPU time reduces noticeably due to fewer EM simulations for less training data samples.

Table 3.1 Comparison of Conventional and Proposed ANN Formulation with AMG [113] and Manual Step-by-step ANN Models

| Modeling Algorithm | Total hidden neurons | Training samples | Error (%) | | CPU Time |
|---|---|---|---|---|---|
| | | | Validation | Testing | |
| AMG [113] (Conventional Architecture) | 88-88 | 1699 | 0.22 | 0.24 | 85 hr |
| AMG [113] (Proposed Architecture) | 61-61 | 1137 | 0.18 | 0.21 | 60 hr |
| Manual Modeling (Conventional Architecture) | 88-88 | 1699 | 0.28 | 0.32 | 93 hr |
| Manual Modeling (Proposed Architecture) | 61-61 | 1137 | 0.23 | 0.28 | 66 hr |

The complete surrogate model of the cruciform coupler is illustrated in Figure 3.3. The target design frequency band of the SIW cruciform coupler is 110-160 GHz. The required return loss and isolation is 15dB with 3dB coupling. The initial design variables are determined to achieve the 3dB coupling as dx=0.38mm, dy=0.8mm, $D_1$=0.05, $D_2$=0.08, and r=0.8mm. The S-parameters magnitudes are calculated by above mentioned four surrogate ANN models with the initial design values as illustrated in Figure 3.4. The EM-ANN model developed by AMG [113] with proposed ANN formulations provides the best accuracy as shown in Table 3.1. During the homotopy optimization, this model is used as surrogate model to replace the full wave EM simulations.

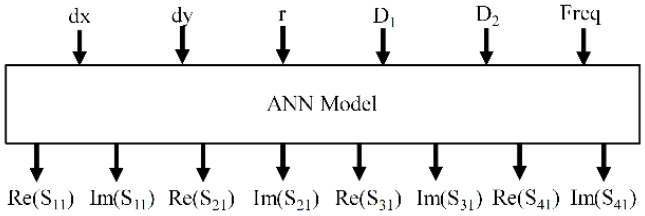


Figure 3.3 ANN model for the cruciform coupler

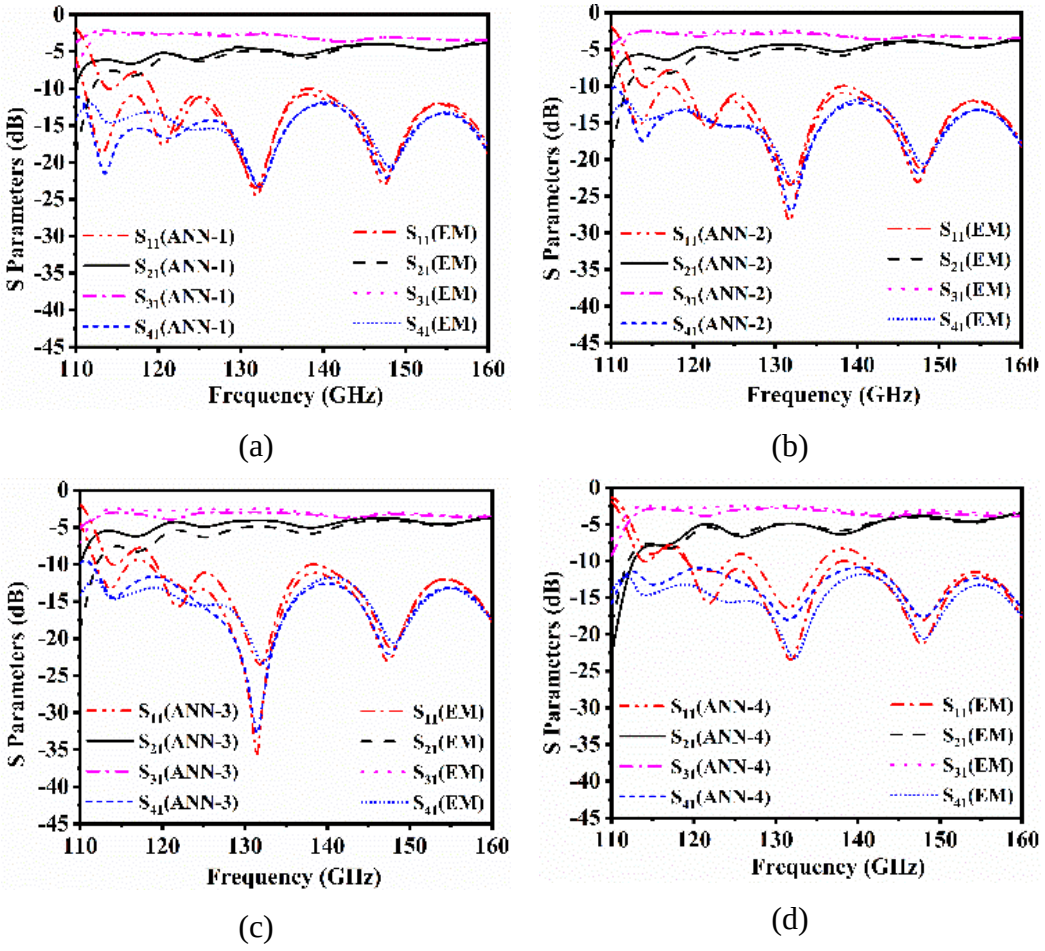


Figure 3.4 SIW cruciform coupler responses calculated by four surrogate models using the initial design values. (a) AMG [113] (Conventional Architecture). (b) AMG [113] (Proposed Architecture). (c) Manual Modeling (Conventional Architecture). (d) Manual Modeling (Proposed Architecture).

### 3.4.2 Homotopy optimization

Figure 3.4 shows that the resulting return loss and isolation level are only 2dB and 12dB, respectively. Commercial EM software packages such as CST and HFSS integrated direct

optimization techniques usually take exceptionally longer computational time to find the optimum set of five geometrical variables using the initial variables. Now, let's demonstrate how to use the homotopy optimization technique to achieve the design goal of 15dB return loss, 15dB isolation, and 3dB coupling in the specified band of frequency [110, 160] GHz. In this optimization, the main goal is to minimize the cost function, $C_H$ as expressed by

$$C_H = w_1 * \max[db(S_{11}), -R] + w_2 * \max[db(S_{41}), -I] + w_3 * \min[db(S_{31}), -C] \quad (3.23)$$

In this scenario, this cost function is defined inside the frequency band of interest $[f_L, f_H]$. The normalized frequency can be computed by (3.6) where $f_{min} = 110$ and $f_{max} = 160$. In (23), *R*, *I* and *C* are the target return loss level, isolation level, and coupling level in each optimization process, respectively. If these in-band parameters exceed $-R$, $-I$ and $-C$, respectively, it will not decrease the value of the respective term of the cost function. Note that $w_1$, $w_2$, and $w_3$ are the weighting factors by which the cost function value is comparable. Choice of these weights depends on the contribution of the in-band return loss level, isolation level and coupling level to the cost function. In the characterization of coupler structure, it is often seen that the return loss level and isolation level have the major contribution to the cost function defined in (3.23). Thus, in this example, we chose $w_1$ and $w_2$ as 1 while $w_3$ as 0.2. The parameters in the cost function (3.23) are

$$V = [f_L \; f_H \; R \; I \; C] \quad (3.24)$$

From the coupler's design specifications, the target problem has the parameter values as, $V_{target} = [110\ 160\ 15\ 15\ 3]$. The first iteration of the optimization calculates the initial parameters as, $V_{initial} = [110\ 160\ 2\ 10\ 5]$ where the frequencies can be normalized by (3.6). The rest of the parameters are found trivially. Thus, the optimal solution to the first optimization problem, $V_{initial}$ should be nearby to the initial design parameters. A series of 6 homotopy optimizations are carried out to reduce the cost functions defined by the parameters of (3.24) as a function of ρ which grows from 0 to 1 with the step size 0.2. This can be formulated as

$$V = (1 - \rho)V_{initial} + \rho V_{target} \quad (3.25)$$

The solution from the last optimization is considered as the initial parameters for the second and then third optimizations while the calculated values from (3.21) are considered as the initial parameters in a new optimization from the fourth step. The initial cost function and target cost function are calculated from $V_{initial}$ and $V_{target}$. ρ value is considered as 0, 0.2, 0.4, 0.6, 0.8 and

1.0 in 6 consecutive steps, sequentially. All the homotopy optimizations in this work are solved by the MATLAB's *fmincon* optimization function with a sequential quadratic programming algorithm. Solutions from each step are given in Table 3.2. All the units are in mm. The second and last row of Table II shows the initial and final de-normalized values for these design parameters. Note that single optimization instead of six optimizations cannot achieve the desired coupler performance. However, it only takes few minutes to accomplish six homotopy optimization steps.

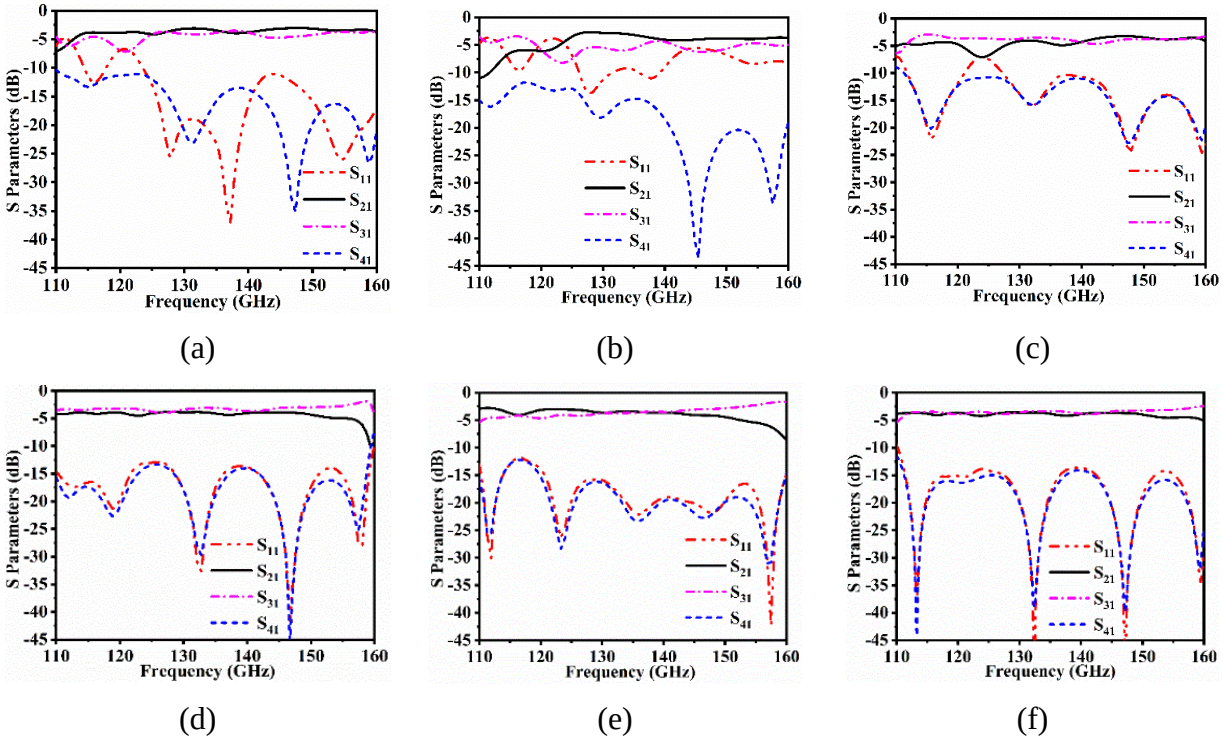


Figure 3.5 Cruciform coupler's optimized performance in the homotopy optimization steps. (a) $\rho = 0$. (b) $\rho = 0.2$. (c) $\rho = 0.4$. (d) $\rho = 0.6$. (e) $\rho = 0.8$. (f) $\rho = 1.0$.

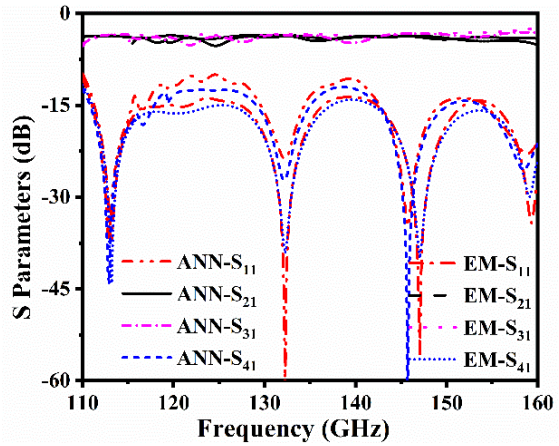


Figure 3.6 Comparison between S-parameters computed by full-wave EM simulation and its related ANN surrogate model.

Table 3.2 Design parameters of the cruciform coupler obtained in each homotopy optimization step

| $\rho$ | dx | dy | $D_1$ | $D_2$ | r |
|---|---|---|---|---|---|
| - | 0.3800 | 0.8000 | 0.0500 | 0.0800 | 0.8000 |
| 0 | 0.3982 | 0.8541 | 0.0582 | 0.0894 | 0.8372 |
| 0.2 | 0.4592 | 0.8803 | 0.0649 | 0.0974 | 0.8691 |
| 0.4 | 0.4778 | 0.9128 | 0.0718 | 0.1032 | 0.8796 |
| 0.6 | 0.4891 | 0.9435 | 0.0793 | 0.1107 | 0.9892 |
| 0.8 | 0.4946 | 0.9793 | 0.0968 | 0.1142 | 1.1974 |
| 1 | 0.5012 | 1.1315 | 0.1209 | 0.1210 | 1.1998 |

Table 3.2 demonstrates that the final solution is rather far away from its initial values. However, the consecutive solutions in the optimization process are very close to each other. This feature makes the homotopy method an excellent candidate for such structure optimizations. Optimized coupler performances at each stage are illustrated in Figure 3.5, which indicates that the homotopy optimization makes the design process gradually approach the target frequency range and achieve the specified in-band return loss, isolation, and coupling simultaneously.

After finding the homotopy optimized solution from the last row of Table 3.2, the EM-ANN model and full-wave EM simulation are used to calculate the S-parameters of the cruciform coupler

against these optimized and de-normalized geometric parameters. The comparison between the ANN model-calculated S parameters and EM simulation results are given in Figure 3.6. An excellent outcome is achieved from the EM-ANN model in spite of a slight discrepancy from the full-wave EM simulation results, which validates the surrogate model.

### 3.4.3 SIW cruciform coupler measurement

The cruciform coupler is processed by our in-house miniature hybrid microwave integrated circuits (MHMICs) technology which allows us to fabricate such a high precision structure for mmW and THz applications. An SIW-waveguide transition was designed to measure its performance. The fabricated prototype is shown in Figure 3.7(a). The metallic mount was built to assist the measurement as shown in Figure 3.7(b). We measured the S-parameters on a THz vector network analyzer with E8257DV05 (from Virginia Diodes Inc - VDI) frequency extension module for WR5.1 which operates in the frequency range of 135 to 225 GHz. This bounds us to test our sample starting from 135GHz. The measurement setup is illustrated in Figure 3.8. Two terminations were used to terminate the other two unused ports. The quality of these two terminations was good enough as the same pair of terminations were used during the calibration process. The measurement results were carried out on the two ports. The SLT (short, line and through) WR5.1 calibration kit was used to de-embed the measurement system at reference plane A-A' and B-B'. This calibration technique needs to carry on the calibration of short circuit plate as well as the matching load in the one-port of the vector network analyzer, and the through in the dual-port. This calibration and the correction algorithm are simple as it does not need multiple assembly standards. Fig. 9 depicts little discrepancies between the simulated and measured results because of the calibration issues and dimensional tolerance. Such differences in measured return loss and isolation are usual for the couplers at THz frequencies [157], [158]. Nevertheless, a minimum coupling of 3 dB over the frequency range from 135 to 160 GHz has been achieved while the return loss and isolation are below 20 dB. The phase imbalance of $90^0$ is achieved between $S_{21}$ and $S_{31}$ over the frequency band. The SIW-waveguide transitions and dielectric loss contribute to a major part of the insertion loss.

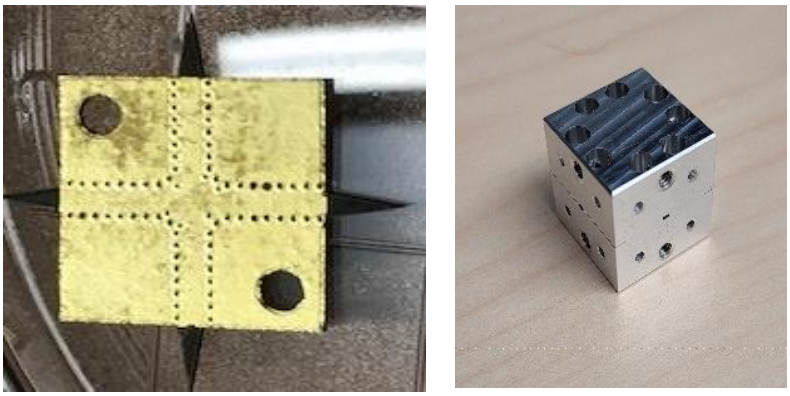

(a) (b)

Figure 3.7 Fabricated prototype. (a) Planar circuit. (b) Metallic mount

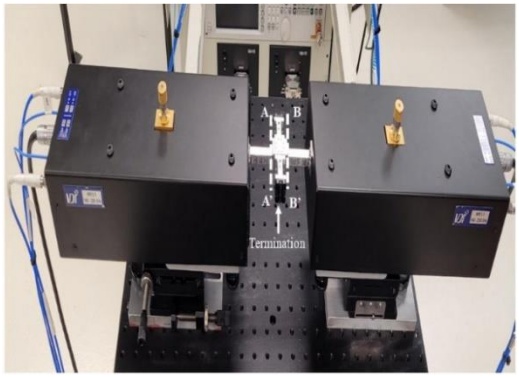


Figure 3.8 Measurement setup of SIW cruciform coupler

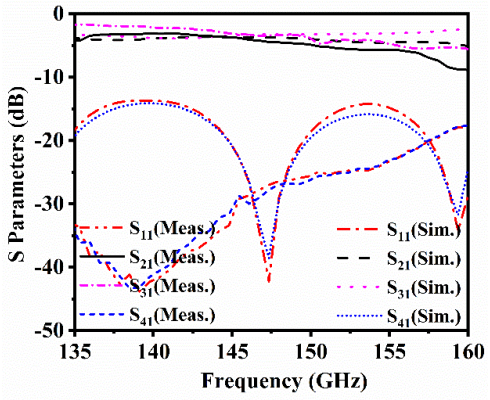


Figure 3.9 S-Parameters comparison between simulation and measurement

### 3.4.4 SIW cruciform coupler bandwidth and equivalent circuit

The bandwidth of an SIW cruciform coupler can be tuned by varying the diameters of the four coupling posts. Four full-wave EM simulations are carried out with varying the diameter of the coupling posts $D_1$. Figure 3.10 shows that a fractional bandwidth of the cruciform coupler can be enhanced from 33% to 43% while the diameter of the four coupling posts increases from 0.04mm to 0.18mm at a fixed position. However, such a size enhancement of these metallic posts reduces the return loss of the coupler from 18dB to 10dB. Thus, we must make an adequate tradeoff between in-band return loss and bandwidth during the coupler optimization and design.

Figure 3.11 illustrates the proposed equivalent circuit model of the cruciform coupler which is inspired by backward directional coupler [159] and H-plane T-junction structure [160]. This equivalent circuit is valid over any frequency range. It is worth mentioning that this circuit satisfies all the unitary conditions, power conservation, and phase imbalance of $90^0$ between $S_{21}$ and $S_{31}$. An algorithm for extracting the circuit parameters in connection with different coupler specifications will be proposed in section V.

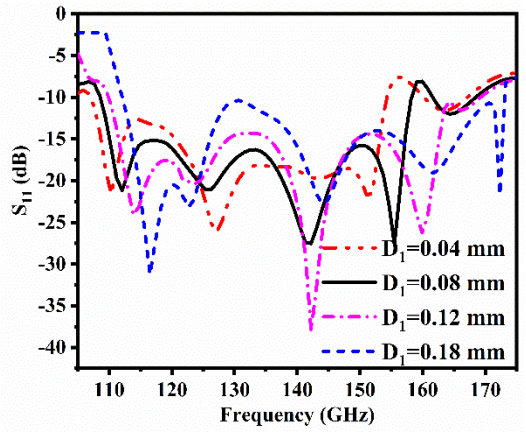


Figure 3.10 Bandwidth analysis of the SIW cruciform coupler

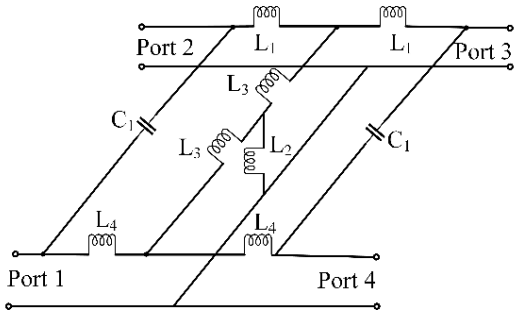


Figure 3.11 Equivalent circuit model of the SIW cruciform coupler

### 3.4.5 Related results

Optimization procedure takes a long EM simulation time due to a significant number of iterations depending on the optimization algorithm. Such operating time can be drastically minimized by EM-ANN model-based optimization. To demonstrate the advantage of homotopy optimization, we use our developed EM-ANN model of the SIW cruciform coupler and implement quasi-Newton optimizer, genetic algorithm, and sequential nonlinear programming optimizer with the same set of initial values and a very similar cost function. After 170, 225 and 115 iterations, respectively, the optimizations converge with the optimized cruciform coupler responses plotted in Figure 3.12(a), Figure 3.12 (b) and Figure 3.12 (c). As Table 3.3 shows, all these optimizations end up in different local minima. The performance comparison between these optimizers is shown in Table 3.4. It shows that the six steps of homotopy optimization takes few minutes while the other optimizers take too long to converge due to the massive number of iterations.

Table 3.3 Design parameters of the cruciform coupler obtained from different optimization algorithms

| Optimization Algorithm | dx | dy | $D_1$ | $D_2$ | r |
|---|---|---|---|---|---|
| Quasi-Newton | 0.3915 | 0.8646 | 0.1360 | 0.0961 | 1.0532 |
| Genetic-Algorithm | 0.4424 | 0.8778 | 0.1148 | 0.1291 | 1.0909 |
| Sequential nonlinear programming | 0.4438 | 0.8912 | 0.1400 | 0.1242 | 1.1009 |
| Homotopy optimization | 0.5012 | 1.1315 | 0.1209 | 0.1210 | 1.1998 |

Table 3.4 Performance comparison of different optimization algorithms

| Optimization Algorithm | Iterations | Time (min.) | Minimized Cost |
|---|---|---|---|
| Quasi-Newton | 170 | 150 | 0.22 |
| Genetic-Algorithm | 225 | 105 | 0.92 |
| Sequential nonlinear programming | 115 | 127 | 0.22 |
| Homotopy optimization | 6 | 6 | 0.02 |

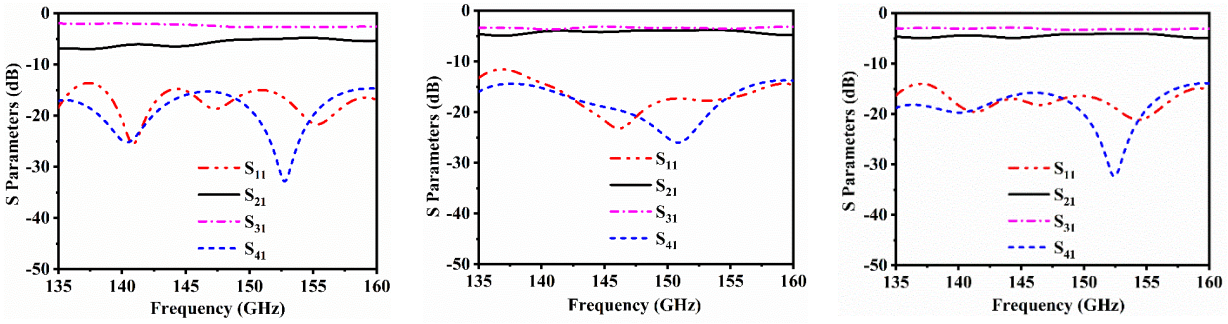


(a) (b) (c)

Figure 3.12 S-Parameters from different optimization algorithms (a) Quasi-newton (b) Genetic algorithm (c) Sequential non-linear programming

## 3.5 ANN modeling of cruciform coupler equivalent circuit

In the previous section, we have demonstrated how an SIW cruciform coupler structure is optimized by the homotopy method while the EM-ANN model is used as a surrogate model. In Figure 3.11, an equivalent circuit model of the cruciform coupler is illustrated, which is intuitively drawn from the equivalent circuit of a conventional coupler and H-plane T-junction structure. We can use the homotopy optimization technique to extract the circuit parameters as we have done with the EM model as described in Section IV. The drawback of deploying an optimization algorithm is the repetition of a process for each specification. For example, a cruciform coupler is designed at 22-27 GHz with 3dB coupling, 20dB of return loss and isolation [148], while another cruciform coupler is designed for 92-96 GHz operation with 4dB coupling, 10dB of return loss and isolation [149]. The equivalent circuit parameters of these two examples can be extracted by the proposed optimization procedure but this process needs two repetitions for two different sets of specification with two sets of initial values. Thus, we need to repeat this process *N* number of times for *N* number of different specifications. To avoid this repetitive use of the optimization algorithm,

for the first time, a novel ANN model development technique is proposed in this work where the inputs are circuit specifications, and the outputs are circuit configuration. This ANN model is trained through an automatic optimization algorithm generated data. Such data generation process eliminates the human intervention in the cost function parameters' variation, circuit parameter extraction and writing these parameters into a file. This novel ANN model with automatic data generation process will provide us with a circuit configuration we need for any specifications without deploying any optimization algorithm.

### 3.5.1 ANN model development algorithm

Now, we propose an ANN model development procedure for the prediction of cruciform coupler's equivalent circuit parameters in terms of a desired specification. In this section, a conventional ANN model (manual step-by-step ANN model) is developed through the automatic data generation process. The specification of a cruciform coupler is usually given in terms of the low and high frequency points of a target band, return loss, isolation, and coupling, as given in (3.24). Thus, our goal is to develop an ANN model that considers these specifications as input variables and provides the equivalent circuit parameters as output variables. We adopt again the homotopy optimization to automate the data generation for different specifications of the cruciform coupler circuit by using a circuit simulator as illustrated in Figure 3.13(a). The overall model development procedure is outlined in the following steps:

Step 1: Introduce a circuit simulator or an analytical approach such as nodal analysis for the circuit illustrated in Figure 3.12 to compute its S-parameters with initial circuit parameters, for example $[L_1\ L_2\ L_3\ L_4\ C_1]$. From the S-parameters, find the initial state variables as cost function variables, $[f_L\ f_H\ R\ I\ C]$ where $[f_L\ f_H]$ is found from the target frequency band, $R$ denotes in-band return loss, $I$ stands for in-band isolation and $C$ indicates the coupling value. If a commercial software package is used for circuit simulation, it is possible to interface it with the MATLAB platform through an application programming interface (API). This will automate the data generation process.

Step 2: Set the initial circuit parameters corresponding to the initial coupler state variables as the cost function variables from Step 1. The optimization needs to be carried out for different combinatory cost function variables, $[f_L\ f_H\ R\ I\ C]$ as mentioned in (3.22). Lower frequency of the target band $f_L$ is varied in the range of $[f_{L1}, f_{L2}]$ with $p$ number of samples. Higher

frequency of the target band $f_H$ is calculated with respect to the fractional bandwidth (FBW) which is varied in the range of $[FBW_1, FBW_2]$ with $q$ number of samples. Then, $f_H$ can be calculated as $f_H = f_L \frac{2+FBW}{2-FBW}$. It is observed from the simulations that the return loss and isolation of coupler maintains the same level inside the band of interest. Therefore, $R$ and $I$ are varied together as a single variable in the range of $[X_1, X_2]$ with $r$ number of samples. Finally, the coupling $C$ is varied in the range of $[C_1, C_2]$ with $s$ number of samples. The total number of combinations from the cost function variables will be $N = p * q * r * s$. Such a set of combinatory variables is constructed inside a nested loop while the variables are swiped in a given range with a certain step size. Update the set of target state variables after each loop operation and store these target state variables in an appending file.

Step 3: Set the upper and lower boundary of the circuit parameters. Such boundary can roughly be found from a few simulations where circuit parameters generated response covers the target frequencies.

Step 4: Define the cost function $C$ as a function of S-parameters which is parameterized in (3.24). The S-parameters are calculated from a circuit simulator as mentioned in Step 1. Set the minimum target cost function value to $K$.

Step 5: Set the initial number of homotopy steps to $i$. Increase the number of homotopy steps by 1 till the minimum cost function value is achieved as $K$. In this way, the number of homotopy steps becomes flexible so that it can increase or decrease, depending on how far the optimal solution of the next optimization is located from the current solution of the optimization problem.

Step 6: Calculate the optimized circuit parameters after minimizing the cost function to its desired level. Store these optimized parameters in an appending file. After completing each optimization cycle, set the optimized circuit parameters as the initial circuit parameters for the next optimization step. Similarly, update the initial state variable of the next optimization as the target state variable of the current optimized state. This strategy keeps the next optimization solution close to the current solution as the state variables of two successive optimization problems remain close to each other. Thus, the number of homotopy steps remains minimum which eventually reduces the optimization time. In addition, the variables change smoothly that speed up the ANN training process later.

Step 7: The loop operation explained in Step 2 stops after executing the process from Step 4 to Step 6 for $N$ times. This whole process provides us $N$ set of data for training and testing the ANN model we want to develop.

Step 8: Collect the data files from Step 2 and Step 6 as inputs and outputs to train the ANN model for the cruciform coupler circuit design. Total $N$ sets of data are divided into training, validation and testing set of data for the target ANN model.

Step 9: Build the ANN model that allows the inputs as the cost function variables as $[f_L\ f_H\ R\ I\ C]$ and provides the outputs as circuit parameters as $[L_1\ L_2\ L_3\ L_4\ C_1]$.

Step 10: Finally, test the developed model accuracy with the test data set. The model will be able to predict the circuit parameters accurately for given cruciform coupler specifications.

Once this ANN model is developed, it provides us with the circuit parameters for different specifications of a cruciform coupler without deploying an optimization algorithm repeatedly.

### 3.5.2 Example model and results

We used application programming interface (API) between HFSS circuit simulation and MATLAB to simulate the exampled circuit in Figure 3.11. Training data is generated by varying the circuit parameters from MATLAB followed by circuit simulation in HFSS and writing the HFSS calculated S-parameter magnitudes into a SNP file in a predefined directory. We generated the training and testing data by swiping the cost function variables $[f_L\ f_H\ R\ I\ C]$ in a range of various design specifications. The lower frequency is swiped as $20GHz \leq f_L \leq 120GHz$ with 100 samples, FBW is swiped as $10\% \leq FBW \leq 40\%$ with 4 samples and the corresponding higher frequency of the band is calculated as $f_H = f_L \frac{2+FBW}{2-FBW}$. The insertion loss and return loss are swiped as a single variable as $16dB \leq X \leq 20dB$ with 5 samples and the coupling value is swiped as $1dB \leq C \leq 9dB$ with 5 samples. In total, $10{,}000$ combinations of these state variables are generated which are set to execute the optimization loop 10,000 times. The data generation time was recorded as 15 hours. The computer we used in this work is Lenovo SR650 Xeon Gold 6150, 2.7 GHz (2 processors, 36 cores) and 512 GB RAM. We covered a large range of frequency band with flexible specifications. It is possible to minimize the data generation time by reducing the range of design frequency band and other state variables' samples.

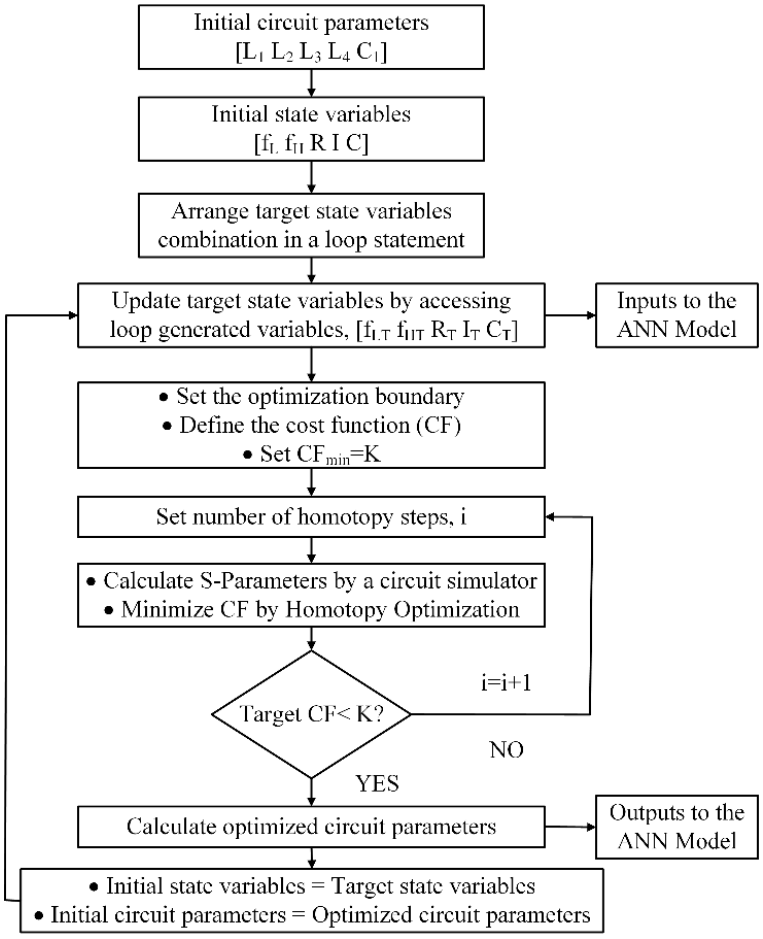


(a)

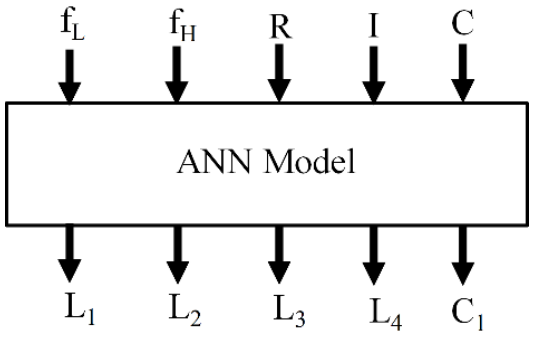


(b)

Figure 3.13 ANN model-assisted circuit parameter extraction. (a) Automatic data generation process (b) ANN model

Table 3.5 ANN model inputs and outputs of the exampled coupler circuits

| Ref. | ANN Inputs (Specifications) | | | | ANN Outputs (Circuit Parameters) | | | | |
|---|---|---|---|---|---|---|---|---|---|
| | $f_L$ | $f_H$ | R, I | C | $L_1$ | $L_2$ | $L_3$ | $L_4$ | $C_1$ |
| [148] | 22 | 26 | 15 | 1 | 160 | 4.0 | 220 | 162 | 166 |
| [149] | 92 | 96 | 30 | 2 | 25.7 | 3.4 | 124 | 25.7 | 60 |
| This work | 135 | 160 | 15 | 3 | 16.0 | 1.7 | 68 | 21 | 36 |

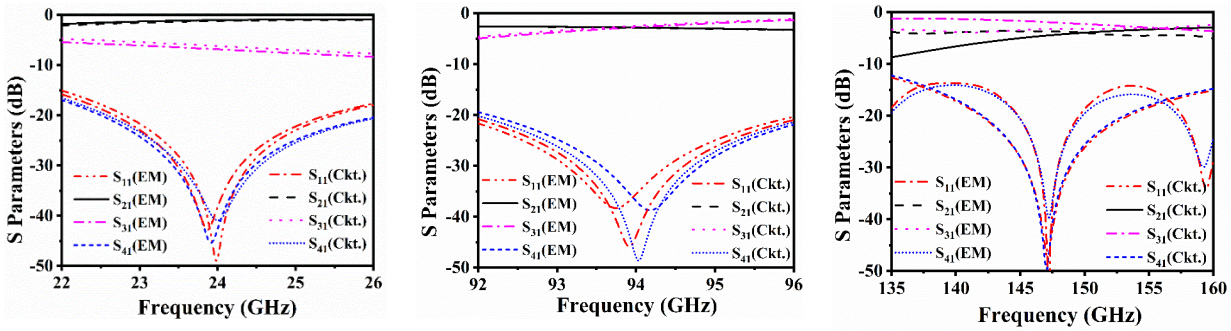


(a) (b) (c)

Figure 3.14 Coupler circuit performance comparison between ANN model extracted parameters based lumped element circuit and full wave EM simulation from (a) [148] , (b) [149] and (c) this work

An ANN model is developed and trained with the generated data as illustrated in Fig. 13(b). From the step-by-step manual ANN modeling process, we found the network of size 5-35-35-5 provides best model accuracy. The model is trained with 7000 and 1500 set of training and validation data, respectively. Another 1500 set of data is used for ANN model testing. It took only 30 minutes to train the model that achieves an average error of 6.5e-8 and 6.7e-8 for training and testing sets, respectively. We used this ANN model to compute the equivalent circuit parameters of the cruciform coupler designed in this work and the other two cruciform couplers designed in [148] and [149] at different specifications. The specifications of the corresponding coupler circuits are fed to the ANN model as the input vector, $[f_L\ f_H\ R\ I\ C]$. The ANN model calculates the equivalent circuit parameters as the output vector, $[L_1\ L_2\ L_3\ L_4\ C_1]$. All the inductances and capacitances are

calculated in pH and fF, respectively. The ANN model inputs, $[f_L\ f_H\ R\ I\ C]$ and calculated outputs, $[L_1\ L_2\ L_3\ L_4\ C_1]$ according to the specifications of the cruciform coupler designed in [148], [149] and this work are given in Table 3.5. These different sets of circuit parameters from the ANN model outputs are fed to the circuit simulator in order to calculate the S parameters from the equivalent circuit in Figure 3.11. These equivalent circuit model generated S parameters are compared with the corresponding full wave EM simulation in Figure 3.14 which shows a good agreement between each other. This validates the proposed equivalent circuit model of the cruciform coupler and the proposed ANN model development technique for equivalent circuit parameter extraction.

Such technique of ANN model development for a given circuit can be deployed for any reconfigurable and tunable circuits with few modifications judging from the optimizer implementation aspect. A 3D structure can also be synthesized through this technique. In this example, we did not consider the SIW structure illustrated in Figure 3.2 as we need to consider $a, d\ and\ p$ along with $dx, dy, D_1, D_2, r$ to fully characterize the coupler circuit in a large frequency band. Such a large number of variables will increase the EM simulation time exponentially. Thus, it is time-efficient to use analytical equations to calculate $a, d\ and\ p$ according to frequency specifications and then deploy the homotopy optimization to optimize $dx, dy, D_1, D_2\ and\ r$ as described in section IV. On the other hand, it can be seen that this method of extracting circuit parameters will be useful for designing tunable circuits.

## 3.6 General discussion

The novelty of this paper has two-fold. On one hand, we have proposed a transmission line impedance equation-based ANN framework which requires fewer hidden neurons with fewer training samples for similar or better accuracy as compared to its conventional counterpart for microwave simulation and optimization problems. On the other hand, we have proposed a circuit parameter extraction technique in terms of desired circuit characteristics. First, we have developed four surrogate EM-ANN model of the SIW cruciform coupler according to the AMG technique from [113] and manual step-by-step ANN modeling method with both of conventional and proposed ANN architecture. From the comparison of these four surrogate models, it is evident that the AMG model with proposed ANN architecture achieves the desired accuracy in minimum CPU time. This EM-ANN model is used for coupler structure optimization according to the desired performance at a certain frequency band. Second, we have devised an equivalent circuit model of

the cruciform coupler and then describe a step-by-step procedure to extract the circuit parameters in terms of the performance parameters. In both cases, we have introduced an homotopy optimization technique. The homotopy optimization was introduced in microwave filter problem in [31] for the first time. In this work, we have further investigated the usefulness of homotopy optimization for the SIW cruciform coupler design where the cost function is more complicated than bandpass filters as reported in [31]. Therefore, the goal of this work is not to outperform the homotopy optimization in [31], rather we have expanded its applications to the design of the SIW cruciform coupler and its equivalent circuit parameter extraction.

In this work, the homotopy optimization was performed on the EM-ANN model of the SIW cruciform coupler where the ANN model uses the transmission line impedance equation in its feedforward network. However, the optimization time is independent of ANN architectural formulations. Thus, whether the optimization is performed on a conventional ANN model or the proposed ANN model, optimization time will remain the same for both of ANN model architectures. This remains true for any other optimization algorithms, too.

The main advantage of this work is the proposed ANN model development technique. This model requires less training samples as well as fewer hidden neuron to provide desired accuracy than the conventional ANN models. Training of such small sized network takes shorter CPU time. Moreover, the step-by-step equivalent circuit parameter extraction technique demonstrated in Section V will be useful for circuit designers.

## 3.7 Conclusion

In this work, we have proposed a new approach to building a feedforward neural network by adopting a transmission line impedance-based equation for the ANN modelling. An D-band SIW cruciform coupler structure is designed, optimized, and characterized to demonstrate the performances of the proposed ANN modeling approach. The homotopy optimization method is introduced to optimize the coupler structure. A set of initial design parameters are obtained from primary dimensions which are followed by a series of homotopy optimizations for fine-tuning the coupler design parameters. The homotopy method can optimize cruciform couplers with different coupling, return loss and isolation over a specified frequency band. The ANN model is adopted as the surrogate model to accelerate the cruciform coupler optimization with several design variables. In addition, we have developed an equivalent circuit model for the cruciform coupler. To extract

the circuit parameters against the coupler specification, we have proposed an ANN model development technique in which the homotopy-assisted data generation is fully automated. This method is verified by extracting the equivalent circuit parameters from the different 3D models of cruciform couplers at different specification. In this work, theoretical and experimental results are also provided to appreciate the proposed hybrid ANN modeling strategy.

# CHAPTER 4 ARTICLE 3: SWARM INTELLIGENCE-HOMOTOPY HYBRID OPTIMIZATION-BASED ANN MODEL FOR TUNABLE BANDPASS FILTER

Chandan Roy and Ke Wu

Published in the *IEEE Transactions on Microwave Theory and Techniques*, vol. 71, no. 6, pp. 2567-2581, 20 January 2023

The style High-performance tunable RF/microwave and millimeter-wave filter design is a challenging task due to the lack of a basic theory. The filtering characteristics are highly sensitive to the variation of tuning elements which are commonly modeled and achieved by optimization algorithms. However, those optimizations only provide satisfactory results with a good set of initial parameters. Such range-limited optimization algorithms generally have issues of falling into local optima, slow convergence, and cumbersome implementation. To mitigate this problem, for the first time, a topology-based local optimizer is integrated with metaheuristic global optimization algorithms in this work. We have hybridized the homotopy method with an improved whale optimization algorithm (WOA) and a grey wolf optimization (GWO) algorithm. In this work, an artificial neural network (ANN) is formulated and studied, which has two-fold applications. First, ANN is used as a surrogate model to represent the time-consuming electromagnetic (EM) model in expediting the hybrid optimization process of tunable filters. Second, an ANN model is developed on data generated by the proposed optimization algorithm for predicting tunable circuit parameters at different tuning stages. The proposed ANN model-based algorithm is then applied to a fifth-order lumped-element tunable circuit and two fourth-order full-wave EM simulation models of two tunable bandpass filters (tBPFs). The calculated results out of the ANN model demonstrate a good agreement with simulation and measurement counterparts.

## 4.1 Introduction

Due to the ever-increasing demand for multifunction, multiband, and multi-standard RF/microwave wireless communications systems, tunable and reconfigurable microwave circuits and techniques have been studied extensively. Typically, such tunable filters are used in band-selective and multiband communication systems where a single transceiver operates on multiple frequency bands. Over the past few decades, various types of planar and non-planar, single-band

and multi-band frequency-tunable filters have been reported with electrical, mechanical, and magnetic tuning methods [161], [162], [163], [164], [165], [166], [167], [168], [169], [170]. Such tuning is often achieved by controlling the resonant frequency of resonators and coupling strength between resonators by activating semiconductor (varactor) diodes [161], [162], MEMS devices [163], tuning screws [164], tuning plungers [165], and so on [166], [167], [168]. Few attempts were made for tuning bandpass filters by deploying computer-aided technologies [169], [170]. Different electrical, magnetic, and mechanical tuning elements have extensively been studied in the literature. However, such tuning mechanisms are not formulated in any well-behaved equation-based analytical models except in a few optimization models.

Different CAD tools have been proposed for tuning microwave filter design parameters such as aggressive space-mapping (ASM) [138], cognition-driven space mapping [139], parallel space mapping [129], homotopy optimization [31], etc. All these algorithms start with initial values that generate the filter response with closely spaced poles. Thus, it is difficult to achieve a good matching for detuned filters from an available optimizer-based filter structure as the initial values cannot keep the poles close enough to each other. Even if the homotopy optimization achieves the design goal from the initial guess, four poles out of five poles are closely placed in the filter response generated from the initial design values [31]. In addition, homotopy optimization is a local optimizer that cannot solve a global optimization problem efficiently. In contrast, global optimization algorithms such as evolutionary algorithms (EAs) involve many parameters which require significant computational resources and running time. In this work, advanced metaheuristic optimization algorithms are proposed, studied, and used, for the first time, to find the optimized parameters of tunable filters.

The limitation of deploying an optimization algorithm on the prediction of tuning elements of a tunable filter lies in its repetitive use over the same circuit. To solve this problem, we formulate a tunable artificial neural network (ANN) model which allows the frequency-tuning state of a tunable circuit as the inputs and generates the tuning parameters as the outputs. A set of smooth training data is required for efficient ANN model training. This inspires us to generate the training data through an optimization algorithm where the state variables change smoothly, and the output parameters vary in the same manner. The trained ANN model is set to solve complicated non-linear input-output mapping problems. Such an ANN model is known as the forward model [3]. Inverse

ANN models have also been well studied in the literature where the inputs are electrical parameters, and the outputs are geometric parameters [4], [88].

Metaheuristic global optimization algorithms are easy to implement as no gradient information is required. The optimization problems solved by nature-inspired metaheuristic algorithms are set to mimic biological or physical phenomena. Swarm-based technique is one of them which mimics the social behavior of groups of animals. These algorithms are more advantageous than EAs as they preserve the search space information over subsequent iterations. Particle swarm optimization (PSO) [34] is the most used algorithm. Whale optimization algorithm (WOA) [74] and grey wolf optimization (GWO) [79] are the two most recent swarm intelligence-based algorithms. The WOA is inspired by the bubble-net hunting behavior of humpback whales and the GWO uses the leadership hierarchy-based hunting behavior of grey wolves. The WOA introduces a stochastic method for population initialization and the leadership hierarchy of GWO is executed by four types of grey wolves named alpha, beta, delta, and omega. Even though both WOA and GWO possess a strong potential for solving optimization problems, these algorithms still suffer from low accuracy, slow convergence, and easy falling probability into local optimal values as in other metaheuristic algorithms. To overcome these drawbacks, various modifications are proposed in the literature [171], [172], [173], [174], [175]. Especially, A nonlinear adaptive weight and golden sine operator (NGS-WOA) based WOA was proposed to overcome the shortcomings of low precision and slow convergence [175]. In this paper, we adopt the NGS-WOA due to its fast convergence behavior. On the other hand, GWO has also been utilized in fuzzy control systems (CSs) [176], photovoltaic (PV) systems [177], ANN model training [178] etc.

Both WOA and GWO demonstrate promising performances in avoiding local optima compared to other conventional algorithms. The search space of microwave tunable filters is usually unknown and complex where many local optima may exist. These metaheuristics handle such problems, efficiently. However, according to the No Free Lunch (NFL) theorem, no metaheuristic can solve all the optimization problems solely [80]. Thus, one algorithm solves a certain problem while other problems cannot be solved satisfactorily. This inspires us to investigate suitable metaheuristics for microwave engineering applications. In this work, we propose a hybrid optimization technique where WOA and GWO are compared intelligently and integrated into a mathematics-based local optimizer to achieve better accuracy for tunable filter optimization. We exploit and develop the NGS-WOA and GWO to generate population randomly in an arbitrary search space and to

converge to the best position by bubble-net feeding behavior and leadership hierarchy, respectively. The best position is achieved from the algorithm that provides a minimum value of a predefined cost function. Then, we apply the homotopy algorithm to search for the best solution in its locality. In this case, the homotopy optimization starts from a good set of initial values generated by the improved WOA or GWO and it can reach the design goal gradually. Usually, global optimizers become slow when the current solution is near to the optimal solution. The homotopy optimization is integrated to these global optimizers to expedite the search for optimal solution. It is worth to mention that the homotopy method as a local optimizer could be used before the implementation of global optimizers. However, the homotopy optimization in that case should begin with a set of initial value which requires the prior knowledge of a tunable filter under consideration. In this work, the swarm intelligence-based optimizations are followed by the homotopy optimization so that the prior knowledge of the tunable filter under design is not required for a good set of initial variables, which are provided by the NGS-WOA or GWO automatically. Hence, the proposed method reduces the workload of a tunable filter designer with an automated algorithm. The homotopy optimization is a mathematics-based algorithm that comes from the concept of topology and differential geometry [152]. This local optimization technique works well with a good set of initial values. It defines a series of intermediate problems rather than solving a problem directly. Finally, we train the ANN model with the proposed hybrid optimizer-generated data to predict the tunable circuit parameters for a given frequency tuning state of the filter. We also use the EM-based ANN model as a surrogate model [82] to expedite the optimization of a tunable bandpass filter (tBPF). In this case, the ANN model uses the tunable parameters as the input and S-parameters as the output.

The rest of the paper is organized as follows. Section II briefly presents the ANN model and the homotopy optimization method. Section III introduces WOA with its improvement and the GWO algorithm. Section IV explains the proposed ANN model development procedure for filter tuning. Section V illustrates one ideal lumped element tunable filter circuit and two full-wave electromagnetic models (EM) of two tBPFs to demonstrate the proposed tuning method. Section VI consists of a comparison of the proposed optimization algorithm with others and related discussions. Section VII concludes the findings of the work.

## 4.2 ANN model and homotopy optimization

### 4.2.1 ANN model

A commonly used neural network structure, multilayer perceptron (MLP), is adopted in this work for ANN model development where neurons are grouped into different layers. The first and last layers are called input and output layers while the remaining layers are known as hidden layers. For the $L$ number of layers, hidden layers are from 2 to $L-1$, assuming that there exists total $N_l$ number of neurons in $l^{th}$ layer, where $l = 1,2,\dots,L$. The connecting weight between $j^{th}$ neuron of $(l-1)^{th}$ layer and $i^{th}$ neuron of the $l^{th}$ layer is denoted as $w_{ij}^{l}$. Let's further assume that $x_i$ as $i^{th}$ input to the MLP while $z_i^l$ represents the output from the $l^{th}$ layer's $i^{th}$ neuron. Let $b_i^l$ be the bias term of each neuron at $l^{th}$ layer's $i^{th}$ neuron. The weight and bias vector are initialized with random variables in the range of [0,1] before the training phase. These parameters get updated through the training process. The feedforward computation is given by

$$z_i^1 = x_i, i = 1,2,\dots,N_1, n = N_1 \tag{4.1}$$

$$z_i^1 = \sigma\left(\sum_{j=0}^{N_{l-1}} w_{ij}^l z_j^{l-1} + b_i^l\right);\ i = 1,2,..,N_l; l = 2,3,\dots,L \tag{4.2}$$

$$y_i = z_i^L, i = 1,2,\dots,N_L, m = N_L \tag{4.3}$$

where the input vector vector $x = [x_1\ x_2\ \dots x_n]^T$ and the output vector $y = [y_1\ y_2\ \dots y_m]^T$. The weighted sum is fed from one layer to the next through an activation function. In this work, the sigmoid and linear functions are used as a hidden neuron and output neuron activation function, respectively.

Two ANN models are developed in this work. The first is the EM-ANN model of a tunable filter structure that accepts tuning screw heights of the tunable filter and frequency variables as inputs. The second is the final tunable ANN model that considers the critical frequency points of a bandpass filter. Such geometric dimensions and frequency variables vary by many orders of magnitudes. The sigmoid activation function saturates for large input values where the derivatives become close to 0. Such values result in a slow ANN model training. To accelerate the model training, we preprocess all the input variables in the range of $[-1,+1]$ during the training phase and afterwards, we map back the scaled model input value to the original value [31]. The EM-ANN model provides the outputs as S-parameter magnitudes which remain in the range of $[0,1]$ for a passive network. Therefore, a preprocessing is not required at the outputs. On the other hand, the

tunable ANN model has the outputs of circuit parameters of lumped element tunable circuit or geometric parameters of the 3D-tunable filter model which requires the preprocessing for the outputs of the ANN model.

In any case, Levenberg-Marquardt's algorithm (LMA) [156] is used for training both the ANN models in this work, which is fast and efficient for small-sized networks.

### 4.2.2 Homotopy optimization

The homotopy analysis method (HAM) is a powerful mathematics-based tool for the solution of nonlinear problems which stems from the concept of topology to generate several convergent series solutions for nonlinear systems. It is an analytical approximation method for solving any small/large physical parameters involving nonlinear problems, which provide us freedom on choosing base functions and initial guesses [152]. The homotopy method can be expressed as

$$H(a,\delta) = (1-\delta)F(a) + \delta G(a) \tag{4.4}$$

where $\delta \in [0,1]$ is the homotopy variable. $F(a)$ and $G(a)$ are homotopic where $F(a)$ is an optimization problem whose solution is known and $G(a)$ is the target problem. With the gradual increment of homotopy variable, $\delta$ from 0 to 1, the function $F(a)$ gradually deforms to $G(a)$. The $\delta$ grows from 0 to 1 as $0 < \delta_1 < \delta_2 < \cdots < 1$, which introduces several intermediate homotopy problems $H(a,\delta)$. Each time $\delta$ grows by a little bit, the renewed optimization problem remains alike to the current problem. Thus, the solution to the renewed problem will be in the current solution's neighborhood.

## 4.3 Swarm-based meta-heuristic algorithms

In this section, we describe the mathematical formulations of the whale optimization algorithm (WOA) [74] with one of its improved version (NGS-WOA) [175] and grey wolf optimizer (GWO) [79].

### 4.3.1 Whale optimization algorithm (WOA)

The mathematical optimization formulations are unfolded in three steps, namely prey encircling, bubble-net feeding maneuver, and prey searching [74]. In the first step for the prey encircling, the whales recognize the prey's location and encircle them. Primarily, the target prey is considered as the current best candidate solution as the optimal solution is unknown. This search candidate will

only be updated if a better candidate solution is figured out. Such behavior can be formulated as

$$\vec{D} = \left|\vec{C}.\ \overrightarrow{X^*}(t) - \vec{X}(t)\right| \tag{4.5}$$

$$\vec{X}(t+1) = \overrightarrow{X^*}(t) - \vec{A}.\vec{D} \tag{4.6}$$

where $\vec{A}$ and $\vec{C}$ are the coefficient vectors, $\overrightarrow{X^*}$ is the so far achieved best solution of the position vector, $\vec{X}$ is the position vector, $||$ is the absolute value and . is an element-by-element multiplication. Upon each iteration *t*, the value of $\overrightarrow{X^*}$ keeps updating if there is a better solution. Here, $\vec{A}$ and $\vec{C}$ are expressed in terms of a random vector $\vec{r}$ in the range of [0,1] and a linearly decreased vector $\vec{a}$ from 2 to 0 throughout iterations (in both exploration and exploitation phases). Different places around the best agent can be achieved with respect to the current position by adjusting the value of $\vec{A}$ and $\vec{C}$ vectors.

$$\vec{A} = |2\vec{a}.\vec{r} - \vec{a}| \tag{4.7}$$

$$\vec{C} = 2.\vec{r} \tag{4.8}$$

The second step, the bubble-net attacking mechanism is mathematically formulated in the exploitation phase by using shrinking the encircling mechanism and spiral updating position. The shrinking encircling mechanism is established by reducing the value of $\vec{a}$ that eventually reduces the value of $\vec{A}$. In the spiral location update, the distance between the prey's location and the whale's current location is calculated. A spiral update equation is developed to simulate the whale's spiral movement between two locations as

$$\vec{X}(t+1) = \overrightarrow{D'}.e^{bl}.cos(2\pi l) - \overrightarrow{X^*}(t) \tag{4.9}$$

$$\overrightarrow{D'} = \left|\overrightarrow{X^*}(t) - \vec{X}(t)\right| \tag{4.10}$$

where $\overrightarrow{D'}$ denotes the distance of the i$^{th}$ whale to the prey, *l* is a random number in the range of [-1,1] and *b* defines the shape of logarithmic spiral which is set to 1 for stable spiral update. To balance between shrinking encircling mechanism and spiral update mechanism, the probability of using these models is equal. To implement the mathematical model, the algorithm generates a random number $p$ in the range of [0,1]. The shrinking encircling mechanism and the spiral update mechanism are chosen for $p < 0.5$ and $p \geq 0.5$, respectively. Such mechanisms are given as

$$\vec{X}(t+1) = \begin{cases} \overrightarrow{X^*}(t) - \vec{A}.\vec{D}, & p < 0.5 \\ \overrightarrow{D'}.e^{bl}.cos(2\pi l) - \overrightarrow{X^*}(t), & p \geq 0.5 \end{cases} \quad (4.11)$$

where p is a random number in the range of [0,1].

In the last step for the prey searching, a similar strategy is adopted based on $\vec{A}$ variation. To perform the global search, the $\vec{A}$ value is selected randomly which is greater than 1. This is mathematically modelled as

$$\vec{D} = \left|\vec{C}.\ \vec{X}_{rand} - \vec{X}\right| \quad (4.12)$$

$$\vec{X}(t+1) = \vec{X}_{rand}(t) - \vec{A}.\vec{D} \quad (4.13)$$

where $\vec{X}_{rand}$ is a random value that represents a random whale selected from the current population.

Even though the above-explained intelligent position updating algorithm renders the WOA superior in the global exploration, it has the drawbacks of too many random parameters; random selection of exploitation and exploration phases; and easy falling into local optima on multi-peak functions. To mitigate these issues, an improved WOA is proposed in [175] based on nonlinear adaptive weight and golden sine operator.

### 4.3.2 Improved whale optimization algorithm (NGS-WOA)

An appropriate transition between global exploration and local exploitation improves the optimization performance significantly. The changes of $\vec{A}$ and $l$ affect the balance between exploitation and exploration, which directly affect the algorithm performance. To minimize the randomness of the algorithm, a nonlinear adaptive weight was introduced to adaptively adjust the parameters $\vec{A}$ and $l$ [175]. The nonlinear adaptive weight $C_1$ is expressed in (4.14) where $k$ is the convergence adjustment factor, $t$ and $T$ are the current iteration and the maximum number of iterations, respectively. Different k values ($< 1$) are experimented, and it is found that 0.5 provides the best convergence effect [175].

$$C_1 = \frac{1}{2}.\left[1 + \cos\left(\frac{\pi t}{T}\right)\right]^k \quad (4.14)$$

Equations (4.6) and (4.13) of the shrinking encircle mechanism are updated after introducing the nonlinear adaptive weight $C_1$ as

$$\vec{X}(t+1) = \overrightarrow{X^*}(t) - C_1.\vec{A}.\vec{D} \quad (4.15)$$

$$\vec{X}(t+1) = \vec{X}_{rand}(t) - C_1.\vec{A}.\vec{D} \tag{4.16}$$

Equation (4.9) of the spiral update mechanism is updated as follows

$$\vec{X}(t+1) = \overrightarrow{D'}.e^{bl}.C_1.cos(2\pi l) - \overrightarrow{X^*}(t) \tag{4.17}$$

Throughout iterations, the nonlinear weight accelerates in the downward direction and the values of $\vec{A}$ and $l$ reduce significantly. The shrinking enclosing mechanism and the spiral update mechanism bring the search agents closer to the target value area, which improves the exploitation ability of the algorithm. The introduced nonlinear adaptive weight adequately adjusts parameters $\vec{A}$ and $l$ to balance the exploration and exploitation stages.

An improved golden sine operator was introduced in WOA for better convergence where the search agent scans the search space effectively with a sinusoidal route that enhances the global search capability of the WOA [175]. In addition, the golden section coefficient narrows the explored space continuously and search agents keep searching the areas with excellent results to improve the local exploitation feature of the algorithm. The improved golden sine operator increases the indentation coefficient based on the golden sine operator and improves the routing of the search agent. The improved golden sine operator is used to update the search agent's position as

$$\vec{X}(t+1) = \vec{X}(t).|\sin(r_1)| + r_2.\sin(r_2).\left|m_1.\overrightarrow{X^*}(t) - m_2.\vec{X}(t)\right| \tag{4.18}$$

$$m_1 = -2\pi + (1-\tau).2\pi \tag{4.19}$$

$$m_2 = -2\pi + \tau.2\pi \tag{4.20}$$

where $r_1$ and $r_2$ are the random variables that control the moving distance and moving direction of the search agent, respectively. $m_1$ and $m_2$ are improved indentation coefficients that drive search agents closer to the target value in longer steps. $\tau$ is the golden section coefficient which is derived as 0.618 [175]. After calculating the search agent's position from (4.15), (4.16) and (4.17), $r_1$, $r_2$, $m_1$ *and* $m_2$ are updated by (4.19) and (4.20). Finally, the position of the search agent is updated by (4.18). This process keeps repeating till the stopping criteria is met, which is the maximum number of iterations in this case.

### 4.3.3 Grey wolf optimization (GWO)

The grey wolf optimization (GWO) is inspired by their social hierarchy and hunting strategy which is executed in three steps [79]. In the mathematical formulations of GWO, alpha (α), beta

(β) and delta (δ) represent the best three solutions in the search space. The entire optimization process is supervised by these three candidates. Other candidates are considered as omegas (ω). Each candidate solution is considered as a vector in

$$\vec{X} = x_1, x_2, \dots \dots, x_n \tag{4.21}$$

where $x_i$ represents the current wolf's position and $n$ is search space dimension.

In the first step, the encircling of prey is formulated as

$$\vec{D} = \left|\vec{C}.\ \overrightarrow{X_p}(t) - \vec{X}(t)\right| \tag{4.22}$$

$$\vec{X}(t+1) = \overrightarrow{X_p}(t) - \vec{A}.\vec{D} \tag{4.23}$$

where $t$ denotes the current iteration, $\vec{A}$ and $\vec{C}$ are the coefficient vectors, $\overrightarrow{X_p}$ is the prey's position vector, $\vec{X}$ is the position vector of a grey wolf, $||$ is the absolute value and . is an element-by-element multiplication. The two coefficient vectors are expressed in terms of two random vectors $\overrightarrow{r_1}$ and $\overrightarrow{r_2}$ in the range of [0,1] and a linearly decreased vector $\vec{a}$ from 2 to 0 over the course of iterations.

$$\vec{A} = 2\vec{a}.\overrightarrow{r_1} - \vec{a} \tag{4.24}$$

$$\vec{C} = 2.\overrightarrow{r_2} \tag{4.25}$$

In the second step, the grey wolves locate the potential position of the prey for hunting, which is guided by the first best solutions, namely alpha (α), beta (β), and delta (δ). These three best solutions will be saved and kept updated over the iteration to support other omegas (ω) for finding their positions. Such a hunting strategy is mathematically modelled as

$$\vec{D}_\alpha = \left|\vec{C}_1.\vec{X}_\alpha - \vec{X}\right| \tag{4.26}$$

$$\vec{D}_\beta = \left|\vec{C}_2.\vec{X}_\beta - \vec{X}\right| \tag{4.27}$$

$$\vec{D}_\delta = \left|\vec{C}_3.\vec{X}_\delta - \vec{X}\right| \tag{4.28}$$

where $\vec{D}_\alpha$, $\vec{D}_\beta$ and $\vec{D}_\delta$ are the updated distance vectors between the position of omegas (ω) and leader wolves (α, β and δ). Coefficient vectors $\vec{C}$ are calculated from (4.25), and $\vec{X}$ is the position of omegas (ω). Each $\vec{X}_i$ represents an approximate position from the distance vector between

omegas and other leader wolves of $\vec{D}_{\alpha}$, $\vec{D}_{\beta}$ and $\vec{D}_{\delta}$, respectively. The mathematical formulations are

$$\vec{X}_1 = \vec{X}_{\alpha} - \overrightarrow{A_1}.(\vec{D}_{\alpha}) \tag{4.29}$$

$$\vec{X}_2 = \vec{X}_{\beta} - \overrightarrow{A_2}.(\vec{D}_{\beta}) \tag{4.30}$$

$$\vec{X}_3 = \vec{X}_{\delta} - \overrightarrow{A_3}.(\vec{D}_{\delta}) \tag{4.31}$$

The newly updated position vectors are expressed as $\vec{X}_i$ where $\vec{X}_1$ is the newly updated position from alpha position $\vec{X}_{\alpha}$ and the distance vector $\vec{D}_{\alpha}$. The coefficient vectors $\overrightarrow{A_i}$ are calculated from (4.24). $\vec{X}_2$ and $\vec{X}_3$ are calculated in the same manner as $\vec{X}_1$. The new position vector can be calculated from a simple average as

$$\vec{X}(t+1) = \frac{\vec{X}_1 + \vec{X}_2 + \vec{X}_3}{3} \tag{4.32}$$

In the third step for attacking prey, the $\vec{a}$ value is decreased from 2 to 0 over the iterations which reduce $\vec{A}$ in the interval of [*-a,a*].

Since WOA and GWO were first proposed in [74] and [79], these optimizers caught researchers' attention from various engineering fields. However, microwave engineering applications are rarely explored with these algorithms, which inspires us to explore their potentials in solving highly nonlinear problems for microwave engineering applications.

## 4.4 Hybrid optimizer assisted ANN model development algorithm

ANN model has been widely used due to its outstanding generalization capability. Such generalization comes from the accuracy of ANN model which relies on the training data to learn the specific problem. In this work, our main goal is to develop an ANN model which provides the filter tuning parameters against the frequency characteristics of a tunable filter. In order to train the ANN model for the tunable filter, we need to generate the tunable parameters corresponding to the critical frequency points of the tunable filter.

It is hard to find the tunable parameters at different stages of the tunable filter due to the lack of a theory. This is usually done by an experienced filter designer on a trial-and-error basis. However, such a technique is impractical for the collection of a large set of training data. Therefore, we

propose a hybrid optimization-based data generation technique without human intervention. Once the training data is generated, the ANN model development becomes easier as the inputs and outputs are smoothly varied during the data generation phase.

### 4.4.1 Cost function definition

The goal of any optimization algorithm is to minimize a certain cost function. Such a cost function is defined in terms of the key parameters involved in a target problem. In the microwave filter characterization problem, the key parameters are passband return loss and stopband insertion loss, respectively. According to the filter specifications, both of passband return loss level and stopband insertion loss level contribute to the overall cost function. In case of BPFs, we prefer the $S_{11}$ response inside the passband that should be below the prescribed return loss level and the $S_{21}$ response inside the stopband should be below the prescribed insertion loss level. In (4.35), such a cost function is mathematically formulated as

$$K = \max[(S_{11})_{PB}, -R] + w * \max[(S_{21})_{SB}, -I] \tag{4.33}$$

where passband (*PB*) is between the edge frequencies $f_2$ and $f_3$; the stopband (*SB*) edge frequencies are $f_1$, $f_4$ and $f_5$ as illustrated in Figure 4.1. $f_5$ is considered, keeping in mind that the spurious frequencies may occur due to the higher-order modes. For the target tunable filter, the passband return loss level *R* is fixed at 20 dB and the stopband insertion loss level *I* is fixed at 30dB. *w* is the balancing coefficient between passband return loss and stopband insertion loss which is set at 0.3 in this work. The parameters in the cost function (4.33) are

$$P = [f_1\ f_2\ f_3\ f_4\ f_5] \tag{4.34}$$

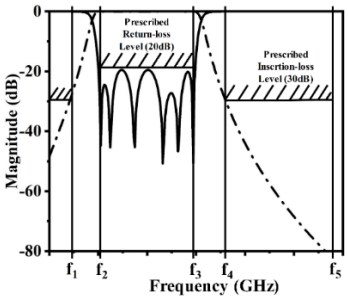


Figure 4.1 Typical S-Parameters of a sixth order BPF

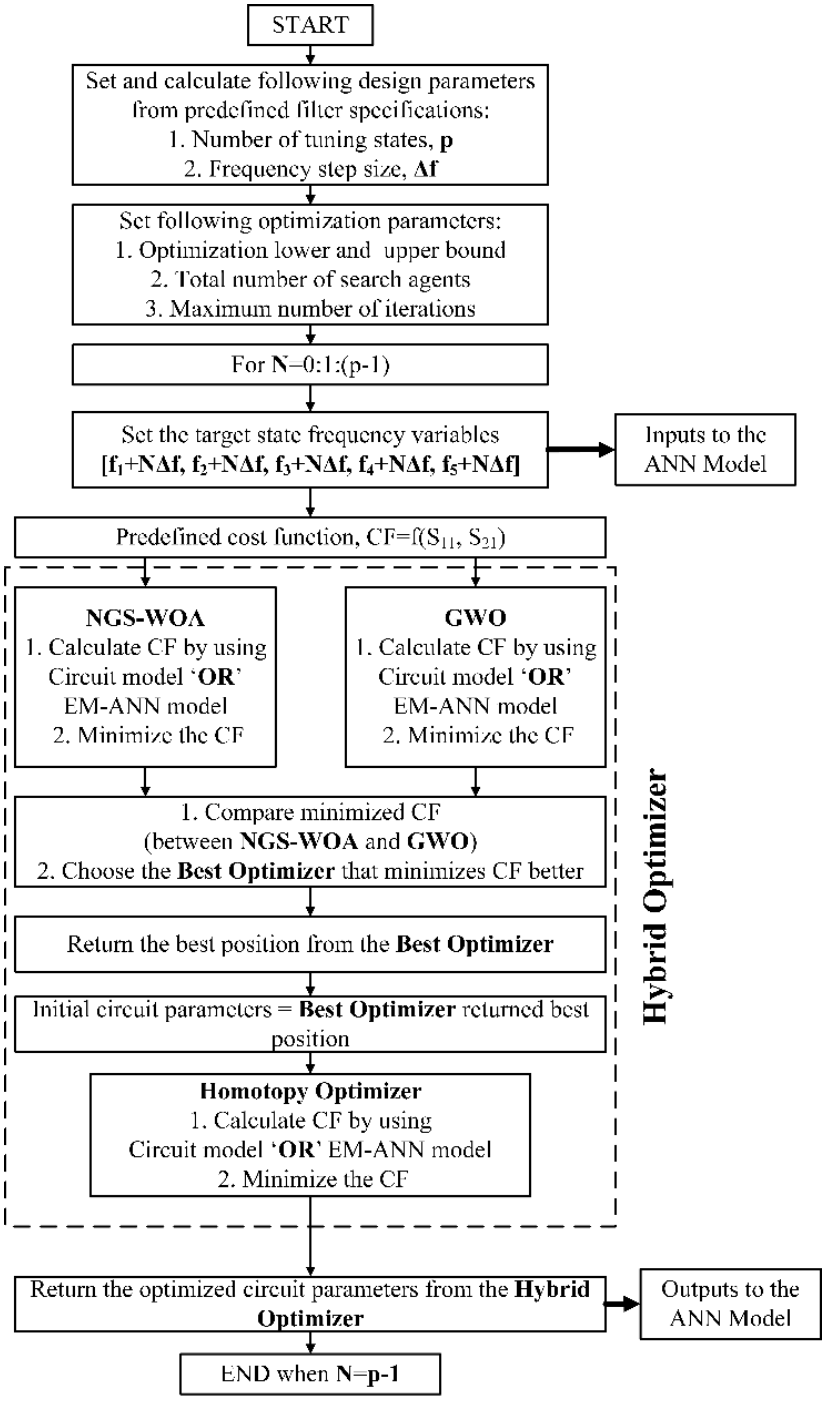


Figure 4.2 Flowchart of training data generation

These parameters in the cost function are considered as state variables for optimizing the tunable filters. Figure 4.1. illustrates critical frequency points from an arbitrary sixth-order tunable filter which are expected to shift right or left according to its specific applications. Our goal is to extract the tunable parameters against certain state variables of the tunable filter. For a continuously

frequency tunable filter, its frequency parameters of (4.34) are supposed to be varied synchronously. Thus, we keep varying these frequency variables during the optimization process to obtain the tunable circuit parameters.

### 4.4.2 ANN model development algorithm

Here, we describe the proposed training data generation technique by the hybridization of advanced optimizers. Once the training data is collected, the ANN model can be developed. The overall model development procedure is as follows:

1. Design a lumped-element circuit or a full-wave EM model of a tunable filter circuit. Define the filter specifications, such as starting and ending of the interested frequency band with the number of frequency points. Get a rough idea of the frequency band over which the filter is tunable. Define the total number of tuning states, $p$ according to the total number of required training data sets and calculate the frequency step size, $\Delta f$. For example, if we want to have $p = 100$ tuning states of the tunable filter in the range of 1 to 10 GHz, the step size, $\Delta f = (10 - 1)/100 = 0.09GHz$.
2. Identify the tunable parameters and set their lower and upper optimization boundary that covers the roughly estimated tunable frequency range as speculated in step 1. Set the maximum number of iterations and the total number of search agents for both NGS-WOA and GWO. These are the only two parameters required to be set up before the optimization starts. Usually, 100-200 iterations are used with 50 to 70 populations. If the optimization problem involves high dimensional variables, the population and the number of iterations can be increased to improve the overall convergence behavior.
3. Setup a loop command for $N$ that is initiated with 0 and increased by 1. For $N = 0$, the first optimization is carried out. As the loop continues, successive optimizations for different tuning states are executed.
4. Update the frequency state variables with the increment added by $N\Delta f$. The target state is preset at $[f_1\ f_2\ f_3\ f_4\ f_5]$ for $N = 0$ which is considered as the first optimization under the operation. The first target state would be tuned at the lowest tuning state of the filter which will be updated according to the increment $N\Delta f$ over each operation of the loop. Basically, in each loop operation, $\Delta f$ is added to each variable of the consecutive tuning states as $N$ is incremented by 1 over each iteration. Therefore, in each operation, the target state variables

change a little. This provides a smooth change in data sets which makes the ANN model training easier afterwards. Write these target state variables in an appending file.

5. Define the cost function or objective function we want to minimize through the course of iteration inside the optimization functions. The cost function for tunable filters is formulated in (4.33). As the parameters in (4.34) keep changing with each loop operation, the value of the cost function also keeps varying.
6. At this stage of the algorithm, the NGS-WOA and GWO run their own optimization procedure separately, which tries to minimize the cost function throughout iterations till the stopping criteria is made which is the maximum number of iterations in this case. The cost function in (4.33) is a function of S parameters which is calculated either from a circuit simulator or a time-consuming full-wave EM model of the tunable filter. This full-wave EM model is replaced with the EM-ANN model of the tunable filter to speed up the optimization process.
7. Once both the optimization process is completed, we end up with two different sets of optimized variables. At this stage, the final cost function value from NGS-WOA and GWO is compared. The optimizer that provides the lowest cost function value among NGS-WOA and GWO, is selected as the best optimizer and corresponding optimized variables are sent to the next stage of the algorithm.
8. The best optimized variables calculated from step 7 is considered as the initial circuit parameters for homotopy optimization at this stage. These initial variables are optimized from either NGS-WOA or GWO which is a swarm-intelligence based global optimizer. Thus, homotopy optimization gets a very good set of initial values to start the optimization procedure further. The population-based optimizers become slow when they are close to the optimal solution. That is why we add homotopy optimization at this stage as a local optimizer to find the best solution in the neighborhood quickly.
9. The homotopy optimization algorithm is applied on the same objective function of (4.33) with a predetermined number of homotopy steps, desired passband return loss and stopband insertion loss, respectively. As the initial variables are already computed by a global optimizer, homotopy needs very few steps (around 4 to 6) to get the best result which takes a few minutes of CPU time only.
10. The hybrid optimizer-based calculation for a single optimization problem ends with the

completion of the homotopy optimization. The final best solution from the hybrid optimizer achieves minimum cost function throughout the process. Record these optimized circuit parameters in an appending file.

11. The loop command that was initiated in step 3 keeps repeating till the stopping criteria is made which is $N = p - 1$. This stopping criterion depends on the number of data sets required for ANN model training.
12. Once the data generation is completed, collect the data files from step 4 and step 10 as the inputs and outputs for target ANN model training and testing. We use 80% and 20% of total data for training and testing of the target ANN model, respectively.

**%Circuit Specification**

Target pass-band Return Loss
Target stop-band Insertion Loss
Target critical frequency points as cost function parameters

**%NGS-WOA and GWO algorithms**

Number of search agents
Maximum Iterations
Optimization boundary
$X = K[Optim(NGS - WOA)]$
$Y = K[Optim(GWO)]$
$Var_{Optim(NGS-WOA)} = [a_1, a_2, \dots\dots, a_i]$
$Var_{Optim(GWO)} = [b_1, b_2, \dots\dots, b_i]$

**%Switch between NGS-WOA and GWO**

$if\ X < Y$
$Initial\ Variables = Var_{Optim(NGS-WOA)}$
$else$
$Initial\ Variables = Var_{Optim(GWO)}$

**%Homotopy Optimization**

$Initial\ Circuit\ Parameters = Initial\ Variables$
Homotopy Steps
Calculate optimized variables starting from initial parameters
$Z = K[Optim(Homotopy)]$
$Var_{Optim(Homotopy)} = [c_1, c_2, \dots\dots, c_i]$
$Final\ Circuit\ Parameters = Var_{Optim(Homotopy)}$

Figure 4.3 Pseudo code of the proposed hybrid algorithm

To better understand the hybridization mechanism of NGS-WOA, GWO and homotopy optimization, the pseudo code of the proposed hybrid algorithm is described and presented in Figure 4.3. Here, the first code block refers to the target tunable filter performance and the second code block represents the NGS-WOA and GWO algorithm as $Optim(NGS-WOA)$ and $Optim(GWO)$ which determines the cost function value as $X$ and $Y$ through the rule of (4.33). $Var_{Optim(NGS-WOA)}$ and $Var_{Optim(GWO)}$ are the NGS-WOA and GWO algorithm optimized variables, respectively. The NGS-WOA and GWO algorithm-generated cost function value is compared in the third code block under an if-else statement. The initial variables are decided according to this comparison, which are forwarded to the next code block as initial circuit parameters for homotopy optimization $Optim(Homotopy)$. The homotopy method starts by a step-by-step optimization process, considering initial circuit parameters as initial variables and obtains the final set of tunable filter's variables as $Var_{Optim(Homotopy)}$ while the cost function value is further minimized to $Z$ . Therefore, the cost function value from the NGS-WOA and GWO is compared, then the best optimized circuit parameters from one of these algorithms are considered for the homotopy optimization as initial variables. Finally, the optimum circuit variables are determined by the homotopy optimization. Such a hybridization technique allows us to take advantages of the swarm optimization algorithms (WOA and GWO) and makes use of a step-by-step mathematics-based optimization algorithm such as homotopy method to obtain the maximum optimization for complicated problems in an accurate and prompt manner.

The proposed hybrid algorithm requires a careful selection of few parameters such as total number of homotopy steps, optimization boundary, total number of search agents/population, and maximum number of iterations for NGS-WOA and GWO algorithm, respectively. The choice of such parameters requires a filter designer experience to some extent. For example, the optimization boundary of the variables is decided according to the desired tuning range of the filter. The number of homotopy steps is decided with reference to the filter response corresponding to the initial circuit parameters. As the initial circuit parameters come from either NGS-WOA or GWO algorithm, a few homotopy steps are enough to find out the optimum circuit parameters. The total number of search agents/population and maximum iterations are chosen based on the dimensionality and complexity of the optimization problem. Highly dimensional optimization problems are

complicated to solve; therefore, they require more population and iteration to better minimize the cost function. These difficulties can be avoided by observing few test optimizations for the target problem.

## 4.5 Illustrative examples

In this section, three tBPF examples are demonstrated to validate the proposed approach. First, a fifth-order lumped element theoretical BPF circuit from [179] is tuned to exhibit that the theoretical BPF models can be tuned appropriately where the practical aspects such as parasitic effects are not considered. Second, a fourth-order, dual mode tBPF from [180] is tuned to show that the proposed model predicts the tunable parameters of a practical circuit successfully. Finally, a fourth-order, dual-post resonator based tBPF from [181] is illustrated to prove that the proposed approach can also be used for the practical constant bandwidth tBPFs.

### 4.5.1 Lumped element tunable filter circuit

Here, we demonstrate a theoretically developed tunable BPF circuit to exhibit the working principle and outcomes of our proposed algorithm. Before starting the data generation process for developing the ANN model, we should select a prototype of tunable bandpass filter. Theoretically, a pair of resonators are coupled by an ideal impedance or admittance inverter. The $\pi$ models with simple elements are widely used among many approximate equivalent circuits of an ideal impedance inverter [182]. Such models have a pole at the infinite frequency or at zero frequency. In [183], a practical impedance inverter places an attenuation pole at a finite frequency which shows that the finite pole lies above and below the passband for a positive and negative value of the inverter, respectively. The negative element values from the approximate inverter model are usually absorbed into adjacent elements, which turns into a mixed coupled circuit. By introducing tunable series and shunt pair of capacitors, it would be possible to tune the finite zeros in the lower or upper stopband along with the resonant frequencies which result in a fully tunable or reconfigurable prototype [179]. Thus, a tunable or reconfigurable filter design starts with a filter prototyping with transmission zeros followed by the tuning of relevant capacitors accordingly.

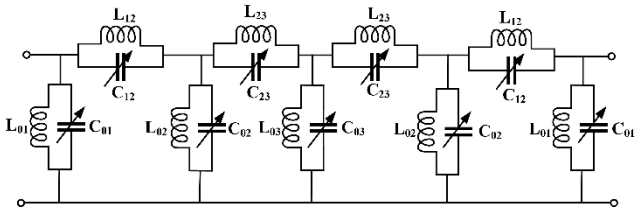


Figure 4.4 Fifth order tunable BPF prototype

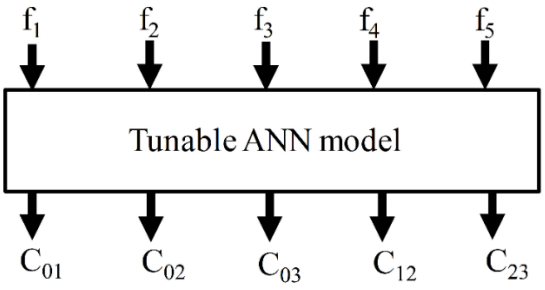


Figure 4.5 Tunable ANN model

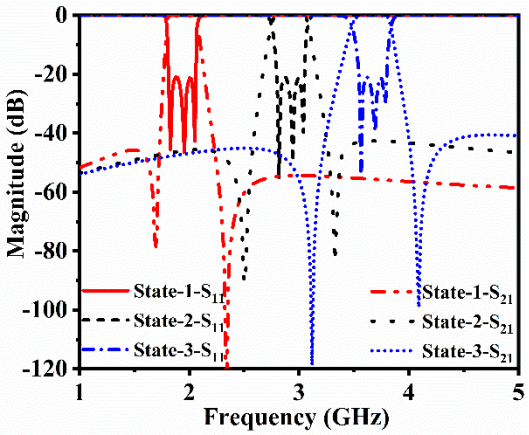


Figure 4.6 S-Parameters from tunable ANN model generated BPF circuit parameters

Table 4.1 State variables at different tuning state (ANN model inputs)

| State | $f_1$ (GHz) | $f_2$ (GHz) | $f_3$ (GHz) | $f_4$ (GHz) | $f_5$ (GHz) |
|---|---|---|---|---|---|
| 1 | 1.61 | 1.81 | 2.05 | 2.25 | 3.0 |
| 2 | 2.60 | 2.80 | 3.04 | 3.24 | 3.99 |
| 3 | 3.34 | 3.54 | 3.78 | 4.08 | 4.83 |

Table 4.2 Tunable circuit parameters of lumped element circuit model (ANN model outputs)

| State | $C_{01}$ (pF) | $C_{02}$ (pF) | $C_{03}$ (pF) | $C_{12}$ (pF) | $C_{23}$ (pF) |
|---|---|---|---|---|---|
| 1 | 8.05 | 8.71 | 6.98 | 3.61 | 6.47 |
| 2 | 3.16 | 3.35 | 4.19 | 3.15 | 1.79 |
| 3 | 2.01 | 2.03 | 2.65 | 2.03 | 1.11 |

The above-mentioned theory is adopted to develop a fifth-order tunable bandpass filter prototype. In such a prototype, two transmission zeros are placed at finite frequencies by deploying mixed coupling between the resonators. Capacitors are the only tunable parameters considered in this case as illustrated in Figure 4.4. Inductors are fixed as $L_{01} = 0.93nH, L_{02} = L_{03} = 0.83nH, L_{12} = 1.28nH \; and \; L_{23} = 1.35nH$. Once the prototype is fixed, we begin with the data generation process. First, we define the filter specification such as frequency range, frequency spacing, desired passband return loss and stopband insertion loss. Then, we write the nodal equations-based MATLAB function of the circuit shown in Figure 4.4. This function calculates the S-parameters against the capacitance variables. Next, we write the cost function as expressed in (4.33) to repeatedly use it inside different optimization functions. At this stage, we specify the optimization parameters such as the number of search agents, maximum number of iterations, lower and upper optimization boundary of the variables. Afterwards, we implement NGS-WOA and GWO separately to calculate the variables after minimizing the cost function. Either NGS-WOA or GWO calculated optimized variables are considered that provides a minimum cost function value. These optimized variables are then fed to homotopy optimization as the initial set of variables to search for the local best solution. A few homotopy steps are required to find the final optimal set of variables. This entire hybrid-optimization process keeps calculating the optimized variables for different set of target tuning state of the filter till the stopping criteria is met. In this example, we generate the data in the range of 1GHz to 5GHz with a step size of 8MHz. The optimization's lower boundary and the upper boundary are set at 1 pF and 12 pF for each capacitor variable. The number of search agents for NGS-WOA and GWO is considered as 80 and the maximum number of iterations is set as 200. Only 5 homotopy steps are used to get the final optimized parameters in each operation. The total data generation time is recorded as 35 minutes.

The ANN model with 5-30-30-5 neurons is developed to train the tunable model as shown in Figure 4.5. After LMA training converges, the 5-30-30-5 model achieves the average error of 2.1e-6 and

2.5e-6 for training and testing sets, respectively. After the ANN model development, we feed the ANN model with three state variables in the form of $[f_1\ f_2\ f_3\ f_4\ f_5]$ as given in Table 4.1. The circuit parameters from corresponding state variables are calculated from the ANN model as given in Table 4.2. We simulate the circuit of Figure 4.4 with the parameters from the ANN model to examine the filter performance. Circuit simulated S-parameters from a different set of circuit parameters mentioned in Table II are plotted in Figure 4.6. It depicts that the passband return loss and stopband insertion loss have been well preserved for a given tuning state of the filter where the passband bandwidth is retained constant (~0.24GHz) over the tuning range. Therefore, the developed tunable ANN model is validated. Point should be noted because of the narrow-bandwidth design of the tBPFs (~0.24GHz), Figure 4.6 illustrates three reflection zeros inside the passband even though all these responses are generated from a $5^{th}$-order tBPF. If the same filter circuit is designed for a larger bandwidth, all the five reflection zeros will be noticeable inside the passband. For example, five reflection zeros are visible in a 0.74GHz bandwidth BPF ($f_2 = 2.22GHz\ and\ f_3 = 2.96GHz$) with the following circuit configuration: $L_{01} = 0.931nH, L_{02} = L_{03} = 0.831nH, L_{12} = 1.791nH, L_{23} = 1.232nH,$ and $C_{01} = C_{02} = 5.1pF, C_{03} = 3.55pF, C_{12} = 0.7pF, C_{23} = 4.86pF$.

### 4.5.2 Electromagnetic model of tunable filter-1

In order to test the performance of the proposed tunable filter design procedure with practical structures, a fourth-order WR-90 standard-based waveguide fed tunable bandpass filter (tBPF) is considered which was originally designed, fabricated, and measured in [180]. In this tBPF, the first and fourth resonators operate in fundamental mode $TE_{010}$ while the second and third resonators operate in dual modes $TE_{120}$ and $TE_{210}$. The tuning screws are positioned inside the cavity where electrical field strength is maximum. These locations can be found from the electric field distributions inside the cavity. As illustrated in Figure 4.7(a), the screws of depth $via_1$ tune the fundamental mode, while the screws of depth $via_2$ and $via_3$ tune the dual modes. Other screws are deployed in the middle of coupling irises for post fabrication coupling tuning. Model-based vector fitting method from [184] and [185] was used to tune the tBPF. Here, we achieve the tuning parameters of this tBPF from the ANN model developed by our proposed technique.

Before starting the data generation for the tunable ANN model, we develop an EM-ANN model for the tBPF as shown in Figure 4.7(b), which accepts the tunable parameters as the inputs and

provides the real and imaginary parts of $S_{11}$ and $S_{21}$ as the output. This EM-ANN model will be used as a surrogate model during the hybrid optimization operation to speed up the data generation process that will be used to train the target tunable ANN model later. To generate the training data for the EM-ANN model of the tunable BPF illustrated in Figure 4.7(a), the design variable $via_1$ has its value in the range of 60-180 mil with a step size of 10 mil, and both design variable $via_2$ and $via_3$ have their value in the range of 140-200 mil with a step size of 10 mil. In total, 343 frequency sweeps for the tunable BPF were carried out in HFSS for six hours of simulation time. Each frequency sweep contains 251 frequency points over 9-12 GHz. The developed EM-ANN model has 4-50-50-4 neurons. After the LMA training converges, the developed ANN model achieves an average error of 3.3e-5 and 3.6e-5 for training and testing sets. The comparison between the EM simulation results and the response calculated by the ANN model at a tuning state is given in Figure 4.8. It demonstrates that the surrogate model matches $S_{21}$ perfectly while the $S_{11}$ is a little deviated from the EM simulated result. Such discrepancy in $S_{11}$ is acceptable as long as it preserves the return loss level inside the passband and the number of noticeable reflection zeros. A designer should make a tradeoff between the model accuracy and model training time. To achieve a better matched $S_{11}$ response from the surrogate model, the model accuracy can be substantiated at the expense of computational cost and training time. Overall, good accuracy is achieved by the surrogate model. Once the EM-ANN model is trained, the data generation process for developing the target tunable ANN model can be initiated.

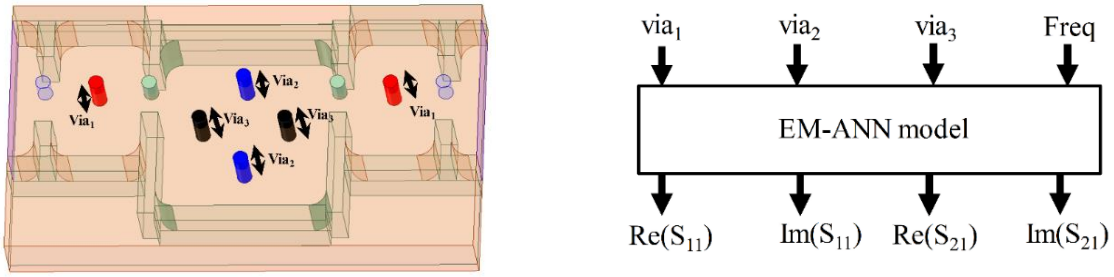


(a) (b)

Figure 4.7 Tunable BPF (a) Electromagnetic model [180]. (b) EM-ANN model

The data generation process is followed step by step as outlined in section IV which took 8 minutes to accomplish. We generate the data in the range of 9GHz to 12GHz with the step size of

11.95MHz. To calculate the cost function inside the optimizer, we use the aforementioned EM-ANN model. The optimization's lower boundary and upper boundary are set for [$Via_1$, $Via_2$, $Via_3$] as [60, 140, 140] and [180, 200, 200], respectively. The number of search agents for NGS-WOA and GWO is considered as 60 and the maximum number of iterations is set as 150. The target tunable ANN model is developed with 5-25-25-3 neurons as illustrated in Figure 4.9. After the LMA training converges, the model achieves the average error of 6.3e-7 and 6.7e-7 for training and testing sets, respectively. After the ANN model development, we feed the ANN model with three state variables in the form of [$f_1$ $f_2$ $f_3$ $f_4$ $f_5$] which provides the tunable parameters as [$Via_1$, $Via_2$, $Via_3$] from corresponding state variables as given in Table 4.3. We simulate the EM model of Figure 4.7(a) with the tunable parameters corresponding to the frequency state variables from the ANN model. The EM model generated S-parameters from a different set of outputs from Table III are plotted in Figure 4.10 along with the measured results. These figures illustrate a good tuning performance of the BPF which is well compared with the simulation and measured results. Therefore, the proposed approach successfully achieves the tunable parameters of the target tBPF design that satisfies the prescribed constant bandwidth requirement. The photograph of the fabricated filter is illustrated in Figure 4.11. Aluminum was used to manufacture the filter. The tuning screws were installed on the top of the cover. During all the EM simulations, the aluminum used in the work was defined in the HFSS library with loss ($3.8 \times 10^7$ siemens/m).

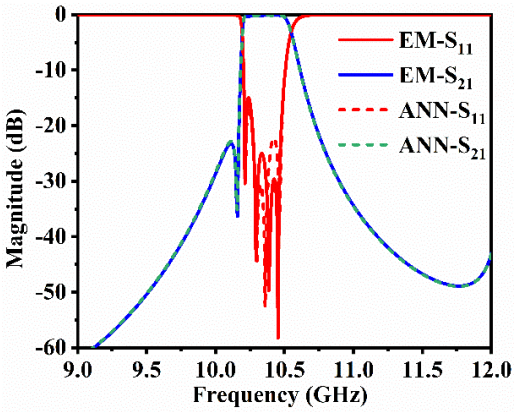


Figure 4.8 S-Parameters comparison between full wave EM model and ANN Surrogate model

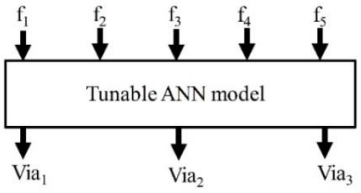


Figure 4.9 Target-tunable ANN model

Table 4.3 Target tunable-ANN model inputs and outputs

| State | ANN inputs (GHz) | | | | | ANN outputs (mil) | | |
|---|---|---|---|---|---|---|---|---|
| | $f_1$ | $f_2$ | $f_3$ | $f_4$ | $f_5$ | $Via_1$ | $Via_2$ | $Via_3$ |
| 1 | 9.30 | 9.52 | 9.78 | 10.18 | 10.78 | 156.2 | 190.87 | 193.49 |
| 2 | 9.92 | 10.14 | 10.40 | 10.80 | 11.20 | 140.9 | 170.91 | 185.53 |
| 3 | 10.40 | 10.62 | 10.88 | 11.28 | 11.88 | 73.61 | 146.50 | 151.05 |

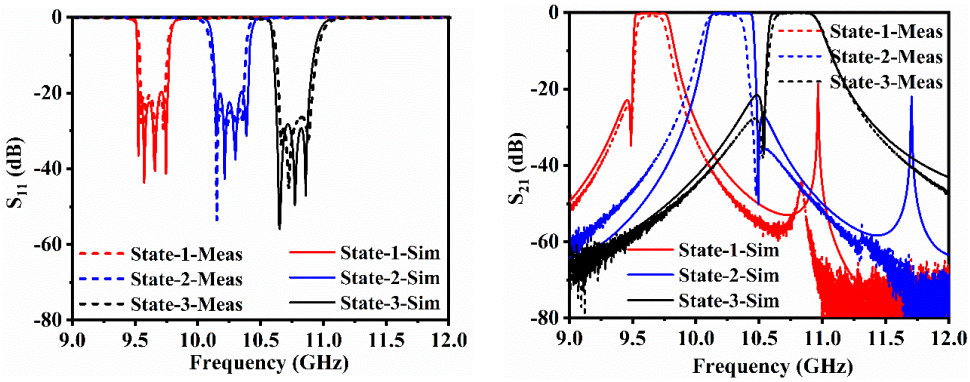


(a) (b)

Figure 4.10 Simulated and measured performance from ANN model generated via heights. (a) Reflection responses (b) Transmission responses

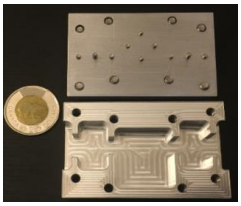

Figure 4.11 Photograph of the fabricated prototype [180]

### 4.5.3 Electromagnetic model of tunable filter-2

The proposed tuning strategy is further validated by implementing it on a fourth-order constant absolute bandwidth tunable cavity filter which was originally designed, fabricated, and measured in [181]. In [181], the tunable BPF is designed by in-line dual-post resonators where the resonance and coupling are tuned by the height of the posts. In the case of such an in-line dual-post resonator based BPF, input-output coupling and inter-resonator coupling vary inversely with a frequency which maintains a constant absolute bandwidth of the tBPF. As illustrated in Figure 4.12, post height $h_{11}$, $h_{12}$, $h_{21}$ and $h_{22}$ combinedly contribute to the tuning of the center frequency of the tBPF.

An EM-ANN model of the tBPF illustrated in Figure 4.12 should be developed prior to the data generation for the target tunable ANN model. This EM-ANN model will be used as a surrogate model during the hybrid optimization that accepts the posts' heights along with the frequency points as the inputs and provides the real and imaginary parts of $S_{11}$ and $S_{21}$ as the outputs. The training data generation for the EM-ANN model has been carried out in the following manner: $9GHz \leq Freq \leq 11GHz$ with 0.025GHz spacing, $6mm \leq h_{11}, h_{21} \leq 8mm$ and $5mm \leq h_{12}, h_{22} \leq 7mm$ with 1mm spacing. Therefore, a total 81 frequency sweep generates 6,561 sets of training data in three hours of HFSS simulation time. The EM-ANN model is developed with 5-45-45-4 neurons that achieves an average error of 5.9e-6 and 6.6e-6 for training and testing sets. After the completion of EM-ANN model training, the data generation process for target tunable ANN model training can be commenced as outlined in section IV.

The data generation time for training of target tunable ANN model was five minutes. The optimization boundary for $[h_{11}\ h_{12}\ h_{21}\ h_{22}]$ was set according to the developed EM-ANN model. Total 65 search agents with 150 maximum iteration were used during NGS-WOA and GWO process. The target tunable ANN model is developed with 5-20-20-4 neurons as illustrated in Figure 4.13. The target tunable ANN model achieves average error of 2.3e-9 and 2.8e-9 for training and testing sets, respectively. Once the model is trained, as mentioned in [181], seven tuning state variables in the form of $[f_1\ f_2\ f_3\ f_4\ f_5]$ is fed to the developed model which provides the tunable parameters as $[h_{11}\ h_{12}\ h_{21}\ h_{22}]$. This corresponding input and output variables from the developed model are given in Table IV and Table 4.5, respectively. The EM model generated S-parameters from a different set of outputs from Table 4.5 are plotted in Figure 4.14. These tuning performances illustrates similar EM simulated results from [181]. In fact, last three tuning states shows better

passband return loss as compared to [181]. Therefore, the proposed approach achieves the tuning parameters correctly for practical constant absolute bandwidth tBPFs.

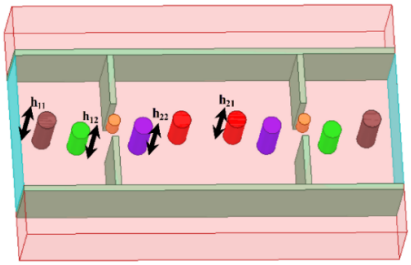


Figure 4.12 Electromagnetic model of a constant absolute bandwidth tunable BPF [181]

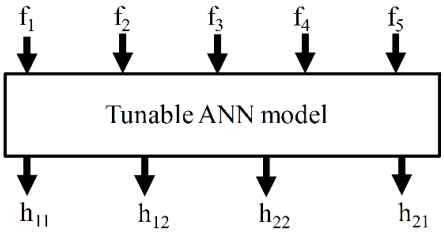


Figure 4.13 Target-tunable ANN model

Table 4.4 Different tuning state of tunable BPF-2 EM model (ANN inputs)

| State | $f_1$ (GHz) | $f_2$ (GHz) | $f_3$ (GHz) | $f_4$ (GHz) | $f_5$ (GHz) |
|---|---|---|---|---|---|
| 1 | 9.05 | 9.15 | 9.35 | 9.45 | 10.45 |
| 2 | 9.30 | 9.40 | 9.60 | 9.70 | 10.70 |
| 3 | 9.55 | 9.65 | 9.85 | 9.95 | 10.95 |
| 4 | 9.80 | 9.90 | 10.10 | 10.20 | 11.20 |
| 5 | 10.05 | 10.15 | 10.35 | 10.45 | 11.45 |
| 6 | 10.30 | 10.40 | 10.60 | 10.70 | 11.70 |
| 7 | 10.55 | 10.65 | 10.85 | 10.95 | 11.95 |

Table 4.5 Height of tuning posts of tunable BPF-2 (ANN outputs)

| State | $h_{11}$ (mm) | $h_{12}$ (mm) | $h_{21}$ (mm) | $h_{22}$ (mm) |
|---|---|---|---|---|
| 1 | 7.855 | 6.208 | 7.918 | 6.304 |
| 2 | 7.683 | 5.989 | 7.651 | 6.097 |
| 3 | 7.443 | 5.782 | 7.518 | 5.896 |
| 4 | 7.284 | 5.620 | 7.294 | 5.699 |
| 5 | 7.120 | 5.387 | 6.923 | 5.190 |
| 6 | 6.893 | 5.174 | 6.918 | 5.336 |
| 7 | 6.639 | 5.096 | 6.772 | 5.097 |

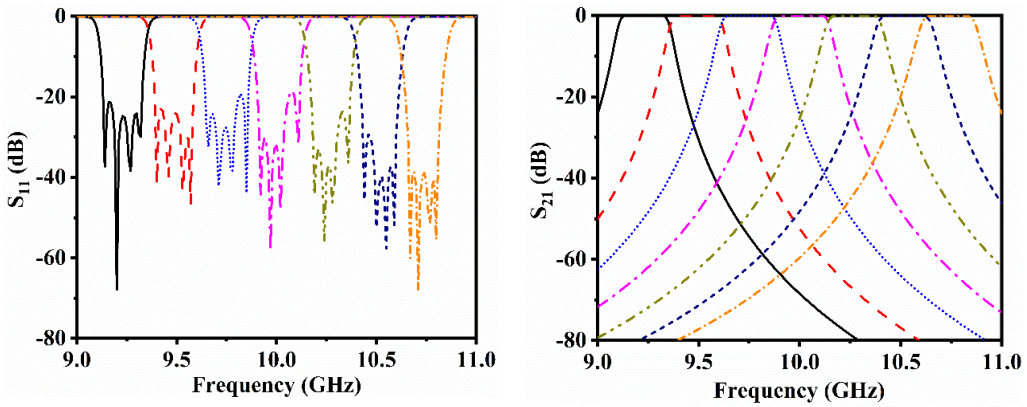


(a) (b)

Figure 4.14 Simulated performance from ANN model generated post heights of tunable BPF-2. (a) Reflection responses (b) Transmission responses

All these simulation works are conducted in the computer with Lenovo SR650 Xeon Gold 6150, 2.7 GHz (2 processors, 36 cores), 512GB RAM. All the developed ANN model is represented in the paper in X-$H_1$-$H_2$-Y format where X, $H_1$, $H_2$ and Y denote the number of neurons in each layer. The first and last layer is the input and output layer while others are hidden layers. All the ANN model uses the sigmoid activation function in the hidden layer and linear activation function in the output layer. We divide the total generated data for each ANN model into 80% and 20% for training and testing, respectively.

These three examples demonstrate the filter tuning methodology through the proposed development strategy of ANN model as depicted in Figure 4.2. These three examples of tBPF deal

with three to five tunable parameters which have been handled by the proposed algorithm efficiently. Practical tBPFs involve a manageable number of variables to cover the desired operating frequency band. On the other hand, pure theoretical tBPFs may consider many more variables to cover a wider frequency range with a fixed passband bandwidth. For example, keeping the design practicability in mind, the lumped element circuit in Figure 4.4 only considers the capacitances as variables while the inductors are kept fixed. From a pure theoretical point of view, to extend the desired frequency band, inductors can be also considered as variable which extends the total number of variables to ten. As the GWO, WOA and NGS-WOA can handle up to thirty variables of a single mathematical function [74], [79], [175], the proposed hybrid optimizer will be able to deal with such a larger set of variables too at the cost of a higher computational expense.

## 4.6 Related works and discussions

This paper presents a novel optimizer that is hybridized by two swarm-intelligence based algorithms and a mathematics-based algorithm. The proposed algorithm switches between NGS-WOA and GWO based on the cost minimization which is followed by the homotopy optimization for the best result.

To demonstrate the convergence behavior of different optimizers, we target three tuning states of the tBPF as illustrated in Figure 4.10. the cost function is defined as mentioned in section IV where passband return loss and stopband insertion loss are considered as 20dB and 30dB, respectively. The cost function achieved at the end of each optimization for 150 iterations is given in Table 4.6. The proposed algorithm takes 5 more steps for additional homotopy optimizations. Convergence curves of PSO, WOA, NGS-WOA, GWO and the proposed algorithm are all compared in Figure 4.15 for different target tuning state of the filter. Figure 4.15 depicts that the proposed hybrid algorithm outperforms the other state-of-the-art meta-heuristic algorithms. Figure 4.15 also shows that the proposed algorithm converges further, immediately from the best one between NGS-WOA and GWO. In some of the cases, NGS-WOA and GWO end up with poor cost function values because the matching conditions of S parameters cannot be satisfied even though the poles are close enough to each other in the expected passband. These types of global optimizers become slow when the current solution is in close proximity to the optimal solution. Therefore, these optimizers may require numerous iterations to reduce the cost function further, which is computationally expensive and time-consuming process. In such situations, the additional

homotopy method finds an exact match quickly, which is set to reduce the cost function value greatly. It is worth mentioning that the homotopy method alone is not compared in this case because the literature suggests that it works very well for a good set of initial parameters. If the initial parameters place the poles very far from each other, the homotopy method cannot get the optimal solution regardless of its number of steps.

The proposed strategy of data generated from the sequential tuning of filter structure provides a smooth transition of variables from one tuning state to another. This allows us to build a small-sized ANN model with one or two hidden layers for predicting the tunable parameters at a given tuning state of the filter. This data generation strategy works well for constant absolute bandwidth BPFs. For bandwidth tunable filters, the proposed strategy in Figure 4.2 can be modified a little bit at step 3 and step 4, respectively.

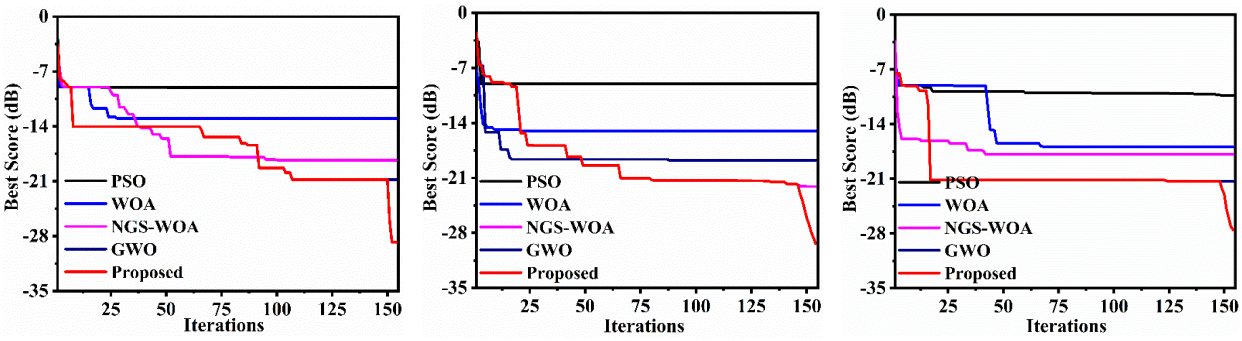


Figure 4.15 Convergence comparison between different optimizers at tuning (a) state-1 (b) state-2 (c) state-3

Table 4.6 Reduced cost function from different optimizers

| State | PSO (dB) | WOA (dB) | NGS-WOA (dB) | GWO (dB) | Proposed (dB) |
|---|---|---|---|---|---|
| 1 | -9.04 | -13.02 | -18.32 | -20.80 | -28.76 |
| 2 | -9.00 | -15.02 | -22.09 | -18.75 | -29.39 |
| 3 | -10.33 | -16.92 | -17.87 | -21.32 | -27.52 |

Two out of three demonstrated examples in this paper have tunable transmission zeros at finite frequencies. During the optimization at the data generation phase, the cost function is defined in terms of passband return loss level and stopband insertion loss level. Thus, the location of TZs does not affect the cost function values. Therefore, it is not possible to extract the tuning parameters at

a specific TZ configuration from this ANN model development strategy. Figure 4.7(b) illustrates such a scenario where the ANN inputs define three frequency tunable states in the form of $[f_1\ f_2\ f_3\ f_4\ f_5]$ and the ANN outputs provide the heights of three tunable vias corresponding to those tunable states. EM simulated S parameters from these three sets of tunable parameters illustrate that the first and third tunable states have the TZ in their lower side of the passband while the second tunable state has the TZ in its upper side of the passband.

The main novelty of this work is the proposed ANN model development strategy for tunable filters. The data generation process for such ANN model is assisted with a group of optimization algorithms. Such an optimizer assisted data generation algorithm has recently been proposed for coupling circuit parameter extraction [32]. In [32], the data generation algorithm starts with a set of initial circuit parameters that correspond to a given set of state variables. Therefore, to initiate the algorithm, the appropriate circuit parameters of a certain state variable should be known beforehand. Moreover, the optimization algorithm-generated circuit parameters are fed back to the data generation algorithm for the next optimization state of the coupler circuit. The accuracy of such a loopback system depends on circuit parameter calculation at each stage. If a single optimization routine fails to extract accurate circuit parameters, the whole data set for ANN training can be erroneous due to the cascaded feeding of inaccurate parameters. Furthermore, only homotopy optimization algorithm is used to generate the training data. Such a local optimizer only works well if the initial guess is good enough to find the local optima. Hence, the data generation algorithm in [32] has drawbacks of initial guess, loopback circuit parameters and a single local optimizer. To overcome these shortcomings, an advanced data generation algorithm with a novel technique of optimizer hybridization is proposed in this work. This hybridization of swarm-intelligence algorithm and homotopy method eliminates the necessity of initial guess. In addition, there is no loopback system involved in this algorithm which guarantees much more accurate data sets for ANN model training. Besides, the NGS-WOA and GWO operate over different optimization problem along with the homotopy method, which provides accurate training data sets as the NGS-WOA and GWO complement each other. Indeed, this fully automated hybrid technique brings the strengths of all these three optimizers together and provide a complete set of smooth training data, which is the key to develop an accurate and fast ANN model.

## 4.7 Conclusion

In this paper, for the first time, metaheuristic optimization algorithms are hybridized with the homotopy optimization method to get the tunable parameters for different tuning states of filter. An ANN model development strategy is also proposed where the data generation is automated with a hybrid optimizer. The NGS-WOA and GWO algorithm is initially employed for the optimization of a tunable filter. Variables calculated from one of these algorithms is fed to a homotopy optimization algorithm as a good set of initial value, which guarantees a good set of optimized parameters for the desired tunable state of the filter. The proposed hybrid optimization technique will be useful for any microwave circuits regardless of the total number of design parameters. Three design examples are given to demonstrate the ANN model development technique based on a hybrid optimizer, including a theoretical mixed coupled fifth-order lumped element tBPF, a practical fourth-order dual mode tBPF and a practical fourth-order dual-post resonator based tBPF. Tunable ANN model generated parameters are further used to compare the simulation and measurement results which show a good agreement between each other.

# CHAPTER 5 ARTICLE 4: ANN-ENABLED MAPPING BETWEEN EQUIVALENT CIRCUIT MODEL AND PHYSICAL FIELD MODEL FOR TUNABLE BANDPASS FILTER

Chandan Roy and Ke Wu

Published in the *IEEE MTT-S International Conference on Numerical Electromagnetic and Multiphysics Modeling and Optimization (NEMO'2023)*, 18 April 2023

In this paper, an ANN model development approach is outlined and studied for the development of tunable bandpass filter (tBPF). Circuit models are fast and efficient for design and optimization while physical models based on electromagnetic full-wave fields are accurate but computationally expensive and slow. In this work, an equivalent circuit model is developed from a full-wave tBPF structure. Then, equivalent circuit parameters are generated and mapped to tunable geometric parameters of the physical field model of the tBPF. The optimization is thus carried out on the equivalent circuit model. Finally, the geometric parameters are obtained by the ANN model from the optimized equivalent circuit parameters. A practical example of tBPF is used to demonstrate the proof of concept.

## 5.1 Introduction

Tunable and reconfigurable microwave circuits have been a prime topic of interest because of an ever-increasing demand of multi-standard and multi-band wireless communication and sensing multifunction systems. Majority of studies on tunable filter are focused in terms of its physical realization of tuning and switchable elements. Various types of single-band and multiband tunable filters have been reported based on electrical, mechanical, and magnetic tuning [186], [162], [165]. In addition, advanced design tools were developed for the design of tunable filters such as aggressive space mapping (ASM) [138], parallel space mapping [129], and cognition-driven space mapping [139]. However, very few works have been carried out to formulate such tuning mechanisms in an equation-based analytical model. Recently, advanced optimizer-assisted ANN models have been used to extract the tuning parameters of tunable filters [33], [41].

Equivalent lumped element circuit can provide a clear idea of a passive microwave structure on electrical behavior. Such a circuit can mimic the field behavior of a particular physical structure without resorting to heavy computational load and long CPU time. Full-wave electromagnetic

(EM) models, on the other hand, are generally computationally expensive and time consuming. A direct optimization of such a physical structure would take a long period of time. Therefore, it would be good to run any optimization algorithm on a lumped element equivalent circuit model and then to transform the optimized equivalent circuit parameters to the geometric parameters of a full-wave physical structure. Space mapping (SM) technology [49] provides us with such a platform which makes use of a coarse model of a target fine model. The coarse model has inaccuracy issue for high frequency applications. Therefore, the coarse model may not be used for high frequency structures.

In this work, the lumped element equivalent circuit of a target tunable filter is studied and developed based on its full-wave structure. Then, an ANN model is formulated for mapping between circuit parameters and geometric parameters. Once the ANN model is set up, the optimization algorithm is employed to find out the optimized equivalent circuit parameters. Finally, these circuit parameters are transformed into the tunable geometric parameters of the target tBPF. The proposed methodology is validated by the example of a tunable circular cavity bandpass filter.

## 5.2 Equivalent circuit model and ANN model

To map circuit model parameters to physical model parameters via an EM full-wave model, it is necessary to develop an accurate circuit model of the corresponding EM model structure. The first step to develop an equivalent circuit model from a physical field model is to divide the complete structure into elementary discontinuities and transmission line sections. The transmission lines can be represented by a series or parallel combination of reactive elements. On the other hand, different elementary discontinuities are characterized by a fundamental T or π section of network. Before finding an appropriate network section of a discontinuity, the field model for that particular elementary discontinuity should be setup in a commercial EM simulator and calculated responses should be calibrated. Such numerical calibration is required to eliminate any introduced numerical noise by external ports. Thru-reflect line (TRL) and short-open (SOC) calibration techniques have been widely used among available numerical calibration techniques in the literature [187], [188].

In this work, an SOC is used for all case studies. Once the elementary discontinuities are characterized with T or π section of network, the mutual coupling between them can be characterized by reactive elements. For low-frequency quasi-TEM mode applications, such mutual couplings can be ignored. However, for high frequency applications, such mutual couplings may

affect circuit performance significantly. Appropriate circuit element can be found by the consistency of extracted circuit parameters over a frequency range of interest. After successfully finding all the equivalent circuit sections for the discontinuities as well as the mutual couplings, a complete circuit model can be developed.

The ANN model used in this work is a multilayer perceptron (MLP) which is a commonly used architecture [31]. Here the neurons are arranged in layer by layer. The input and output layers are first and last layers while other layers are known as hidden layers. The neurons between adjacent layers are connected with a weight and a bias term is added to each neuron. The input to the input layers are presented in a vector form which are calculated along the layers by a feedforward computation. The sigmoid function $\sigma$ is used as the activation function in the hidden neurons while a linear activation function is used in the output layer of the ANN models in this work. Levenberg-Marquardt's algorithm (LMA) [156] is used for training the target ANN model as a fast and efficient algorithm for small-sized networks.

## 5.3 ANN model development algorithm

The ANN model development and its validation for the mapping between equivalent circuit parameters and geometric tunable parameters are conducted by the following few steps. These steps include accurate circuit model development, ANN model training, circuit model optimization, and model verification. These steps are illustrated as a flowchart in Figure 5.1 and explained below:

1. Identify different elementary discontinuities in the target tunable filter structure. Setup a full-wave EM model for a particular discontinuity in a commercial software package. Numerically calibrate the EM model-generated S parameters for the next stage of circuit model development.
2. From the calibrated-S parameters, develop T or $\pi$ section of network that represents a field behavior of the target discontinuity accurately over the interested frequency range. These steps are repeated until all the elementary discontinuities are modeled accurately by respective T or $\pi$ section of networks.
3. Cascade each two neighboring discontinuities and simulate the EM model. Find out the first order mutual coupling network in the form of T or $\pi$ section of network from the calibrated-S parameters. Higher-order mutual couplings are ignored as their impact on circuit performance is insignificant.

4. Finalize the complete equivalent circuit model from all the elementary discontinuities and first-order mutual couplings.
5. Start data generation process by simulating the target EM model structure with different set of tunable parameters. Extract the corresponding circuit parameters in all the cases from calibrated-S parameters. Store these data sets for ANN model training.
6. Build and train the ANN model with the data set generated in step 5. Consider the equivalent circuit parameters as inputs and geometric tunable parameters as outputs of the ANN model.
7. Define the cost function and implement any optimization algorithm on the equivalent circuit model to achieve the optimized circuit parameters that satisfy the desired circuit performance.
8. Use the trained ANN model to calculate the tunable geometric parameters against the optimized circuit parameters. Finally, verify the ANN model calculated tunable geometric parameters by a commercial EM model simulator.

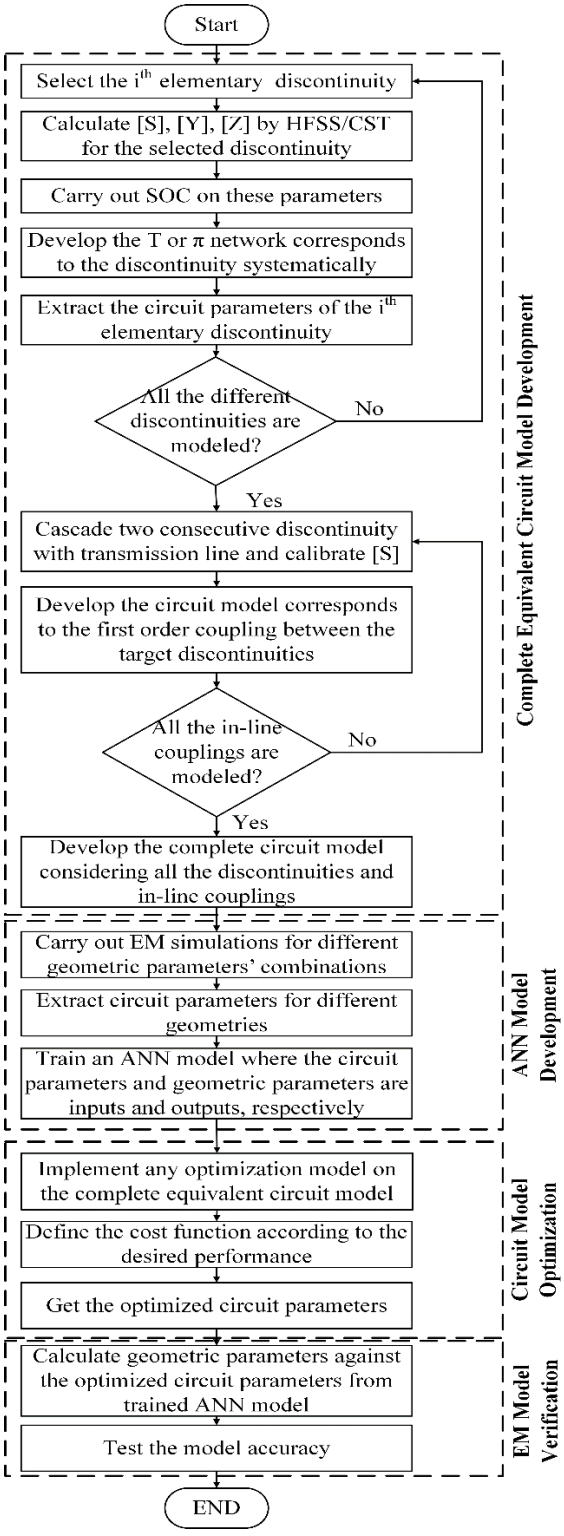


Figure 5.1 Flowchart of the complete model development procedure

## 5.4 Design example

The design example in this work illustrates the modeling of a frequency tunable circular cavity filter [189], shown in Fig. 2(a). In this tunable filter, only the resonant frequency of each resonator is tuned by inserting and rotating a dielectric plate inside the cavity resonators. The first step of finding the equivalent circuit model starts with the equivalent network development of the coupling slot in [189]. The suitable coupling network is found as a π-network with series capacitance and shunt inductances. The shunt inductances are get absorbed in the surrounding resonator circuits. The couplings of this tBPF remain fixed. Therefore, only the parallel LC network is considered as variables for the resonant frequency tuning. The EM model of the target tBPF and developed equivalent circuit model are shown in Fig. 2(a) and Fig. 2(b), respectively. It illustrates that the EM model has 2 rotating dielectric plates (rotational angle of the first and fourth resonator is $\theta_1$ while $\theta_2$ implies the second and third resonators' rotational angle) as variables where the equivalent circuit has 4 variables ($L_1$, $C_1$, $L_2$, and $C_2$). Therefore, the target ANN model will have 4 input neurons for equivalent circuit parameters and 2 output neurons for rotating dielectric plates. To generate the training and testing data for the ANN model development, the rotational angles of two different dielectric plates are varied from $0^0$ to $180^0$ at $5^0$ interval. Rest of the geometric parameters are preserved as the same as mentioned in [189]. Therefore, total $36 \times 36 = 1296$ frequency sweeps for the target tunable BPF were carried out in HFSS. Each frequency sweep has 81 frequency points over 18–21 GHz. For each EM simulation, equivalent circuit parameters are extracted from the numerically calibrated-S parameters. Once all the circuit parameters are extracted from all the EM simulations, the ANN model is trained. We use 80% and 20% data for training and testing of the target ANN model, respectively. We use 2 hidden layers where each hidden layer consists of 40 hidden neurons. Figure 5.3 illustrates the developed ANN model that achieves an excellent accuracy with only 1% fitting error.

After the successful ANN model development, we implement the well-known quasi-newton optimization algorithm on the developed equivalent circuit model of the target tBPF. The cost function is defined as formulated in [31]. This cost function is formulated in terms of four frequencies as $[f_1, f_2, f_3, f_4]$, where $f_2$ and $f_3$ are passband edge frequencies while $f_1$ and $f_4$ are stop band-edge frequencies. For different target passbands, the cost function parameters will be changed accordingly. The optimization algorithm provides us with the optimized equivalent circuit

parameters against the desired performance of the tBPF at certain tuning stages. The three target tuning states of the tBPF are defined as [19.0 19.2 19.4 19.6], [19.3, 19.5, 19.7, 19.9] and [19.5, 19.7, 19.9, 20.1]. All the frequencies are in GHz. The optimized equivalent circuit parameters calculated from the optimization model are listed first. Finally, the tunable parameters of the target EM model of the tBPF are computed by the developed ANN model against three desired tuning states. The equivalent circuit parameters and tunable parameters of the EM model against three desired tuning states are given in Table 5.1. The fixed circuit parameters in Figure 5.2 are $C_a = 2pF, C_b = 0.1pF \; and \; C_c = 0.05pF$, respectively. The HFSS simulated EM model S parameters with these tunable parameters are illustrated in Figure 5.4. Even though the designed tBPF is of fourth order, Fig. 4 shows only two poles in the passband because of its narrowband characteristics. These S parameters at different tuning states illustrate similar performance to the actual fabricated filter in [189]. Therefore, the proposed methodology for the mapping of the circuit model parameters to the EM model parameters is useful for tunable filter designers.

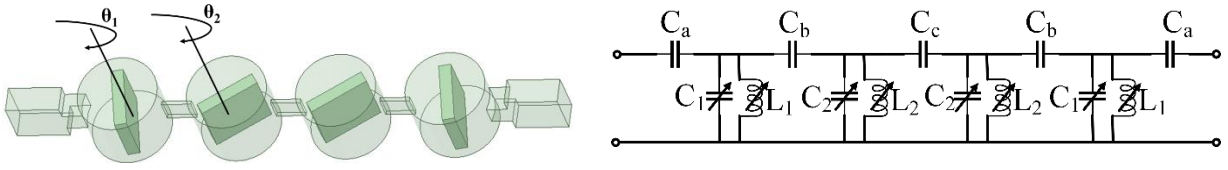


(a) (b)

Figure 5.2 Target tBPF (a) EM model [189] (b) Equivalent circuit model

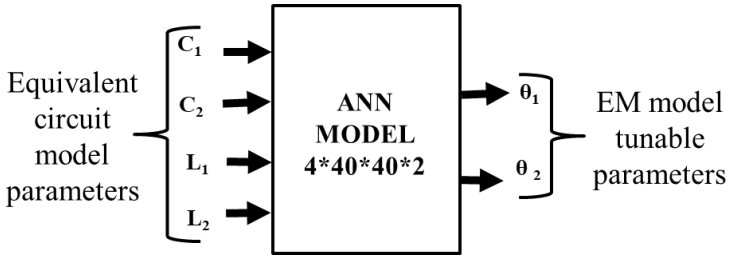


Figure 5.3 Target ANN model for equivalent circuit parameters mapping to EM model tunable parameters

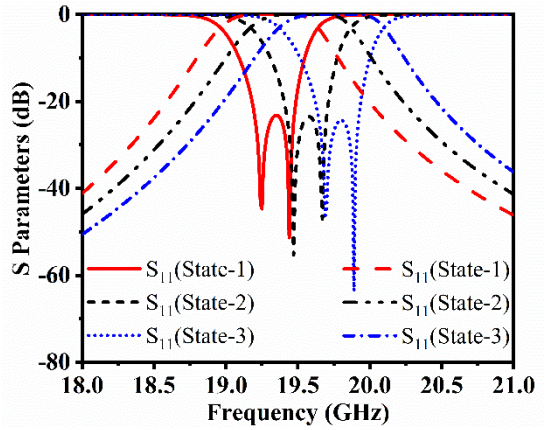


Figure 5.4 HFSS generated S Parameters of the target tunable filter at different tuning states

Table 5.1 EM model tunable parameters against equivalent circuit model parameters at different tuning states

| Tuning State | Equivalent circuit parameters | | | | Tunable EM model parameters | |
|---|---|---|---|---|---|---|
| | $C_1$ (pF) | $C_2$ (pF) | $L_1$ (nH) | $L_2$ (nH) | $\theta_1^0$ | $\theta_2^0$ |
| 1 | 2.28 | 1.89 | 0.027 | 33.91 | 28 | 32 |
| 2 | 2.23 | 1.86 | 0.029 | 33.66 | 30 | 35 |
| 3 | 2.26 | 1.82 | 0.028 | 33.63 | 33 | 39 |

## 5.5 Conclusion

The proposed mapping between equivalent circuit parameters and EM physical tunable parameters provides us with a systematic design guideline of tunable filters. A small discrepancy in the demonstrated example with fabricated sample suggests that the equivalent circuit model development requires further considerations such as loss and other parasitic effects. A further detailed study of the proposed technique will allow us to develop accurate equivalent circuit model of any target EM model structures for high frequency applications. Consequently, the ANN model will successfully map the optimized equivalent circuit parameters to the critical geometric parameters of the target EM model.

# CHAPTER 6 ARTICLE 5: A GENERALIZED CIRCUIT MODEL DEVELOPMENT APPROACH WITH SHORT OPEN THRU (SOT) DE-EMBEDDING TECHNIQUE AND ITS APPLICATIONS

Chandan Roy and Ke Wu

Accepted in the *IEEE Transactions on Microwave Theory and Techniques*, 10 June 2023

A short-open-thru (SOT) numerical de-embedding technique is proposed and studied in this work. In particular, a generalized methodology for circuit model development is derived for the extraction of accurate circuit parameters over a wide range of frequency. The entire de-embedding process is described, and the circuit model development strategy is explained step-by-step. A variety of electrically small planar circuit elements, such as microstrip line (MSL) gap discontinuities, step discontinuities, and via-holes in two-layered substrate discontinuities, are numerically de-embedded and extracted conventional circuit model parameters are compared with results generated by a recently published short-open-load (SOL) technique. In addition, the circuit parameters extracted by the proposed generalized decomposition technique are comparatively studied through both SOT and SOL methods. The outcomes confirm that the circuit parameters extracted by the proposed circuit model has better model behavior over a wide range of frequency as opposed to those coming out of its conventional counterpart. Furthermore, the SOT technique-based circuit parametrization provides better stability as compared to the SOL scheme. Numerical convergence over a wide range of frequency is demonstrated for each example. Finally, a third-order Chebyshev end-coupled filter is designed by the proposed technique. Its equivalent circuit model, full-wave electromagnetic S-parameters simulation, and measured results have validated the approach.

## 6.1 Introduction

Due to the growing larger-scale and higher-density integration of diversified structures (planar and non-planar) and functional elements (passive and active) in recent wireless circuits and systems at higher frequencies, accurate electromagnetic modeling of circuits for system design, analysis, and optimization is beefing up day by day. The implementation of a highly reliable numerical calibration technique in full-wave electromagnetic (EM) simulator is an efficient strategy to generate a “noiseless” field model (S-parameters, e.g.), then leading to a highly accurate circuit

model characterized by circuit parameters (LCRG, e.g.) [9].

The understanding of the electromagnetic nature of any given physical layout for the optimized/accurate design and development of state-of-the-art RF/microwave and millimeter-wave circuits such as multifunction modules requires the generation of its high-fidelity equivalent circuit model based on lumped circuit elements and/or distributed transmission lines [188]. On the other hand, an accurate equivalent circuit topology is critical, which is set to characterize the corresponding physical layout such as discontinuities. Generally, the extracted lumped elements of such a circuit topology should be dispersion-less over a wide frequency range so that the circuit model genuinely represents the corresponding discontinuity.

To implement a numerical calibration technique, the whole circuit of interest should be partitioned into a few sections including targeted electrically small circuit elements or structure discontinuities, input and output feed lines [9]. Afterwards, each of these sections will be formulated and characterized by corresponding transmission or chain matrix. Finally, numerical noises introduced by unphysical excitations, modeling approximations, and feed networks will be extracted and removed through the use of multiple numerical standards [9]. This is the application of a calibration process in numerical modeling similar to practical measurement. In [188], a short-open numerical calibration (SOC) technique was realized on the de-embedding of unbounded electrically small microstrip discontinuity by utilizing an impressed voltage source-based two and half dimensional method of moment (MoM) algorithm [190]. In [191], a numerical SOC method was used in a full-wave finite-element method (FEM) algorithm for the accurate extraction of circuit parameters for different 3-D non-planar periodic guided-wave and discontinuity structures. In microwave measurements, the well-known thru-reflect-line (TRL) calibration technique [187] was adopted [192] in conjunction with a full-wave MoM commercial simulator for the circuit parameter extraction of planar discontinuities so to obtain their equivalent circuit models. A hybrid algorithm of domain decomposition finite-difference time-domain (DD-FDTD) and numerical thru-line (TL) calibration technique was developed for accurate parameter extraction of microwave circuits [193]. In [194], a short-open-load (SOL) calibration technique was deployed for the electromagnetic modeling of a circuit system through the use of the full-wave HFSS EM simulator with a detailed parameter extraction process.

These calibration methods have been successfully applied to numerically deembed different circuit

parameters through the removal of numerical noises for various electromagnetic TEM-mode and non-TEM mode structures [9]. For example, the SOC technique was used to de-embed the complex propagation constant of half-mode substrate integrated waveguides (HMSIW) [195]. The SOL technique was deployed for the de-embedding of effective wave impedances of SIW structures [196]. The SOC technique was applied in [197] for the investigation of a variety of periodic coplanar waveguides (CPWs) with inductive loading. The equivalent-circuit models of different finite-ground coplanar waveguides (FGCPW) were developed and characterized [198]. In [199], lumped-element circuit models of various coplanar strip-line (CPS) circuits were proposed and studied. Furthermore, a variety of sophisticated or complex structures were examined through numerical calibration models. For instance, a joint field/circuit model was demonstrated in [200] for the characterization of a class of line-to-ring coupling structures. A circuit model of microstrip interdigital capacitor (IDC) was proposed in [201] for the design of innovative quasi-lumped miniaturized filters. Moreover, different radiating structures were also modeled for accurate electrical representation. In [202], a circuit model of a microstrip fed slot radiator was developed with arbitrary slot width for the first time, as opposed to conventional geometrical assumptions of either narrow or wide slot scenario. A circuit model of a CPS fed printed dipole radiator was proposed using the SOC scheme [203]. These successful applications of numerical calibration methods provide highly accurate and reliable circuit models with noise-free parameters over a wide frequency range which makes the design and optimization of different structures much easier.

Indeed, the TRL, SOC and SOL calibration methods have widely been used with different sets of numerical standards as compared to other available calibration techniques in the literature. The popular TRL calibration technique suffers from singularity issue as the electrical lengths of “thru” and “line” standards differ by integer multiples of a half-guided wavelength. Multiline TRL (M-TRL) calibration is similar to the TRL method, which has widely been used in microwave and RF measurements to determine the characteristics of a DUT [204]. It involves the use of a group of transmission lines to construct a reference plane that establishes a predetermined set of impedances and delay values at specific points throughout the measurement system. This scheme is set to ensure accurate and reliable measurements, and it requires measurements to be taken at multiple frequencies, thus allowing the measurement system to be characterized over a range of frequencies. Thru-Line (TL) is also a well-known calibration method for RF/microwave measurements [155], which has advantages of simplicity, accuracy, and repeatability. The well-known SOC technique

relies on the accurate calculation of current and/or voltage distributions over the structure of interest (usually at the input and output terminal) of feed lines. Such terminal voltage and current values can be regarded as the equivalent third standard for calibration in addition to the short and open standards. They can only be obtained accurately from in-house codes which are usually unavailable to the users of a commercial full-wave EM simulator. On the other hand, the recently proposed SOL calibration technique employs one matched-load standard along with the short and open standards, which were implemented with a perfectly matched layer (PML), perfectly electric wall, and perfectly magnetic wall, respectively, in commercial full-wave electromagnetic simulators [194]. The transmission or chain matrix of each error box in SOL involves the characteristic impedance ($Z_0$) of infinitely long uniform transmission feed lines. The quasi-TEM microstrip lines will manifest inaccuracy at high frequencies because of dispersion effects in connection with the involvement of $Z_0$. Overall, these available calibration techniques, which require 3 different standards including one equivalent standard, generally suffer from limited bandwidth, implementation difficulty, and inaccuracy issue (numerical stability). In addition, the parameter extraction through all of those numerical calibration techniques has been made with a specific circuit model for a given structure geometry. This is because experienced researchers and designers can easily identify and derivate appropriate circuit models through structural capacitive and inductive effects, for example, for conventional discontinuities or junctions or bends. This is not true anymore for arbitrary and complex physical structure whose circuit models may be frequency-band-dependent. Therefore, a universal and robust modeling strategy is needed for automated generation of circuit models for any given electromagnetic structures.

Inspired by the SOL technique in [194], the thru standard is paired with short and open standards in our work. In this way, such three standards are set to de-embed a device under test (DUT) or a structure discontinuity without employing the $Z_0$ term, which is considered as the origin of inaccuracy for broadband and high frequency applications. The proposed short-open-thru (SOT) numerical de-embedding technique is implemented on the full wave electromagnetic simulators such as HFSS and CST for the modeling of targeted circuits made of elementary discontinuities. In addition, a holistic circuit model development strategy is proposed and studied for accurate automated circuit representation from 3D discontinuity over a wideband frequency range. Both the conventional and proposed equivalent circuit models of microstrip steps, gaps and via-hole discontinuities in two-layered substrate structures are numerically de-embedded with the proposed

SOT technique. Extracted circuit parameters are discussed and compared with published numerical counterparts. Finally, a simple third-order Chebyshev end-coupled filter is designed by the proposed technique as its experimental validation.

## 6.2 Numerical SOT de-embedding technique

A variety of complex geometric two-port circuit structures can be numerically modeled with different excitation mechanisms at their external ports. To achieve accurate characteristics of the core circuit, the complete structure should be partitioned into three parts, namely, the core circuit network along with the two feed networks at input and output sides. These feed networks are usually represented by error boxes, which include the port mismatch effects, numerical approximations, and discontinuity errors in the modeling. The role of calibration technique is to eliminate the effects of error boxes from the whole structure through the extraction of error boxes with the application of selected numerical standards before the actual modeling of a real circuit problem. To appreciate interesting features of the proposed SOT technique, the TRL and SOC techniques are briefly discussed as follows.

### 6.2.1 TRL calibration

To begin with, the S-matrix parameters at input and output ports are obtained by an electromagnetic simulator such as MoM, FEM, FDTD, etc. Then, the S-matrix is converted to the corresponding transmission matrix $[M]$, which is expressed in terms of two error boxes$[M_{EB1}]$ and $[M_{EB2}]$ as in (6.1). A standard TRL calibration procedure is then carried out where the discontinuity and feeding lines are considered as structure under modeling (SUM, equivalent to DUT for measurements) and two error boxes, respectively. The transmission matrices of thru and line standards are denoted as $[M_T]$ and $[M_L]$ while their relationships with the error boxes are expressed as (6.2) and (6.3). One can calculate the S-matrices for the two-ports thru, line connections and reflection coefficients of one-port reflect connection, namely, $S_{11R}$ and $S_{22R}$. Then, the first two S-matrices can be converted into their related cascading transmission matrices $[M_T]$ and $[M_L]$. Based on the cascaded network topologies, eight parameters of the two error boxes can be calculated in terms of $[M_T]$, $[M_L]$, $S_{11R}$, and $S_{22R}$ [6]. Finally, the transmission matrix of the core circuit is determined from (6.4).

$$[M] = [M_{EB1}] \cdot [M_0].[M_{EB2}] \tag{6.1}$$

$$[M_T] = [M_{EB1}] \cdot [M_{EB2}] \tag{6.2}$$

$$[M_L] = [M_{EB1}].\begin{bmatrix} e^{-\gamma l} & 0 \\ 0 & e^{\gamma l} \end{bmatrix}.[M_{EB2}] \tag{6.3}$$

$$[M_0] = [M_{EB1}]^{-1}[M][M_{EB2}]^{-1} \tag{6.4}$$

### 6.2.2 SOC technique

In the case of an SOC calibration, the port voltage and current are defined while the current at the reference plane is calculated. For the short standard as illustrated in Figure 6.1(b), the reference plane voltage is zero while the current only is to be obtained. As far as the open standard is concerned, the reference plane current is set to zero as depicted in Figure 6.1(c). The relation between the excited fields and the remaining two elements of the error boxes are established as the reference plane voltages are cumbersome to calculate in an MoM algorithm. The two error boxes are considered as a reciprocal two-port network, which brings an additional condition for calculating all the eight transmission-matrix elements of the input and output error boxes [188].

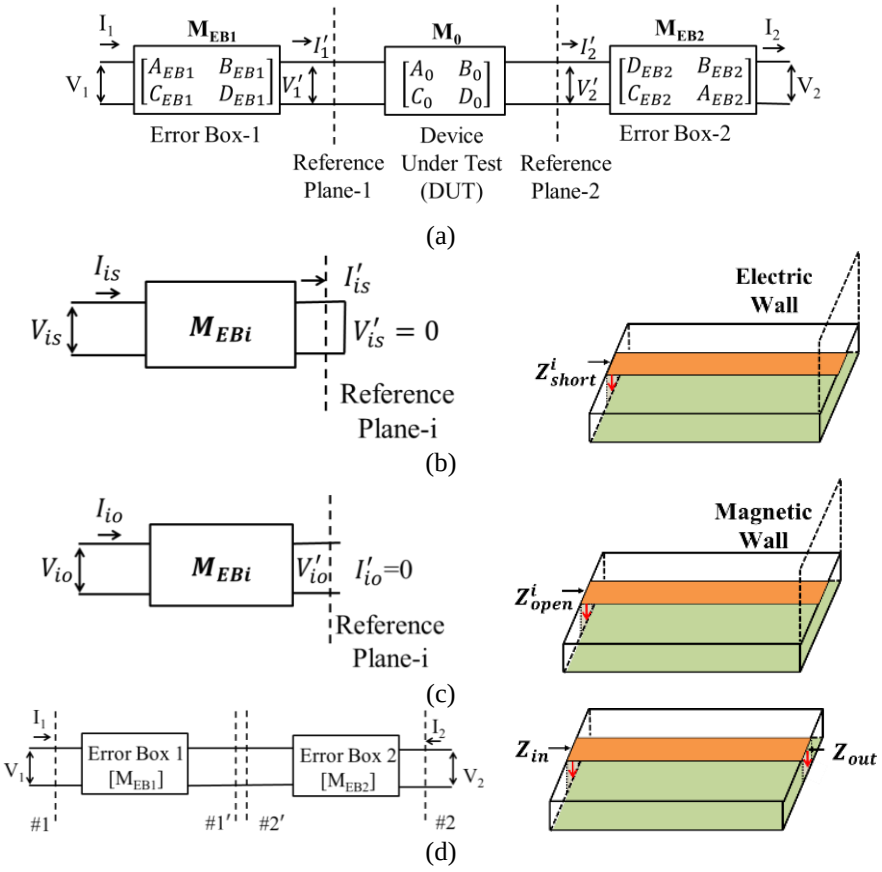


Figure 6.1 Schematic of SOT methods with cascaded equivalent error boxes and 3D geometries: (a) The whole equivalent circuit representation; (b) Equivalent short-end circuit standard for ideal

SOC and SOT techniques; (c) Equivalent open-end circuit standard for ideal SOC and SOT techniques. (d) Equivalent thru connection standard of SOT technique

### 6.2.3 Implementation of the proposed SOT method

As briefly explained above, the TRL calibration is easy to implement, the line standard expression in (6.3), however, involves the complex propagation constant term that adds up significant errors at higher frequencies. On the other hand, to implement the SOC technique from [188], the user needs access to the field qualities of the structures through a complete code package of MoM algorithm, which is not readily available for users. In this work, the thru standard along with the short and open standards is formulated to form the proposed short-open-thru (SOT) technique. This three-standard calibration technique is set to create a flexible numerical calibration procedure that can effectively avoid the dispersion-related inaccuracy problem at high frequencies. The SOT technique can be implemented in the full-wave HFSS electromagnetic software in this work or other similar commercial electromagnetic simulation packages.

Let's formulate the proposed SOT technique through the following description. Figure 6.1(a) illustrates the whole equivalent circuit. To obtain the whole two-port reciprocal transmission matrix of input and output error boxes, the so-called "short" and "open" standards in the SOC are described at the reference plane along the feed section, as illustrated in Figure 6.1(b) and Figure 6.1(c). The ideal short and open circuit conditions of the equivalent circuit are guaranteed by considering the perfect electric and magnetic walls in the HFSS software. The input impedances are calculated under the short and open standards to develop a relationship among circuit parameters of the error boxes in the following manner [194]

$$Z_{shi} = \frac{B_{EBi}}{D_{EBi}} \tag{6.5}$$

$$Z_{opi} = \frac{A_{EBi}}{C_{EBi}} \tag{6.6}$$

Here, $Z_{shi}$ and $Z_{opi}$ denote the input impedances while short and open standards are applied to the reference plane, respectively. As a supplemental condition to calculate the complete transmission matrix of the input and output error boxes, the thru standard is used as shown in Figure 6.1(d). The thru standard can be expressed in terms of all the elements of each error box as follows,

$$\begin{bmatrix} A_T & B_T \\ C_T & D_T \end{bmatrix} = \begin{bmatrix} A_{EB1} & B_{EB1} \\ C_{EB1} & D_{EB1} \end{bmatrix} \begin{bmatrix} D_{EB2} & B_{EB2} \\ C_{EB2} & A_{EB2} \end{bmatrix} \tag{6.7}$$

Here, the left side of (6.7) denotes all the four elements of the thru standard that can numerically be derived from HFSS software for the two-ports thru connection. The multiplication of matrices in (6.7) provides us with the following four sets of linear equations:

$$A_T = A_{EB1}D_{EB2} + B_{EB1}C_{EB2} \tag{6.8}$$

$$B_T = A_{EB1}B_{EB2} + A_{EB2}B_{EB1} \tag{6.9}$$

$$C_T = C_{EB1}D_{EB2} + C_{EB2}D_{EB1} \tag{6.10}$$

$$D_T = B_{EB2}C_{EB1} + A_{EB2}D_{EB1} \tag{6.11}$$

Equation (6.5) and (6.6) can be written separately for the two error-boxes as follows.

$$B_{EB1} = Z_{sh1}D_{EB1} \tag{6.12}$$

$$B_{EB2} = Z_{sh2}D_{EB2} \tag{6.13}$$

$$A_{EB1} = Z_{op1}C_{EB1} \tag{6.14}$$

$$A_{EB2} = Z_{op2}C_{EB2} \tag{6.15}$$

In addition, as each error box is defined as a reciprocal two-port network, one more condition is considered to calculate all the four transmission-matrix elements of each error box as

$$A_{EB1}D_{EB1} - B_{EB1}C_{EB1} = 1 \tag{6.16}$$

$$A_{EB2}D_{EB2} - B_{EB2}C_{EB2} = 1 \tag{6.17}$$

This linear reciprocity condition is imposed on the two-port networks as only linear reciprocal cases are concerned in the calibration process, which do not contain any active devices or non-reciprocal media such as ferrites or plasmas [155]. Such linear reciprocal networks are commonly used for de-embedding passive circuits [188], [194].

$A_{EBi}$ and $B_{EBi}$ are expressed in terms of $C_{EBi}$ and $D_{EBi}$ in equations (6.12) - (6.15) that establish a relation between $C_{EB1}$ and $D_{EB1}$ by using (6.16) as

$$C_{EB1}D_{EB1} = \frac{1}{Z_{op1} - Z_{sh1}} \tag{6.18}$$

Let's consider (6.11) and replace $A_{EB2}$ and $B_{EB2}$ by $C_{EB2}$ and $D_{EB2}$ from (6.13) and (6.15).

$$C_{EB1}D_{EB2} = \frac{D_T}{Z_{sh2}} - \frac{Z_{op2}}{Z_{sh2}}C_{EB2}D_{EB1} \tag{6.19}$$

In consideration of (6.19) in (6.10), the relation between $C_{EB2}$ and $D_{EB1}$ can be arranged as

$$C_{EB2}D_{EB1} = \frac{D_T - C_T Z_{sh2}}{Z_{sh2} - Z_{op2}} \tag{6.20}$$

Substituting (6.20) in (6.19) leads to the following relation between $C_{EB1}$ and $D_{EB2}$

$$C_{EB1}D_{EB2} = \frac{D_T - C_T Z_{sh2}}{Z_{op2} - Z_{sh2}} \tag{6.21}$$

Let's divide (6.21) by (6.18) and consider $D_{EB1} = 1$ to find $D_{EB2}$, which can be expressed by

$$D_{EB2} = (C_T Z_{op2} - D_T)\left(\frac{Z_{op1} - Z_{sh1}}{Z_{op2} - Z_{sh2}}\right) \#(6.22)$$

We can then obtain $C_{EB1}$ and $C_{EB2}$ from (6.18) and (6.20) as

$$C_{EB1} = \frac{1}{Z_{op1} - Z_{sh1}} \tag{6.23}$$

$$C_{EB2} = \frac{C_T Z_{sh2} - D_T}{Z_{op2} - Z_{sh2}} \tag{6.24}$$

Once $C_{EBi}$ and $D_{EBi}$ are derived, we can calculate $A_{EBi}$ and $B_{EBi}$ from (6.14), (6.15), (6.12), and (6.13).

In general, the error box can be given by using the SOT method as

$$[M_{EBi}] = \begin{bmatrix} \frac{Z_{opi}.P^{i-1}}{Z_{opi} - Z_{shi}} & Z_{shi}.Q^{i-1} \\ \frac{P^{i-1}}{Z_{opi} - Z_{shi}} & Q^{i-1} \end{bmatrix} \tag{6.25}$$

$$P = C_T.Z_{sh2} - D_T \tag{6.26}$$

$$Q = \frac{Z_{op1} - Z_{sh1}}{Z_{op2} - Z_{sh2}}.\left(C_T.Z_{op2} - D_T\right) \tag{6.27}$$

The transmission matrix of the input and output error box can be determined from (6.25)-(6.27), which is utilized afterwards for the numerical calibration of a two-port circuit or discontinuity having two arbitrary feed networks. Finally, the transmission matrix of the core circuit is de-embedded from (6.4).

In case of an identical feeding two-port circuit, $Z_{op} = Z_{op1} = Z_{op2}$ and $Z_{sh} = Z_{sh1} = Z_{sh2}$. Consequently, as a symmetrical circuit, the two error boxes will have the same ABCD matrix [205], [206], i.e., $M_{EB1} = M_{EB2} = M$. The four matrix elements of the core circuit $A_0, B_0, C_0 and\ D_0$ are

expressed in terms of the four matrix elements of the whole two-port circuit $A, B, C\ and\ D$ as follows.

$$A_0 = \frac{Z_{op}A - Z_{op}Z_{sh}C - B + Z_{sh}D}{Q(Z_{op} - Z_{sh})} \tag{6.28}$$

$$B_0 = \frac{Z_{sh}^2 C + B - Z_{sh}(A + D)}{P} \tag{6.29}$$

$$C_0 = \frac{Z_{op}^2 C + B - Z_{op}(A + D)}{Q(Z_{op} - Z_{sh})^2} \tag{6.30}$$

$$D_0 = \frac{Z_{sh}A - Z_{op}Z_{sh}C - B + Z_{op}D}{P(Z_{op} - Z_{sh})} \tag{6.31}$$

in which,

$$P = C_T . Z_{sh} - D_T \tag{6.32}$$

$$Q = \left(C_T . Z_{op} - D_T\right) \tag{6.33}$$

It is worth mentioning that being different from the SOL method in [194], the expression of the error box transmission matrix in (6.25)-( 6.27) as well as the core circuit's four matrix elements expressed in (6.28)-( 6.33) are free of the $Z_0$ term, which mitigates the inaccuracy issue at higher frequencies.

## 6.3 Holistic circuit model development

The use of equivalent circuits to represent an arbitrary two-port (actually multiport) network can be encountered so frequently in practice. Conventionally, the equivalent circuit of such an arbitrary network is represented by a T or π equivalent two-port circuit. However, the circuit parameters of such a T or π network are stable over a narrow band frequency only, and this means that those network parameters are dispersive in frequency or frequency dependent. However, the generated LCRG parameters should be frequency-independent over a wide range of frequency if a true equivalent circuit model is established. In this section, we will discuss a generalized equivalent circuit model development technique for any two-port discontinuity that demonstrates constant circuit parameters over a significantly wider frequency range.

The terminal planes of a transmission line with a circuit discontinuity or transitions are usually defined at arbitrary points along the two transmission line sections. Different transitions and physical discontinuities in the transmission line store magnetic and/or electric energy that leads to

different reactive effects. Such effects can be characterized through measurement results or numerical analyses, which are represented in terms of two-port network parameters such as Z, Y, S, or ABCD. This type of analysis is applicable to different types of two-port junctions, such as transitions between different types of transmission lines, transmission line step discontinuities or bends, etc. In practice, the modeling of a microwave junction is often conducted by replacing the two-port "black box" with an equivalent circuit containing a few idealized components. This approach is useful to relate the component values with some physical features of the actual junction [155]. To generate an accurate equivalent circuit model of any given discontinuity or junction, a holistic approach to circuit model development technique is required. In addition, the equivalent circuit parameters related to such a discontinuity or junction should be consistent over a wide range of frequency. To define the characteristics of extracted circuit parameters over the desired band of frequency, we use an average rate of change (AROC) as a scale. AROC is a measure of how much the function changes per unit, on average, over that interval. It is derived from the slope of a straight line connecting the interval's endpoints on the circuit parameter's characteristic curve. To minimize the computational load, AROC is implemented instead of the instantaneous rate of change of the circuit parameters.

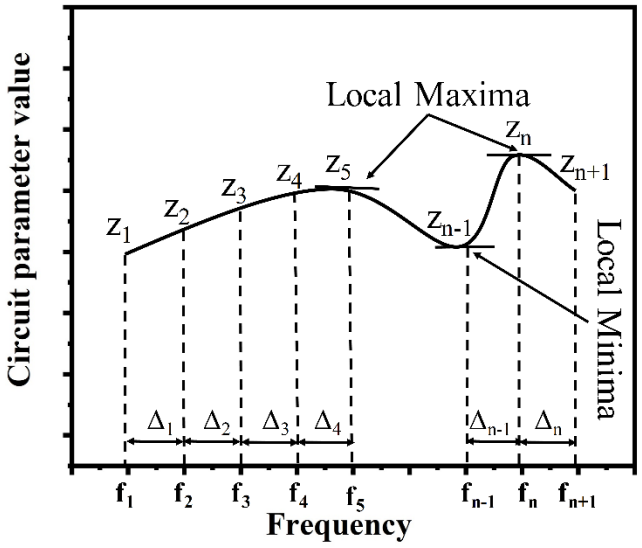


Figure 6.2 Sampling strategy of arbitrary circuit parameters over a frequency band of interest

Figure 6.2 illustrates a variation curve of an arbitrary circuit parameter over a range of frequency. To utilize the concept of AROC effectively, the circuit parameter value over the desired band of frequency is discretized into $n$ number of nonuniform sections. The variation of a certain circuit

parameter over the entire frequency band cannot be discretized uniformly due to possible resonant conditions or sharp variations at different frequencies. Resonances may occur at low or high frequencies depending on the type of discontinuity. In such cases, circuit parameters vary abruptly in a short interval of frequency. These sharp changes in circuit parameters can be located by finding the maxima and/or minima of the variation curve. Such maxima and minima can be found by setting zero to the first and second derivatives of circuit parameter value functions with respect to frequency. Around these maxima and minima, frequency should be densely sampled. Otherwise, resonant frequencies may be overlooked, and circuit decompositions may be erroneous.

Let us denote the first section as $\Delta_1$ where $z_1$ refers to a certain circuit parameter's value at the starting frequency $f_1$ and $z_2$ stands for that circuit parameter's value against the ending frequency $f_2$. The AROC for the first section is expressed as

$$AROC_{\Delta_1} = \left|\frac{z_2 - z_1}{f_2 - f_1}\right| \tag{6.34}$$

Similarly, AROC for the $n^{th}$ section, $\Delta_n$ is expressed as

$$AROC_{\Delta_n} = \left|\frac{z_{n+1} - z_n}{f_{n+1} - f_n}\right| \tag{6.35}$$

The mean AROC over the whole band of frequency is calculated as

$$\overline{AROC} = \frac{1}{n}\sum_{i=1}^{n} AROC_{\Delta_i} \tag{6.36}$$

Equation (6.36) provides the mean AROC of a single circuit parameter over the desired range of frequency. Let $\overline{AROC}_{avg}$ denote the average of all the individual mean AROC of each circuit parameter. A value of $\overline{AROC}_{avg}$ should be set to define an acceptable flatness of the circuit parameter curve.

$$\overline{AROC}_{avg} = \frac{1}{N}\left(\overline{AROC}_{cp1} + \overline{AROC}_{cp2} + \cdots + \overline{AROC}_{cpN}\right) \tag{6.37}$$

In equation (6.37), $N$ is the number of total circuit parameters and $\overline{AROC}_{cpN}$ denotes the mean AROC of the N$^{th}$ circuit parameter over the frequency range of interest.

The step-by-step procedure for the equivalent circuit model generation is explained below and the workflow is illustrated in Figure 6.3.

1. Extract full-wave simulated S-parameters of a target sample for a given discontinuity. Calibrate electromagnetically simulated S-parameters through the proposed SOT calibration technique.

Extract ABCD, Y and Z parameters from calibrated S-parameters. Then, numerical noise-free circuit parameters (ABCD, Y and Z) are ready for the next stage extraction process.

2. For a given discontinuity, we may start with a fundamental T or π equivalent two-port circuit. Parameters of such an equivalent circuit are extracted from the calibrated Y or Z parameters. These individually extracted circuit parameters should be invariant over a wideband of frequency range.
3. If the circuit parameters are inconsistent over the frequency range, the variation of circuit parameters over frequency should be sampled to initiate the circuit model decomposition. The first step of frequency sampling is to set the derivative of a circuit parameter with respect to frequency, which should be equal to zero. The frequencies corresponding to local minima and maxima are noted.
4. Except for neighboring frequencies of local minima and/or local maxima, consider the sample size based on the characteristic of the corresponding circuit parameter against frequency (we used 4%-6% of the entire frequency band). The frequency sampling rate around the local minima and/or local maxima should be at least twice as compared to other frequencies. This nonuniform frequency sampling provides a faster calculation while the circuit parameter values are adequately sampled in different situations such as at their maxima and minima.
5. After a careful discretization of all the circuit parameter values over the frequency range, $\overline{AROC}_{avg}$ should be calculated using (6.37). This $\overline{AROC}_{avg}$ will play a vital role in the circuit model decomposition.
6. A threshold value of $\overline{AROC}_{avg}$ should be set to define an acceptable variation of all the circuit parameters on average over a range of frequency. Let us set $K$ as such a threshold value for defining the acceptable flatness of circuit parameters vs frequency curve. If $\overline{AROC}_{avg} \leq K$, then the fundamental T or π equivalent circuit model is good enough. However, for $\overline{AROC}_{avg} > K$, the fundamental T or π equivalent circuit model is still represented by dispersive lumped elements and it is not good enough. Therefore, the individual elements of the fundamental circuit themselves should be decomposed into another T or π model (higher order). This first stage (or first order) of decomposition ends up with numerous circuit parameters. However, the finally decomposed circuit topology can be simplified by a well-known circuit theory that can effectively minimize the total number of circuit parameters in the model.

7. After the first decomposition followed by the circuit simplification process, the $\overline{AROC}_{avg}$ should be calculated again. If the $\overline{AROC}_{avg} \leq K$ condition is still unsatisfied with the circuit parameters, the individual circuit elements should be further decomposed into another T or π model. The decomposed circuit should go through the simplification process further.
8. The previous step keeps repeating till the $\overline{AROC}_{avg} \leq K$ condition is satisfied. When all the circuit elements become stable or consistent over an interested wideband of frequency, the developed circuit model is finalized to its most compact form.

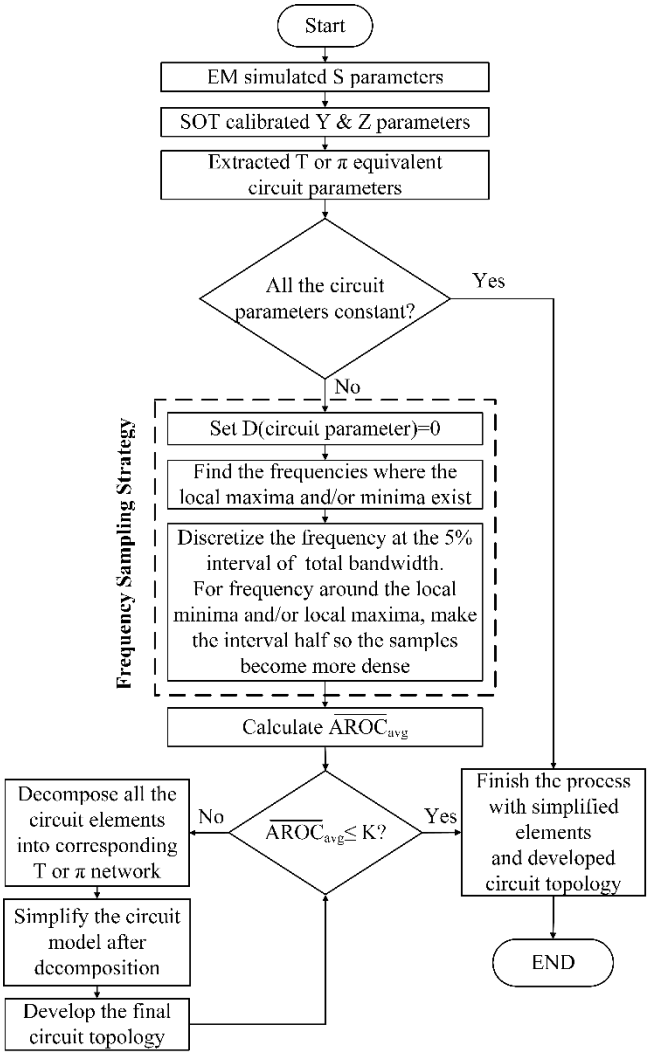


Figure 6.3 Flowchart of the proposed circuit model generation

According to our experiments, the equivalent circuit parameters of elementary discontinuities such as steps, gaps, via holes etc. usually become stable over a wide range of frequency after the second

stage (order) of the proposed decomposition process. Circuits with a series of discontinuities may require further decomposition stages to stabilize all the circuit parameters over an interested range of frequency.

In order to demonstrate the proposed multistage or multi-order network development technique, let us consider an arbitrary discontinuity, which can primarily be represented by either a fundamental T or π network. Let us also assume that the circuit parameters of the fundamental T or π network do not satisfy the $\overline{AROC}_{avg}$ condition over a wide range of frequency. Therefore, the network should be decomposed as explained below.

If the primary network is considered as a fundamental T network, the decomposition should start in the following manner. First, three elements of the fundamental T network, $Z_1, Z_2\ and\ Z_3$ are decomposed into another T network as shown in Figure 6.4(b) - Figure 6.4(c). Following a few steps of the circuit simplification process as illustrated in Figure 6.4(d) - Figure 6.4(e), the first decomposition provides us with the final circuit topology as shown in Figure 6.4(f).

$$Z_a = Z_{22}(Z_{13} + Z_{21}) + (Z_{13} + Z_{21})(Z_{23} + Z_{31}) + Z_{22}(Z_{23} + Z_{31}) \tag{6.38}$$

$$Z_x = \frac{Z_a}{Z_{23}+Z_{31}} \tag{6.39}$$

$$Z_y = \frac{Z_a}{Z_{13}+Z_{21}} \tag{6.40}$$

$$Z_z = \frac{Z_a}{Z_{22}} \tag{6.41}$$

$$Z_p = Z_{12} \parallel Z_x \tag{6.42}$$

$$Z_q = Z_{32} \parallel Z_y \tag{6.43}$$

Here $Z_{11}, Z_{12}, Z_{13}; Z_{21}, Z_{22}, Z_{23}\ and\ Z_{31}, Z_{32}, Z_{33}$ are decomposed from the primary fundamental T network element $Z_1, Z_2, Z_3$, respectively. As a part of the circuit simplification process, a conversion between the circuit topology shown in Figure 6.4(d) and Figure 6.4(e) is made by the T to π conversion formula. $Z_x, Z_y\ and\ Z_z$ are calculated from such a conversion. The final simplified network after the first decomposition is illustrated in Figure 6.4(f).

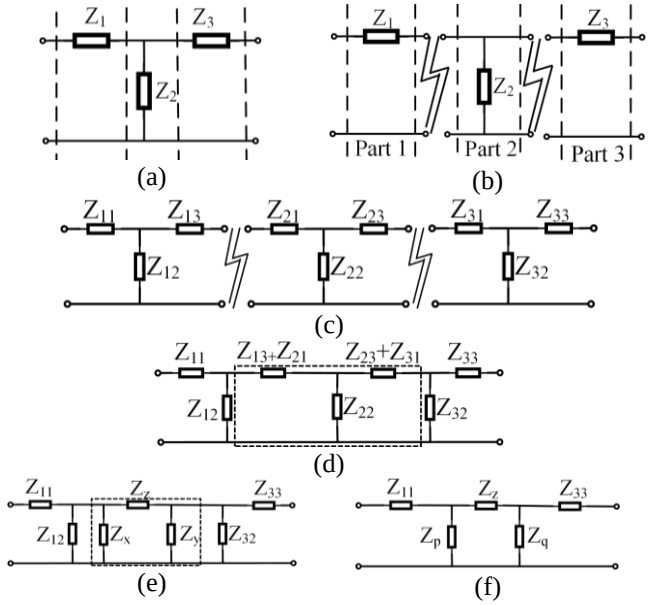


Figure 6.4 Step-by-step first stage network decomposition (T-T Combination)

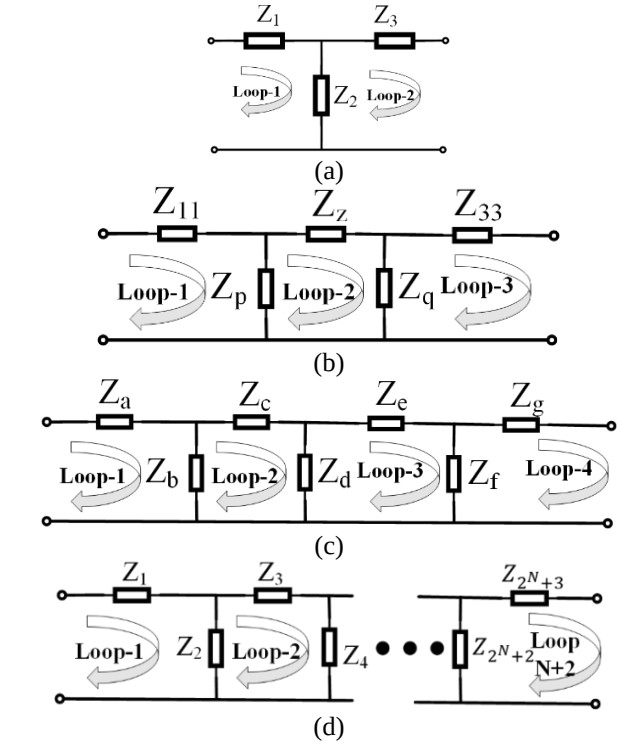


Figure 6.5 Evolution of T-equivalent circuit through different stages (a) Primary topology (b) $1^{st}$ stage decomposed topology $[T-T]$ (c) $2^{nd}$ stage decomposed topology $[T-T-T]$ (d) $N^{th}$ stage decomposed topology $[T-T-\cdots-T]$

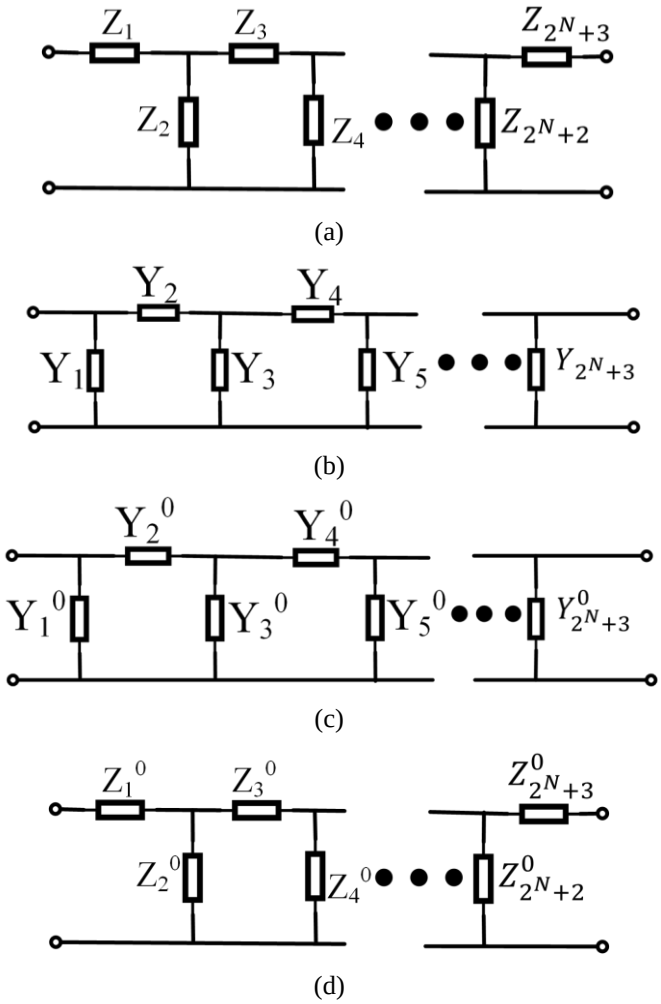


Figure 6.6 Network topology after $N^{th}$ stage decomposition (a) $[T-T-T-\cdots-T-T]$ (b) $[T-\pi-T-\cdots-\pi-T]$ (c) $[\pi-\pi-\pi-\cdots-\pi-\pi]$ (d) $[\pi-T-\pi-\cdots-T-\pi]$

After the first decomposition, the $\overline{AROC}_{avg}$ from all the five components of Figure 6.4(f) should be calculated. If the $\overline{AROC}_{avg}$ does not satisfy the desired threshold value over the frequency range, the circuit model should go through a further decomposition process. In the second stage of decomposition, these five elements are decomposed into fifteen elements as each section of the T equivalent network consists of another three elements. However, after simplifying these fifteen elements, the final circuit comes down to seven elements. In this way, the $N^{th}$ stage decomposed network can be derived with $(2^N+3)$ number of elements. Figure 6.5 depicts the evolution of T-network at different stages of decomposition. Figure 6.5(a) shows the primary T-network that has two loops, Figure 6.5(b) illustrates the $1^{st}$ stage decomposed network $[T-T]$ with three loops while the $2^{nd}$ stage decomposed $[T-T-T]$ network with four loops is demonstrated in Figure

6.5(c). Similarly, the $N^{th}$ stage decomposed $[T-T-\cdots-T]$ network consists of $(N+2)$ loops as shown in Figure 6.5(d).

The above-described circuit decomposition technique is explained for $[T-T-\cdots-T]$ combination. The other possible combinations are $[T-\pi-T-\cdots-\pi-T]$, $[\pi-\pi-\pi-\cdots-\pi-\pi]$ and $[\pi-T-\pi-\cdots-T-\pi]$, respectively. The step-by-step first-order decomposition follows a similar procedure as illustrated in Fig. 4. The $[T-\pi-T-\cdots-\pi-T]$, $[\pi-\pi-\pi-\cdots-\pi-\pi]$ and $[\pi-T-\pi-\cdots-T-\pi]$ combinational circuit topology after $N^{th}$ stage decomposition is illustrated in Figure 6.6(b), Figure 6.6(c), and Figure 6.6(d) respectively. Figure 6.6 describes that $[T-T-\cdots-T]$ and $[\pi-T-\pi-\cdots-T-\pi]$ combinational circuit topology are the same while $[\pi-T-\pi-\cdots-T-\pi]$ and $[\pi-\pi-\pi-\cdots-\pi-\pi]$ end up with an identical circuit topology. Therefore, the first decomposition criterion decides the final circuit topology of the equivalent circuit model.

## 6.4 Illustrative examples of elementary discontinuities

In this section, three examples of elementary discontinuity are demonstrated to validate the proposed SOT calibration technique and circuit model development approach. These three examples are microstrip gap discontinuity, microstrip step discontinuity and via-hole discontinuity in two-layered substrates. Such dual-port electrically small microstrip discontinuities are characterized to extract their conventional and decomposed circuit models by using the proposed SOT calibration technique. In all the cases, extracted circuit parameters are compared between SOT and SOL methods.

### 6.4.1 Microstrip gap discontinuity

The physical layout of a microstrip gap discontinuity is illustrated in Figure 6.7(a) where the structure has identical feedline length $L_0$ with linewidth $W$ and spacing$S$between two lines. The substrate's dielectric permittivity $\varepsilon_r = 10.2$ and thickness $h = 1.27mm$. The gap discontinuity with different spacing between microstrip lines has widely been used in different types of circuits. The primary equivalent circuit model of such a gap discontinuity is represented by a conventional π-network as shown in Figure 6.7(b). The SOL and SOT calibration techniques are both employed to extract the primary circuit parameters over a frequency range of 1-20GHz. Extracted circuit parameters are plotted against frequency in Figure 6.8(a) while $L_0 = 4mm$, $W = 3.6mm$ and $S =$

$0.4mm$. Figure 6.8(a) shows that the SOL extracted mutual capacitance $C_a$ and the shunt capacitance $C_b$ vary drastically in the frequency range of interest. As frequency increases, $C_a$ shifts exponentially upward while $C_b$ declines linearly. The SOT-extracted circuit parameters are also plotted in Figure 6.8(a) to illustrate a comparison with its SOL method-based results. The SOT-extracted parameters show stable characteristics over a frequency range of 1-10GHz while the SOL-extracted parameters are only invariant over a frequency range of 1-5GHz. Therefore, the SOT calibration method provides much better-extracted circuit parameters in terms of stability over a wider bandwidth.

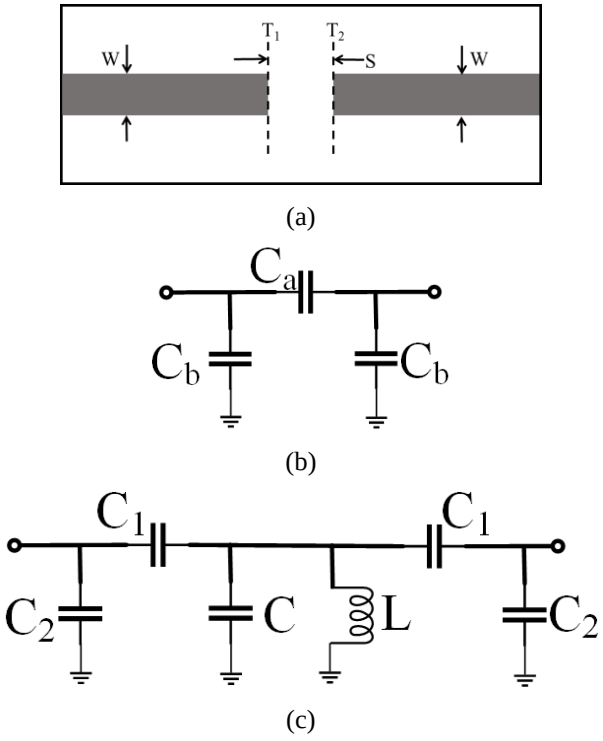


Figure 6.7 Microstrip line gap discontinuity: (a) Layout; (b) Primary circuit topology; (c) Circuit topology from 1st stage decomposition

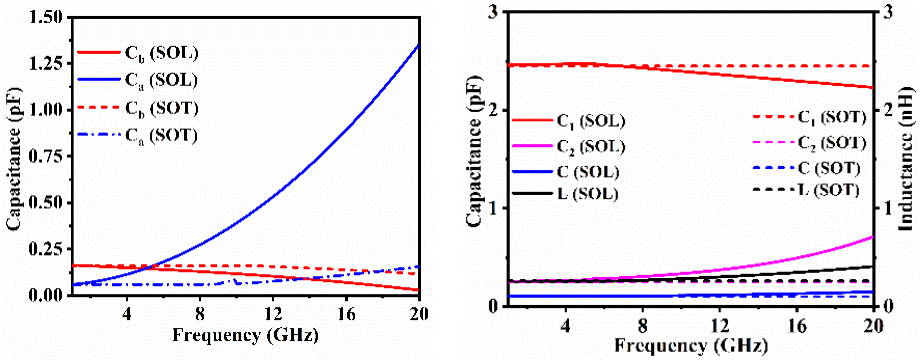


(a) (b)

Figure 6.8 Extracted circuit parameters by the SOL and the proposed SOT: (a) primary circuit; (b) 1st stage decomposed circuit. In all the cases, S=0.4mm

In order to maximize the stability of circuit parameters over a wider bandwidth, the primary circuit should further be decomposed by the described method in Section III. The decomposition process starts with the $AROC$ analysis of the SOT extracted $C_a$ and $C_b$ curves. The total frequency span of 1-20GHz is uniformly segmented into 20 pieces for ease of $AROC$ analysis. The $\overline{AROC}_{C_a} = 5 \times 10^{-3}$ and $\overline{AROC}_{C_b} = 5 \times 10^{-3}$. Therefore, $\overline{AROC}_{avg} = 5 \times 10^{-3}$. Our desired $\overline{AROC}_{avg}$ is $1 \times 10^{-6}$ which provides all the parameters with a better consistency over 20GHz bandwidth. As the primary equivalent circuit topology is a $\pi$ network as shown in Figure 6.7(b), we proceed with the $[\pi - \pi]$ combination for the 1st stage decomposition. The $[\pi - \pi]$ combinational decomposed circuit topology is illustrated in Figure 6.6(c). Similarly, we end up with the 1st stage decomposed circuit as shown in Figure 6.7(c) that achieves the desired $\overline{AROC}_{avg}$. A further decomposition is not required as the desired $\overline{AROC}_{avg}$ is already met. The SOL and SOT extracted 1st stage decomposed circuit parameters are illustrated in Figure 6.8(b). It is clearly seen that the SOT calibration extracts the circuit parameters that behave invariantly over the 20GHz bandwidth while the SOL extracted circuit parameters are only flat over 1-10GHz. In order to broaden the bandwidth for the SOL method, further decomposition is required. Therefore, the SOT calibration technique is a better candidate in terms of stability and accuracy for equivalent circuit parameters.

For the case of varying gap space $S$, the SOT-calibrated 1st stage decomposed circuit parameters are illustrated in Figure 6.9 while other parameters such as $L_0, W,\ \varepsilon_r$ $and$ $h$ are fixed at their previous value. It shows that all the equivalent circuit parameters except $C_1$ of Figure 6.7(c) are highly sensitive to the gap length between two uniform microstrip lines.

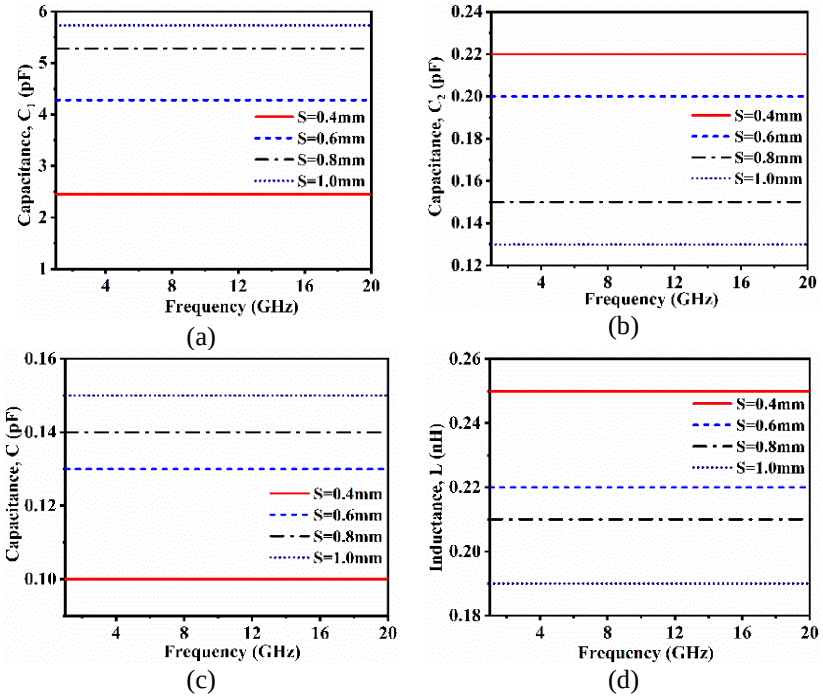


Figure 6.9 SOT-Extracted (1st stage decomposed) circuit parameters at different gap length $S$. (a) $C_1$; (b) $C_2$; (c) C; (d) L

## 6.4.2 Microstrip step discontinuity

A variety of MSL circuits vastly make use of microstrip step discontinuities of different strip widths at two sides. An equivalent circuit model of such step discontinuities is analyzed in [207], [208]. The two-port excited physical layout of a symmetrical step discontinuity is depicted in Figure 6.10(a), which is conventionally modeled as a T-network, as shown in Figure 6.10(b). Two $L_x$ and $L_y$ lengths of feed lines with $W_1$ and $W_2$ strip-widths. The conventional equivalent T-network consists of a shunt capacitance along with two series inductances. The equivalent inductances in T-network are usually calculated as a sum of $L_i$.

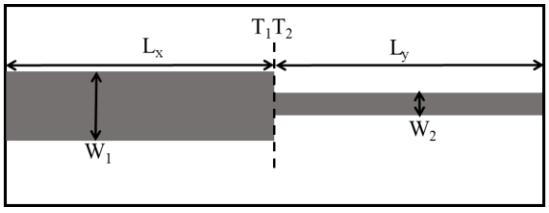


(a)

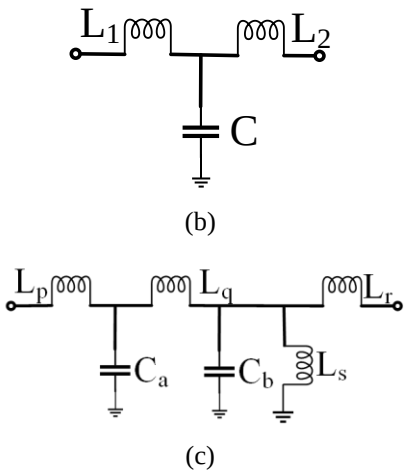


Figure 6.10 MSL step discontinuity: (a) Layout; (b) Primary circuit topology; (c) Circuit topology from 1st stage decomposition

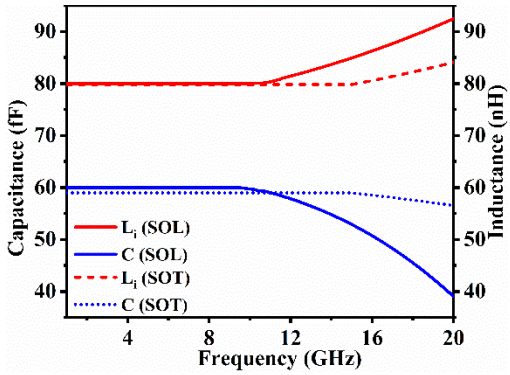


Figure 6.11 Extracted primary circuit parameters by the SOL and proposed SOT

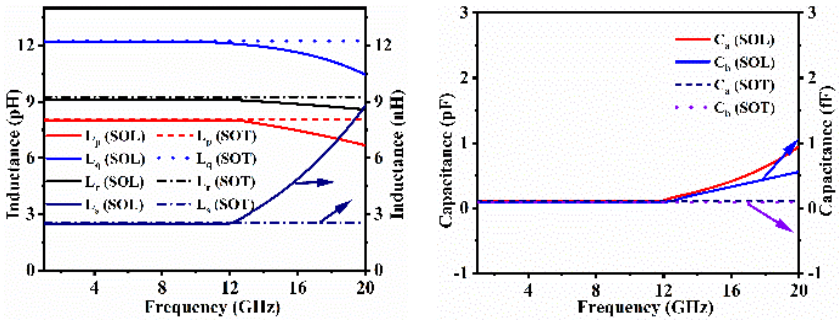


Figure 6.12 Extracted 1st stage decomposed circuit parameters by the SOL and proposed SOT: (a) Inductances; (b) Capacitances

In the symmetrical step discontinuity layout shown in Figure 6.10(a), substrate dielectric permittivity $\varepsilon_r = 10.2$ and thickness $h = 0.635mm$. Two identical feedline length $L_x = L_y = 5mm$. The width of these two feedlines is $W_1 = 0.6mm$ and $W_2 = 0.2mm$, respectively. The primary circuit parameters of Figure 6.10(b) are extracted through the SOL and SOT calibration methods. The extracted parameters are plotted against frequency in Figure 6.11, which shows stable SOL-extracted parameters over 10GHz bandwidth while the SOT-extracted parameters are invariant over 14GHz bandwidth.

To enhance the representation bandwidth further for the equivalent circuit model, the primary circuit in Figure 6.10(b) should be decomposed according to the proposed procedure. The SOT-extracted $C$ and $L_i$ yield $\overline{AROC}_{avg} = 0.625$. The 1st stage decomposed circuit topology is followed by a $T - T$ configuration and illustrated in Figure 6.10(c) that minimizes the $\overline{AROC}_{avg}$ to $1 \times 10^{-8}$. This $\overline{AROC}_{avg}$ achieves the desired level. Therefore, the 2nd stage of decomposition is not required. Figure 6.12 illustrates the SOL- and SOT-extracted 1st stage decomposed circuit parameters. The SOL-extracted circuit parameters are frequency-independent over 12GHz bandwidth while the SOT-extracted circuit parameters are stable over 20GHz bandwidth.

Figure 6.13 illustrates the variation of circuit parameters over frequency at different width $W_1$ while all the other parameters are kept constant at their prior value. It is evident from these figures that all the circuit parameters move up as $W_1$ is linearly widened. Such a phenomenon is observed due to the raising curvature extent of a current density flowing from the longitudinal to transverse direction on the wide microstrip conductor around the step interface.

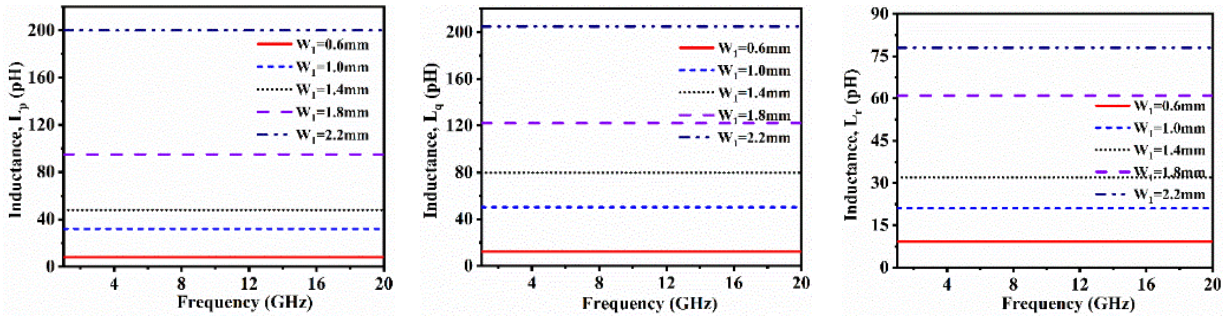


(a) (b) (c)

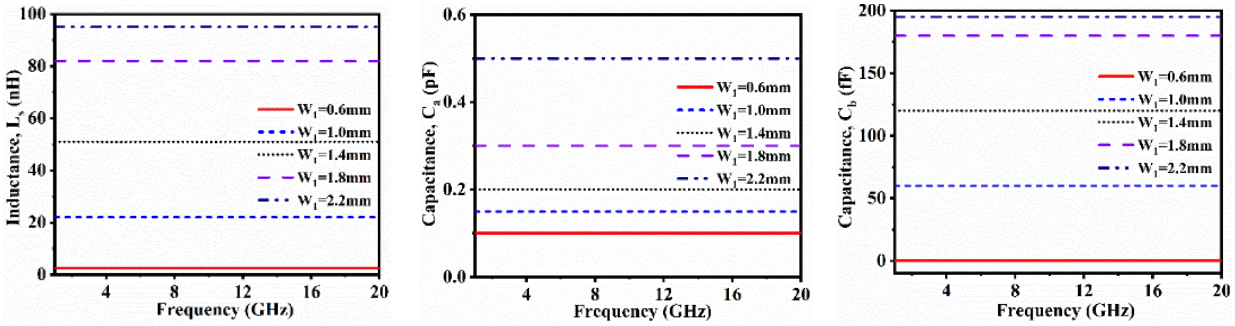


(d) (e) (f)

Figure 6.13 SOT extracted (1st stage decomposed) circuit parameters at different $W_1$ width: (a) $L_p$; (b) $L_q$; (c) $L_r$; (d) $L_s$; (e) $C_a$; (f) $C_b$

### 6.4.3 Via-hole discontinuity in a two-layered substrate

The via-hole is commonly used in different RF/microwave multilayered structures. Such a via-hole allows uninterrupted transmission between different layers at low frequency. A 3D sketch of via-hole discontinuity across a two-layered substrate is depicted in Figure 6.14(a). The dielectric permittivity of substrates $\varepsilon_r = 3.6$ while microstrip width $W = 3.6mm$, inner and outer diameters of the via hole are denoted by $d_1$ and $d_2$, respectively.

The conventional equivalent circuit of the via-hole defined at the two reference planes is modeled as a $\pi$-network [208], and it is illustrated in Figure 6.14(b). For $d_1 = 0.9mm$ and $d_2 = 3.6mm$, the SOT- and SOL-extracted circuit parameters of the primary topology are plotted against frequency in Figure 6.15. The inductance $L$ decreases and the capacitance $C$ increases as frequency goes up. The SOL-extracted parameters are invariant in 4GHz bandwidth while the SOT-extracted circuit parameters are stable over 9GHz bandwidth. To further extend the circuit parameter stability over frequency range, a further circuit model decomposition is conducted with reference to the SOT-extracted circuit parameter curves. From these curves, the $\overline{AROC}_L = 0.08$ and $\overline{AROC}_C = 0.05$ that give us 0.065 of $\overline{AROC}_{avg}$.

To minimize the $\overline{AROC}_{avg}$, the 1st stage of decomposition is carried out following the proposed method. Here, a $[\pi - \pi]$ combination is used for the 1st stage decomposition and the topology is illustrated in Figure 6.14(c). This 1st stage of decomposed circuit topology consists of two inductances and two capacitances. Even though the $\overline{AROC}_{avg}$ is reduced to $5 \times 10^{-3}$, this circuit topology cannot meet the desired $\overline{AROC}_{avg}$. Therefore, further circuit decomposition is required to

stabilize the circuit parameters as expected over a wider frequency range. Figure 6.14(d) shows the 2nd stage decomposed circuit topology, which consists of three inductances and three capacitances, respectively. The $\overline{AROC}_{avg}$ comes down to $9 \times 10^{-7}$ that meets the desired threshold value. The SOL- and SOT-extracted 2nd stage decomposed circuit parameters are plotted against frequency in Figure 6.16. The SOL-extracted circuit parameters are stable over 9GHz bandwidth while the SOT-extracted circuit parameters are invariant over 19GHz bandwidth. Figure 6.17 illustrates the SOT-extracted circuit parameters for different inner diameter of via-hole $d_1$ while other geometric parameters are fixed at their prior value.

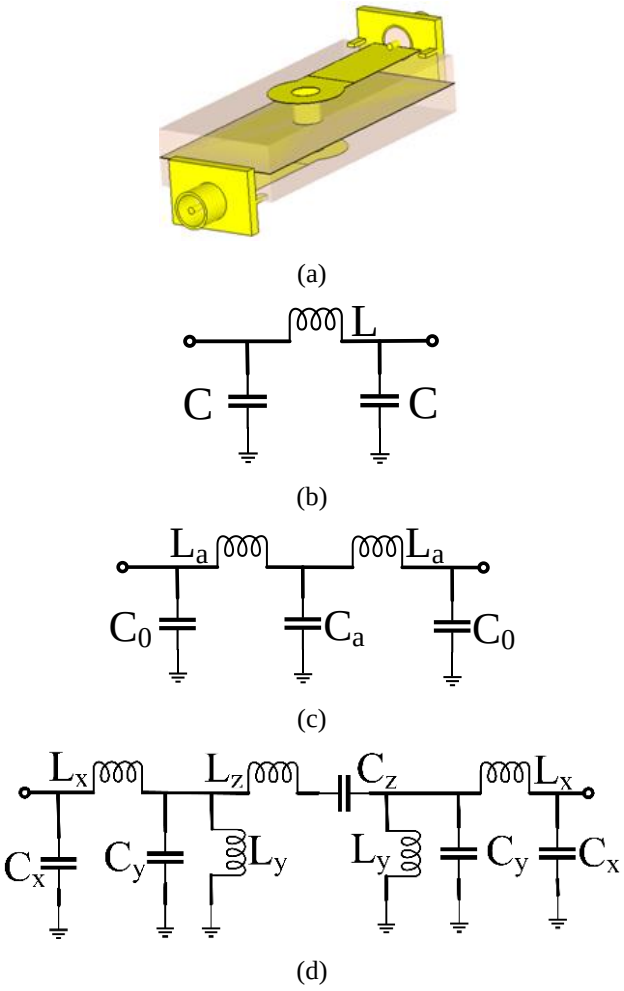


Figure 6.14 Via-hole discontinuity in two-layered substrate: (a) 3D Layout; (b) Primary circuit topology; (c) Circuit topology from 1st stage decomposition; (d) Circuit topology from 2nd stage decomposition

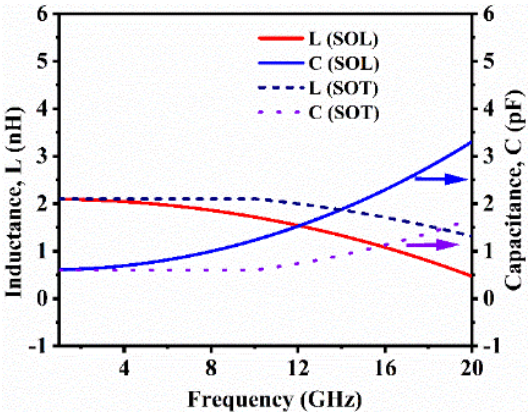


Figure 6.15 Extracted primary circuit parameters by the SOL and proposed SOT

From the above-described case studies, these three different discontinuity examples provide us with convincing arguments and interesting observations. First, the proposed SOT calibration technique proposed in this work provides much more stable equivalent circuit parameters over a larger bandwidth as opposed to the recently proposed SOL calibration technique [194]. Second, the proposed decomposition technique provides a holistic strategy to generate a unified equivalent circuit model for any given structure discontinuity or circuit element. Circuit parameters of such decomposed circuits are more invariant and robust over a larger bandwidth as compared to its conventional counterpart. In all the cases, the SOT calibration method outperforms the SOL technique in terms of maximum frequency bandwidth for a robust circuit model. On the other hand, with the conventional J or K inverter concept, the equivalent circuit of such discontinuities are composed of single section of T or π network. Such inverter circuits can only be relied on a narrow bandwidth application. Our proposed step-by-step circuit decomposition technique is set to derive the appropriate equivalent circuit of a target discontinuity over a larger bandwidth at high frequencies.

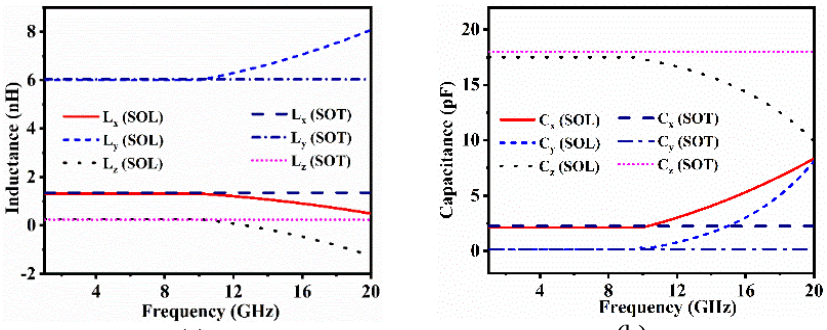


(a) (b)

Figure 6.16 Extracted 2nd stage decomposed circuit parameters by the SOL and proposed SOT: (a) Inductances (b); Capacitances

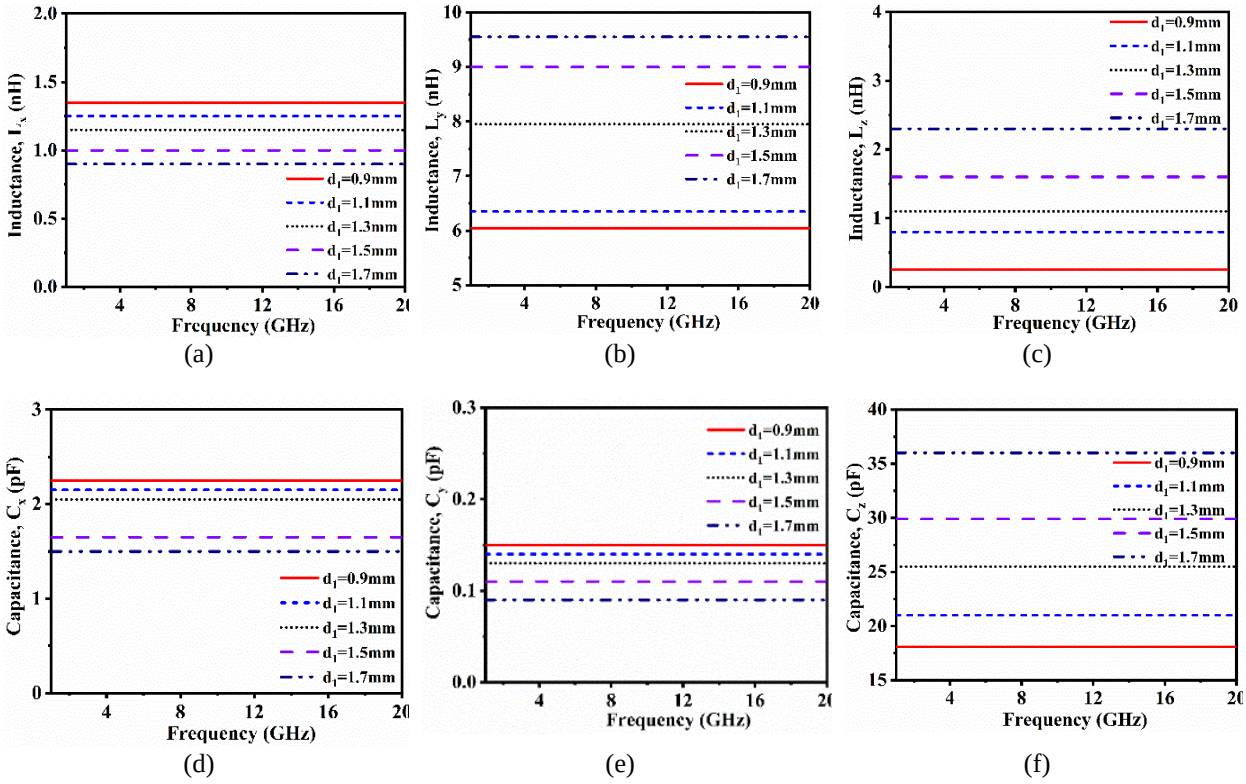


Figure 6.17 SOT-extracted (2nd stage decomposed) circuit parameters at different inner diameter $d_1$: (a) $L_x$; (b) $L_y$; (c) $L_z$; (d) $C_x$; (e) $C_y$; (f) $C_z$

## 6.5 Circuit design and experimental validation

To validate the proposed SOT calibration method and equivalent circuit model development technique, a third-order end-coupled microstrip bandpass filter (midband frequency $f_0$ = 6GHz) with 3% fraction bandwidth and 15-dB return loss is designed on a 1.27mm Rogers 6010 substrate with a dielectric constant of 10.7 and a loss tangent of 0.0023. The layout is presented in Figure 6.18(a). The equivalent circuit of the microstrip gap discontinuity has been derived in previous section which is used along with capacitive input/output tight coupling to represent the complete equivalent circuit of the target three-pole microstrip end-coupled resonator filter as shown in Figure 6.18(b). Shunt connected capacitors at the two ends of the inter-resonator coupling circuits are absorbed into the parallel LC circuits that represent the resonators.

The length of the microstrip gap discontinuities as inter-resonator coupling can initially be determined by the prescribed circuit parameter values according to our proposed circuit model development technique. The filter layout is finalized after minor modifications. Figure 6.18(a) describes third order filter's geometric parameters, which are $L_a = 8.15$ , $L_b = 8.4, S_1 = 0.06, S_2 = 0.8$ and $W = 1.1$; where all the units are in mm. The extracted equivalent circuit model parameters of Figure 6.18(b) from the proposed SOT de-embedded results are $C_{i/0} = 0.07, C_a = 0.05, C_b = 3.01, C_1 = 0.157, C_2 = 0.1, C_3 = 0.3,\ L_1 = 2.69, L_2 = 3.89$ and $L_3 = 90$ where all the capacitances and inductances are expressed in pF and nH, respectively. The equivalent circuit parameters are also extracted from M-TRL calibrated results to compare with the circuit responses from the extracted circuit parameters out of the SOT de-embedded results. The extracted equivalent circuit model parameters of Figure 6.18(b) from the M-TRL calibrated results are close to the SOT de-embedded results derived circuit parameters which are $C_{i/0} = 0.07, C_a = 0.04, C_b = 2.99, C_1 = 0.156, C_2 = 0.104, C_3 = 0.307,\ L_1 = 2.691, L_2 = 3.896$ and $L_3 = 90$ where all the capacitances and inductances are expressed in pF and nH, respectively. The comparison of S-parameters among the SOT de-embedded result-driven equivalent circuit, M-TRL calibrated result-driven equivalent circuit, full-wave EM simulations, and experiments are illustrated in Figure 6.19. The filter was measured using Keysight N5224B PNA microwave network analyzer. The equivalent circuit model generated S-parameters differs a little bit from the full-wave EM simulation results. However, the EM simulation results demonstrate that the filter has achieved the desired performance such as passband return loss and stopband insertion loss. An excellent agreement is found between the measured and simulated results.

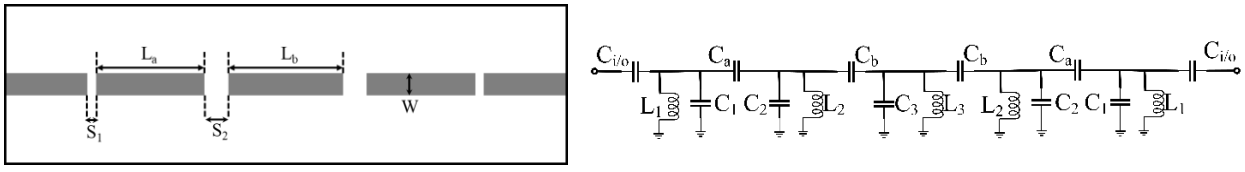


(a) (b)

Figure 6.18 Three-pole microstrip end-coupled half-wavelength resonator filter. (a) Layout; (b) Equivalent circuit

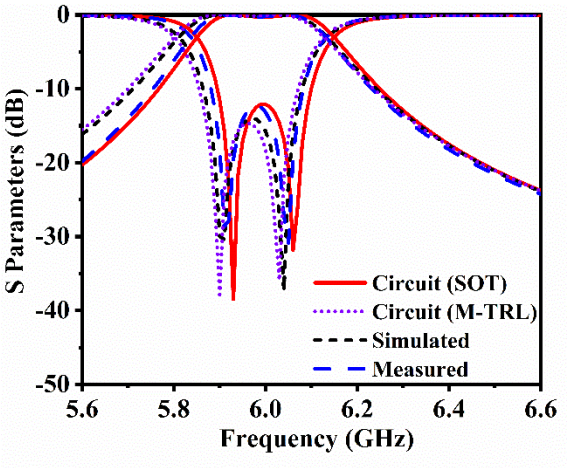


Figure 6.19 Comparison of S-parameters among equivalent circuits, EM simulation, and measurement results

## 6.6 Discussions

This paper presents a holistic circuit model development technique from the proposed SOT de-embedded results of any given discontinuity or geometry. The major goal of this work is to establish a unified methodology for automated equivalent circuit model development where circuit parameters can be made invariant or frequency-independent over a broad range of frequency. The concept of AROC is introduced to estimate and decide the performance of an $N^{th}$-stage (order) network decomposition in connection with circuit parameters over a given range of frequency. Such analysis provides robust guidance towards automated circuit model decomposition and generation.

Table 6.1 summarizes the achieved maximum bandwidth from different methods such as SOC, SOL and SOT. Extracted primary circuit parameters of microstrip line gap discontinuity, microstrip line step discontinuity and via-hole through two-layered substrates are analyzed in this case. In addition, decomposed circuit parameters from the proposed circuit model development method are extracted from the SOL- and SOT-calibrated results for all three examples. Such a comparison demonstrates that the proposed SOT technique provides a much better bandwidth as compared to other calibration techniques. In addition, the proposed circuit decomposition technique provides a systematic procedure to formulate and generate an equivalent circuit model from the calibrated results of a given discontinuity or element. These decomposed circuit parameters can further extend the achieved bandwidth for better invariance. The proposed circuit model decomposition algorithm

provides us with a number of lumped elements while conventional circuit models consist of only three lumped elements to describe the field behavior of a certain discontinuity or element. Therefore, the proposed multi-stage decomposed circuit model has a better degree of freedom with any series and shunt lumped elements that accurately describes the field behavior for any given physical geometry.

Table 6.1 Bandwidth invariant circuit parameters

| Discontinuity | SOC* (GHz) | SOL* (GHz) | SOT* (GHz) | SOL# (GHz) | SOT# (GHz) |
|---|---|---|---|---|---|
| MSL Gap | 5 [188] | 4 | 9 | 9 | 20 |
| MSL step | 7 [209] | 9 | 15 | 11 | 20 |
| Via-hole (2 layers subs.) | 3 [191] | 3 | 11 | 9 | 20 |

*Conventional circuit model

#Decomposed circuit model from the proposed method

These numerical experiments show that the SOT-based results along with the decomposed circuit techniques may provide maximum 25-30 GHz bandwidth for stable microstrip line circuit parameters with those conventional PCB-processed circuit layouts. There are two fundamental reasons behind such instability of circuit parameters over 30GHz in this case. First, we only consider the lossless cases in this work. For higher-frequency modeling, losses become more and more pronounced. Second, higher-order modes become imminent at high frequencies. If the effect of higher modes should be considered, the established two-port equivalent circuit is not enough. In that case, a multiport equivalent circuit model is required for generalized S-parameters. Two port equivalent circuit can only be utilized to describe the fundamental mode characteristics. These bandwidth-limiting cases should be further studied.

## 6.7 Conclusion

In this paper, the SOT de-embedding method is proposed and presented for accurate modeling and characterization of unbounded structure discontinuities and circuit elements for a variety of high-frequency applications. This approach rigorously considers all the dynamic effects over a broad range of frequency in an equivalent circuit model. The short, open and thru calibration standards are established with a full-wave electromagnetic algorithm, which are used to conduct a robust numerical extraction process through a circuit network theory. Equivalent circuit models of three example discontinuities are extracted and their extracted parameters are compared against other

published calibration methods such as SOC and SOL. It is found that the proposed SOT technique outperforms the other schemes, which provides better circuit parameters in terms of modeling stability over maximum bandwidth. In addition, a step-by-step circuit model development technique is described and validated. Such a circuit model development approach provides a guideline for potentially automated equivalent circuit model generation with stable circuit parameters over a wide bandwidth. The three discontinuity examples are demonstrated to show the usefulness of the proposed model generation. In addition, a third-order end-coupled bandpass filter has been measured and characterized by the proposed method-derived equivalent circuit. The agreement among simulation and measurement results has validated our proposed technique well.

# CHAPTER 7 ARTICLE 6: HIGH-ORDER EQUIVALENT CIRCUIT MODEL DEVELOPMENT ACCOUNTING FOR MUTUAL-COUPLING EFFECTS

Chandan Roy and Ke Wu

Submitted to the *IEEE Transactions on Microwave Theory and Techniques* on 23 June 2023

Mutual-coupling effects are of utmost importance in high-frequency circuits and systems as they may significantly impact the overall performances. However, it is a common practice that unintentionally overlooks or deliberately ignores these couplings when developing equivalent circuit models. Neglecting these couplings may lead to inaccurate circuit models and characteristics. Therefore, it becomes imperative to account for mutual couplings in the development of accurate equivalent circuit models. By incorporating these models into the circuit analysis, we can effectively capture the intricate interconnections and behaviors among different components and elements, leading to a more precise representation of a complete circuit. This work presents a systematic process for synthesizing the equivalent circuit model of a target field model structure that incorporates mutual and cross couplings of varying orders. The proposed high-order framework begins by developing the equivalent circuit models for each individual transmission line discontinuity within the target circuit. Subsequently, the mutual couplings of different orders are meticulously modeled in a step-by-step manner when a series of mutually-coupled blocks are considered from low-to-high orders. Throughout this process, full-wave electromagnetic (EM) simulations are deployed, along with a circuit parameter extraction method that utilizes de-embedded circuit responses. By combining these techniques, a comprehensive and accurate equivalent circuit model is generated, enabling a detailed analysis of the target field model structure, and facilitating a deeper understanding of its electrical behavior and performance. This paper utilizes two microstrip filter examples for theoretical and experimental demonstration of the proposed technique.

## 7.1 Introduction

Microwave and millimeter-wave circuits are becoming increasingly complex and electrically large due to factors such as enhanced functionality, higher frequency operation, and reduced component size. Traditional design and optimization methods relying on direct full-wave simulations are often

impractical or infeasible with the computational resources typically available. This is especially true when dealing with extensive arrays of mutually coupled elements or intricate waveguide structures. To address this challenge, an efficient and flexible design approach involves dividing the complex structure into geometrically simple and electrically small discontinuities or building blocks, along with uniform transmission line sections that possess physical interpretability. Equivalent circuit models are then characterized and established for these discontinuities and transmission line sections, enabling easy regeneration with modifications to the original structure. This method facilitates a direct synthesis and optimization process that can be performed within a circuit simulator. However, it is important to note that electromagnetic parasitic effects arising from element-to-element mutual couplings may generally be disregarded in this approach, potentially leading to inaccuracies in circuit design and performance prediction when the coupling effects becomes significant. Thus, it is anticipated that incorporating an accurate equivalent circuit model of the primary or dominant mutual couplings into the circuit simulator can enhance the accuracy of results obtained through this segmentation and optimization procedure.

Mutual coupling, whether it manifests as adjacent effect or crosstalk, is a pervasive phenomenon occurring between electromagnetic circuit elements in proximity, regardless of their size. This observation holds true for various scenarios. For instance, in the case of a filter, parasitic mutual coupling between any pair of resonators can exert a significant influence on the overall filtering response, regardless of the employed synthesis procedures. Another example pertains to the mutual coupling between parallel transmission lines, which affects high-speed signal propagation and can have implications for digital signal integrity and synchronization performance.

The calculation of mutual coupling between discontinuities in planar circuits has been addressed using the equivalent source method [210], [211]. In the context of large but finite-extent antenna arrays, two primary approaches have been employed for modeling mutual coupling: the spatial domain (element-by-element) method and the spectral domain (periodic cell) method [212]. The spatial domain method is well-suited for modeling small- to medium-sized arrays, as it involves the computation of mutual impedance or mutual admittance for each pair of elements. However, when dealing with large arrays, this method can demand substantial computational resources and time. In contrast, the spectral domain method has been recognized for its computational efficiency in such scenarios. This method incorporates all mutual coupling effects by imposing periodic boundary conditions on a single element, assuming that the excitations for all elements.

Consequently, this technique neglects edge or border effects and nonuniform current distributions, which become relevant when dealing with large but finite arrays, where the periodic array theorem (Floquet's theorem) is no longer applicable, especially near the array edges. Furthermore, several alternative algorithms have been developed to reduce computational requirements by combining the strengths of these two methods [213], [214]. The consideration of mutual coupling has been limited to first-order effects, with the assumption that higher-order mutual coupling is either negligible or does not impact system performance [211]. A method specifically addressing the evaluation of mutual coupling among microstrip dipoles within an array environment was reported and discussed in [215]. However, this method is not applicable to large arrays, as it does not explicitly account for high-order mutual coupling effects.

Equivalent circuit models have been extensively studied and employed to establish a well-behaved correlation between physical phenomena and electrical properties of electromagnetic structures. Within these equivalent circuit models, electromagnetic field interactions and coupling effects among circuit elements or building blocks are typically represented by the impedance or admittance networks of a specific form. This approach enables the utilization of equivalent circuit models to describe both low- and high-order couplings in multiple-/cross-coupled circuits and elements, as any form of coupling is intrinsically associated with electric and/or magnetic fields. Consequently, the incorporation of equivalent circuit models for mutual coupling is expected to enhance the comprehensiveness and consistency of the large-to-small geometrical segmentation method. Mutual coupling modeling method of any order was proposed and briefly discussed, utilizing the parameter extraction and formulation of an equivalent circuit. This approach was realized through a field-theoretical electromagnetic modeling technique [216], [217]. In this method, the mutual coupling of arbitrary order was explicitly modeled and characterized within an equivalent circuit framework. The description of the equivalent circuit enables the successive extraction of circuit models for high-order mutual coupling (specifically, crosstalk coupling) based on the established models for low-order mutual coupling (adjacent coupling). In this work, similar strategy is followed with the introduction of average rate of change (AROC) concept. Such concept was utilized first in [218] where the equivalent circuit model of elementary transmission line discontinuities are developed. We combine these concepts to deduce the complete equivalent circuit model of a target structure that consists of multiple transmission line discontinuities and mutual couplings of different order between them.

The remaining sections of this paper are organized as follows. Section II presents an overview of the complete process for developing the equivalent circuit model. In Section III, the modeling of elementary discontinuity is discussed, focusing on the circuit decomposition technique. Section IV provides a detailed step-by-step explanation of how the lower- to-higher order mutual couplings between various transmission line discontinuities are deduced. To validate the proposed circuit model development method, Section V showcases two microstrip filter examples. General discussion is presented in Section VI, followed by the conclusion in Section VII.

## 7.2 Equivalent circuit model development technique

The development of a comprehensive equivalent circuit model always commences with the selection of a target structure in connection with a specific application scenario. Subsequently, the target structure undergoes its segmentation into distinct transmission line sections and discontinuities. It is important to note that a target structure may comprise diverse types of discontinuities. The initial step in this process involves deducing an appropriate equivalent circuit model corresponding to each discontinuity. However, it has been demonstrated in [218] that the conventional T and $\pi$ network representation is restricted in terms of bandwidth for these discontinuities. To overcome this limitation and achieve a wide bandwidth representation of the equivalent circuit model, [218] outlines a step-by-step circuit model decomposition technique.

Once the equivalent circuit models for specific transmission line discontinuities have been obtained, it becomes necessary to incorporate in the models, mutual couplings between these discontinuities. The determination of these mutual couplings should be conducted in a sequential manner, beginning with the first-order coupling referred to as side-by-side coupling, and subsequently progressing to higher-order couplings such as cross-couplings. Ultimately, the comprehensive equivalent circuit model of the target structure is constructed by combining the equivalent networks of the segmented discontinuities and the equivalent networks representing all the mutual couplings. Figure 7.1 illustrates an arbitrary structure that consists of K number of transmission line discontinuities. These discontinuities are connected by different lengths or sections of transmission lines where the first discontinuity is connected to the input port and last discontinuity is connected to the output port. Here, we choose a two-port circuit example where mutual couplings are indicated as $M_a^b$. Here, $a$ stands for the order of mutual coupling and $b$ indicates the sequence of a particular coupling. In this illustration, mutual couplings of up to third

order are indicated here. For K number of total discontinuities, there are (K-1) number of 1st order coupling. Similarly, the number of 2nd and 3rd order mutual couplings are (K-2) and (K-3), respectively.

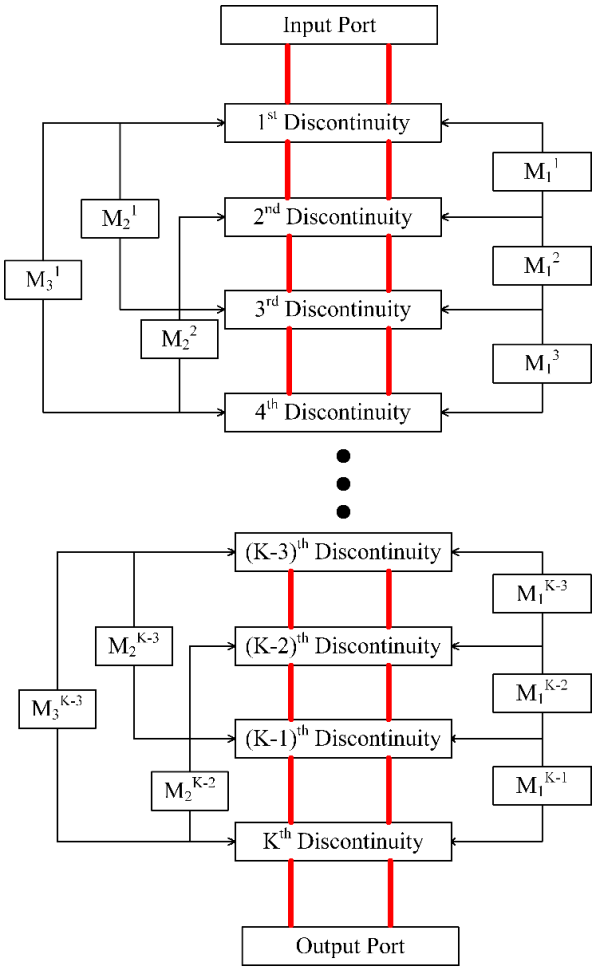


Figure 7.1 Maximum 3rd order mutual coupling involved target structure with K-number of discontinuities

## 7.3 Equivalent network of transmission line discontinuities

Concerning the development of an equivalent circuit model from field model, conventional approaches involve the utilization of T or π networks to represent the characteristics of specific types of discontinuities. Various instances of such discontinuities include microstrip gap, microstrip step, via hole, E-plane, and H-plane waveguide iris, among many others. Prior to commencing the extraction of circuit parameters for a particular type of transmission line discontinuity from its full-wave electromagnetic simulation outcome, the application of a

numerical calibration technique becomes necessary to eliminate or alleviate any introduced numerical noise originating from external ports and excitation sources for any potential deterministic solutions. This numerical calibration procedure is essential to ensure the accurate extraction of circuit parameters pertaining to the device under test (DUT). Within the available literature, the thru-reflect line (TRL) and short-open (SOC) calibration techniques have gained wide acceptance as numerical calibration methods [187], [192], [188]. In [218], a short-open-thru (SOT) de-embedding technique was presented to offer enhanced reliability and stability in the extraction of circuit parameters across a wide frequency range. Subsequently, the equivalent circuit is formulated corresponding to each discontinuity within the target structure, utilizing our recent work on an equivalent circuit model for elementary discontinuities, which relies on the extraction of primary circuit parameters [218].

The proposed technique for circuit model decomposition, as introduced in [218], initiates with the extraction of circuit parameters for the conventional T or π section of the network from the calibrated Y or Z parameters of an elementary discontinuity's full-wave electromagnetic (EM) model. To assess the uniformity of the extracted circuit parameters across a frequency range of interest, the average rate of convergence (AROC) concept is employed. In this work, we also utilize the AROC concept to develop a comprehensive equivalent circuit model for a full-wave EM structure. AROC quantifies the average rate of change of a function per unit within a specified interval. It is determined by the slope of a straight line connecting the endpoints of the interval on the function's graph. The circuit parameter under consideration exhibits potentially sharp variations throughout the frequency range of interest. To analyze these variations, the curve representing the circuit parameter can be divided into multiple non-uniform segments, allowing for the calculation of the average rate of change (AROC) within each segment over the specified frequency range. The adoption of a non-uniform frequency sampling strategy enables us to densely discretize the curve in the vicinity of potential resonant conditions across the desired frequency band, where the graph may exhibit maxima or minima. These extremal points can be determined mathematically by equating the first and second derivatives of the circuit parameter value with respect to frequency to zero. By employing this technique, we achieve a precise circuit decomposition process, enhancing the accuracy of our analysis.

From [218], the analysis of the average rate of change (AROC) in the extracted circuit parameter serves as a fundamental criterion for assessing the precision of the equivalent circuit model for

both an elementary discontinuity and a three-dimensional electromagnetic (EM) structure. By examining the AROC, we can effectively evaluate the fidelity of the constructed equivalent circuit models in accurately representing the behavior of the discontinuity and the overall EM structure. The core concept behind the circuit model decomposition technique relies on the utilization of the $\overline{AROC}_{avg}$ as a measure of circuit parameter stability within the equivalent circuit model. The objective is to decompose the primary T or π network elements in a manner that ensures consistency among all circuit parameters across a broad frequency range of interest. By achieving this goal, the decomposed circuit model maintains coherence and accuracy throughout the entire frequency spectrum under examination. In [218], during the circuit model decomposition process, every parameter of a primary T or π network is disassembled into another set of T or π networks. This iterative technique is applied successively until all the extracted circuit parameters exhibit constancy across the desired frequency range. At each stage of decomposition, an additional loop is introduced into the primary equivalent circuit. This stepwise expansion and refinement procedure facilitates the attainment of a more comprehensive and accurate representation of the circuit behavior, ensuring stability and consistency of the circuit parameters over the entire frequency band of interest. Fig. 2 illustrates the final circuit topology after $N^{th}$ stage decomposition in case of $[T-T-T-\cdots-T-T]$, $[T-\pi-T-\cdots-\pi-T]$, $[\pi-\pi-\pi-\cdots-\pi-\pi]$ and $[\pi-T-\pi-\cdots-T-\pi]$ combinational circuit topology.

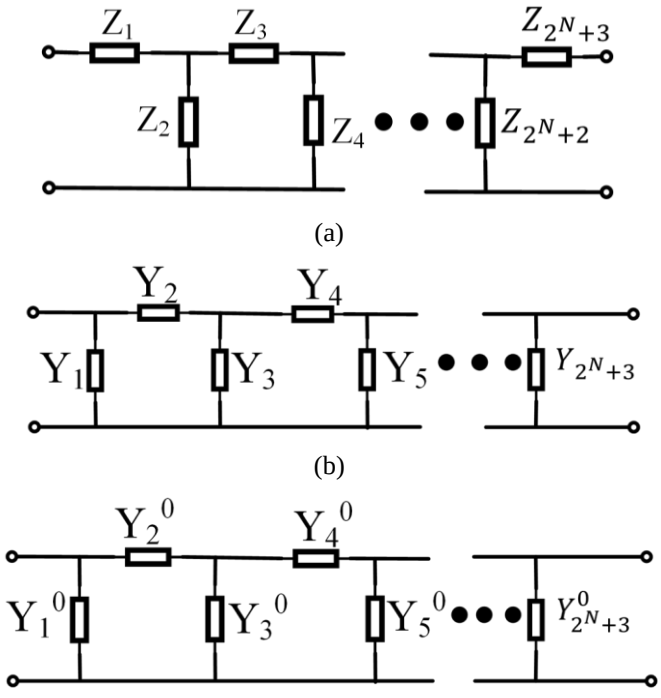

(c)

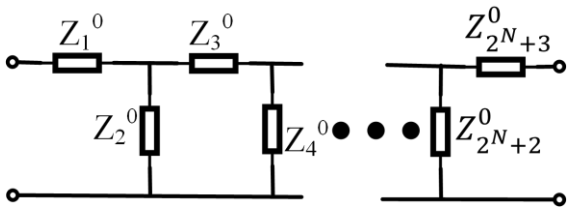


(d)

Figure 7.2 Network topology after $N^{th}$ stage decomposition [9] (a) $[T-T-T-\cdots-T-T]$; (b) $[T-\pi-T-\cdots-\pi-T]$; (c) $[\pi-\pi-\pi-\cdots-\pi-\pi]$; (d) $[\pi-T-\pi-\cdots-T-\pi]$

## 7.4 Equivalent network of mutual couplings

In the context of modeling mutual couplings using equivalent networks, the process involves extracting the equivalent network for lower-order mutual couplings initially. Subsequently, higher-order mutual couplings are deduced in a sequential manner. Throughout this procedure, $\overline{AROC}_{avg}$ is computed to determine the extent of circuit model decomposition, ensuring the consistency of all circuit parameters across the frequency band of interest. This approach allows us to iteratively refine the circuit model, ensuring an accurate representation of the mutual coupling effects while maintaining stability and coherence within the overall network model. Three generalized examples of mutual couplings in structures with various transmission line discontinuities are illustrated in Figure 7.3. Three, four and five discontinuity consisting examples are illustrated here to show the arrangement of mutual couplings in different scenario.

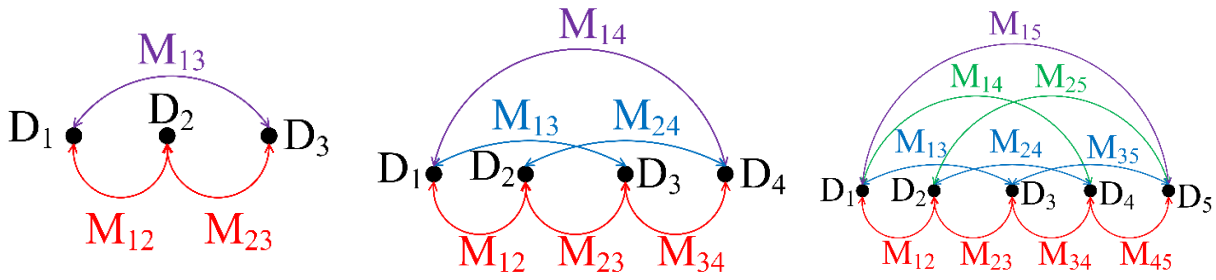


(a) (b) (c)

Figure 7.3 Mutual couplings of different order in circuits (a) three transmission line discontinuities (b) four transmission line discontinuities (c) five transmission line discontinuities

### 7.4.1 Equivalent network of first order mutual coupling

The first order mutual coupling is also known as in-line coupling. Figure 7.3 illustrates few

examples consisting with various number of transmission line discontinuities and mutual couplings between them. Different order of mutual couplings are indicated by $M_{mn}$ where $m$ is former discontinuity and $n$ is later discontinuity. The discontinuities are indicated by $D_i$ where $i = 1,2,3,\dots,p$. Here, $p$ represents the total number of transmission line discontinuity. In case of first order mutual coupling, $m$ and $n$ of $M_{mn}$ are subsequent number which represent the mutual coupling between adjacent transmission line discontinuities. For better generalization, let us consider that all the discontinuities are non-uniform in the illustrated cases in Figure 7.3(a Figure 7.3(b) and Figure 7.3(c). Therefore, all the adjacent couplings are non-uniform due to the asymmetry in the structures.

In Section III, we present the strategy for developing an equivalent circuit model for a specific transmission line discontinuity. This approach allows us to determine the equivalent circuit topology for $D_i$. To establish the mutual coupling circuit between two consecutive discontinuities, we begin by obtaining the electromagnetic (EM) simulation results for these coupled discontinuities. Once the results are numerically de-embedded, we extract the circuit parameters from them. Before proceeding, it is necessary to define the desired circuit topology. The equivalent network for the respective transmission line discontinuity is derived following the instructions outlined in the previous section. Moreover, the primary equivalent T or π network for the in-line mutual coupling should be connected between the other two equivalent networks corresponding to the discontinuities as shown in Fig. 4. The circuit parameters will be extracted from this circuit topology and the $\overline{AROC}_{avg}$ will be calculated. Figure 7.2 illustrated network decomposition technique should be applied on the primary equivalent T or π network corresponding to the in-line coupling. After each decomposition step, the $\overline{AROC}_{avg}$ will be calculated and compared with the $\overline{AROC}_{avg}$ found from previous decomposition stage. The network decomposition process for the in-line coupling's equivalent circuit should be stopped when the $\overline{AROC}_{avg}$ reach to its minimum value. By this way, equivalent circuit corresponding to the in-line coupling between two discontinuities can be developed while the extracted circuit parameters are consistent over a broadband frequency.

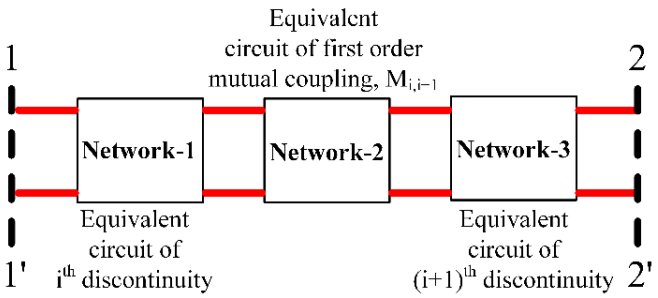


Figure 7.4 Complete equivalent circuit consisting of two mutually coupled transmission line discontinuities

### 7.4.2 Equivalent network of higher order mutual coupling

Once the accurate equivalent circuit model for the first-order mutual coupling has been determined, the next stage in the model development process involves deriving the higher-order mutual couplings in the form of their equivalent circuits. To obtain the second-order mutual coupling, a series of three consecutive transmission line discontinuities is cascaded, and their corresponding EM simulation results are obtained. These results are numerically de-embedded and used to extract the circuit parameters. The equivalent circuit topology should be arranged as shown in Figure 7.5. In Figure 7.5, network-2 shows the equivalent circuit model of the first order mutual coupling between network-1 (i.e. equivalent network of (i-1)$^{th}$ discontinuity) and network-3 (i.e. equivalent network of i$^{th}$ discontinuity). Similarly, network-4 represents the equivalent circuit model of the first order mutual coupling between network-3 (i.e. equivalent network of i$^{th}$ discontinuity) and network-5 (i.e. equivalent network of (i+1)$^{th}$ discontinuity). From section IV.A, network-2 and network-4 is derived according to the circuit decomposition process. The equivalent circuit corresponding to the second order mutual coupling between (i-1)$^{th}$ and (i+1)$^{th}$ discontinuity is indicated in the Fig. 5 as network-6. The derivation of the second-order mutual coupling circuit follows a similar approach to the modeling of the in-line coupling discussed in Section IV.A. With the knowledge of the existing networks obtained from previous steps, the primary network of the T or $\pi$ section serves as the equivalent network for the second-order mutual coupling. The $\overline{AROC}_{avg}$ is calculated as a measure of performance. Subsequently, the primary network is decomposed into its extended version, as depicted in Figure 7.2. This iterative network decomposition process continues until the $\overline{AROC}_{avg}$ reaches its minimum value. This process can be repeated for determining other higher order mutual couplings' circuit equivalent in the target structure

sequentially.

Once all the transmission line discontinuities and mutual couplings of different orders are modelled, we may cascade these equivalent networks by parts in order to develop the complete equivalent circuit model of the target structure as illustrated in Figure 7.1.

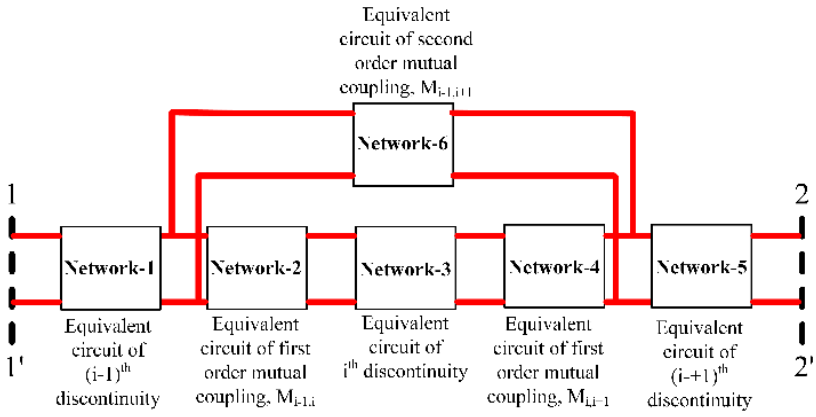


Figure 7.5 Complete equivalent circuit consisting of three mutually coupled transmission line discontinuities

The proposed equivalent circuit model development technique from a target structure is summarized as follows.

1. Choose a target field model structure whose complete equivalent circuit model should be developed.
2. Divide the target structure into segments. These segments include transmission line discontinuities and connecting lines between these discontinuities.
3. Identify different types of discontinuities in the target structures.
4. Develop equivalent circuit models of these different transmission line discontinuities one-by-one in the following manner.
    a. Do the full-wave EM simulation of a particular type of transmission line discontinuity in a commercial EM model simulator such as HFSS and CST.
    b. Numerically de-embed the [S], [Y] and [Z] parameters from the EM simulation results and extract the circuit parameters.
    c. Compute the $\overline{AROC}_{avg}$ from all the circuit parameters and decompose the circuit elements further to meet the desired $\overline{AROC}_{avg}$ value to get the circuit parameters constant over the

frequency band.

d. Finish the equivalent circuit model development of the particular discontinuity by cascading all the decomposed networks together.

5. After developing the equivalent circuit models of all types of discontinuities in the target circuit independently, mutual couplings should be modelled next. Modelling of in-line coupling will be the first step.
6. First order coupling between two discontinuities will be modelled as follows.
   a. Each two consecutive discontinuities will be simulated in HFSS/CST. De-embedded S-parameters will be used to extract the circuit parameters.
   b. The complete equivalent circuit topology will be set-up by cascading a T or π network representing the mutual coupling surrounded by the deduced equivalent circuit of two discontinuities obtained in step 4. This T or π network will be decomposed for the minimum $\overline{AROC}_{avg}$ value. By this way, the in-line couplings between different set of consecutive discontinues will be modelled.
7. In order to find the equivalent circuit representation of second order mutual coupling, three consecutive discontinuities will be arranged in a row and their full-wave EM simulation results should be recorded. The equivalent circuit topology for these coupled three discontinuities will consist of networks for three discontinuities, networks for two first order couplings and a single network for second order coupling. Other networks are derived in step 4 and step 6 while a T or π network represents the second order coupling primarily. The de-embedded results are used to extract the circuit parameters. The $\overline{AROC}_{avg}$ is computed for all the circuit parameters. The second order coupling represented primary T or π network will be decomposed to minimize the value of $\overline{AROC}_{avg}$.
8. Other higher order mutual coupling will be modelled in a similar manner.
9. While all the circuit equivalents are deduced from the above explained steps, the complete equivalent circuit model of the target structure can be built up.

## 7.5 Illustrative examples

In this section, two examples of microstrip filter are demonstrated. The step-by-step equivalent circuit model development process is illustrated through these examples. The transmission line discontinuities and various couplings between these discontinuities are considered towards the

whole equivalent circuit model development. The first example of fifth order hairpin filter shows all these steps in detail along with EM simulation and circuit equivalent responses. The second example of third order parallel coupled microstrip filter is demonstrated with its EM simulation results and equivalent circuit responses along with measurement results.

### 7.5.1 Application example of fifth-order microstrip filter

The first example is a fifth-order hairpin microstrip filter [219]. The target structure of the fifth-order microstrip filter is shown in Figure 7.6. The U-shaped microstrip lines' lengths are indicated as $L_1$, $L_2$, $L_3$, $L_4$ and $L_5$; widths are presented as $W_1$, $W_2$ and the gap length between these lines are denoted by $S_1$ and $S_2$. This hairpin bandpass filter is a symmetrical structure. The optimum geometric variables for the desired filter response from [219] is found as $[W_1, W_2, S_1, S_2, L_1, L_2, L_3, L_4, L_5] = [1.361, 1.363, 0.226, 0.411, 1.973, 9.946, 2.565, 9.532, 1.267]$, where all the lengths are measured in mm.

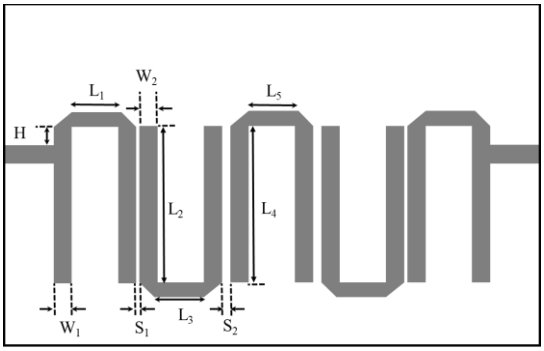


Figure 7.6 Target structure of a fifth-order microstrip filter

The first step of the equivalent circuit model development of target structure illustrated in Fig. 6, is to develop the equivalent circuit corresponding to the gap discontinuity between two U-shaped resonators as shown in Figure 7.7(a). We setup the full-wave EM simulation environment while the two U-shaped resonators are weekly coupled to its input and output port. Then we follow the circuit model development process for transmission line discontinuity structures with the help of AROC curve of extracted circuit parameters as proposed in [218] as well as further explained in section III of this work. A conceptual block diagram of such setup and the developed equivalent circuit model of the transmission line gap under consideration is illustrated in Figure 7.7(b) and Figure 7.7(c), respectively.

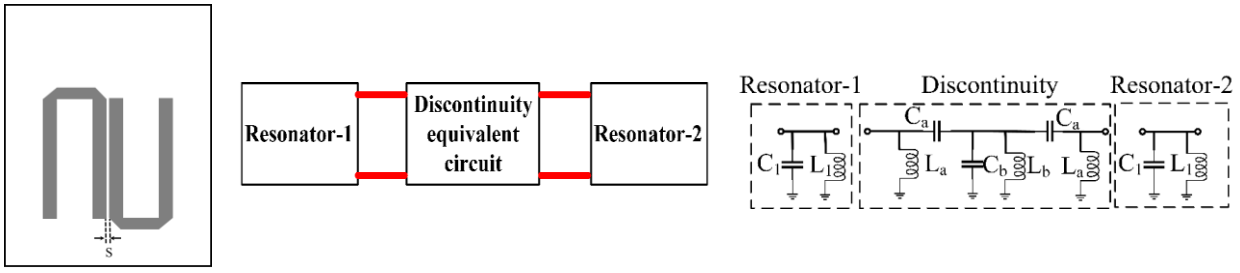


(a) (b) (c)

Figure 7.7 Two gap coupled U-shaped resonators. (a) Full-wave structure (b) block diagram (c) equivalent circuit

In the second step, we need to find out the first-order mutual couplings between two consecutive discontinuities. In order to do that, three U-shaped resonators should be line-up in a row for its full-wave EM simulation. Similar to the previous step, first and last resonators are weekly coupled to the input and output port. The block diagram of the equivalent circuit arrangement is shown in Figure 7.8(a). The equivalent network corresponding to the transmission line discontinuity in the target circuit is already deduced in previous step as shown in Figure 7.7(c). The resonators are represented by a parallel LC network as usual. The remainder circuital part (first order mutual coupling) should be deduced with the help of de-embedded circuit parameters from the full-wave EM simulation results. Figure 7.8(b) illustrates the equivalent circuit model of three gap coupled U-shaped resonator that meets the desired level of $\overline{AROC}_{avg}$.

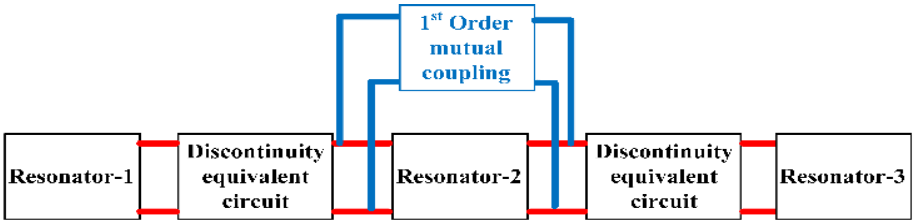


(a)

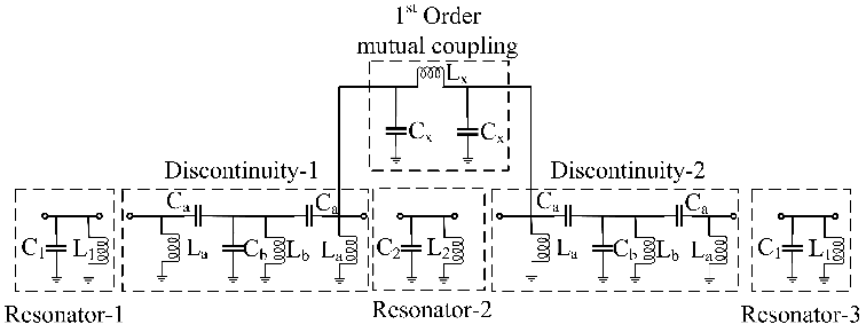


(b)

Figure 7.8 Three cascaded gap coupled U-shaped resonators represented by (a) block diagram (b) equivalent circuit

In the third step, the second order mutual coupling should be derived in the similar manner. Four U-shaped resonators are lined up in a row so that there are three transmission line discontinuities exist and the second order mutual coupling between first and third discontinuity can be easily identified. The conceptual block diagram of equivalent circuit model arrangement is illustrated in Figure 7.9(a). From previous two steps, gap discontinuity corresponding equivalent circuits and equivalent circuit corresponding to the first order mutual couplings between each two consecutive discontinuities are already deduced. The de-embedded circuit parameters from the four cascaded gap coupled hairpin resonators' EM simulation results are utilized to deduce the second order mutual couplings in terms of their equivalent circuit models. Figure 7.9(b) illustrates the equivalent circuit model of four gap coupled U-shaped resonator that meets the desired level of $\overline{AROC}_{avg}$.

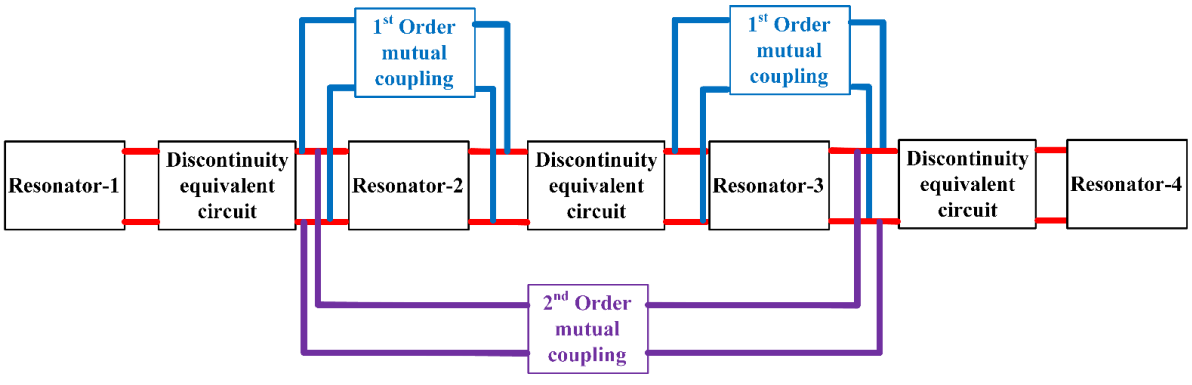


(a)

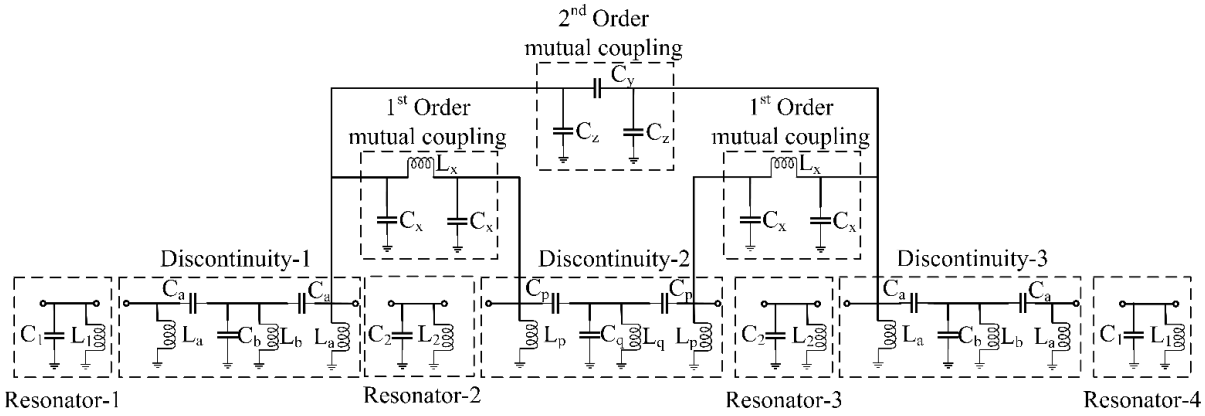


(b)

Figure 7.9 Four cascaded gap coupled hairpin resonators setup (a) block diagram (b) equivalent circuit.

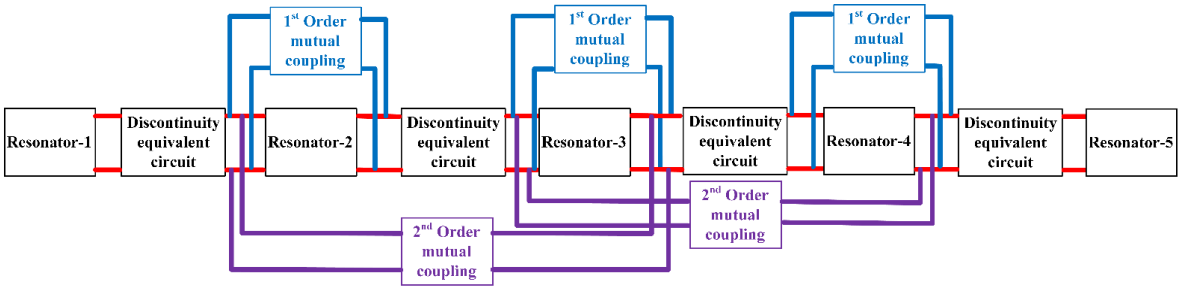


(a)

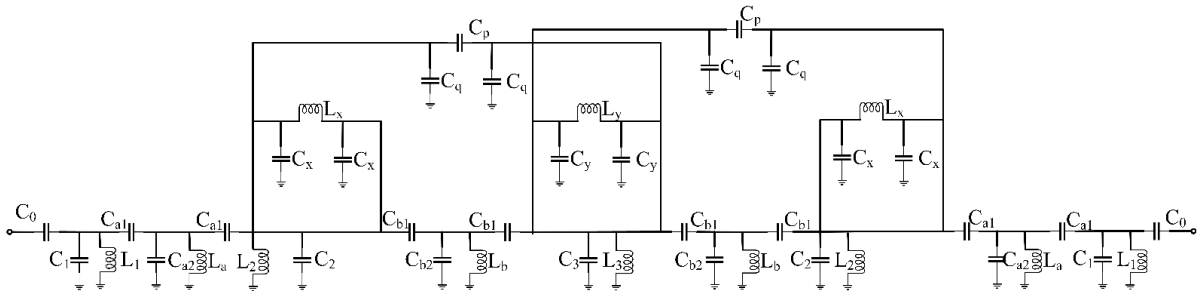

(b)

Figure 7.10 Complete equivalent model of the target structure (a) block diagram (b) equivalent circuit model

Finally, the complete conceptual block diagram of the target structure and the equivalent circuit model is developed as shown in Fig. 10. The extracted circuit parameters are: $L_1 = 0.66$, $L_2 = 0.73$, $L_3 = 3.63$, $L_a = 0.31$, $L_b = 5.0$, $L_x = 2.7$, $L_y = 7.61$, $C_0 = 7.69$, $C_1 = 1.96$, $C_2 = 1.07$, $C_3 = 1.03$, $C_{a1} = 0.9$, $C_{a2} = 4.3$, $C_{b1} = 79$, $C_{b2} = 0.002$, $C_x = 0.01$, $C_y = 0.01$, $C_p = 96.7$ and

$C_q = 0.37$. Here, all the inductances and capacitances are measured in $nH$ and $pF$, respectively. The calculated $\overline{AROC}_{avg}$ meets the desired level ($1 \times 10^{-5}$) from all the extracted circuit parameters. Fig. 11 illustrates the S parameters comparison between the EM simulation result and the equivalent lumped element circuit simulation result.

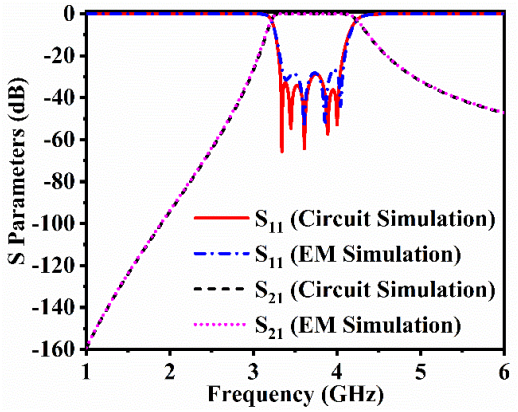


Figure 7.11 Target five-order microstrip filter response comparison between EM simulation and equivalent circuit simulation

To highlight the effects of higher order couplings, equivalent circuit performance at different level of mutual couplings of fifth order microstrip filter example from Figure 7.6 is illustrated in Figure 7.12. Circuit parameters are listed in Table 7.1 and Table 7.2 where the unit of inductances and capacitances are nH and pF, respectively. Figure 7.12 shows that the filter performance without any mutual couplings can not achieve the desired response. Equivalent circuit with first order coupling network shows better performance. However, the stopband insertion loss cannot achieve the desired level and the return loss curve does not show all the transmission poles. On the other hand, equivalent circuit that considers both of first order and second order couplings, achieves the desired filter performance. Therefore, the mutual couplings of different order is important to develop complete equivalent circuit model of a target structure.

Table 7.1 Inductances at different model development stages (Fifth order microstrip filter example)

| Circuit | $L_1$ | $L_2$ | $L_3$ | $L_a$ | $L_b$ | $L_x$ | $L_y$ |
|---|---|---|---|---|---|---|---|
| 1st and 2nd order mutual coupling | 0.66 | 0.73 | 3.63 | 0.31 | 5.0 | 2.7 | 7.61 |
| Only 1st order mutual coupling | 0.68 | 0.96 | 3.39 | 0.37 | 5.0 | 2.7 | 7.67 |
| No mutual coupling | 0.81 | 0.97 | 3.4 | 0.42 | 5.0 | - | - |

Table 7.2 Inductances at different model development stages (Fifth order microstrip filter example)

| Circuit | $C_0$ | $C_1$ | $C_2$ | $C_3$ | $C_{a1}$ | $C_{a2}$ | $C_{b1}$ | $C_{b2}$ | $C_x$ | $C_y$ | $C_p$ | $C_q$ |
|---|---|---|---|---|---|---|---|---|---|---|---|---|
| 1st and 2nd order mutual coupling | 7.69 | 1.96 | 1.07 | 1.03 | 0.9 | 4.3 | 79 | 0.002 | 0.01 | 0.01 | 96.7 | 0.37 |
| Only 1st order mutual coupling | 9.19 | 1.85 | 1.13 | 1.14 | 0.95 | 3.57 | 79.2 | 0.029 | 0.01 | 0.03 | - | - |
| No mutual coupling | 9.09 | 1.53 | 116 | 1.28 | 0.90 | 2.94 | 55.0 | 0.077 | - | - | - | - |

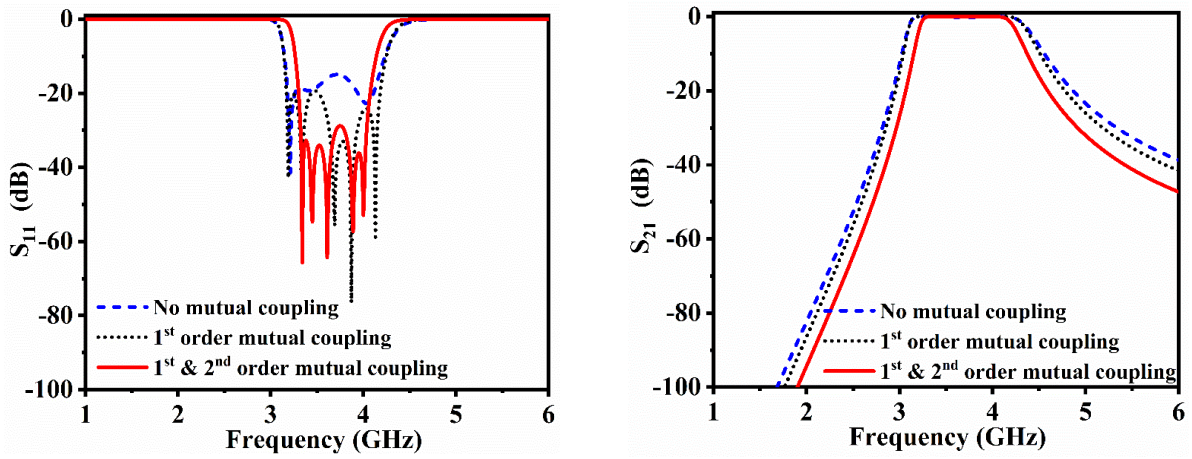


(a) (b)

Figure 7.12 Equivalent circuit performance comparison of Example-1 at different mutual coupling situation (a) $S_{11}$(dB) (b) $S_{21}$(dB)

## 7.5.2 Application example of parallel-coupled microstrip filter

To validate the proposed equivalent circuit model development technique, a third-order parallel-coupled microstrip bandpass filter (midband frequency $f_0$ = 3.6GHz) with 4% fraction bandwidth and 20-dB return loss is designed on a 0.635mm Rogers 6010 substrate with a dielectric constant of 10.7 and a loss tangent of 0.0023. The layout is presented in Figure 7.13(a) which consists of half-wavelength line resonators. These resonators are strategically arranged such that neighboring

resonators run parallel to one another for half of their length. This parallel configuration enables a substantial coupling effect, even with relatively small spacing between resonators. Consequently, this filter structure proves highly advantageous for the construction of filters with wider bandwidths [220]. The optimized geometric parameters are as follows: $L_1 = 7.86, L_2 = 7.8, W_1 = 0.41, W_2 = 0.5, S_1 = 0.24$ and $S_2 = 0.8$ where all the lengths are in mm unit.

The equivalent circuit model of the target filter structure is developed from the procedure outlined at the end of section IV. The half-wavelength line resonators are modelled as a parallel LC network. The gap corresponding equivalent circuit model is derived as a network consisting of series inductances and parallel LC section. Two shunt connected inductance from two end of the network absorbs to the resonators' LC network. The first order mutual coupling between two consecutive gap is modelled as a π-network where capacitances are shunt connected. The input and output coupling to the first and last resonator is modelled as capacitive coupling with the input and output port. The overall equivalent circuit model is shown in Figure 7.13(b).

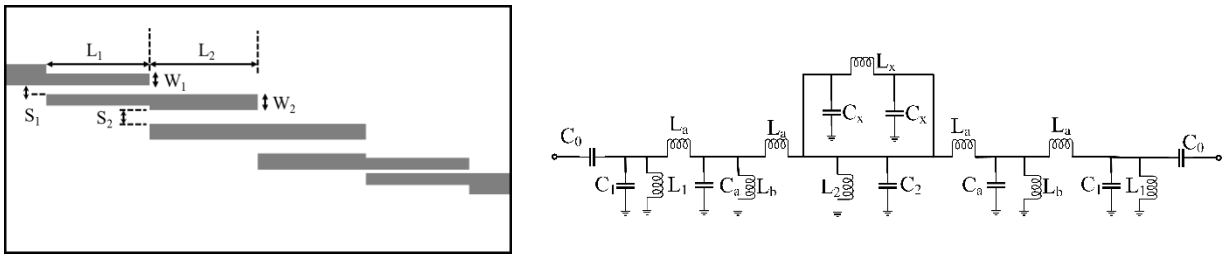


(a) (b)

Figure 7.13 Third-order parallel-coupled microstrip filter. (a) Layout (b) Equivalent circuit

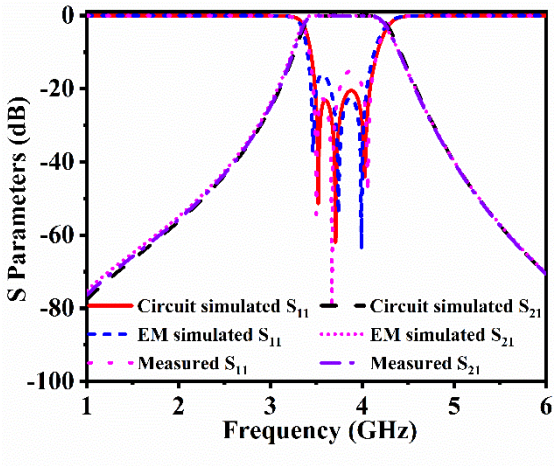


Figure 7.14 Target three-order parallel-coupled microstrip filter response comparison between measurement, EM simulation and equivalent circuit simulation results

The extracted circuit parameters are: $L_1 = 1.06$, $L_2 = 0.31$, $L_a = 2.3$, $L_b = 0.55$, $L_x = 1.5$, $C_0 = 2.931$, $C_1 = 1.86$, $C_2 = 5.34$, $C_a = 4.41$, and $C_x = 0.81$. Here, all the inductances and capacitances are measured in $nH$ and $pF$, respectively. The calculated $\overline{AROC}_{avg}$ meets the desired level ($1 \times 10^{-5}$) from all the extracted circuit parameters. Figure 7.14 illustrates the S parameters comparison between the measurement result, EM simulation result and the equivalent lumped element circuit simulation result. The target third-order parallel-coupled microstrip filter was measured using Keysight N5224B PNA microwave network analyzer. The equivalent circuit model generated S-parameters differs a little bit from the full-wave EM simulation results. However, the EM simulation results demonstrate that the filter has achieved the desired performance such as passband return loss and stopband insertion loss. An excellent agreement is found between the measured and simulated results.

## 7.6 Discussions

In case of the two exampled bandpass filter circuits, we have employed simple capacitive and/or inductive couplings to model the input/output (I/O) couplings. The circuit model decomposition technique can also be used to model these elements using the AROC concept. However, incorporating such a step would complicate the final equivalent circuit, which is unnecessary to a certain extent for low-frequency applications. Nevertheless, in structures operating in millimeter-

wave and sub-THz frequencies, the rigorous modeling of mutual couplings between input and output discontinuities may be required, necessitating the additional design step.

This paper extensively examines the modeling technique for mutual couplings of different orders. It is observed that higher-order couplings between transmission line discontinuities may not have a significant impact on the overall circuit performance. The influence of these higher-order couplings varies depending on the sensitivity and operating frequency of the target structures. To determine this sensitivity, we utilize the AROC concept. If the considered higher-order coupling does not affect the circuit performance within the desired operating frequency range, the $\overline{AROC}_{avg}$ will not decrease any further. By considering this aspect, we can determine the number of higher-order couplings that need to be modeled.

Two examples of planar circuits are demonstrated in this work for the validation of proposed equivalent circuit model development method. Other circuit realizations such as conventional waveguides, non-radiating dielectric (NRD) waveguides etc. can also be modeled through the proposed method as the AROC concept and circuit model decomposition technique are valid regardless of circuit realization technology.

## 7.7 Conclusion

In conclusion, this research has presented a comprehensive technique for developing a complete equivalent circuit model from a target electromagnetic (EM) structure. The proposed methodology is based on two key pillars: the average rate of change (AROC) concept and the circuit model decomposition technique. By leveraging EM model simulation results obtained from different segments of the target circuit, the equivalent circuit models for segmented discontinuities or elements are derived. The cascading of these segmented networks results in the complete equivalent circuit model. The focus of this work has been on modeling the mutual coupling of arbitrary orders between transmission line discontinuities. Two planar filter structures were used as examples to demonstrate and validate the effectiveness of the proposed method. The equivalent circuit model responses were compared favorably with the field modeling responses for both examples. This highlights the accuracy and applicability of the developed methodology in capturing the behavior of the target structures.

# CHAPTER 8 ARTICLE 7: ANN MODEL-BASED ELECTROMAGNETIC OPTIMIZATION BY FIELD-CIRCUIT MODEL MAPPING

Chandan Roy and Ke Wu

Submitted to *IEEE Transactions on Microwave Theory and Techniques* on 24 June 2023

In this paper, an ANN model development technique is described for efficient and fast high frequency structure design and optimization. Unlike the well-documented space mapping and aggressive space mapping technology, we map equivalent circuit model parameters to field model geometric parameters through a neural modeling. First, a complete EM structure is segmented into a series of different discontinuities. Then, the equivalent circuit model corresponding to each discontinuity is derived from a set of calibrated circuit parameters. Next, couplings of different orders between the discontinuities are represented as a part of equivalent circuits. Finally, the complete equivalent circuit model of a full-wave EM structure is developed. All the circuit parameters are extracted against different combinations of critical geometric parameters of the target EM structure. This dataset is used to develop the ANN model for mapping the equivalent circuit model parameters to EM model geometric parameters. At this stage, the circuit model can be used for optimization purposes. The optimized circuit parameters are then mapped back to the geometric parameters in connection with the pre-designated performance. In this work, a dual-band resonant-aperture (RA) rectangular waveguide filter and a third order nonradiative dielectric (NRD) waveguide filter are exampled to demonstrate the proposed methodology. Both the examples show a good agreement between simulation and measurement results.

## 8.1 Introduction

With the ever-increasing applications of high-frequency and broad-band structures in wireless communication systems, accurate electromagnetic (EM) structure design becomes critical and complex as structure composition and integration density get more and more involved. Well-known EM field numerical analysis is set to solve the modeling problem accurately. Such high-frequency structures deal with lots of detailed geometric parameters whose slight deviation may significantly affect the system performance. The design and optimization of such complicated structures usually require repetitive adjustments of numerous geometrical parameters. However, these repetitive EM

simulations may exceptionally be time consuming and computationally expensive. To mitigate these issues of EM modeling, analytical or empirical circuit models corresponding to specific EM models are well-studied in literature [49], [51], [123], [127], [128], [56], [57], [100], [221], [222]. The full-wave EM model and empirical circuit model are generally named as fine model and coarse model, respectively. The fine model is accurate but computationally expensive while the coarse model is fast but less accurate. Space mapping (SM) technology and its evolving versions provide a combination of fine model and coarse model which offers both of high accuracy and fast speed [49], [51], [123], [127], [128]. However, such empirical circuit models become unacceptably inaccurate while operating frequency is extremely high, such as the THz frequency range. In this case, lumped-element equivalent circuit model become more accurate and preferred.

The well known space mapping (SM) theory was proposed in [49] for the circuit optimization using a parameter space transformation. This SM technique reduces the computational load by shifting the optimization task to the coarse model and require only a few fine model simulations in the complete design process. In [51], a new SM approach named aggressive space mapping (ASM) employs an aggressive strategy for updating the SM approximation. A trust region aggressive space mapping (TRASM) algorithm is proposed in [123] to integrate a methodology of trust region with ASM technique. In [127], a hybrid aggressive space mapping (HASM) optimization algorithm is proposed which exploits both the direct optimization and trust-region aggressive space-mapping (TRASM) strategy. In [128], a tuning space-mapping technology is introduced where the general tuning space-mapping algorithm is formulated based on a so-called tuning model for microwave design optimization. The validity range of such mapping techniques is limited to the low frequency. At the high frequency applications, these mapping techniques become less accurate.

Neuro space mapping has been another interesting approach for modeling of microwave circuits. SM-based neuro-models reduce the training time, improve generalization ability, and simplifies the ANN topology. In [56], five techniques are presented to generate a variety of SM-based neuro-models. These techniques are named as space-mapped neurons (SMN), frequency dependent SMN (FDSMN), frequency SMN (FSMN), frequency mapped neuron (FMN), and frequency partially mapped SMN (FSMN). In [57], neural space-mapping (NSM) optimization is proposed for EM design which exploits the conventional SM based neuro-modeling techniques for the efficient approximation of mapping. In [100], a knowledge based automatic model generation (KAMG) technique is proposed which is derived to integrate the concepts of automatic model generation,

knowledge based neural networks, and space mapping. Here, fast coarse data generators and fine data generators are utilized simultaneously. In [221], a systematic computer-aided design (CAD) method is proposed for the automatic nonlinear device model enhancement by advancing the concept of Neuro-space mapping. In [222], Neural inverse space-mapping (NISM) optimization is proposed that explicitly uses the inverse of the space mapping from the fine model parameter space to the coarse model parameter space. These neuro-models extract the circuit parameters through ANN modeling which may deviates from real physical model parameters. In addition, the basic SMN maps the fine to coarse model parameter space by ANN. Majority of the coarse/empirical models are valid over the low frequencies only. Such problems can be solved by introducing frequency as input parameter in the coarse space. However, majority of these models consider frequency as an input/output variable of a target ANN model. Such an additional parameter introduces more complexity in the model generation procedure and makes the data collection period longer.

Space mapping technology and its subsequent variants are useful for EM structure optimization in low frequency applications. Neural networks, on the other hand, enhance the coarse and fine model parameters mapping accuracy and speed. However, such neuro-space mapping technique involves frequency as an additional parameter that makes the model more complicated. To overcome all these shortcomings, we propose an ANN model development technique that maps equivalent circuit model parameters to full-wave EM model geometric parameters. First, from our proposed method, an accurate equivalent circuit model is developed from a full-wave EM model structure. Then, the equivalent circuit model parameters are extracted from different combinational sets of EM model's geometric variables. Finally, the target ANN model is developed and trained with these datasets. This ANN model helps us to apply direct optimization algorithm to the lumped-element equivalent circuit model that achieves the desired performance and then it maps the equivalent circuit model parameters to the EM model geometric parameters.

This paper is organized as follows. Section II first introduces a step-by-step process of developing an equivalent circuit model from a full-wave EM model-based structure. This equivalent circuit model development procedure is initiated by partitioning the target full-wave EM structure into different elementary discontinuities and mutual coupling between all the discontinuities. Each partitioned structure is represented by an equivalent circuit model. Such equivalent circuit models are developed by the calibrated full-wave EM simulation results of a particular segment followed

by the accurate circuit parameter extraction process. The complete circuit model is formed by joining these partitioned equivalent circuit models altogether. In section III, the ANN model architecture is described along with the data generation technique. In addition, a hybrid optimization algorithm is briefly described which will be used for the circuit model optimization. The whole workflow is explained step-by-step with a flowchart in section IV. Section V demonstrates two design examples of dual-band RA filter and third-order NRD waveguide bandpass filter. The circuit equivalent results show a good agreement with full-wave EM simulation results and measurement results in both the cases.

## 8.2 Equivalent circuit model development technique

To develop a mathematical model between the full-wave EM model geometric parameters and lumped-element equivalent circuit model parameters, an accurate equivalent circuit model should be developed first from the target EM model. The primary step towards the equivalent circuit model development is to partition the whole structure into different discontinuities. Then, one utilizes the full-wave EM simulation results of those elementary discontinuities followed by three steps of the circuit model development. In the first step, the full-wave EM model simulated S-parameters should be numerically calibrated to eliminate the introduced numerical noise by external ports and others. Such a numerical calibration is required to extract the circuit parameters of device under test (DUT) accurately. Thru-reflect line (TRL) and short-open (SOC) calibration techniques have widely been used among available numerical calibration techniques in the literature [187], [192], [188]. In our recent work, we have introduced the short-open-thru (SOT) calibration technique which provides more stable extracted circuit parameters over a large range of frequency [218]. In this work, SOT calibration technique is utilized to calibrate out the numeric noises. In the second step, the equivalent circuit corresponding to each discontinuity will be developed according to our recent work on equivalent circuit model for elementary discontinuity which is based on extracted primary circuit parameters [218]. Once the equivalent circuit model of each discontinuity is obtained successfully, in the third step, the equivalent circuit model should be developed for mutual coupling between each discontinuity. In high frequency structures, the dimension of discontinuities are electrically short with respect to each other which introduces in-line coupling and cross-coupling between any two discontinuities. After developing the equivalent circuit model corresponding to all the elementary discontinuities, in-line couplings and cross-couplings, the complete equivalent circuit model can be generated for the complete full-wave EM structure.

### 8.2.1 Equivalent circuit model of elementary discontinuity

The conventional equivalent circuit model of any discontinuity is usually represented by a $T$ or $\pi$ section of network. Such networks have been utilized extensively in the literature for the design optimization of full-wave EM structures [217]. However, these small section of networks can only represent the circuit behavior accurately over a narrowband of frequency. In order to develop an accurate equivalent circuit model of a full-wave EM structure, we need to have the extracted circuit parameters constant over a wide band of frequency. In [218], we introduced a generalized methodology to develop such lumped element equivalent circuit model from a 3D EM structure of a discontinuity. However, we did not consider different losses such as radiation and leakage losses in [218]. In this work, we extend the equivalent circuit model development process in case of the lossy structures for high frequency applications considering all the mutual-coupling effect in a target 3D EM structure.

The proposed circuit model decomposition technique in [218] starts from the circuit parameter extraction of a conventional $T$ or $\pi$ section of network from the calibrated $Y$ or $Z$ parameters of an elementary discontinuity's full-wave EM model. To measure the flatness of extracted circuit parameters over a frequency range of interest, the concept of average rate of convergence (AROC) is utilized. The AROC concept is briefly explained here as it is also used in this work for developing the complete equivalent circuit model of a full-wave EM structure. Generally, AROC defines the average change of function per unit in a given interval. It is calculated from a straight line's slope that connects the endpoints of the given interval on the function's graph. Let's assume an arbitrary circuit parameter $K_1$ that varies over a frequency band $[F_1, F_{N+1}]$ as shown in Fig. 1. This curve is segmented into $N$ number of non-uniform portions to calculate the AROC over that specific section. Such a non-uniform frequency sampling allows us to discretize the curve densely nearby possible resonant conditions over an interested band of frequency where the maxima or minima of the curve may be located in the graph. These maxima and minima can mathematically be located by equating zero to the first derivative and second derivative of circuit parameter value with respect to frequency. This technique leads us to an accurate circuit decomposition process.

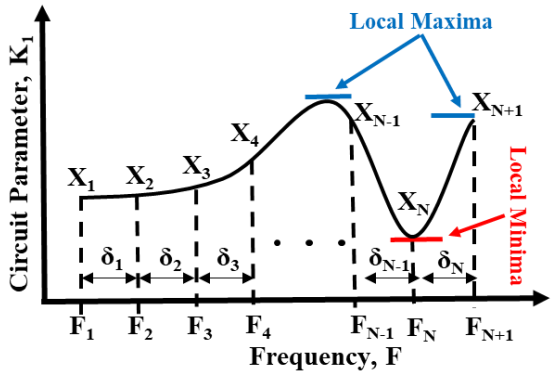


Figure 8.1 Frequency sampling of an arbitrary circuit parameter, $K_1$ over the band of interest

In Figure 8.1, the first section is denoted as $\delta_1$ while $X_1$ is the value of circuit parameter, $K_1$ at the starting frequency $F_1$ and $X_2$ is the value of that circuit parameter at the ending frequency, $F_2$ of the first section. Therefore, the AROC for the first section is formulated as

$$AROC_{\delta_1} = \left|\frac{X_2 - X_1}{F_2 - F_1}\right| \tag{8.1}$$

Similarly, AROC for the $N^{th}$ section, $\delta_N$ is formulated as

$$AROC_{\delta_n} = \left|\frac{X_{N+1} - X_N}{F_{N+1} - F_N}\right| \tag{8.2}$$

The mean AROC over the whole frequency band of interest is expressed as

$$\overline{AROC}_{K_1} = \frac{1}{N}\sum_{i=1}^{N} AROC_{\delta_i} \tag{8.3}$$

The mean AROC of a particular circuit parameter, $K_1$ is calculated from (3) over a given frequency range.

$$\overline{AROC}_{avg} = \frac{1}{n}\left(\overline{AROC}_{K_1} + \overline{AROC}_{K_2} + \cdots + \overline{AROC}_{K_n}\right) \tag{8.4}$$

In equation (4), $\overline{AROC}_{avg}$ denotes the average of all the circuit parameter's mean AROC, $n$ represents the total number of circuit parameters and $\overline{AROC}_{K_n}$ denotes the mean AROC of the n$^{th}$ circuit parameter, $K_n$ over the frequency range. A specific value of $\overline{AROC}_{avg}$ should be decided to define the acceptable flatness of the circuit parameters curve.

The above explained AROC analysis of extracted circuit parameter is used as a guideline for judging the accurate equivalent circuit model of an elementary discontinuity as well as a 3D EM

structure. The main idea of circuit model decomposition technique is based on the $\overline{AROC}_{avg}$ of all the circuit parameters those are involved in the equivalent circuit model. The target is to decompose the primary $T$ or $\pi$ network elements in such a way that all the circuit parameters preserve the consistency over the wide range of interested frequency. In [218], each parameter of a primary $T$ or $\pi$ network decomposed into another set of $T$ or $\pi$ network. This technique is repeatedly applied until all the extracted circuit parameters are constant over the interested frequency band. In each decomposition stage, one additional loop is added to the primary equivalent circuit. Fig. 2 illustrates the final circuit topology after $N^{th}$ stage decomposition in case of $[T-T-T-\cdots-T-T]$, $[T-\pi-T-\cdots-\pi-T]$, $[\pi-\pi-\pi-\cdots-\pi-\pi]$ and $[\pi-T-\pi-\cdots-T-\pi]$ combinational circuit topology.

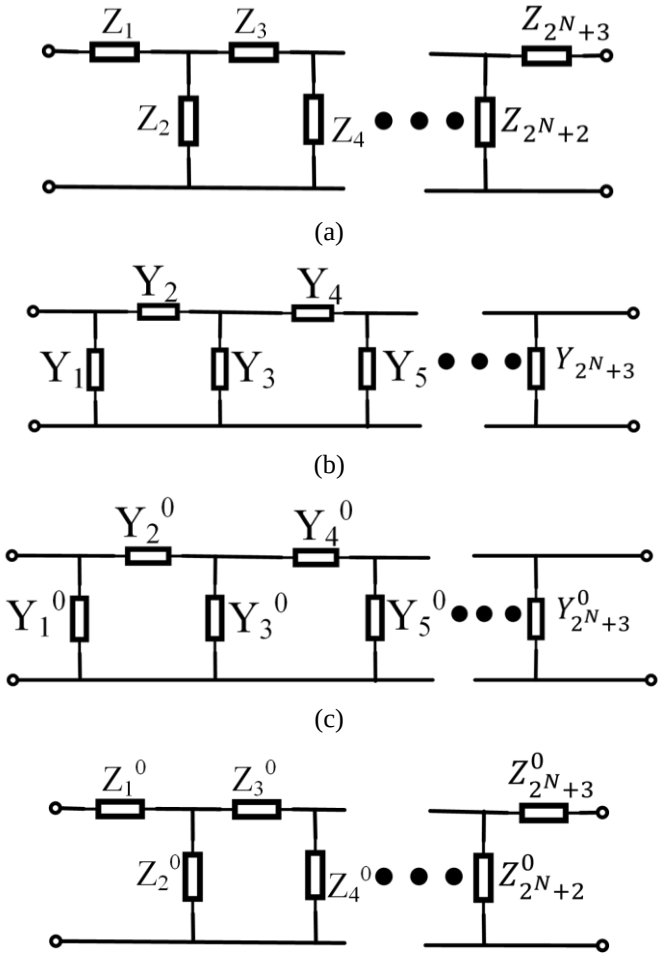

(d)

Figure 8.2 Network topology after $N^{th}$ stage decomposition [218] (a) $[T-T-T-\cdots-T-T]$; (b) $[T-\pi-T-\cdots-\pi-T]$; (c) $[\pi-\pi-\pi-\cdots-\pi-\pi]$; (d) $[\pi-T-\pi-\cdots-T-\pi]$

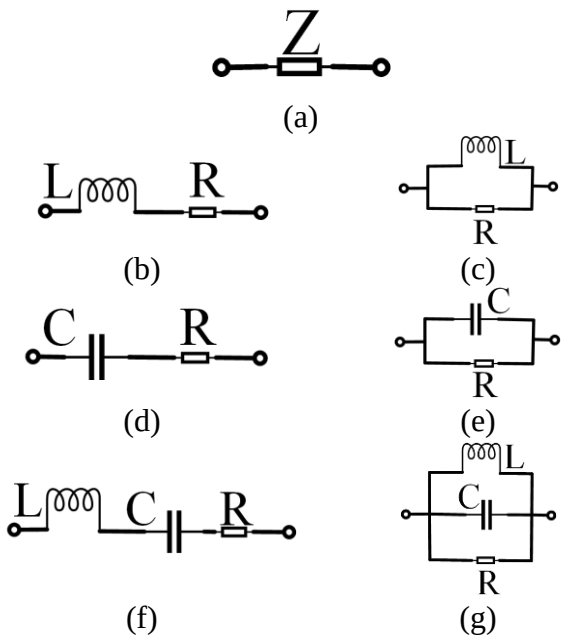


Figure 8.3 Component decomposition (a) ideal component; (b) Series RL combination; (c) Parallel RL combination; (d) Series RC combination; (e) Parallel RC combination; (f) Series RLC combination; (c) Parallel RLC combination

A single element derived from any decomposed network of Fig. 2 can be represented by a series or a shunt combination of a reactive element and a resistive element. Alternatively, it can be formulated as a series or parallel combination of all the three lumped elements. Fig. 3(a) illustrates an ideal component which can be composed of the following combination of a series RL branch, parallel RL branch, series RC branch, parallel RLC branch, and parallel RLC branch as shown in Fig. 3(b)-Fig. 3(g). In each stage of the equivalent circuit model development through the model decomposition process, these branches will be utilized and AROC will be analyzed. Finally, the circuit that retains minimum $\overline{AROC}_{avg}$ will be finalized to represent the corresponding discontinuity. By this way, equivalent circuit model is developed for each different discontinuity that is involved in the complete EM model structure. The next step is to develop the equivalent circuit model for mutual couplings.

### 8.2.2 Equivalent circuit model of mutual couplings

Mutual coupling or electromagnetic field interactions between different circuit elements can be represented by a particular impedance/admittance network topology in the equivalent circuit models. This phenomena leads us to use equivalent circuit models to represent both in-line and cross coupling for multiple-coupled circuits. In [217] , $T$ and $\pi$ section of networks are utilized to represent the equivalent circuits of first order and higher order of mutual couplings. In this work, we have introduced our model decomposition technique to represent the mutual couplings between the discontinuities of a 3D full-wave EM structure. The equivalent circuit development process for the mutual couplings should be initiated after finding the equivalent circuit model for different individual elementary discontinuities of a target 3D full-wave EM structure. In [217], the modeling technique of $N^{th}$ order mutual coupling is outlined and demonstrated for a phased array antenna, a 10-element periodic structure and a planar low pass filter. It shows that the first and second order coupling between the elements are significant while other higher order couplings are negligible due to the larger physical relative distance between two coupled elements. In this work, we have considered first and second order mutual coupling between two coupled elements for the ease of developing the complete equivalent circuit model.

The first step towards the equivalent circuit model development of mutual couplings is to derive the first order mutual coupling between any two coupled discontinuities. Firstly, we need to cascade the developed equivalent circuit model of the consecutive individual discontinuity around the 1st order mutual coupling network as shown in Figure 8.4(a). The equivalent circuit model development technique for individual discontinuity is explained in section II.A. In the first iteration, the conventional $T$ or $\pi$ section of network should be considered as the equivalent section for the representation of 1st order mutual coupling. Then the full-wave EM model should be setup where the two discontinuities are connected with a piece of transmission line. The calibrated EM model simulated S parameters should be utilized to extract the circuit model parameters and $\overline{AROC}_{avg}$ should be calculated from all the extracted circuit parameters. If the desired value of $\overline{AROC}_{avg}$ is not achieved, 1st stage decomposed circuit topology should be carried out for the 1st order mutual coupling network from the $N^{th}$ stage decomposed circuit topology shown Figure 8.2. As the 2nd order mutual coupling network introduces more degree of freedom, we limit the circuit decomposition procedure for mutual coupling networks till the 1st stage.

The equivalent circuit for $2^{nd}$ order mutual coupling should be introduced if the $1^{st}$ stage decomposed networks for $1^{st}$ order mutual coupling can not achieve the desired value of $\overline{AROC}_{avg}$ for the complete EM model of the target structure. Firstly, as Figure 8.4 illustrates, three consecutive elementary discontinuities are cascaded along with $1^{st}$ order mutual coupling while the conventional $T$ or $\pi$ section of network is considered as the equivalent circuit model for $2^{nd}$ order mutual coupling. If the topology is still unable to achieve the desired value of $\overline{AROC}_{avg}$, $1^{st}$stage decomposed circuit topology should be carried out for the $2^{nd}$ order mutual coupling network from the $N^{th}$ stage decomposed circuit topology shown Figure 8.2. As it is mentioned previously that the network decomposition approach is limited to 1st order decomposed network due to enough degree of freedom for the complete equivalent circuit model. If the derived complete equivalent circuit cannot achieve the desired $\overline{AROC}_{avg}$, we can proceed with the development of higher order mutual coupling network. However, in our experiments on different structures for sub-THz applications, all the extracted circuit parameters are stabilized at this stage of the equivalent circuit model development. These equivalent circuit model development steps will be illustrated in the flowchart of Figure 8.4.

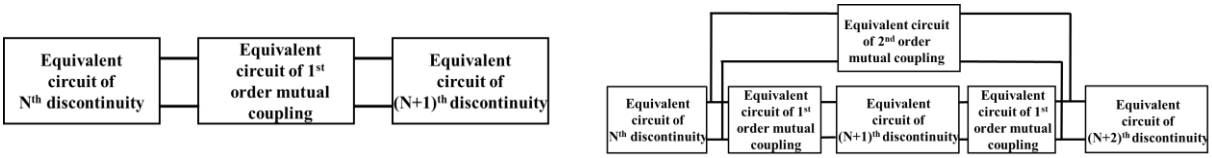


(a) (b)

Figure 8.4 Mutual coupling between discontinuities (a) 1st order mutual coupling in two discontinuity scenario (b) 1st and 2nd order mutual coupling in three discontinuity scenario

## 8.3 ANN model and hybrid optimization algorithm

### 8.3.1 ANN model

In this work, a widely utilized neural network architecture, multilayer perceptron (MLP), is applied for ANN model development where neurons are arranged in different layers. The input and output layers are placed at the first and last layers of the network while other layers are considered as hidden layers. The connection between neurons of adjacent layer is assigned with a weight and each neuron is fed with a biasing value. The inputs to the input layer are presented in a vector form

which are calculated along the layers by a feedforward computation. In this work, we use the transmission line impedance equation inspired feedforward computational equation which is numerically efficient for microwave problems [32]. Here, $w_{jk}^{l}$ denotes the weighted connection between $k^{th}$ neuron of $(l-1)^{th}$ layer and $j^{th}$ neuron of $l^{th}$ layer. Bias is denoted as $b_j^l$ for $j^{th}$ neuron in the $l^{th}$ layer while $a_j^l$ refers to the activation of the $j^{th}$ neuron in the $l^{th}$ layer. The intermediate quantity is $z_j^l$. The $z_j^l$ and $a_j^l$ are formulated as

$$z_j^l = \sum_k Re\left[\frac{a_k^{l-1}+(i\times tanw_{jk}^l)}{1+(i\times a_k^{l-1}\times tanw_{jk}^l)}\right] + b_j^l \tag{8.5}$$

$$a_j^l = \sigma\left(\sum_k Re\left[\frac{a_k^{l-1}+(i\times tanw_{jk}^l)}{1+(i\times a_k^{l-1}\times tanw_{jk}^l)}\right] + b_j^l\right) \tag{8.6}$$

Here, $i$ refers to the imaginary unit and $tan$ denotes the trigonometric tangent operator. The sigmoid function, $\sigma$ is used as the activation function in the hidden neurons while a linear activation function is used in the output layer of the ANN models in this work.

The ANN model developed in this work deals with equivalent circuit parameters in its input and geometric parameters of a full-wave EM model structure in its output. Such geometric dimensions and equivalent circuit parameters vary by many orders of magnitudes. The sigmoid activation function gets saturated as the derivatives of large input numeric values are close to 0 which slow downs the ANN model training. We preprocess all the input and output variables in the range of $[-1,+1]$ in order to accelerate the model training. Finally, the scaled model input value will be mapped back to the original value [31]. Levenberg-Marquardt's algorithm (LMA) [156] is used in this work for training the target ANN model as a fast and efficient algorithm for small-sized networks. The adjustment of weight and bias matrix of the ANN model during the training session has been computed through the error backpropagation algorithm as outlined in [32].

### 8.3.2 Hybrid optimization algorithm

In this work, optimization procedure will be first applied to the complete equivalent circuit model to achieve the desired circuit performance. From the optimized circuit parameters, the ANN model will be used to find the associated geometric parameters. Different types of optimization algorithms are available in the commercial circuit simulators. However, lots of advanced optimization algorithms are recently reported for different types of optimization problems. In [41], we proposed

a hybrid optimization technique which solves the microwave engineering specific optimization problems fast and accurately. This hybrid optimization technique compares the minimized cost function between Grey wolf optimizer (GWO) [79] and nonlinear adaptive weight and golden sine operator (NGS-WOA) based WOA (NGS-WOA) [175] and finally proceed with the optimizer that minimizes the cost function better. These optimized parameters are considered as initial solution during the consecutive homotopy optimization process. Finally, the optimized parameters are provided by the algorithm. In this work, we use this hybrid optimization algorithm for the equivalent circuit optimization.

## 8.4 ANN model development and mapping technique

In this section, we explain the complete step-by-step process of equivalent circuit parameters to critical geometric parameters mapping for the desired performance of a full-wave EM structure. This process starts with the equivalent circuit model development from a full-wave EM model of a structure. The ANN model training data is collected from such full-wave EM simulation and corresponding equivalent circuit parameter extraction. Once the data generation is completed, the ANN model is trained. Afterwards, the equivalent circuit parameters are optimized according to the desired performance. Finally, map these optimized equivalent circuit parameters to the geometric parameters and verify the EM simulation results. The step-by-step procedure is explained below and the workflow is illustrated in Figure 8.5.

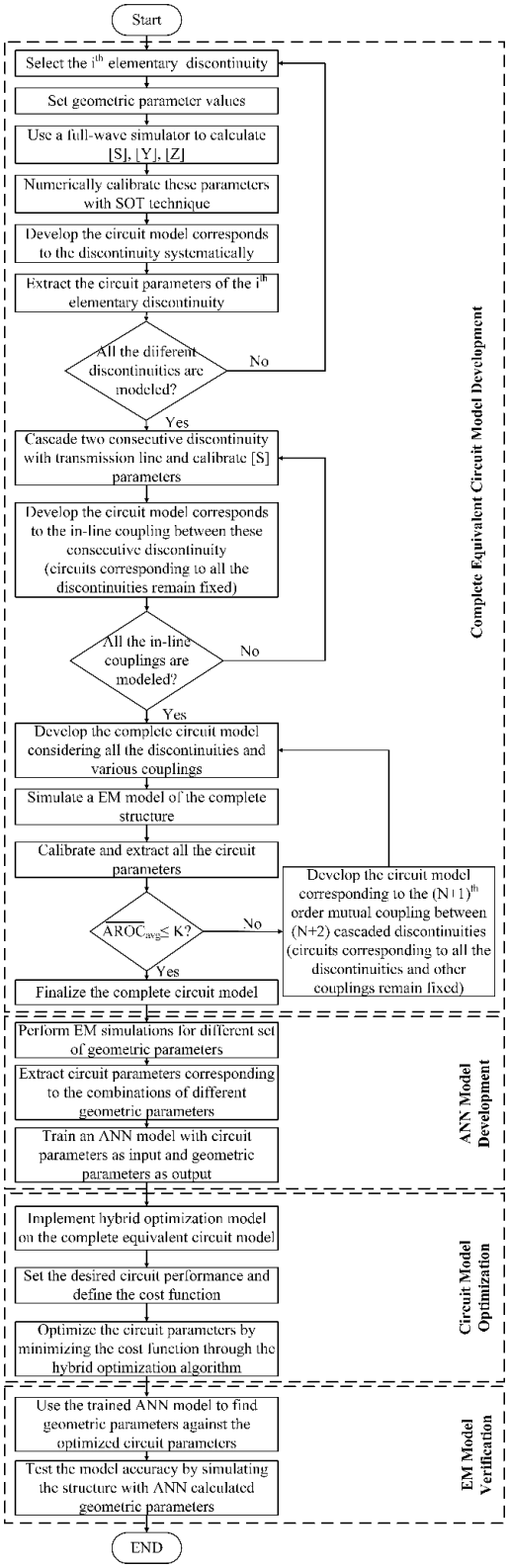


Figure 8.5 Flowchart of proposed mapping technique

1. Indicate different discontinuities associated with the target EM structure. Start with one of the discontinuities and setup a full-wave EM model with arbitrary geometric parameters in a commercial software package such as CST, HFSS etc.
2. Simulate the selected elementary discontinuity in the frequency range of interest. Numerically calibrate the parameters such as [S], [Y] and [Z]. In this work, SOT calibration technique is used.
3. Develop the equivalent circuit model of the discontinuity under consideration. Extract the circuit parameters of the primary $T$ or $\pi$ network and analyze the $\overline{AROC}_{avg}$. Decompose the circuit parameters according to the technique outlined in section II.A to meet the desired value of $\overline{AROC}_{avg}$ for stable circuit parameters.
4. Develop equivalent circuit model of all the elementary discontinuities in the target EM structure. Save these equivalent circuits for the later part of the process.
5. At this stage, the mutual couplings should be modeled. The 1st order mutual coupling between successive discontinuities should be considered first. The primary $T$ or $\pi$ network for the in-line couplings may not achieve the desired value of $\overline{AROC}_{avg}$. In that case, the 1st order element decomposition technique should be applied as explained in section II.B. If the $\overline{AROC}_{avg}$ is not satisfied, the 2nd order mutual coupling should be considered.
6. Usually, the 1st order decomposed network for 2nd order mutual coupling circuit meets the desired value of $\overline{AROC}_{avg}$. If not, higher order mutual coupling circuits can be developed in similar way.
7. After developing equivalent circuits of all the elementary discontinuities and mutual couplings, the complete equivalent circuit of the target EM structure can be developed. As the desired value of $\overline{AROC}_{avg}$ is met for the whole circuit model, the developed equivalent circuit model will be accurate enough to represent the full-wave EM model of the target structure.
8. After the successful development of equivalent circuit model of a full-wave EM structure, the ANN model training data should be generated. Such training data should be prepared by simulating the EM model of the structure for different geometric parameter combination and extracting the circuit parameters from the calibrated S parameters. The geometric parameters will be uniformly distributed based on a rough idea on EM model performance against the variation of geometric parameters.

9. The EM model is simulated against each set of geometric parameters. The numerical SOT calibration technique is employed to the EM model calculated S parameters. The equivalent circuit parameters will be extracted from the calibrated performance parameters. These geometric parameters and equivalent circuit parameters will be considered as the input and output data of the target ANN model, respectively.
10. The ANN model will be trained with the generated data from the previous step. The ANN model accuracy will be determined from the testing data set.
11. After the ANN model is successfully developed, the complete equivalent circuit model will be optimized by the hybrid optimization model as explained in section III.B. The cost function will be carefully formulated in order to meet the desired performance from the EM model of the target structure.
12. The optimized circuit parameters from the hybrid optimization model will be fed to the trained ANN model. The ANN model will provide the geometric parameters against the optimized equivalent circuit parameters. Finally, the ANN model provided geometric parameters will be utilized to design the target structure. The EM model simulated S parameters will be compared with the desired performance.

## 8.5 Illustrative Examples

In this section, two examples of non-TEM mode structures are demonstrated to validate the proposed equivalent circuit model development and ANN model mapping approach. Firstly, an accurate equivalent circuit model of a dual-band rectangular waveguide filter with resonant apertures (RAs) [223] structure is derived and ANN model is used to find out the critical geometric parameters from optimized equivalent circuit model parameters. Secondly, a gap-coupled third order NRD waveguide filter [224] structure is optimized by equivalent circuit model to field model parameters' mapping. In both the cases, equivalent circuit model and field model performances are compared.

### 8.5.1 Dual-band resonant aperture (RA) filter

The classic capacitive and inductive microwave filters are designed based on coupled half-wavelength resonators through thick capacitive and inductive irises, respectively. The capacitive and inductive irises are considered as equivalent to a shunt capacitor or inductor, respectively. In [223], both capacitive and inductive characteristics are represented by RAs with a single aperture.

Fig. 6 shows the RA structure as a main resonant structure of the target filter. Fig. 6 illustrates the dimensions of the RA as width (w), height (h) and thickness (t) with rectangular waveguide dimensions a and b ($a > b$).

In this work, we target to design a dual-band RA filter operating in sub-THz frequency range. According to [223], the second passband of such filter topology demonstrates one more pole than its first passband. Therefore, three cavity resonators will demonstrate three poles and four poles in the first and second passband, respectively. Fig. 7 shows the EM model of the target dual-band RA filter. It indicates six design variables as $w_1$, $w_2$, $h_1$, $h_2$, $l_1$ and $l_2$. We use the standard WR5.1 rectangular waveguide as we are designing a D-band filter. Due to fabrication tolerance, the thickness of the RAs is chosen as 0.15 mm (5.9 mil). As we measure the fabricated prototype without any transitions, the first and last RA should be located 4mm (160 mil) far from the headers of the extension module.

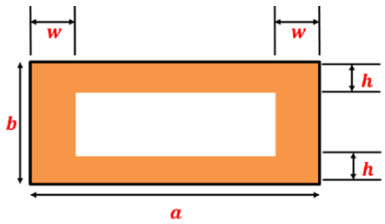


Figure 8.6 Resonant aperture in a rectangular waveguide

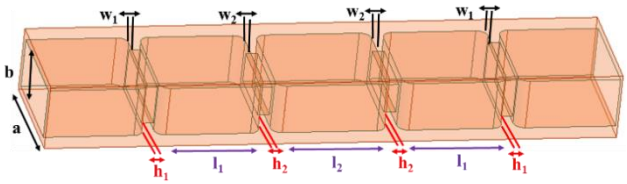


Figure 8.7 EM model of a dual-band RA filter structure

The equivalent circuit model of the dual-band RA filter from [223] is shown in Figure 8.8(a). In order to achieve the desired response from the equivalent circuit model, we use the hybrid optimization algorithm which is described in Section III.B. The cost function is defined in terms of return loss in the passband and insertion loss in the stopband. Such a cost function is mathematically formulated as

$$K_1 = \max\left[(S_{11})_{PB_1}, -RL\right] + \max\left[(S_{11})_{PB_2}, -RL\right] + w * \max[(S_{21})_{SB}, -IL] \qquad (8.7)$$

where the first passband ($PB_1$) is between the edge frequencies $f_1$ and $f_2$; the second passband ($PB_2$) is between the edge frequencies $f_3$ and $f_4$; the stopband ($SB$) is between the edge frequencies are, $f_5$ and $f_6$. For the target dual-band RA filter, the passband return loss level $RL$ is prescribed at 20 dB and the stopband insertion loss level $IL$ is fixed at 20dB. $w$ refers to the balancing coefficient between stopband insertion loss and passband return loss which is set at 0.2 in this work. The parameters in the cost function (7) are

$$P_1 = [f_1\ f_2\ f_3\ f_4\ f_5\ f_6] \tag{8.8}$$

In this example, $f_1$=130, $f_2$=150, $f_3$=170, $f_4$=230, $f_5$=150 and $f_6$=170; where all the frequencies are in GHz. There are eight optimization variables in the conventional equivalent circuit model shown in Figure 8.8(a). The optimized circuit parameters are $L_{R1}$=2.37, $L_{R2}$=0.2, $L_a$=1.48, $L_b$=5.8, $C_{R1}$=6, $C_{R2}$=5.1, $C_a$=0.42, $C_b$=0.1, where all the capacitances and inductances are measured in fF and nH. Fig. 9(a) illustrates the S parameters generated by the optimized equivalent circuit model. Even though the conventional equivalent circuit model represents the low frequency filters well, Figure 8.9(a) shows that the S parameters from this equivalent circuit model with optimized circuit parameters cannot achieve the desired performance. Parasitic effects and different mutual couplings between the RAs should be considered in order to meet the desired circuit performance.

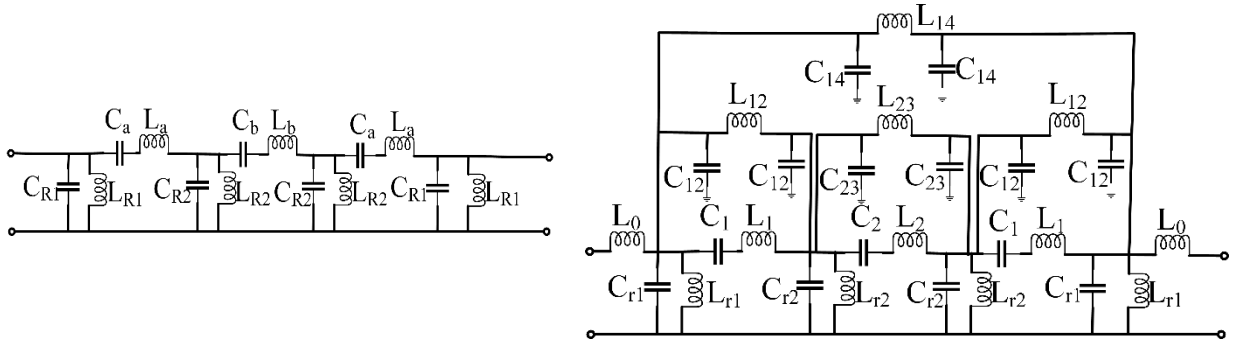


(a) (b)

Figure 8.8 Equivalent circuit model (a) Conventional model [223]; (b) Proposed circuit model

To find the accurate equivalent circuit model of the target dual-band RA filter, the proposed circuit model development technique is applied. The desired value of $\overline{AROC}_{avg}$ is set to $2 \times 10^{-5}$ for the stable extracted circuit parameters over the complete D-band. In order to derive the complete lumped element equivalent circuit model from the field model, we have to follow the steps outlined in Section III. Firstly, we have to start with setting up an elementary discontinuity EM model which

is a RA in this case. Then the HFSS simulated S parameters are numerically calibrated. The circuit parameters are extracted from this numerically calibrated results. Primarily, the conventional T or π network is considered for the circuit parameter extraction. In order to meet the desired value of $\overline{AROC}_{avg}$, we decompose the primary network as it is illustrated in Fig. 2. After finding the appropriate network for the RA, we cascade two RAs connected by a piece of transmission line to find the first order mutual coupling between two discontinuities. Equivalent networks for the first order mutual couplings are derived in similar manner. Similarly, multiple RAs are connected through a piece of transmission line to derive the equivalent networks of higher order mutual couplings. Finally, the complete equivalent circuit model is developed that satisfies the desired value of $\overline{AROC}_{avg}$. Fig. 8(b) illustrates the final equivalent circuit model of target dual-band RA filter. There are fifteen optimization variables in this proposed equivalent circuit model. The same optimization condition is applied here and the optimized circuit parameters are $L_1$=4.4, $L_2$=0.6, $L_{r1}$=0.6, $L_{r2}$=0.12, $L_{12}$=1.5, $L_{23}$=0.55, $L_{14}$=0.17, $L_0$=0.08, $C_1$=0.3, $C_2$=1, $C_{r1}$=0.03, $C_{r2}$=6, $C_{12}$=3.2, $C_{23}$=3.4, $C_{14}$=12 where all the capacitances and inductances are measured in fF and nH. S parameters response from the optimized circuit is shown in Figure 8.9(b) which clearly demonstrates better results as compared to its conventional counterpart.

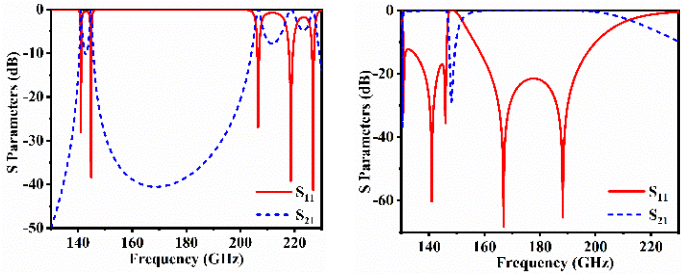


Figure 8.9 S parameters generated from; (a) Conventional equivalent circuit model; (b) Proposed equivalent circuit model

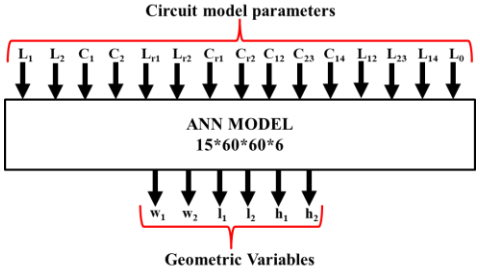


Figure 8.10 ANN model for geometric variables calculation against circuit model parameters

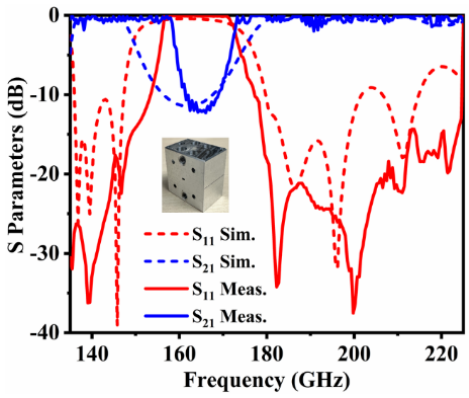


Figure 8.11 Simulated and measured performance of the designed dual-band RA filter

After the successful development of an equivalent circuit model of the targeted field model of the filter structure, we start to collect the training data for the target ANN model. The training data generation has been done in following manner: 6 mil $\leq w_1, w_2 \leq 9$ mil with 1 mil spacing, 1 mil $\leq h_1, h_2 \leq 7$ mil with 2 mil spacing and 50 mil $\leq l_1, l_2 \leq 59$ mil with 3 mil spacing. Therefore, 4096 set of training data is generated in 68 h of HFSS simulation time. Circuit parameters of the proposed equivalent circuit model should be extracted from each HFSS simulation results. These extracted equivalent circuit parameters should be recorded against each combination of the geometric variables. During the ANN model training, we use these circuit model parameters as inputs and geometric variables of the field model as outputs. As Fig. 10 illustrates that the target ANN model is developed with 15-60-60-6 neurons. The ANN model achieves an average error of $1.7e^{-7}$ and $1.9e^{-7}$ for training and testing sets, respectively.

Once the ANN model is trained, we recall the optimized circuit parameter values for the desired response. These equivalent circuit parameters are fed to the developed ANN model. The geometric parameters calculated by the ANN model against given circuit model parameters are as follows: $w_1$=6.7, $w_2$=8.8, $h_1$=2.9, $h_2$=5.2, $l_1$= 52 and $l_2$= 57 where all the length are measured in mil. A prototype is fabricated in order to validate the simulation results. The S-parameters were measured on a THz vector network analyzer with E8257DV05 (from Virginia Diodes Inc.—VDI) frequency extension module for WR5.1 where the operating frequency range is 135GHz - 225 GHz. The short, open, line and thru (SOLT) WR5.1 calibration kit was used to de-embed the measurement system at two reference planes. Figure 8.11 illustrates that both the simulated and measured results meet the desired filter performance. A slight discrepancy is observed due to the calibration issues and dimensional tolerance.

### 8.5.2 Three-pole bandpass NRD filter

Nonradiative dielectric waveguide (NRD) based filter circuits are promising due to their applications in millimeter-wave (mmW) integrated circuits. Such NRD waveguide circuits have not been studied in terms of their equivalent circuit in the literature. In this work, a mmW gap-coupled three-pole bandpass NRD filter is studied which was designed and measured in [224] and theoretically analyzed in [225]. Fig. 12(a) illustrates a EM model of gap coupled third order NRD BPF. Teflon strips ($\varepsilon_r$=2.04) are used (a=2.7 mm and b=3.5 mm) to form the NRD filter. The gap lengths between three dielectric blocks ($D_1$, $D_2$) and resonator lengths ($L_1$, $L_2$) are considered as design variables. Our goal is develop an ANN model to calculate these variables against its equivalent circuit model parameters.

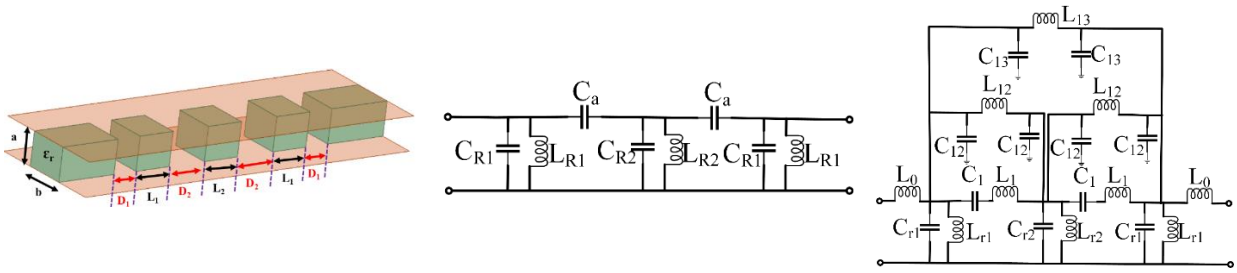


(a) (b) (c)

Figure 8.12 Third order NRD BPF (a) EM model [224]; (b) Conventional equivalent circuit model; (c) Proposed equivalent circuit model

The conventional equivalent circuit model of such gap-coupled circuit is shown in Figure 8.12(b) where the resonators are formed as a parallel LC brunch and gap coupling is represented by an inverter model (electric/magnetic/mixed coupling). This conventional equivalent circuit model has five optimization variables. We use the same hybrid optimizer as previous example to get the optimized circuit parameters. The cost function is defined in same manner which is mathematically formulated as

$$K_2 = \max[(S_{11})_{PB}, -RL] + w * max[(S_{21})_{SB}, -IL] \tag{8.9}$$

where the passband (*PB*) lies between the frequencies $f_2$ and $f_3$; the stopband (*SB*) edge frequencies are, $f_1$ and $f_4$ with $f_1 < f_2 < f_3 < f_4$. For the target NRD filter, the target passband return loss level *RL* and the stopband insertion loss level *IL* is prescribed at 15 dB and 20dB, respectively. *w*

is set to be 0.2 as same as the previous example. The parameters in the cost function (7) are

$$P_2 = [f_1\ f_2\ f_3\ f_4\ ] \tag{8.10}$$

In this example, $f_1$=48, $f_2$=49, $f_3$=50, $f_4$=51; where all the frequencies are in GHz. Optimized circuit parameters are $L_{R1}$=2, $L_{R2}$=0.1, $C_{R1}$=200, $C_{R2}$=47, $C_a$=33; where all the capacitances and inductances are measured in fF and nH. The calculated S parameters from optimized circuit model cannot achieve the desired stopband insertion loss. Therefore, we proceed to develop the accurate equivalent circuit model from the field model of the target NRD filter according to our proposed approach. Figure 8.12(b) illustrates the derived equivalent circuit model from the field model of the target NRD filter that satisfies the desired value of $\overline{AROC}_{avg}$ as $2 \times 10^{-5}$. The optimized circuit parameters of the proposed circuit model are $L_0$=0.27, $L_{r1}$=0.03, $L_{r2}$=0.8, $L_1$=0.37, $L_{12}$=0.18, $L_{13}$=0.52, $C_{r1}$=232, $C_{r2}$=32.7, $C_1$=17.92, $C_{12}$=13.38, $C_{13}$=17.03; where all the capacitances and inductances are measured in fF and nH. S parameters calculated from the conventional and proposed equivalent circuit model are plotted in Figure 8.13. The proposed circuit model generated S parameters meet the desired filter performance better than the conventional circuit model.

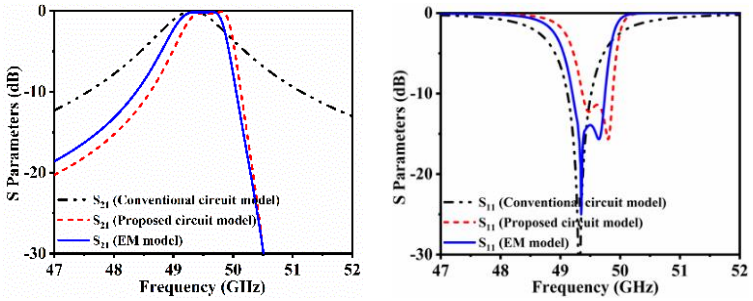


(a) (b)

Figure 8.13 Performance comparison between conventional circuit model, proposed circuit model and EM model. (a) $S_{21}$; (b) $S_{11}$

Once the equivalent circuit model is developed, we prepare to gather the target ANN model training data. The training data generation has been carried out as follows: 0.5 mm ≤ $D_1$ ≤ 2 mm with 0.5 mm spacing, 2.5 mm ≤ $D_2$ ≤ 4 mm with 0.5 mm spacing and 1 mm ≤ $L_1$, $L_2$ ≤ 4 mm with 1 mm spacing. In total, 256 EM simulations were carried out in the range of 47GHz and 52GHz. The total HFSS simulation time was measured as 8.5 hours. The equivalent circuit parameters of the proposed model are extracted in each HFSS simulation. The extracted circuit parameters should be noted against each geometric variables' combination. The circuit model parameters and geometric variables of the field model are used as inputs and outputs during the ANN model training,

respectively. Figure 8.14 illustrates that the target ANN model is developed with 11-50-50-4 neurons. The ANN model demonstrates an average error of $2.3e^{-8}$ and $2.7e^{-8}$ for training and testing sets, respectively. After the ANN model is successfully developed, the optimized equivalent circuit model parameters are considered as the inputs of the trained ANN model. The ANN model provides us with following geometric variables: $D_1$=1.58mm, $D_2$=3.6mm, $L_1$=2.7mm and $L_2$= 2.75mm. The EM model simulated S parameters with these geometric parameters are plotted and compared with conventional and proposed circuit model generated performances in Fig. 13. The proposed circuit model and EM model generated filter performances are close to the measured filter performance and theoretical filter performance demonstrated in [224] and [225], respectively.

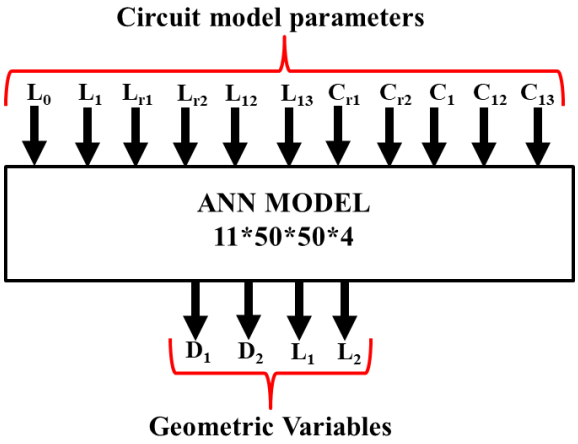


Figure 8.14 ANN model for geometric variables calculation against circuit model parameters

These two examples of dual-band RA filter and NRD filter demonstrates the proposed circuit model development technique and ANN model development approach sequentially. The proposed equivalent circuit model provides pretty identical performance to the field model. Such an accurate equivalent circuit model allows us to find the geometric parameters of the field model through the ANN model easily.

## 8.6 Discussions

Our proposed circuit models of designed examples consist of both the in-line couplings and cross couplings between cascaded discontinuities in its' full wave EM model. The conventional basic equivalent circuit model cannot match the field model response while the step-by-step introduction of different mutual couplings improves the circuit response gradually. Figure 8.15 illustrates the gradual improvement of transmission loss in case of two design examples. Optimized circuit

parameters at different stage of circuit modelling for two examples are given Table 8.1 and Table 8.2, respectively.

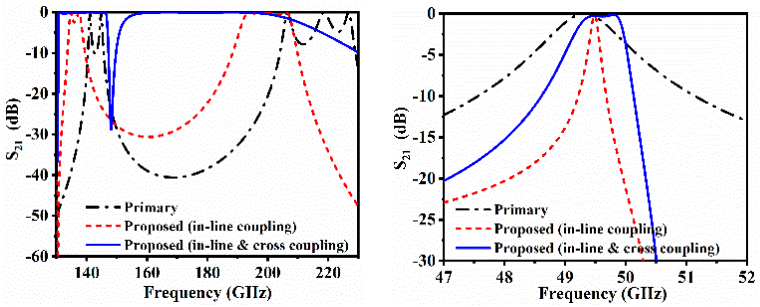


Figure 8.15 Transmission loss characteristics in primary circuit model, proposed circuit model with in-line coupling only, and proposed circuit model with in-line and cross coupling. (a) RA filter example; (b) NRD filter example

Table 8.1 Circuit parameters at different model development stages (RA filter example)

| Circuit | $L_0$ | $L_1$ | $L_2$ | $L_{r1}$ | $L_{r2}$ | $L_{12}$ | $L_{23}$ | $L_{14}$ | $C_1$ | $C_2$ | $C_{r1}$ | $C_{r2}$ | $C_{12}$ | $C_{23}$ | $C_{14}$ |
|---|---|---|---|---|---|---|---|---|---|---|---|---|---|---|---|
| Primary | - | 1.48 | 5.8 | 2.37 | 0.2 | - | - | - | 0.42 | 0.1 | 6 | 5.1 | - | - | - |
| Proposed (in-line coupling) | 0.39 | 4.53 | 0.89 | 0.65 | 0.12 | 1.52 | 0.54 | - | 0.32 | 3.22 | 0.07 | 6.01 | 3.22 | 3.4 | - |
| Proposed (in-line and cross couplings) | 0.08 | 4.4 | 0.6 | 0.6 | 0.12 | 1.5 | 0.55 | 0.17 | 0.3 | 1 | 0.03 | 6 | 3.2 | 3.4 | 12 |

Table 8.2 Circuit parameters at different model development stages (NRD filter example)

| Circuit | $L_0$ | $L_1$ | $L_{r1}$ | $L_{r2}$ | $L_{12}$ | $L_{13}$ | $C_1$ | $C_{r1}$ | $C_{r2}$ | $C_{12}$ | $C_{13}$ |
|---|---|---|---|---|---|---|---|---|---|---|---|
| Primary | - | - | 2 | 0.1 | - | - | 33 | 200 | 47 | - | - |
| Proposed (in-line coupling) | 0.39 | 0.35 | 0.024 | 2.57 | 0.15 | - | 19.75 | 265 | 34 | 14.13 | - |
| Proposed (in-line and cross couplings) | 0.27 | 0.37 | 0.03 | 0.8 | 0.18 | 0.52 | 17.92 | 232 | 32.7 | 13.38 | 17.03 |

Figure 8.15(a) shows that the primary circuit model cannot preserve the return loss in any of the passband. After introducing the in-line couplings between RA structures, the second passband starts achieving desired return loss. Finally, simultaneous application of in-line and cross couplings in the final proposed circuit model achieves target return loss in both the passbands. Figure 8.15(b)

illustrates that the primary circuit response cannot achieve prescribed stopband insertion loss. The in-line couplings between dielectric gaps start pushing the insertion loss down. Finally, both the in-line and cross couplings achieves the desired stopband insertion loss. Therefore, mutual couplings plays a vital role to achieve desired circuit performance.

In the demonstrated examples, we did not consider different losses as a part of equivalent circuit to minimize the number of variables. If the resistances are considered at different branches of the equivalent circuit model, the target ANN model size should be larger which will augment the data generation period as well as the model training time significantly. This is the primary reason for a slight deviation of equivalent circuit model response from the EM model response. In addition, higher-order modes become prominent in high frequency applications. The proposed equivalent circuit model development technique cannot introduce such multimode effects. To consider the higher-order modes, a multiport equivalent circuit model is necessary to find the generalized-S parameters. A two-port equivalent circuit is only capable of describing the fundamental mode behavior of the circuit. This is one of the main reasons for having more poles in the EM model response of the second passband of the RA filter example. These issues will be studied further in future for a better matching of EM model response and equivalent circuit model response.

## 8.7 Conclusion

This paper presents a systematic equivalent circuit model development technique from the field model of a target structure. Such a circuit model is set to provide stable circuit parameters over a wide range of frequency band. We have considered mutual couplings as a part of target equivalent circuit model as our goal is to characterize high-frequency structures. In our experiments, we have demonstrated filter examples of rectangular waveguide and NRD waveguide structures. Finally, we have developed ANN model in both cases for the mapping of equivalent circuit model parameters and field model geometric parameters. In both examples, equivalent circuit model responses are well-compared with field model responses and measured results.

# CHAPTER 9 GENERAL DISCUSSIONS

This thesis introduces a pioneering technique for optimizing the design structure of various passive circuit structures. Our approach leverages a specialized artificial neural network (ANN) model and equivalent circuit model, as different from the conventional ANN model and space mapping technique traditionally employed in the design optimization of passive structures.

The primary objective of our research was to establish a methodology that effectively optimizes the desired design structure. To accomplish this objective, firstly, we introduced a novel feedforward computational formulation specialized for microwave structures in the development of our ANN model. This specialized ANN model demonstrates superior efficiency in solving microwave structure-related problems compared to conventional approaches. Secondly, we introduced a hybrid optimization technique that combines the accuracy of metaheuristics-based global optimization technique with the speed of mathematics-based local optimization technique. This hybrid optimizer demonstrates exceptional efficiency in handling a significant number of optimization variables associated with complex microwave structures, including higher order tunable filters. Thirdly, we presented a numerical deembedding technique designed to mitigate port errors inherent in electromagnetic (EM) simulated results. The deembedded results are then employed to meticulously develop an accurate equivalent circuit model of the target structure through a systematic step-by-step circuit model decomposition process. This proposed technique was implemented to create a precise circuit model for the target structure. Subsequently, the developed hybrid optimizer was utilized to optimize the equivalent circuit parameters in order to attain the desired performance objectives. Finally, the optimized circuit parameters were mapped back to geometric parameters by employing our proposed ANN model.

The objective of optimizing the design structure has traditionally been addressed through the widely known space mapping optimization technique, as discussed in the literature review. However, this technique relies on a coarse model's performance as a representation of the target fine model (EM model), which is inherently inaccurate for high-frequency applications. Furthermore, neuro-space mapping techniques have also been extensively explored in the literature, but the neural models developed are based on generic mathematical models. In our proposed solution, we modify the ANN model to specifically cater to microwave applications.

Additionally, instead of employing an inaccurate coarse model, we utilize an accurate equivalent circuit model for mapping between circuit model parameters and EM model parameters.

The fabrication and measurement results exhibit a remarkable concurrence with the theoretical foundations and simulations, thus affirming the validity of the proposed method. Consequently, we assert that we have successfully formulated, developed, and demonstrated a comprehensive framework for the efficient and robust optimization of circuit structures in accordance with the desired performance criteria.

In the case of sub-THz example structures in this thesis, some discrepancies are notable between the measurement and simulated results. Dielectric and conductor losses become much pronounced at sub-THz frequencies and would contribute to the measurement of the fabricated SIW cruciform coupler. In addition, surface roughness may also have a significant issue for such a high frequency application. Therefore, to enhance the accuracy of the proposed mapping technique, such losses should be considered during the equivalent circuit model development stage.

For extreme high-frequency applications, structures become exceptionally small. Machining or mechanical tolerance may cause some visible deviation in measurement results from expected or simulated results. Such tolerance issues can be minimized through a prior knowledge during the manufacturing process. However, high precision manufacturing techniques such as advanced CNC or EDM machining can only bring down the tolerance value to the minimum but cannot make it to absolute zero. Therefore, such tolerance issues are somewhat beyond our control during the manufacturing process.

In this thesis, electromagnetic simulations were conducted using HFSS and CST Microwave Studio. The numerical coding was implemented through MATLAB software, and the circuit model simulations along with PCB drawings were conducted using ADS software. All fabrication and measurement processes were executed within the well-equipped laboratories of Poly-Grames.

# CHAPTER 10 CONCLUSION AND RECOMMENDATIONS

## 10.1 Conclusion

This thesis aims to develop a novel methodology for the optimization of a target structure's full-wave electromagnetic model. To accomplish this task, we developed a framework of mapping between target structure's geometric parameters and equivalent circuit model parameters. This framework consists of novel ANN model, numerical calibration technique, circuit model development method, parameter extraction method and optimization algorithm. Based on the proposed framework, we proposed unprecedented and fresh insights revealing new and far more efficient methodologies to deal with design optimization problems associated with passive circuits. We envision that this new methodology would light the path for future research to expand this solution and employ our framework to design passive structures for new radio 5G and future wireless systems.

In this Ph.D. thesis, we have accomplished four objectives prior to achieve the final goal that was defined at the beginning of our research journey. We developed a transmission line impedance equation-based feedforward ANN model that generalizes the microwave problems efficiently as compared to conventional ANN models in chapter 3. Second, in chapter 4, we developed a hybrid optimization model by the help of metaheuristic and mathematics-based optimizers that does the efficient optimization of high-dimensional microwave structures. Third, in chapter 5, we outlined a mapping technique between equivalent circuit model and physical field model for tunable bandpass filter, specifically. Finally, in chapters 6 and 7, we proposed a methodology of developing accurate equivalent circuit model from the field model design of a target structure considering the de-embedded circuit parameters. This complete equivalent circuit model considers all the elementary transmission-line discontinuities and mutual couplings of different order. These ANN model development technique, optimization algorithm, equivalent circuit model development strategy and field to circuit model parameter mapping method allow us to build the final framework for the successful optimization of target structure's field model parameters. The simulated and measured results of illustrated examples validate the proposed framework.

## 10.2 Recommendations

Efforts have been invested into this Ph.D. thesis to provide the most promising techniques for the microwave application-based ANN model, optimization framework, equivalent circuit model development strategy and mapping between physical field model and equivalent circuit model. However, more research work is still required, which can be summarized below:

- In most of our formulations, de-embedding techniques, and illustrative examples, we primarily focused on two-port circuits. However, it's crucial to acknowledge the significance of multiport devices like couplers and dividers in communication systems. Hence, the methods developed in this Ph.D. thesis can be extended to characterize multiport devices accurately.
- In this Ph.D. thesis, a strategy for developing equivalent circuit models for elementary microstrip discontinuities, such as gaps, steps, and via holes, is proposed. However, further research is required to explore the characterization of different waveguide discontinuities, such as those found in conventional waveguides and NRD waveguides, for more accurate high-frequency analysis.
- In the modeling of multi-port circuits, losses of various types are frequently disregarded. Nevertheless, losses assume significance in high-frequency applications, particularly in millimeter-wave and sub-THz frequency applications. Losses such as radiation loss and dielectric loss become extremely critical at these frequencies. In our equivalent circuit models, we did not account for losses. In the future, the scope of developing such equivalent circuit models lies in considering lossy structures, such as radiating dielectric waveguides.
- Antennas play a crucial role as radiating structures in RF front-end circuits, making them one of the most widely utilized components. To achieve improved characterization, it is essential to develop equivalent circuit models for various types of antennas. The utilization of our proposed technique for developing equivalent circuit models will be able to offer a promising approach for antenna characterization. By employing this technique, significant advancements can be made in addressing antenna analysis problems. The potential impact of employing our approach will be enhancing the understanding and optimization of antenna performance in diverse applications.

# REFERENCES


[1] J. W. Bandler, "Optimization Methods for Computer-Aided Design," *IEEE Transactions on Microwave Theory and Techniques,* vol. 17, pp. 533-552, 1969.

[2] J. W. Bandler, S. Ye, R. M. Biernacki, S. H. Chen, and D. G. Swanson, "Minimax microstrip filter design using direct EM field simulation," in *1993 IEEE MTT-S International Microwave Symposium Digest*, 1993, pp. 889-892 vol.2.

[3] F. Feng, W. Na, J. Jin, W. Zhang, and Q. J. Zhang, "ANNs for Fast Parameterized EM Modeling: The State of the Art in Machine Learning for Design Automation of Passive Microwave Structures," *IEEE Microwave Magazine,* vol. 22, pp. 37-50, 2021.

[4] H. Kabir, Y. Wang, M. Yu, and Q. J. Zhang, "Neural Network Inverse Modeling and Applications to Microwave Filter Design," *IEEE Transactions on Microwave Theory and Techniques,* vol. 56, pp. 867-879, 2008.

[5] H. Kabir, Y. Wang, M. Yu, and Q. J. Zhang, "High-Dimensional Neural-Network Technique and Applications to Microwave Filter Modeling," *IEEE Transactions on Microwave Theory and Techniques,* vol. 58, pp. 145-156, 2010.

[6] Q. J. Zhang, E. Gad, B. Nouri, W. Na, and M. Nakhla, "Simulation and Automated Modeling of Microwave Circuits: State-of-the-Art and Emerging Trends," *IEEE Journal of Microwaves,* vol. 1, pp. 494-507, 2021.

[7] W. Fang and Z. Qi-Jun, "Knowledge-based neural models for microwave design," *IEEE Transactions on Microwave Theory and Techniques,* vol. 45, pp. 2333-2343, 1997.

[8] Z. Ye, W. Shao, X. Ding, B. Z. Wang, and S. Sun, "Knowledge-Based Neural Network for Multiphysical Field Modeling," *IEEE Transactions on Microwave Theory and Techniques,* vol. 71, pp. 1967-1976, 2023.

[9] K. Wu, S. Sun, L. Li, L. Han, L. Zhu, and C. K. M. Tse, "The Match Game: Numerical De-Embedding of Field Simulation and Parameter Extraction of Circuit Models for Electromagnetic Structure Using Calibration Techniques," *IEEE Microwave Magazine,* vol. 17, pp. 77-92, 2016.

[10] J. W. Bandler and S. H. Chen, "Circuit optimization: the state of the art," *IEEE Transactions on Microwave Theory and Techniques,* vol. 36, pp. 424-443, 1988.

[11] D. D. Zutter, J. Sercu, T. Dhaene, J. D. Geest, F. J. Demuynck, S. Hammadi, "Recent trends in the integration of circuit optimization and full-wave electromagnetic analysis," *IEEE Transactions on Microwave Theory and Techniques,* vol. 52, pp. 245-256, 2004.

[12] J. W. Bandler and J. E. Rayas-Sánchez, "An Early History of Optimization Technology for Automated Design of Microwave Circuits," *IEEE Journal of Microwaves,* vol. 3, pp. 319-337, 2023.

[13] J. W. Bandler, "The journey to automated design optimization and a vision for the future," in *2017 IEEE MTT-S International Microwave Symposium (IMS)*, 2017, pp. 1517-1519.

[14] J. T. Alos and M. Guglielmi, "Simple and effective EM-based optimization procedure for microwave filters," *IEEE Transactions on Microwave Theory and Techniques,* vol. 45, pp. 856-858, 1997.

[15] X. Li, F. Feng, J. Zhang, W. Zhang, and Q. J. Zhang, "Advanced Simulation-Inserted Optimization Using Combined Quasi-Newton Method With Lagrangian Method for EM-Based Design Optimization," *IEEE Transactions on Microwave Theory and Techniques*, vol. 70, pp. 3753-3764, 2022.

[16] J. W. Bandler, R. M. Biernacki, C. Shao Hua, D. G. Swanson, and Y. Shen, "Microstrip filter design using direct EM field simulation," *IEEE Transactions on Microwave Theory and Techniques*, vol. 42, pp. 1353-1359, 1994.

[17] F. Alessandri, M. Dionigi, R. Sorrentino, and L. Tarricone, "Rigorous and efficient fabrication-oriented CAD and optimization of complex waveguide networks," *IEEE Transactions on Microwave Theory and Techniques*, vol. 45, pp. 2366-2374, 1997.

[18] A. Pietrenko-Dabrowska and S. Koziel, "Low-Cost Design Optimization of Microwave Passives Using Multifidelity EM Simulations and Selective Broyden Updates," *IEEE Transactions on Microwave Theory and Techniques*, vol. 70, pp. 4765-4771, 2022.

[19] M. M. Gavrilovic and J. P. Webb, "Accuracy control in the optimization of microwave devices by finite-element methods," *IEEE Transactions on Microwave Theory and Techniques*, vol. 50, pp. 1901-1911, 2002.

[20] J. Jin, F. Feng, J. Zhang, J. Ma, and Q. J. Zhang, "Efficient EM Topology Optimization Incorporating Advanced Matrix Padé Via Lanczos and Genetic Algorithm for Microwave Design," *IEEE Transactions on Microwave Theory and Techniques*, vol. 69, pp. 3645-3666, 2021.

[21] L. Ming-Iu and J. Shyh-Kang, "Compact microstrip dual-band bandpass filters design using genetic-algorithm techniques," *IEEE Transactions on Microwave Theory and Techniques*, vol. 54, pp. 160-168, 2006.

[22] Y. A. Hussein and S. M. El-Ghazaly, "Modeling and optimization of microwave devices and circuits using genetic algorithms," *IEEE Transactions on Microwave Theory and Techniques*, vol. 52, pp. 329-336, 2004.

[23] T. Nishino and T. Itoh, "Evolutionary generation of microwave line-segment circuits by genetic algorithms," *IEEE Transactions on Microwave Theory and Techniques*, vol. 50, pp. 2048-2055, 2002.

[24] S. Kirkpatrick, C. D. Gelatt, and M. P. Vecchi, "Optimization by Simulated Annealing," *Science*, vol. 220, pp. 671-680, 1983/05/13 1983.

[25] V. Černý, "Thermodynamical approach to the traveling salesman problem: An efficient simulation algorithm," *Journal of Optimization Theory and Applications*, vol. 45, pp. 41-51, 1985/01/01 1985.

[26] D. Budimir and G. Goussetis, "Design of asymmetrical RF and microwave bandpass filters by computer optimization," *IEEE Transactions on Microwave Theory and Techniques*, vol. 51, pp. 1174-1178, 2003.

[27] A. Garcia-Lamperez, S. Llorente-Romano, M. Salazar-Palma, and T. K. Sarkar, "Efficient electromagnetic optimization of microwave filters and multiplexers using rational models," *IEEE Transactions on Microwave Theory and Techniques*, vol. 52, pp. 508-521, 2004.

[28] K. Krohne and R. Vahldieck, "On the application of model-order reduction in the fast and reliable optimization of microwave filters and diplexers," *IEEE Transactions on Microwave Theory and Techniques,* vol. 52, pp. 2285-2291, 2004.

[29] E. Musonda, R. A. Paradkar, I. C. Hunter, and R. Parry, "Synthesis of Multiband Filters by Linear Optimization," *Ieee Transactions on Microwave Theory and Techniques,* vol. 67, pp. 4764-4772, Dec 2019.

[30] J. W. Bandler, R. M. Biernacki, S. H. Chen, P. A. Grobelny, and S. Ye, "Yield-Driven Electromagnetic Optimization Via Multilevel Multidimensional Models," *Ieee Transactions on Microwave Theory and Techniques,* vol. 41, pp. 2269-2278, Dec 1993.

[31] P. Zhao and K. Wu, "Homotopy Optimization of Microwave and Millimeter-Wave Filters Based on Neural Network Model," *IEEE Transactions on Microwave Theory and Techniques,* vol. 68, pp. 1390-1400, Apr 2020.

[32] C. Roy and K. Wu, "Homotopy Optimization and ANN Modeling of Millimeter-Wave SIW Cruciform Coupler," *IEEE Transactions on Microwave Theory and Techniques,* vol. 70, pp. 4751-4764, Nov 2022.

[33] C. Roy, P. Zhao, and K. Wu, "ANN Model Development for Tunable Bandpass Filter," *51st European Microwave Conference*, 2022.

[34] J. Kennedy and R. Eberhart, "Particle swarm optimization," *1995 IEEE International Conference on Neural Networks Proceedings, Vols 1-6,* vol. - 4, pp. 1942-1948, 1995.

[35] X. Luo, B. Z. Yang, and H. J. Qian, "Adaptive Synthesis for Resonator-Coupled Filters Based on Particle Swarm Optimization," *IEEE Transactions on Microwave Theory and Techniques,* vol. 67, pp. 712-725, Feb 2019.

[36] N. B. Jin and Y. Rahmat-Samii, "Advances in particle swarm optimization for antenna designs: Real-number, binary, single-objective and multiobjective implementations," *IEEE Transactions on Antennas and Propagation,* vol. 55, pp. 556-567, Mar 2007.

[37] A. A. Minasian and T. S. Bird, "Particle Swarm Optimization of Microstrip Antennas for Wireless Communication Systems," *IEEE Transactions on Antennas and Propagation,* vol. 61, pp. 6214-6217, Dec 2013.

[38] K. Fu, X. W. Cai, B. Yuan, Y. Yang, and X. Yao, "An Efficient Surrogate Assisted Particle Swarm Optimization for Antenna Synthesis," *IEEE Transactions on Antennas and Propagation,* vol. 70, pp. 4977-4984, Jul 2022.

[39] H. Wu, J. P. Geng, R. H. Jin, J. Z. Qiu, W. Liu, J. Chen, *et al.*, "An Improved Comprehensive Learning Particle Swarm Optimization and Its Application to the Semiautomatic Design of Antennas," *IEEE Transactions on Antennas and Propagation,* vol. 57, pp. 3018-3028, Oct 2009.

[40] R. Bhattacharya, T. K. Bhattacharyya, and R. Garg, "Position Mutated Hierarchical Particle Swarm Optimization and its Application in Synthesis of Unequally Spaced Antenna Arrays," *IEEE Transactions on Antennas and Propagation,* vol. 60, pp. 3174-3181, Jul 2012.

[41] C. Roy, W. Lin, and K. Wu, "Swarm Intelligence-Homotopy Hybrid Optimization-Based ANN Model for Tunable Bandpass Filter," *IEEE Transactions on Microwave Theory and Techniques*, vol. 71, no. 6, pp. 2567 - 2581, Jan 2023.

[42] J. E. Rayas-Sanchez and V. Gutierrez-Ayala, "EM-based Monte Carlo analysis and yield prediction of microwave circuits using linear-input neural-output space mapping," *IEEE Transactions on Microwave Theory and Techniques*, vol. 54, pp. 4528-4537, Dec 2006.

[43] J. Jin, F. Feng, W. C. Na, J. N. Zhang, W. Zhang, Z. H. Zhao, *et al.*, "Advanced Cognition-Driven EM Optimization Incorporating Transfer Function-Based Feature Surrogate for Microwave Filters," *IEEE Transactions on Microwave Theory and Techniques*, vol. 69, pp. 15-28, Jan 2021.

[44] L. Xue, B. Liu, Y. Yu, Q. S. Cheng, M. Imran, and T. Qiao, "An Unsupervised Microwave Filter Design Optimization Method Based on a Hybrid Surrogate Model-Assisted Evolutionary Algorithm," *IEEE Transactions on Microwave Theory and Techniques*, vol. 71, pp. 1159 - 1170, Nov 2023.

[45] B. Liu, H. Yang, and M. J. Lancaster, "Global Optimization of Microwave Filters Based on a Surrogate Model-Assisted Evolutionary Algorithm," *IEEE Transactions on Microwave Theory and Techniques*, vol. 65, pp. 1976-1985, Jun 2017.

[46] Z. Zhang, B. Liu, Y. Yu, and Q. S. Cheng, "A Microwave Filter Yield Optimization Method Based on Off-Line Surrogate Model-Assisted Evolutionary Algorithm," *IEEE Transactions on Microwave Theory and Techniques*, vol. 70, pp. 2925-2934, Jun 2022.

[47] J. E. Rayas-Sanchez, "EM-based optimization of microwave circuits using artificial neural networks: The state-of-the-art," *IEEE Transactions on Microwave Theory and Techniques*, vol. 52, pp. 420-435, Jan 2004.

[48] Y. Yu, Z. Zhang, Q. S. Cheng, B. Liu, Y. Wang, C. Guo, *et al.*, "State-of-the-Art: AI-Assisted Surrogate Modeling and Optimization for Microwave Filters," *IEEE Transactions on Microwave Theory and Techniques*, vol. 70, pp. 4635-4651, Nov 2022.

[49] J. W. Bandler, R. M. Biernacki, S. H. Chen, P. A. Grobelny, and R. H. Hemmers, "Space Mapping Technique for Electromagnetic Optimization," *IEEE Transactions on Microwave Theory and Techniques*, vol. 42, pp. 2536-2544, Dec 1994.

[50] J. W. Bandler, R. M. Biernacki, S. H. Chen, R. H. Hemmers, and K. Madsen, "Aggressive Space Mapping for Electromagnetic Design," *1995 Ieee MTT-S International Microwave Symposium Digest, Vols 1-3*, vol. -, pp. 1455-1458, 1995.

[51] J. W. Bandler, R. M. Biernacki, S. H. Chen, R. H. Hemmers, and K. Madsen, "Electromagnetic optimization exploiting aggressive space mapping," *IEEE Transactions on Microwave Theory and Techniques*, vol. 43, pp. 2874-2882, Dec 1995.

[52] J. Bandler, "Space Mapping-Have You Ever Wondered About the Engineer's Mysterious "Feel" for a Problem? Speaker's Corner," vol. - 19, pp. - 122, 2018.

[53] J. W. Bandler, Q. S. Cheng, S. A. Dakroury, A. S. Mohamed, M. H. Bakr, K. Madsen, *et al.*, "Space mapping: the state of the art," *IEEE Transactions on Microwave Theory and Techniques*, vol. 52, pp. 337-361, 2004.

[54] M. B. Steer, J. W. Bandler, and C. M. Snowden, "Computer-aided design of RF and microwave circuits and systems," *IEEE Transactions on Microwave Theory and Techniques*, vol. 50, pp. 996-1005, 2002.

[55] J. E. Rayas-Sanchez, "Power in Simplicity with ASM: Tracing the Aggressive Space Mapping Algorithm Over Two Decades of Development and Engineering Applications," *IEEE Microwave Magazine*, vol. 17, pp. 64-76, 2016.

[56] J. W. Bandler, M. A. Ismail, J. E. Rayas-Sanchez, and Z. Qi-Jun, "Neuromodeling of microwave circuits exploiting space-mapping technology," *IEEE Transactions on Microwave Theory and Techniques*, vol. 47, pp. 2417-2427, 1999.

[57] M. H. Bakr, J. W. Bandler, M. A. Ismail, J. E. Rayas-Sanchez, and Z. Qi-Jun, "Neural space-mapping optimization for EM-based design," *IEEE Transactions on Microwave Theory and Techniques*, vol. 48, pp. 2307-2315, 2000.

[58] L. Zhang, Q. J. Zhang, and J. Wood, "Statistical Neuro-Space Mapping Technique for Large-Signal Modeling of Nonlinear Devices," *IEEE Transactions on Microwave Theory and Techniques*, vol. 56, pp. 2453-2467, 2008.

[59] K. Madsen, "Minimization of non-linear approximation functions," Doctorate Dr. tech. thesis, Institute of Numerical Analysis, Technical University of Denmark, 1985.

[60] C. G. Broyden, "A Class of Methods for Solving Nonlinear Simultaneous Equations," *Mathematics of Computation*, vol. 19, pp. 577-593, 1965.

[61] C. G. Broyden, "Quasi-Newton methods and their application to function minimisation," *Mathematics of Computation*, vol. 21, pp. 368-381, 1967.

[62] R. Fletcher and M. J. D. Powell, "A Rapidly Convergent Descent Method for Minimization," *Comput. J.*, vol. 6, pp. 163-168, 1963.

[63] H. Kuhn and A. Tucker, "Nonlinear programming," presented at the Proceedings of the Second Berkeley Symposium on Mathematical Statistics and Probability, 1950, Berkeley and Los Angeles, 1950.

[64] C. G. Broyden, "A new double-rank minimization algorithm," *AMS Notices*, vol. 16, 1969.

[65] R. Fletcher, "A new approach to variable metric algorithms," *The Computer Journal*, vol. 13, pp. 317-322, 1970.

[66] D. Goldfarb, "A Family of Variable-Metric Methods Derived by Variational Means," *Mathematics of Computation*, vol. 24, pp. 23-26, 1970.

[67] D. F. Shanno, "Conditioning of quasi-Newton methods for function minimization," *Mathematics of Computation*, vol. 24, pp. 647-656, 1970.

[68] W. C. Davidon, "Variable metric method for minimization," Argonne National Laboratories, Argonne, IL1959-05-01 1959.

[69] M. J. D. Powell, "A New Algorithm for Unconstrained Optimization," in *Nonlinear Programming*, J. B. Rosen, O. L. Mangasarian, and K. Ritter, Eds., ed: Academic Press, 1970, pp. 31-65.

[70] J. Hald and K. Madsen, "Combined lp and quasi-Newton methods for minimax optimization," *Mathematical Programming*, vol. 20, pp. 49-62, 1981/12/01 1981.

[71] J. Hald and K. Madsen, "Combined LP and Quasi-Newton Methods for Nonlinear $l_1$ Optimization," *SIAM Journal on Numerical Analysis*, vol. 22, pp. 68-80, 1985.

[72] J. W. Bandler, W. Kellermann, and K. Madsen, "A Superlinearly Convergent Minimax Algorithm for Microwave Circuit Design," *IEEE Transactions on Microwave Theory and Techniques*, vol. 33, pp. 1519-1530, 1985.

[73] K. Madsen, H. Schjaer-Jacobsen, and J. Voldby, "Automated minimax design of networks," *IEEE Transactions on Circuits and Systems*, vol. 22, pp. 791-796, 1975.

[74] S. Mirjalili and A. Lewis, "The Whale Optimization Algorithm," *Advances in Engineering Software*, vol. 95, pp. 51-67, 2016/05/01/ 2016.

[75] J. H. Holland, "Genetic Algorithms," *Scientific American*, vol. 267, pp. 66-73, 1992.

[76] J. W. Demmel, *Applied numerical linear algebra*: Society for Industrial and Applied Mathematics, 1997.

[77] K. V. Price, R. M. Storn, and J. A. Lampinen, *Differential Evolution: A Practical Approach to Global Optimization*, 1 ed.: Springer Berlin, Heidelberg.

[78] B. Liu, H. Yang, and M. J. Lancaster, "Synthesis of Coupling Matrix for Diplexers Based on a Self-Adaptive Differential Evolution Algorithm," *IEEE Transactions on Microwave Theory and Techniques*, vol. 66, pp. 813-821, 2018.

[79] S. Mirjalili, S. M. Mirjalili, and A. Lewis, "Grey Wolf Optimizer," *Advances in Engineering Software*, vol. 69, pp. 46-61, 2014/03/01/ 2014.

[80] D. H. Wolpert and W. G. Macready, "No free lunch theorems for optimization," *IEEE Transactions on Evolutionary Computation*, vol. 1, pp. 67-82, 1997.

[81] K. C. Gupta and Q. J. Zhang, *Neural Networks for RF and Microwave Design*. Norwood, MA, USA: Artech House, 2000.

[82] Z. Qi-Jun, K. C. Gupta, and V. K. Devabhaktuni, "Artificial neural networks for RF and microwave design - from theory to practice," *IEEE Transactions on Microwave Theory and Techniques*, vol. 51, pp. 1339-1350, 2003.

[83] F. Feng, W. Na, J. Jin, J. Zhang, W. Zhang, and Q. J. Zhang, "Artificial Neural Networks for Microwave Computer-Aided Design: The State of the Art," *IEEE Transactions on Microwave Theory and Techniques*, vol. 70, pp. 4597-4619, 2022.

[84] P. M. Watson and K. C. Gupta, "EM-ANN models for microstrip vias and interconnects in dataset circuits," *IEEE Transactions on Microwave Theory and Techniques*, vol. 44, pp. 2495-2503, 1996.

[85] R. K. Mishra, "An overview of neural network methods in computational electromagnetics," *International Journal of RF and Microwave Computer-Aided Engineering*, vol. 12, pp. 98-108, 2002/01/01 2002.

[86] J. W. Bandler, J. E. Rayas-Sánchez, and Q.-J. Zhang, "Yield-driven electromagnetic optimization via space mapping-based neuromodels," *International Journal of RF and Microwave Computer-Aided Engineering*, vol. 12, pp. 79-89, 2002/01/01 2002.

[87] G. Gosal, E. Almajali, D. McNamara, and M. Yagoub, "Transmitarray Antenna Design Using Forward and Inverse Neural Network Modeling," *IEEE Antennas and Wireless Propagation Letters*, vol. 15, pp. 1483-1486, 2016.

[88] C. Zhang, J. Jin, W. Na, Q. J. Zhang, and M. Yu, "Multivalued Neural Network Inverse Modeling and Applications to Microwave Filters," *IEEE Transactions on Microwave Theory and Techniques*, vol. 66, pp. 3781-3797, 2018.

[89] S. A. Sadrossadat, Y. Cao, and Q. J. Zhang, "Parametric Modeling of Microwave Passive Components Using Sensitivity-Analysis-Based Adjoint Neural-Network Technique," *IEEE Transactions on Microwave Theory and Techniques*, vol. 61, pp. 1733-1747, 2013.

[90] P. M. Watson and K. C. Gupta, "Design and optimization of CPW circuits using EM-ANN models for CPW components," *IEEE Transactions on Microwave Theory and Techniques*, vol. 45, pp. 2515-2523, 1997.

[91] W. Zhang, F. Feng, V. M. R. Gongal-Reddy, J. Zhang, S. Yan, J. Ma, *et al.*, "Space Mapping Approach to Electromagnetic Centric Multiphysics Parametric Modeling of Microwave Components," *IEEE Transactions on Microwave Theory and Techniques*, vol. 66, pp. 3169-3185, 2018.

[92] W. Zhang, F. Feng, S. Yan, W. Na, J. Ma, and Q. J. Zhang, "EM-Centric Multiphysics Optimization of Microwave Components Using Parallel Computational Approach," *IEEE Transactions on Microwave Theory and Techniques*, vol. 68, pp. 479-489, 2020.

[93] W. Zhang, F. Feng, W. Liu, S. Yan, J. Zhang, J. Jin, *et al.*, "Advanced Parallel Space-Mapping-Based Multiphysics Optimization for High-Power Microwave Filters," *IEEE Transactions on Microwave Theory and Techniques*, vol. 69, pp. 2470-2484, 2021.

[94] F. Wang, V. K. Devabhaktuni, C. Xi, and Q.-J. Zhang, "Neural network structures and training algorithms for RF and microwave applications," *International Journal of RF and Microwave Computer-Aided Engineering*, vol. 9, pp. 216-240, 1999/05/01 1999.

[95] L. Y. Xiao, W. Shao, F. L. Jin, B. Z. Wang, W. T. Joines, and Q. H. Liu, "Semisupervised Radial Basis Function Neural Network With an Effective Sampling Strategy," *IEEE Transactions on Microwave Theory and Techniques*, vol. 68, pp. 1260-1269, 2020.

[96] J. P. Garcia, F. Q. Pereira, D. C. Rebenaque, J. L. G. Tornero, and A. A. Melcon, "A neural network method for the analysis of multilayered shielded microwave circuits," in *IEEE MTT-S International Microwave Symposium Digest, 2005.*, 2005, pp. 1601-1604.

[97] F. Dandurand and D. A. Lowther, "Electromagnetic device performance identification using knowledge based neural networks," *IEEE Transactions on Magnetics*, vol. 35, pp. 1817-1820, 1999.

[98] W. Na, F. Feng, C. Zhang, and Q. J. Zhang, "A Unified Automated Parametric Modeling Algorithm Using Knowledge-Based Neural Network and $l_1$ Optimization," *IEEE Transactions on Microwave Theory and Techniques*, vol. 65, pp. 729-745, 2017.

[99] Y. Cao, L. Simonovich, and Q. J. Zhang, "A Broadband and Parametric Model of Differential Via Holes Using Space-Mapping Neural Network," *IEEE Microwave and Wireless Components Letters*, vol. 19, pp. 533-535, 2009.

[100] V. K. Devabhaktuni, B. Chattaraj, M. C. E. Yagoub, and Z. Qi-Jun, "Advanced microwave modeling framework exploiting automatic model generation, knowledge neural networks, and space mapping," *IEEE Transactions on Microwave Theory and Techniques*, vol. 51, pp. 1822-1833, 2003.

[101] H. Kabir, L. Zhang, M. Yu, P. H. Aaen, J. Wood, and Q. J. Zhang, "Smart Modeling of Microwave Devices," *IEEE Microwave Magazine*, vol. 11, pp. 105-118, 2010.

[102] Y. Cao, G. Wang, and Q. J. Zhang, "A New Training Approach for Parametric Modeling of Microwave Passive Components Using Combined Neural Networks and Transfer Functions," *IEEE Transactions on Microwave Theory and Techniques*, vol. 57, pp. 2727-2742, 2009.

[103] J. Zhang, F. Feng, W. Zhang, J. Jin, J. Ma, and Q. J. Zhang, "A Novel Training Approach for Parametric Modeling of Microwave Passive Components Using Padé via Lanczos and EM Sensitivities," *IEEE Transactions on Microwave Theory and Techniques*, vol. 68, pp. 2215-2233, 2020.

[104] F. Feng, V. M. R. Gongal-Reddy, C. Zhang, J. Ma, and Q. J. Zhang, "Parametric Modeling of Microwave Components Using Adjoint Neural Networks and Pole-Residue Transfer Functions With EM Sensitivity Analysis," *IEEE Transactions on Microwave Theory and Techniques*, vol. 65, pp. 1955-1975, 2017.

[105] Y. LeCun, Y. Bengio, and G. Hinton, "Deep learning," *Nature*, vol. 521, pp. 436-444, 2015/05/01 2015.

[106] G. W. Cottrell, "New Life for Neural Networks," *Science*, vol. 313, pp. 454-455, 2006/07/28 2006.

[107] M. A. Nielsen, *Neural Networks and Deep Learning*. Princeton, NJ, USA: Determination Press, 2015.

[108] J. Jin, C. Zhang, F. Feng, W. Na, J. Ma, and Q. J. Zhang, "Deep Neural Network Technique for High-Dimensional Microwave Modeling and Applications to Parameter Extraction of Microwave Filters," *IEEE Transactions on Microwave Theory and Techniques*, vol. 67, pp. 4140-4155, 2019.

[109] S. Koziel, A. Pietrenko-Dabrowska, and U. Ullah, "Low-Cost Modeling of Microwave Components by Means of Two-Stage Inverse/Forward Surrogates and Domain Confinement," *IEEE Transactions on Microwave Theory and Techniques*, vol. 69, pp. 5189-5202, 2021.

[110] B. Pu, H. Kim, X. D. Cai, B. Sen, C. Sui, and J. Fan, "Training Set Optimization in an Artificial Neural Network Constructed for High Bandwidth Interconnects Design," *IEEE Transactions on Microwave Theory and Techniques*, vol. 70, pp. 2955-2964, 2022.

[111] F. Feng, C. Zhang, J. Ma, and Q. J. Zhang, "Parametric Modeling of EM Behavior of Microwave Components Using Combined Neural Networks and Pole-Residue-Based Transfer Functions," *IEEE Transactions on Microwave Theory and Techniques*, vol. 64, pp. 60-77, 2016.

[112] F. Feng, W. Na, W. Liu, S. Yan, L. Zhu, and Q. J. Zhang, "Parallel Gradient-Based EM Optimization for Microwave Components Using Adjoint- Sensitivity-Based Neuro-

Transfer Function Surrogate," *IEEE Transactions on Microwave Theory and Techniques,* vol. 68, pp. 3606-3620, 2020.

[113] V. K. Devabhaktuni, M. C. E. Yagoub, and Z. Qi-Jun, "A robust algorithm for automatic development of neural-network models for microwave applications," *IEEE Transactions on Microwave Theory and Techniques,* vol. 49, pp. 2282-2291, 2001.

[114] J. Cui, F. Feng, W. Na, and Q. J. Zhang, "Bayesian-Based Automated Model Generation Method for Neural Network Modeling of Microwave Components," *IEEE Microwave and Wireless Components Letters,* vol. 31, pp. 1179-1182, 2021.

[115] J. Zhang, S. Yan, F. Feng, J. Jin, W. Zhang, J. Wang, *et al.*, "A Novel Surrogate-Based Approach to Yield Estimation and Optimization of Microwave Structures Using Combined Quadratic Mappings and Matrix Transfer Functions," *IEEE Transactions on Microwave Theory and Techniques,* vol. 70, pp. 3802-3816, 2022.

[116] W. Zhang, W. Liu, S. Yan, F. Feng, J. Zhang, J. Jin, *et al.*, "Surrogate-Assisted Multistate Tuning-Driven EM Optimization for Microwave Tunable Filter," *IEEE Transactions on Microwave Theory and Techniques,* vol. 70, pp. 2015-2030, 2022.

[117] A. Liu, M. Leng, G. Pan, and M. Yu, "Automatic Coupler Design Based on Artificial Neural Network With Self-Adaptive Local Surrogates," *IEEE Transactions on Microwave Theory and Techniques,* vol. 70, pp. 4711-4725, 2022.

[118] S. Koziel, N. Çalık, P. Mahouti, and M. A. Belen, "Reliable Computationally Efficient Behavioral Modeling of Microwave Passives Using Deep Learning Surrogates in Confined Domains," *IEEE Transactions on Microwave Theory and Techniques,* vol. 71, pp. 956-968, 2023.

[119] F. Feng, W. Na, W. Liu, S. Yan, L. Zhu, J. Ma, *et al.*, "Multifeature-Assisted Neuro-transfer Function Surrogate-Based EM Optimization Exploiting Trust-Region Algorithms for Microwave Filter Design," *IEEE Transactions on Microwave Theory and Techniques,* vol. 68, pp. 531-542, 2020.

[120] N. M. Alexandrov, J. E. Dennis, R. M. Lewis, and V. Torczon, "A trust-region framework for managing the use of approximation models in optimization," *Structural optimization,* vol. 15, pp. 16-23, 1998/02/01 1998.

[121] A. R. Conn, N. I. M. Gould, and P. L. Toint, *Trust-Region Methods*. Philadelphia, PA: SIAM, 2000.

[122] J. J. Moré and D. C. Sorensen, "Computing a Trust Region Step," *SIAM Journal on Scientific and Statistical Computing,* vol. 4, pp. 553-572, 1983/09/01 1983.

[123] M. H. Bakr, J. W. Bandler, R. M. Biernacki, C. Shao Hua, and K. Madsen, "A trust region aggressive space mapping algorithm for EM optimization," *IEEE Transactions on Microwave Theory and Techniques,* vol. 46, pp. 2412-2425, 1998.

[124] J. W. Bandler, R. M. Biernacki, S. H. Chen, and Q. H. Wang, "Multiple space mapping EM optimization of signal integrity in high-speed digital circuits," in *5th Int. Integrated Nonlinear Microwave Millimeter-Wave Circuits Workshop*, Duisburg, Germany, 1998, pp. 138-140.

[125] J. W. Bandler, N. Georgieva, M. A. Ismail, J. E. Rayas-Sanchez, and Q. J. Zhang, "A Generalized Space Mapping Tableau Approach to Device Modeling," in *1999 29th European Microwave Conference*, 1999, pp. 231-234.

[126] J. W. Bandler, Q. S. Cheng, N. K. Nikolova, and M. A. Ismail, "Implicit space mapping optimization exploiting preassigned parameters," *IEEE Transactions on Microwave Theory and Techniques*, vol. 52, pp. 378-385, 2004.

[127] M. H. Bakr, J. W. Bandler, N. Georgieva, and K. Madsen, "A hybrid aggressive space-mapping algorithm for EM optimization," *IEEE Transactions on Microwave Theory and Techniques*, vol. 47, pp. 2440-2449, 1999.

[128] S. Koziel, J. Meng, J. W. Bandler, M. H. Bakr, and Q. S. Cheng, "Accelerated Microwave Design Optimization With Tuning Space Mapping," *IEEE Transactions on Microwave Theory and Techniques*, vol. 57, pp. 383-394, 2009.

[129] F. Feng, C. Zhang, V. M. R. Gongal-Reddy, Q. J. Zhang, and J. Ma, "Parallel Space-Mapping Approach to EM Optimization," *IEEE Transactions on Microwave Theory and Techniques*, vol. 62, pp. 1135-1148, 2014.

[130] J. W. Bandler, A. S. Mohamed, M. H. Bakr, K. Madsen, and J. Sondergaard, "EM-based optimization exploiting partial space mapping and exact sensitivities," *IEEE Transactions on Microwave Theory and Techniques*, vol. 50, pp. 2741-2750, 2002.

[131] J. W. Bandler, D. M. Hailu, K. Madsen, and F. Pedersen, "A space-mapping interpolating surrogate algorithm for highly optimized EM-based design of microwave devices," *IEEE Transactions on Microwave Theory and Techniques*, vol. 52, pp. 2593-2600, 2004.

[132] J. E. Rayas-sanchez and V. Gutierrez-Ayala, "EM-Based Statistical Analysis and Yield Estimation Using Linear-Input and Neural-Output Space Mapping," in *2006 IEEE MTT-S International Microwave Symposium Digest*, 2006, pp. 1597-1600.

[133] K. C. Gupta, R. Garg, and I. J. Bahl, *Microstrip lines and slotlines*. Norwood, MA: Artech House, 1979.

[134] M. Kirschning, R. H. Jansen, and N. H. L. Koster, "Measurement and Computer-Aided Modeling of Microstrip Discontinuities by an Improved Resonator Method," in *1983 IEEE MTT-S International Microwave Symposium Digest*, 1983, pp. 495-497.

[135] S. Koziel, J. W. Bandler, and K. Madsen, "Space-mapping-based interpolation for engineering optimization," *IEEE Transactions on Microwave Theory and Techniques*, vol. 54, pp. 2410-2421, 2006.

[136] Q. S. Cheng, J. W. Bandler, and S. Koziel, "Space Mapping Design Framework Exploiting Tuning Elements," *IEEE Transactions on Microwave Theory and Techniques*, vol. 58, pp. 136-144, 2010.

[137] J. W. Bandler, "Computer Optimization of Inhomogeneous Waveguide Transformers," *IEEE Transactions on Microwave Theory and Techniques*, vol. 17, pp. 563-571, 1969.

[138] J. V. M. Ros, P. S. Pacheco, H. E. Gonzalez, V. E. B. Esbert, C. B. Martin, M. T. Calduch, *et al.*, "Fast automated design of waveguide filters using aggressive space mapping with a new segmentation strategy and a hybrid optimization algorithm," *IEEE Transactions on Microwave Theory and Techniques*, vol. 53, pp. 1130-1142, 2005.

[139] C. Zhang, F. Feng, V. M. R. Gongal-Reddy, Q. J. Zhang, and J. W. Bandler, "Cognition-Driven Formulation of Space Mapping for Equal-Ripple Optimization of Microwave Filters," *IEEE Transactions on Microwave Theory and Techniques*, vol. 63, pp. 2154-2165, 2015.

[140] S. Koziel and J. W. Bandler, "A Space-Mapping Approach to Microwave Device Modeling Exploiting Fuzzy Systems," *IEEE Transactions on Microwave Theory and Techniques*, vol. 55, pp. 2539-2547, 2007.

[141] S. Koziel and J. W. Bandler, "Interpolated Coarse Models for Microwave Design Optimization With Space Mapping," *IEEE Transactions on Microwave Theory and Techniques*, vol. 55, pp. 1739-1746, 2007.

[142] C. M. Armstrong, "The truth about terahertz," *IEEE Spectrum*, vol. 49, pp. 36-41, 2012.

[143] I. Hosako, N. Sekine, M. Patrashin, S. Saito, K. Fukunaga, Y. Kasai, *et al.*, "At the Dawn of a New Era in Terahertz Technology," *Proceedings of the IEEE*, vol. 95, pp. 1611-1623, 2007.

[144] D. Graham-Rowe, "Terahertz takes to the stage," *Nature Photonics*, vol. 1, pp. 75-77, 2007/02/01 2007.

[145] M. Tonouchi, "Cutting-edge terahertz technology," *Nature Photonics*, vol. 1, pp. 97-105, 2007/02/01 2007.

[146] I. Ohta, Y. Yumita, K. Toda, and M. Kishihara, "Cruciform directional couplers in H-plane rectangular waveguide," in *2005 Asia-Pacific Microwave Conference Proceedings*, 2005, p. 4 pp.

[147] M. Kishihara, K. Yamane, and I. Ohta, "Design of Cruciform Directional Couplers in E-Plane Rectangular Waveguide," in *2006 IEEE MTT-S International Microwave Symposium Digest*, 2006, pp. 1722-1725.

[148] T. Djerafi and K. Wu, "Super-Compact Substrate Integrated Waveguide Cruciform Directional Coupler," *IEEE Microwave and Wireless Components Letters*, vol. 17, pp. 757-759, 2007.

[149] J. Attari, T. Djerafi, and K. Wu, "A Compact 94 GHz Image Substrate Integrated Non-Radiative Dielectric (iSINRD) Waveguide Cruciform Coupler," *IEEE Microwave and Wireless Components Letters*, vol. 23, pp. 533-535, 2013.

[150] A. Doghri, T. Djerafi, A. Ghiotto, and K. Wu, "Substrate Integrated Waveguide Directional Couplers for Compact Three-Dimensional Integrated Circuits," *IEEE Transactions on Microwave Theory and Techniques*, vol. 63, pp. 209-221, 2015.

[151] M. Kishihara, M. Komatsubara, K. Okubo, and I. Ohta, "Broad-band cruciform substrate integrated waveguide couplers," *2009 Asia Pacific Microwave Conference*, pp. 2100-2103, 2009.

[152] S. Liao, *Homotopy Analysis Method in Nonlinear Differential Equations*, 1 ed. Berlin, Heidelberg: Springer, 2012.

[153] H. Kabir, M. Yu, and Q. J. Zhang, "Recent advances of neural network-based EM-CAD," *International Journal of RF and Microwave Computer-Aided Engineering*, vol. 20, pp. 502-511, 2010/09/01 2010.

[154] J. Jin, F. Feng, J. Zhang, S. Yan, W. Na, and Q. Zhang, "A Novel Deep Neural Network Topology for Parametric Modeling of Passive Microwave Components," *IEEE Access,* vol. 8, pp. 82273-82285, 2020.

[155] D. M. Pozar, *Microwave Engineering*, 4 ed. USA: John Wiley & Sons, 2012.

[156] M. T. Hagan and M. B. Menhaj, "Training feedforward networks with the Marquardt algorithm," *IEEE Transactions on Neural Networks,* vol. 5, pp. 989-993, 1994.

[157] Z. Niu, B. Zhang, D. Ji, Y. Yang, Y. Liu, Y. Feng, *et al.*, "A Novel 3-dB Waveguide Hybrid Coupler for Terahertz Operation," *IEEE Microwave and Wireless Components Letters,* vol. 29, pp. 273-275, 2019.

[158] Z. Niu, B. Zhang, K. Yang, Y. Yang, D. Ji, Y. Liu, *et al.*, "Mode Analyzing Method for Fast Design of Branch Waveguide Coupler," *IEEE Transactions on Microwave Theory and Techniques,* vol. 67, pp. 4733-4740, 2019.

[159] S. Taek-Young, K. Jae-Ho, K. Sang-Hyuk, L. Jae-Bong, and P. Jun-Seok, "Design of a novel lumped element backward directional coupler based on parallel coupled-line theory," in *2002 IEEE MTT-S International Microwave Symposium Digest (Cat. No.02CH37278)*, 2002, pp. 213-217 vol.1.

[160] N. Marcuvitz, *Waveguide handbook* vol. 10. USA: The Institution of Engineering and Technology, 1986.

[161] H. Y. Tsai, T. Y. Huang, and R. B. Wu, "Varactor-Tuned Compact Dual-Mode Tunable Filter With Constant Passband Characteristics," *IEEE Transactions on Components, Packaging and Manufacturing Technology,* vol. 6, pp. 1399-1407, 2016.

[162] M. Ohira, S. Hashimoto, Z. Ma, and X. Wang, "Coupling-Matrix-Based Systematic Design of Single-DC-Bias-Controlled Microstrip Higher Order Tunable Bandpass Filters With Constant Absolute Bandwidth and Transmission Zeros," *IEEE Transactions on Microwave Theory and Techniques,* vol. 67, pp. 118-128, 2019.

[163] Y. Wang, J. Hu, and Y. Luo, "A Terahertz Tunable Waveguide Bandpass Filter Based on Bimorph Microactuators," *IEEE Microwave and Wireless Components Letters,* vol. 29, pp. 110-112, 2019.

[164] D. S. Wu, Y. C. Li, Q. Xue, and B. J. Hu, "Balanced Dielectric Resonator Filters With Multiple Reconfigurable Passbands," *IEEE Transactions on Microwave Theory and Techniques,* vol. 70, pp. 180-189, 2022.

[165] S. Nam, B. Lee, C. Kwak, and J. Lee, "Contactless Tuning Plunger and its Application to K-Band Frequency-Tunable Cavity Filter," *IEEE Transactions on Microwave Theory and Techniques,* vol. 67, pp. 2713-2719, 2019.

[166] B. Yassini, M. Yu, D. Smith, and S. Kellett, "A $Ku$ -Band High-$Q$ Tunable Filter With Stable Tuning Response," *IEEE Transactions on Microwave Theory and Techniques,* vol. 57, pp. 2948-2957, 2009.

[167] S. W. Jeong, G. Lee, J. Lee, and J. Lee, "Frequency-Tunable Absorptive Bandpass Filter Using Substrate-Integrated Waveguide Structure," *IEEE Transactions on Microwave Theory and Techniques,* vol. 69, pp. 5351-5359, 2021.

[168] T. Yang and G. M. Rebeiz, "Tunable 1.25–2.1-GHz 4-Pole Bandpass Filter With Intrinsic Transmission Zero Tuning," *IEEE Transactions on Microwave Theory and Techniques,* vol. 63, pp. 1569-1578, 2015.

[169] V. Miraftab and R. R. Mansour, "Fully Automated RF/Microwave Filter Tuning by Extracting Human Experience Using Fuzzy Controllers," *IEEE Transactions on Circuits and Systems I: Regular Papers,* vol. 55, pp. 1357-1367, 2008.

[170] M. Meng and K. L. Wu, "An Analytical Approach to Computer-Aided Diagnosis and Tuning of Lossy Microwave Coupled Resonator Filters," *IEEE Transactions on Microwave Theory and Techniques,* vol. 57, pp. 3188-3195, 2009.

[171] H. M. Hasanien, "Performance improvement of photovoltaic power systems using an optimal control strategy based on whale optimization algorithm," *Electric Power Systems Research,* vol. 157, pp. 168-176, 2018/04/01/ 2018.

[172] D. Oliva, M. Abd El Aziz, and A. Ella Hassanien, "Parameter estimation of photovoltaic cells using an improved chaotic whale optimization algorithm," *Applied Energy,* vol. 200, pp. 141-154, 2017/08/15/ 2017.

[173] N. Kumar, I. Hussain, B. Singh, and B. K. Panigrahi, "MPPT in Dynamic Condition of Partially Shaded PV System by Using WODE Technique," *IEEE Transactions on Sustainable Energy,* vol. 8, pp. 1204-1214, 2017.

[174] X. Zhang and S. Wen, "Hybrid whale optimization algorithm with gathering strategies for high-dimensional problems," *Expert Systems with Applications,* vol. 179, p. 115032, 2021/10/01/ 2021.

[175] J. Zhang and J. S. Wang, "Improved Whale Optimization Algorithm Based on Nonlinear Adaptive Weight and Golden Sine Operator," *IEEE Access,* vol. 8, pp. 77013-77048, 2020.

[176] R. E. Precup, R. C. David, and E. M. Petriu, "Grey Wolf Optimizer Algorithm-Based Tuning of Fuzzy Control Systems With Reduced Parametric Sensitivity," *IEEE Transactions on Industrial Electronics,* vol. 64, pp. 527-534, 2017.

[177] S. Mohanty, B. Subudhi, and P. K. Ray, "A New MPPT Design Using Grey Wolf Optimization Technique for Photovoltaic System Under Partial Shading Conditions," *IEEE Transactions on Sustainable Energy,* vol. 7, pp. 181-188, 2016.

[178] E. Emary, H. M. Zawbaa, and C. Grosan, "Experienced Gray Wolf Optimization Through Reinforcement Learning and Neural Networks," *IEEE Transactions on Neural Networks and Learning Systems,* vol. 29, pp. 681-694, 2018.

[179] W. M. Fathelbab and M. B. Steer, "A reconfigurable bandpass filter for RF/microwave multifunctional systems," *IEEE Transactions on Microwave Theory and Techniques,* vol. 53, pp. 1111-1116, 2005.

[180] W. Lin, K. Zhou, and K. Wu, "Tunable Bandpass Filters With One Switchable Transmission Zero by Only Tuning Resonances," *IEEE Microwave and Wireless Components Letters,* vol. 31, pp. 105-108, 2021.

[181] Y. Xie, F. C. Chen, and Q. X. Chu, "Tunable Cavity Filter and Diplexer Using In-Line Dual-Post Resonators," *IEEE Transactions on Microwave Theory and Techniques,* vol. 70, pp. 3188-3199, 2022.

[182] I. Hunter, *Theory and Design of Microwave Filters*. London, U.K: IET, 2001.

[183] R. Levy and P. Petre, "Design of CT and CQ filters using approximation and optimization," *IEEE Transactions on Microwave Theory and Techniques,* vol. 49, pp. 2350-2356, 2001.

[184] B. Gustavsen and A. Semlyen, "Simulation of transmission line transients using vector fitting and modal decomposition," *IEEE Transactions on Power Delivery,* vol. 13, pp. 605-614, 1998.

[185] P. Zhao and K. L. Wu, "Model-Based Vector-Fitting Method for Circuit Model Extraction of Coupled-Resonator Diplexers," *IEEE Transactions on Microwave Theory and Techniques,* vol. 64, pp. 1787-1797, 2016.

[186] C. Lugo and J. Papapolymerou, "Six-state reconfigurable filter structure for antenna based systems," *IEEE Transactions on Antennas and Propagation,* vol. 54, pp. 479-483, 2006.

[187] G. F. Engen and C. A. Hoer, "Thru-Reflect-Line: An Improved Technique for Calibrating the Dual Six-Port Automatic Network Analyzer," *IEEE Transactions on Microwave Theory and Techniques,* vol. 27, pp. 987-993, 1979.

[188] L. Zhu and K. Wu, "Unified equivalent-circuit model of planar discontinuities suitable for field theory-based CAD and optimization of M(H)MIC's," *IEEE Transactions on Microwave Theory and Techniques,* vol. 47, pp. 1589-1602, 1999.

[189] S. Nam, B. Lee, C. Kwak, and J. Lee, "A New Class of K-Band High-Q Frequency-Tunable Circular Cavity Filter," *IEEE Transactions on Microwave Theory and Techniques,* vol. 66, pp. 1228-1237, 2018.

[190] L. Zhu and K. Wu, "Characterization of unbounded multiport microstrip passive circuits using an explicit network-based method of moments," *IEEE Transactions on Microwave Theory and Techniques,* vol. 45, pp. 2114-2124, 1997.

[191] Y. Li and L. Zhu, "A Short–Open Calibration Method for Accurate De-Embedding of 3-D Nonplanar Microstrip Line Structures in Finite-Element Method," *IEEE Transactions on Microwave Theory and Techniques,* vol. 66, pp. 1172-1180, 2018.

[192] L. Lin, K. Wu, and Z. Lei, "Numerical TRL calibration technique for parameter extraction of planar integrated discontinuities in a deterministic MoM algorithm," *IEEE Microwave and Wireless Components Letters,* vol. 12, pp. 485-487, 2002.

[193] X. Feng, K. Wu, and W. Hong, "Domain decomposition FDTD algorithm combined with numerical TL calibration technique and its application in parameter extraction of substrate integrated circuits," *IEEE Transactions on Microwave Theory and Techniques,* vol. 54, pp. 329-338, 2006.

[194] J. Duan and L. Zhu, "Numerical Short-Open-Load (SOL) Calibration Technique for Accurate Extraction of Electrically-Small Planar/Non-Planar Microstrip-Line Circuits," *IEEE Transactions on Microwave Theory and Techniques,* vol. 70, pp. 2067-2076, 2022.

[195] Z. Liu, L. Zhu, G. Xiao, and Q. S. Wu, "An Effective Approach to Deembed the Complex Propagation Constant of Half-Mode SIW and Its Application," *IEEE Transactions on Components, Packaging and Manufacturing Technology,* vol. 6, pp. 109-116, 2016.

[196] Q. S. Wu and L. Zhu, "Numerical De-Embedding of Effective Wave Impedances of Substrate Integrated Waveguide With Varied Via-to-Via Spacings," *IEEE Microwave and Wireless Components Letters,* vol. 26, pp. 1-3, 2016.

[197] Z. Lei, "Guided-wave characteristics of periodic coplanar waveguides with inductive loading - unit-length transmission parameters," *IEEE Transactions on Microwave Theory and Techniques,* vol. 51, pp. 2133-2138, 2003.

[198] Z. Lei and K. Wu, "Characterization of finite-ground CPW reactive series-connected elements for innovative design of uniplanar M(H)MICs," *IEEE Transactions on Microwave Theory and Techniques,* vol. 50, pp. 549-557, 2002.

[199] Z. Lei and K. Wu, "Field-extracted lumped-element models of coplanar stripline circuits and discontinuities for accurate radiofrequency design and optimization," *IEEE Transactions on Microwave Theory and Techniques,* vol. 50, pp. 1207-1215, 2002.

[200] Z. Lei and K. Wu, "A joint field/circuit model of line-to-ring coupling structures and its application to the design of microstrip dual-mode filters and ring resonator circuits," *IEEE Transactions on Microwave Theory and Techniques,* vol. 47, pp. 1938-1948, 1999.

[201] Z. Lei and K. Wu, "Accurate circuit model of interdigital capacitor and its application to design of new quasi-lumped miniaturized filters with suppression of harmonic resonance," *IEEE Transactions on Microwave Theory and Techniques,* vol. 48, pp. 347-356, 2000.

[202] Z. Lei and K. Wu, "Complete circuit model of microstrip-fed slot radiator: theory and experiments," *IEEE Microwave and Guided Wave Letters,* vol. 9, pp. 305-307, 1999.

[203] L. Zhu and K. Wu, "Model-based characterization of CPS-fed printed dipole for innovative design of uniplanar integrated antenna," *IEEE Microwave and Guided Wave Letters,* vol. 9, pp. 342-344, 1999.

[204] R. B. Marks, "A multiline method of network analyzer calibration," *IEEE Transactions on Microwave Theory and Techniques,* vol. 39, pp. 1205-1215, 1991.

[205] J. E. Zuniga-Juarez, J. A. Reynoso-Hernández, M. d. C. Maya-Sanchez, and R. S. Murphy-Arteaga, "A New Analytical Method to Calculate the Characteristic Impedance Zc of Uniform Transmission Lines," 2012.

[206] J. E. Zúñiga-Juárez, J. A. Reynoso-Hernández, J. R. Loo-Yau, and M. C. Maya-Sánchez, "An improved two-tier L-L method for characterizing symmetrical microwave test fixtures," *Measurement,* vol. 44, pp. 1491-1498, 2011/11/01/ 2011.

[207] P. Benedek and P. P. Silvester, "Equivalent Capacitances for Microstrip Gaps and Steps," *IEEE Transactions on Microwave Theory and Techniques,* vol. 20, pp. 729-733, 1972.

[208] A. Gopinath, A. F. Thomson, and I. M. Stephenson, "Equivalent Circuit Parameters of Microstrip Step Change in Width and Cross Junctions (Short Papers)," *IEEE Transactions on Microwave Theory and Techniques,* vol. 24, pp. 142-144, 1976.

[209] Z. Lei and K. Wu, "Short-open calibration technique for field theory-based parameter extraction of lumped elements of planar integrated circuits," *IEEE Transactions on Microwave Theory and Techniques,* vol. 50, pp. 1861-1869, 2002.

[210] A. Benalla and K. C. Gupta, "Multiport network approach for modeling the mutual coupling effects in microstrip patch antennas and arrays," *IEEE Transactions on Antennas and Propagation,* vol. 37, pp. 148-152, 1989.

[211] B. L. A. V. Thielen and G. A. E. Vandenbosch, "Method for the calculation of mutual coupling between discontinuities in planar circuits," *IEEE Transactions on Microwave Theory and Techniques,* vol. 50, pp. 155-164, 2002.

[212] R. C. Hansen, *Phased array antennas*, Second ed.: Wiley, 2009.

[213] A. K. Skrivervik and J. R. Mosig, "Analysis of finite phase arrays of microstrip patches," *IEEE Transactions on Antennas and Propagation,* vol. 41, pp. 1105-1114, 1993.

[214] A. Ishimaru, R. Coe, G. Miller, and W. Geren, "Finite periodic structure approach to large scanning array problems," *IEEE Transactions on Antennas and Propagation,* vol. 33, pp. 1213-1220, 1985.

[215] P. B. Katehi, "Mutual coupling between microstrip dipoles in multielement arrays," *IEEE Transactions on Antennas and Propagation,* vol. 37, pp. 275-280, 1989.

[216] H. Liang and K. Wu, "Modeling of arbitrary-order mutual coupling," in *2008 IEEE MTT-S International Microwave Symposium Digest*, 2008, pp. 1389-1392.

[217] L. Han and K. Wu, "Modeling of mutual coupling of arbitrary order in coupled circuits and array antennas," *International Journal of RF and Microwave Computer-Aided Engineering,* vol. 21, pp. 5-16, 2011.

[218] K. W. C. Roy, "A generalized circuit model development approach with short open thru (SOT) de-embedding technique and its applications," *IEEE Transactions on Microwave Theory and Techniques,* June 2023.

[219] Y. Zhuo, F. Feng, J. Zhang, and Q. J. Zhang, "Parametric Modeling Incorporating Joint Polynomial-Transfer Function With Neural Networks for Microwave Filters," *IEEE Transactions on Microwave Theory and Techniques,* vol. 70, pp. 4652-4665, 2022.

[220] J.-S. H. a. M. J. Lancaster, *Microstrip Filters for RF/Microwave Applications*. New York: Wiley, 2001.

[221] Z. Lei, X. Jianjun, M. C. E. Yagoub, D. Runtao, and Z. Qi-Jun, "Efficient analytical formulation and sensitivity analysis of neuro-space mapping for nonlinear microwave device modeling," *IEEE Transactions on Microwave Theory and Techniques,* vol. 53, pp. 2752-2767, 2005.

[222] J. W. Bandler, M. A. Ismail, J. E. Rayas-Sánchez, and Q.-J. Zhang, "Neural inverse space mapping (NISM) optimization for EM-based microwave design," *International Journal of RF and Microwave Computer-Aided Engineering,* vol. 13, pp. 136-147, 2003/03/01 2003.

[223] J. F. V. Sullca, S. Cogollos, V. E. Boria, and M. Guglielmi, "Compact Dual-Band and Wideband Filters With Resonant Apertures in Rectangular Waveguide," *IEEE Transactions on Microwave Theory and Techniques,* vol. 70, pp. 3125-3140, 2022.

[224] T. Yoneyama, F. Kuroki, and S. Nishida, "Design of Nonradiative Dielectric Waveguide Filters (Short Papers)," *IEEE Transactions on Microwave Theory and Techniques,* vol. 32, pp. 1659-1662, 1984.

[225] J. A. Monsoriu, B. Gimeno, E. Silvestre, and M. V. Andres, "Analysis of inhomogeneously dielectric filled cavities coupled to dielectric-loaded waveguides: application to the study of NRD-guide components," *IEEE Transactions on Microwave Theory and Techniques*, vol. 52, pp. 1693-1701, 2004.

# APPENDIX A LIST OF PUBLICATIONS

1. **Peer-reviewed journal papers:**

(J1) C. Roy and K. Wu, "Homotopy optimization and ANN modeling of millimeter-wave SIW cruciform coupler", *IEEE Transactions on Microwave Theory and Techniques*, vol. 70, no. 11, pp 4751-4764, Nov 2022.

(J2) C. Roy, W. Lin and K. Wu, "Swarm intelligence-homotopy hybrid optimization-based ANN Model for tunable bandpass filters", *IEEE Transactions on Microwave Theory and Techniques*, vol. 71, no. 6, pp 25677-2581, Jan 2023.

(J3) C. Roy and K. Wu, "A generalized circuit model development approach with numerical short open thru (SOT) de-embedding technique and its applications", *IEEE Transactions on Microwave Theory and Techniques* (Accepted – June 2023).

(J4) C. Roy and K. Wu, "High-order equivalent circuit model development accounting for mutual-coupling effects" , *IEEE Transactions on Microwave Theory and Techniques* (Submitted – 23 June, 2023).

(J5) C. Roy and K. Wu, "ANN model based electromagnetic optimization by a field-circuit model mapping", *IEEE Transactions on Microwave Theory and Techniques* (Submitted – 24 June, 2023).

(J6) C. Roy and K. Wu, "A review on Electromagnetics-based microwave circuit design optimization", *IEEE Transactions on Microwave Theory and Techniques* (Submitted – 27 June, 2023).

2. **Conference papers**:

(C1) C. Roy, P. Zhao and K. Wu, "ANN model development for tunable bandpass filter", *51st European Microwave Conference (EuMC),* pp 297-300, April 2022.

(C2) C. Roy and K. Wu, "ANN-enabled Mapping between equivalent circuit model and physical field model for tunable bandpass filter", *IEEE MTT-S International Conference on Numerical Electromagnetic and Multiphysics Modeling and Optimization (NEMO'2023)*. (Accepted-June 2023).